

Vortex Evolution and Heat Transfer Enhancement

in a

Quasi-Two-Dimensional Magnetohydrodynamic Duct Flow

by

Ahmad Hussein Abdul Hamid

A Thesis submitted to Monash University

for the degree of

Doctor of Philosophy

September 2016

Department of Mechanical and Aerospace Engineering

Monash University

To my wonderful family.

Statement of originality

This thesis contains no material which has been accepted for the award of any other degree or diploma at any university or equivalent institution and that, to the best of my knowledge and belief, this thesis contains no material previously published or written by another person, except where due reference is made in the text of the thesis.

Ahmad Hussein Abdul Hamid

September 2016

Copyright notice

© 2016 Ahmad Hussein Abdul Hamid. Except as provided in the Copyright Act 1968, this thesis may not be reproduced in any form without the written permission of the author.

I certify that I have made all reasonable efforts to secure copyright permissions for third-party content included in this thesis and have not knowingly added copyright content to my work without the owner's permission.

*Remember that all models are wrong;
the practical question is how wrong do
they have to be to not be useful.*

George E. P. Box, 1987.

*Knowledge is that which benefits,
not that which is memorized.*

Imam as-Syafi'e, 767–820.

Abstract

The quest for cleaner, cheaper and reliable energy has motivated the development of magnetic confinement fusion reactor technology as a possible means of harnessing the energy produced by nuclear fusion for power generation. It is known that magnetohydrodynamic effects act to reduce the thermal-hydraulic performance of the duct flows within the cooling blankets by greatly increasing the pressure drop and reducing the heat transfer coefficient through Laminarisation of the flow. Despite the considerable efforts that have already been dedicated to the study of convective heat transfer in these flows, a further investigation for a more efficient and practical solution to the aforementioned issues is yet to be carried out. In this thesis, a numerical investigation of an electrically conducting fluid flowing in a heated duct under the influence of a strong magnetic field is presented. The major driving motivation of this work is to propose a better mechanism for improving convective heat transfer transversely from a hot wall into a cooler fluid flowing within the duct.

The idea of heat-transfer enhancement from a duct wall is based on generating intensive vortices parallel to a magnetic field. As a prelude to the heat transfer analysis, the decay of these vortices has been quantified, whereby a vortex decay model has been proposed. The devised model describes the decay behaviour of the peak vorticity within stable wake vortices behind a circular cylinder under the influence of a strong magnetic field. Comparison with published data demonstrates remarkable consistency. The model suggests that the instantaneous spatial decay rate of vorticity is strongly dependent on friction parameter and Reynolds number at their higher and lower ranges, respectively. The model also proposes that far downstream, the vortex decay is mainly due to magnetic damping, where the decay rate asymptotes to the rate described by the Hartmann friction term, and that the viscous dissipation remain important only in the near wake. When the friction parameter is above the critical value, Hartman braking dominates the decay for the entire wake. Further analysis on the model also reveals that this critical friction parameter is dependent on Reynolds number and blockage ratio, and the dependency becomes more apparent at lower ranges of these parameters.

However, these passively generated wake vortices tend to be suppressed by the strong magnetic damping. The potential of current injection to intensify these vortices is therefore explored. The derivation of an analytical solution of the electrical forcing velocity fields and the outcomes from the investigation are presented in Chapter 5.

Electric current enters the flow through electrodes around the base of the cylinder, and radiates outward, imparting a rotational forcing around the electrode due to the Lorentz force. The results indicate that the employment of current injection as a vortex enhancer appears to be principally viable. The results indicate that the imposed magnetic field strength and current injection significantly alter the kinematic behaviour of the wake behind a cylinder. Spectral analysis of the response in the wake of the cylinder to the current injection revealed a distinct spectrum of cylinder lift coefficient in the unlock-in regime. A maximum Nusselt number improvement of almost twofold was observed, with a moderate additional pump power required to drive the flow in the presence of current injection (a maximum additional pressure drop of approximately 30% was recorded).

Following this, the performance of electrically-driven vortex generator without the presence of the cylinder is then evaluated. The only source of vorticity that is responsible for the thinning of the thermal boundary layer is induced by the current injection. The aim is to investigate the sensitivity of the Nusselt number to the variations of the current injection parameters. Findings are presented in Chapter 6 and they revealed a gain in thermal-hydraulic performance over the case when the cylinder is present, particularly for cases with high current amplitude, long pulse widths, and strong magnetic field. This is likely due to the absence of the detrimental nonlinear interaction between the electrically generated vortices and the naturally shed vortices from the cylinder. The results also indicate a maximum pressure drop induced by the current injection of less than 2%, which is an order of magnitude less than the gain in pressure drop due to the employment of the current injection in the presence of a cylinder. Ultimately, this thesis has found that a perturbation system composed solely of electrically generated vorticity is far more effective for increasing heat transfer in high Hartmann number MHD duct flows than systems employing physical obstacles for vortex promotion.

Acknowledgements

I would like to express my special appreciation to my supervisor, Associate Professor Gregory J. Sheard, for his endless support and expertise that are crucial for the completion of this work in due time. Despite his busy time schedule, he has shown an exemplary enthusiasm and patience while proof reading the draft of my papers and thesis. The guidance he has provided will be cherished forever.

Sincere thanks to my second supervisor, Dr Wisam K. Hussam, who has been a great mentor to me and has guided me on the daily basis. His brotherly assistance has made my PhD journey easier and an enjoyable moment. My thanks also extend to Professor Alban Pothérat, Coventry University, for helpful discussion and advice.

I would like to express my gratitude for the financial support provided through the Ministry of Education Malaysia and the Universiti Teknologi MARA, Malaysia. I would also like to acknowledge the Monash e-Research Centre and the National Computational Infrastructure for granting access to their high performance computing facilities, which were crucial to this research.

Thanks also go to all the individuals and colleagues, particularly to Dr. Tony Vo, Tze Kih Tsai, Mohd Azan Mohammed Sapardi, Zhi Yuen Ng, Oliver Cassels and Mehdi Derakhsan for the many interesting discussions relating to this research, and also for the enjoyable lunches we had together.

In addition to the technical support, this work would not have been possible without the enduring love and prayers I have received from home. Words cannot express how grateful I am to my family, particularly my mother Maziah Waad and my in-laws Kudiran Jaiz and Sutimah Ismail for all the sacrifices that they've made and love they've given me.

My wife, Nor Hayati Kudiran has been my dearest assistant. She has inspired me to continue to strive for excellence and has always held my goals as her goals. In addition, my lovely children, Aisyah, Aminah, Hamzah, Sofiyah and Mariyah have been my continual source of inspiration. Thank you for understanding on those times when I was writing this thesis instead of playing.

Last, and above all, I must give my thanks to God, from whom all blessing flow. It has only been through faith that I have known which direction to travel. May my future endeavors always be a testament to His glory.

Publications arising from thesis

Peer-reviewed journal papers

HAMID, A. H. A., HUSSAM, W. K., POTHÉRAT A. & SHEARD, G. 2015 Spatial evolution of a quasi-two-dimensional Kármán vortex street subjected to a strong uniform magnetic field. *Phys. Fluids* **27**, 053602.

HAMID, A. H. A., HUSSAM, W. K. & SHEARD, G. 2016 Combining an obstacle and electrically driven vortices to enhance heat transfer in a quasi-two-dimensional MHD duct flow. *J. Fluid Mech.* **792**, 364–396.

HAMID, A. H. A., HUSSAM, W. K. & SHEARD, G. 2016 Heat transfer augmentation of a quasi-two-dimensional MHD duct flow via electrically driven vortices (published online), DOI: 10.1080/10407782.2016.1214518. *Numer. Heat Tr. A-Appl.*

Peer-reviewed conference papers

HAMID, A. H. A., HUSSAM, W. K. & SHEARD, G. 2014 Vortex decay in quasi-2D MHD ducts: Application to Kármán vortex streets behind turbulence promoters. In *Proceedings of the 19th Australasian Fluid Mechanics Conference (19th AFMC)* (Eds: H. Chowdhury & F. Alam, Pub: Australasian Fluid Mechanics Society, ISBN: 978-0-646-59695-2, Paper 197), RMIT University, Melbourne, Australia, 8-11 December 2014.

HAMID, A. H. A., HUSSAM, W. K. & SHEARD, G. 2014 Dynamics of a quasi-two-dimensional wake behind a cylinder in an MHD duct flow with a strong axial magnetic field. In *Proceedings of the 19th Australasian Fluid Mechanics Conference (19th AFMC)* (Eds: H. Chowdhury & F. Alam, Pub: Australasian Fluid Mechanics Society, ISBN: 978-0-646-59695-2, Paper 198), RMIT University, Melbourne, Australia, 8-11 December 2014.

HAMID, A. H. A., HUSSAM, W. K. & SHEARD, G. 2014 Heat transfer augmentation of MHD duct flow via current injection. In *Proceedings of the 13th International Symposium on Fluid Control, Measurement and Visualization (FLUCOME2015)* (Eds: Y. Haik, Pub: Qatar University, 277–286), Qatar University, Doha, Qatar, 15-18 November, 2015.

HAMID, A. H. A., HUSSAM, W. K. & SHEARD, G. 2014 Convective heat transfer enhancement via electrically driven vortices in an MHD duct flow. In *Proceedings of the Eleventh International Conference on CFD in the Minerals and Process Industries* (Eds: C. B. Solnordal, P. Liovic, G. W. Delaney, S. J. Cummins, M. P. Schwarz and P. J. Witt, Pub: CSIRO, Australia, 163HAM), Melbourne Convention and Exhibition Centre, Melbourne, Australia, 7-9 December, 2015.

HAMID, A. H. A., HUSSAM, W. K. & SHEARD, G. 2014 Current injection vortex promoter for heat transfer enhancement in a magnetohydrodynamic duct flow. In *Proceedings of the Fifth International Conference on Advances in Civil, Structural and Mechanical Engineering (ACSM 2016)* (Eds: R. Kumar, Pub: IRED-CPS, United States of America, ACSM -16-218), Hotel Lebua at State Tower, Bangkok, Thailand, 24-25 September, 2016.

Nomenclature

SI units were used throughout this work. Parameters not listed here are denoted explicitly in the text.

Symbol	Description
<i>Acronyms</i>	
EMF	Electromotive force
GLL	Gauss-Legendre-Lobatto
HD	Hydrodynamic
ITER	International Thermonuclear Experimental Reactor
MHD	Magnetohydrodynamic
RSE	Relative standard error
<i>Miscellaneous symbols</i>	
§	Thesis section
<i>Mathematical symbols</i>	
erf	Gauss error function
\int	Integration
∇	Vector gradient operator (grad)
∇^2	Del squared (or div grad) operator
$\sum_{i=a}^b$	Sum of arguments with i incrementing from a to b
W	Lambert W function
<i>Greek symbols</i>	
\mathcal{O}	Order
α	Duct aspect ratio ($\alpha = 2L/a$)
α_{LO}	Lamb–Oseen constant
β	Blockage ratio ($\beta = d/2L$)
β_L	Lin parameter
δ	Boundary layer thickness

Continued on the next page.

Continued from previous page.

Symbol	Description
δ_{Ha}	Hartmann boundary layer thickness
δ_S	Shercliff boundary layer thickness
ε	Approximation error of integrals
η	Efficiency index
η^*	Overall efficiency index
κ_T	Thermal diffusivity
λ	Cylinder wake wavelength
μ	Fluid dynamic viscosity
μ_m	Magnetic permeability
ν	Fluid kinematic viscosity
Φ	Electrical potential
ψ_0	Scalar potential
ρ	Density
ϱ	Real variable in equation solved to find Gauss-Legendre-Lobatto quadrature points
ϱ_i	i^{th} Gauss-Legendre-Lobatto quadrature points (or zeroes)
σ	Electrical conductivity
σ_i	Angular oscillation frequency during the linear growth phase
σ_r	Linear growth rate of the perturbation
θ	Temperature
θ_w	Heated wall temperature
θ_0	Cold wall temperature
Γ	Circulation
τ	Current injection pulse width
τ_{2D}	2-dimensionality establishment time
τ_H	Hartmann damping time
τ_J	Joule damping time
τ_U	Inertia or eddy turnover time
τ_ν	Viscous diffusion time
ξ	Vorticity

Continued on the next page.

Continued from previous page.

Symbol	Description
ξ_p	Peak vorticity
χ	Electrode streamwise coordinate
ζ	Electrode transverse coordinate
ω_f	Current forcing frequency
<i>Roman symbols</i>	
a	Duct height (out-of-plane)
a_n	Fourier cosine series expansion coefficient
\mathbf{A}	Vector potential
A	Complex amplitude in Landau equation
$ A _{\text{sat}}$	Saturation amplitude
b_n	Fourier sine series expansion coefficient
B_0	Imposed magnetic field
B_i	Induced magnetic field
B	Magnetic field strength
c	Landau constant
c'	Velocity of light
C_D	Cylinder drag coefficient
$C_{D,p}$	Pressure component of drag coefficient
$C_{D,\text{visc}}$	Viscous component of drag coefficient
C_L	Cylinder lift coefficient
C_p	Constant pressure specific heat
D	Current pulse duty cycle
d_c	Vortex core diameter
\mathbf{E}	Electrical vector field
\mathbf{E}_r	Effective electrical vector field
Ec	Eckert number
f	Vortex shedding frequency
f_f	Current injection frequency
f_0	Natural vortex shedding frequency
F	Normalized forcing frequency

Continued on the next page.

Continued from previous page.

Symbol	Description
F_L	Lift force
G	Gap between a cylinder and a heated wall
G_e	Spacing between two adjacent electrodes
G/d	Gap ratio
h	Vortex street lateral spacing
h/l	Spacing ratio
H	Friction parameter
H_{cr}	Critical friction parameter
Ha	Hartmann number
HR	Heat transfer enhancement ratio
HR^*	Overall heat transfer enhancement ratio
I	Current injection amplitude
\mathbf{j}	Current density vector
k	Thermal conductivity
l	Vortex street longitudinal spacing
l_r	Cubic saturation term in Landau equation
l_x	Streamwise electrode position
l_y	Transverse electrode position
L	Half duct width
L_F	Vortex street formation length
L_d	Length of downstream flow region
L_u	Length of upstream flow region
L_w	Length of duct ($L_u + L_d$)
\mathcal{L}^2	Integral of velocity magnitude throughout the domain
M	Mean absolute percentage deviation
n	Number of Hartmann layers
n_ξ	Number of cycles of shed vortices
N	Interaction parameter
N_d	Interaction parameter based on cylinder diameter

Continued on the next page.

Continued from previous page.

Symbol	Description
N_p	Number of nodes per element employed in computations
N_t	True interaction parameter
Nu	Time-averaged Nusselt number
Nu_0	Time-averaged Nusselt number for a base case with a cylinder
Nu_0^*	Time-averaged Nusselt number for a base case with no cylinder
Nu_w	Time-averaged local Nusselt number
$\overline{Nu_x}$	Local instantaneous Nusselt number
N_Γ	Interaction parameter based on circulation
p	Pressure
Δp	Time-averaged pressure drop
Δp_0	Time-averaged pressure drop for a base case with a cylinder
Δp_0^*	Time-averaged pressure drop for a base case with no cylinder
P	Monitored parameter
P_{heat}	Heat power
P_{flow}	Pumping power
ΔP_{net}^*	Overall net power enhancement
P_x	Driving pressure gradient
P_{Q-1}	Legendre Polynomial of order $(Q - 1)$
PR	Pressure penalty ratio
PR^*	Overall pressure penalty ratio
Pe	Peclet number
Pr	Prandtl number
Pr_m	Magnetic Prandtl number
q	Electric charge density
r	Radial ordinate
r_c	Vortex core radius
r_e	Electrode radius
r_{max}	Radius at which the tangential velocity is maximum
Re	Reynolds number

Continued on the next page.

Continued from previous page.

Symbol	Description
Re_{cr}	Critical Reynolds number for the onset of vortex shedding
Re_d	Reynolds number based on cylinder diameter
Re'_d	MEan effective Reynolds number
Re_L	Reynolds number based on half duct width
Re_Γ	Reynolds number based on circulation
Rm	Magnetic Reynolds number
St	Srouhal number
s	Spacing between two adjacent cylinders
S	Lundquist number
t	Time
T_0	Period of an oscillating flow
T	Period of a current oscillation
u	x -direction velocity component
u_p	x -direction velocity component normalized by the driving pressure gradient
u_r	radial velocity component
u_θ	tangential velocity component
$u_{\theta,\max}$	maximum tangential velocity
\mathbf{u}	Velocity vector
\mathbf{u}_\perp	Velocity projected onto (x,y) plane
\mathbf{u}^*	Velocity field at first substep
\mathbf{u}^{**}	Velocity field at second substep
\mathbf{u}_0	Force vector field
U_0	Peak fluid velocity at duct inlet
U_{avg}	Area-averaged velocity
U_ξ	Wake advection velocity
v	y -direction velocity component
w_i	i^{th} Gauss–Legendre–Lobatto weighting coefficient
x	Streamwise coordinate
x_{cr}	Critical transition location

Continued on the next page.

Continued from previous page.

Symbol	Description
x_d	Streamwise coordinate nondimensionalized with the cylinder diameter
y	Transverse coordinate
z	Spanwise coordinate

Contents

1	Introduction	1
1.1	MHD duct flow	1
1.2	Fusion-relevant MHD duct flow governing parameters	5
1.3	Statement of the problem	7
1.4	Aims of the research	8
1.5	Research delimitations	8
1.6	Structure of the thesis	9
2	A review of the literature	11
2.1	Cylinder vortex shedding in hydrodynamic flows	11
2.1.1	Formation region	12
2.1.2	Stable region	15
2.1.3	Unstable region	17
2.2	MHD duct flow	17
2.3	Bluff body wake flow in an MHD duct	18
2.3.1	Vortex shedding dynamics	19
2.3.2	Decay of wake vortices	21
2.4	Heat transfer in MHD duct flows	25
2.5	Heat transfer enhancement using a bluff body	26
2.6	Heat transfer enhancement by electromagnetic promoters	29
2.7	Review summary	32
3	Methodology	35
3.1	Magnetohydrodynamic flow equations	35
3.1.1	MHD flow at low- Rm	39
3.1.2	Analytical solutions of electrically insulated MHD duct flows	40
3.1.3	A quasi-two-dimensional MHD duct flow model	43
3.2	The governing equations	44
3.3	Numerical scheme	46
3.3.1	Spatial discretisation	47
3.3.2	Temporal discretisation	48
3.4	Numerical solver validation	49

3.4.1	Hydrodynamic validation tests	50
3.4.2	Magnetohydrodynamic validation tests	50
3.5	Chapter summary	55
4	Spatial evolution of quasi-2-D Kármán vortex street	57
4.1	Problem setup	58
4.2	Grid resolution study	59
4.3	Stability analysis	60
4.4	Dynamics of the wake flow	64
4.4.1	Shedding frequency analysis	65
4.4.2	Vortex distributions	68
4.5	Decay of wake vortices	71
4.5.1	Analytical solution for vortex decay in a quasi-2-D flow	71
4.5.2	Analytical model for the decay of wake vortices	75
4.5.2.1	Derivation	75
4.5.2.2	Validation of the model	82
4.5.3	Suggestions for the spacing in periodic arrays of cylindrical vortex promoters	87
4.5.4	Interpretation of the model	89
4.5.5	Comparison with three-dimensional data at low and moderate interaction parameter	96
4.6	Chapter summary	100
5	Electrically augmented cylinder wake vortices	103
5.1	Problem setup	103
5.2	Electrical forcing velocity field	104
5.3	Validity of the forcing field in a quasi-2-D domain	108
5.4	Quantification of duct flows thermal-hydraulic performance	111
5.5	Domain size study	112
5.6	Grid resolution study	112
5.7	Results	114
5.7.1	Base cases	114
5.7.2	Effects of the current injection frequency and amplitude on heat transfer	116
5.7.2.1	Shedding frequency analysis	121
5.7.3	Effects of the current injection amplitude and gap ratio on heat transfer	124
5.7.4	Effects of the current injection pulse width and frequency on heat transfer	127

5.7.5	Effects of the electrode position relative to the cylinder on heat transfer	130
5.7.6	Effects of friction parameter and Reynolds number on heat transfer	132
5.7.7	Power and efficiency analysis	136
5.8	Chapter summary	139
6	Convective heat transfer enhancement via electrically driven vortices	141
6.1	Problem setup	142
6.2	Grid resolution study	142
6.3	Results	142
6.3.1	Base cases	142
6.3.2	Comparisons with the obstructed duct flow cases	145
6.3.2.1	Thermal performance	145
6.3.2.2	Vortex trajectory and decay	153
6.3.3	Reynolds number dependence	156
6.3.4	Effects of the current injection profile and frequency on heat transfer	161
6.3.5	Effects of the electrode transverse position on heat transfer . . .	165
6.3.6	Power and efficiency analysis	167
6.4	Chapter summary	170
7	Conclusions	173
7.1	Vortex dynamics	173
7.1.1	Dynamics of naturally shed vortices	173
7.1.2	Dynamics of electrically augmented/driven vortices	174
7.2	Vortex decay	175
7.2.1	Decay of naturally shed vortices	175
7.2.2	Decay of electrically augmented/driven vortices	176
7.3	Thermal analysis	176
7.3.1	Dependency on governing parameters	176
7.3.2	Obstructed against unobstructed duct flows with current injection	177
7.4	Power and efficiency analysis	178
7.5	Directions for future work	178
	Appendices	181
A	Fourier series representation of a modified square wave	183
B	Analytical solution of forcing velocity fields from a periodic array of electrodes	185

Chapter 1

Introduction

In this thesis, the duct flow of electrically conducting fluid subjected to a uniform strong magnetic field is numerically investigated. The following section introduces the overview of magnetohydrodynamic concepts and its relevant applications. Following this, the statement of the problem considered in this thesis is provided and the aims of the investigation are stated. Finally, the structure of the thesis is outlined.

1.1 MHD duct flow

Magnetohydrodynamics (MHD) covers phenomena in electrically conducting fluids that interact with magnetic fields. The term “magnetohydrodynamic” was first introduced by Hannes Alfvén (1908 - 1995), winner of the 1970 Nobel Prize in Physics for his work on MHD. The coupled effects of the dynamics of electrically conducting fluids and electromagnetism see MHD flow problems deserving specific attention quite apart from their hydrodynamic (HD) counterparts. Broadly speaking, the fluid-magnetic fields interaction occurs either naturally or in a controlled environment. An example of the former case are the interaction that occur in the interstellar medium, where the presence of magnetic fields influence many astrophysical phenomena. In the latter case, magnetic fields are used either to control electrically conducting fluids (typically liquid metals) in materials processing or to confine high-temperature plasma in magnetic-confinement fusion reactors. In the context of metal casting operations, the direction and the strength of the imposed magnetic fields are varied to control the stability, mixing rate or velocity of the flow of interest (Davidson 1999). The ultimate goal is high-quality end product (e.g. steel or aluminum slabs).

However, in the context of a fusion reactor, which is the main motivation of the present study, the plasma is confined within a vacuum chamber by a series of magnetic

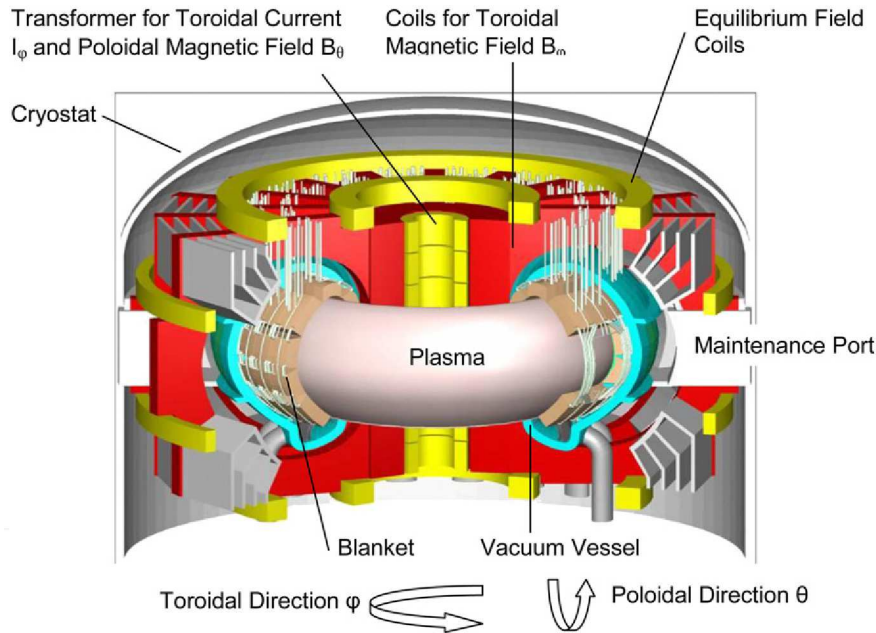


FIGURE 1.1: Typical tokamak fusion reactor for electrical power generation, where the plasma is confined in the shape of a torus by strong magnetic fields. This figure is reproduced from Dobran (2012) with permission from Elsevier.

fields due to its very high temperature (which can reach values of the order of 10^8 K; Dobran 2012). Magnetic confinement fusion is one of two major concepts of confining plasma, the other being inertial confinement. In the more developed tokamak magnetic confinement system (Dobran 2012), the chamber has a torus shape (refer Figure 1.1). In this configuration, the plasma is confined by toroidal and poloidal magnetic fields which are generated by both electromagnets that surround the breeding blanket and an electrical current flowing in the plasma itself. The current is induced by field coils at the centre of the torus.

In a deuterium-tritium fusion reactor, the main fuels are the hydrogen isotopes deuterium and tritium. The deuterium can be extracted from water using electrolysis, where 1 part in 6700 of water is deuterium. Considering the fact that the total volume of water in the oceans is about 1.5 billion cubic kilometers (Simon 1975), this amounts to over 10^{15} tons of deuterium - enough to supply the energy requirements for over trillion years (based on the current energy consumption of approximately 3×10^{11} GJ; McCracken & Stott 2005). However, the tritium, which is the radioactive isotope of hydrogen, does not occur naturally on Earth. Hence, it is produced in situ in the

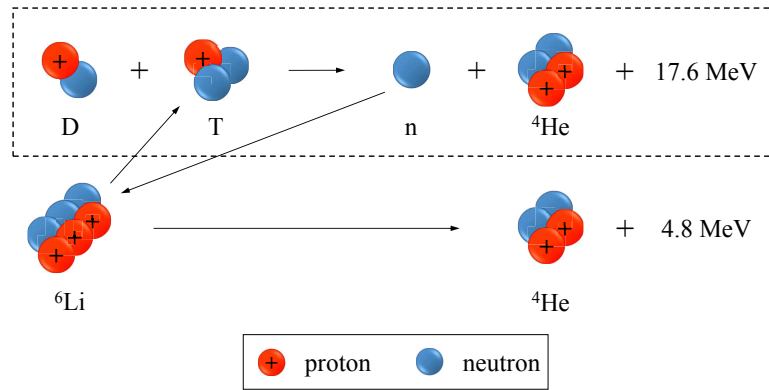


FIGURE 1.2: The overall fusion reactions, which consist of the reactions between deuterium (D) and tritium (T), yields an inert gas helium-4 (⁴He) and a neutron (n), with release of 17.6 mega electronvolts of energy (reaction within the box), and the reaction between neutrons and lithium-6 (⁶Li), producing helium-4 and tritium, and releasing 4.8 mega electronvolts of energy.

reactor (Barleon *et al.* 1996). The fuels are injected into a near-vacuum within the fusion chamber. In a high-temperature environment, these fuels become ionized and form a plasma. The fusion process takes place and the reaction produces helium, freeing a neutron and releasing a substantial amount of energy (the reaction is shown schematically in Figure 1.2).

Some of the energy from the fusion reaction is transferred to the coolant, which is typically lithium or lithium lead, through high-energy neutrons that bombard the plasma facing wall and heat them (refer Figure 1.3). The heat is then used to produce superheated steam via a heat exchanger, which is used to drive a steam turbine and produce electricity. In the cooling blanket, the neutrons released from the fusion reaction are absorbed by lithium to produce tritium; hence the name “breeding blanket” (the reaction is also shown schematically in Figure 1.2). The plasma exhaust is removed from the chamber and processed to extract the deuterium for re-injection into the fuelling cycle.

Lithium ducts within the cooling blanket module are arranged in either pure poloidal direction or in a combination of poloidal-radial-toroidal direction (Malang *et al.* 1991). In the former arrangement, which is proposed for the International Thermonuclear Experimental Reactor (ITER) self-cooled blanket (Hua & Gohar 1995), lithium flows in a poloidal direction perpendicular to the main magnetic field that is oriented in a toroidal direction. The cooling blanket consists of various duct flow geometries, such as

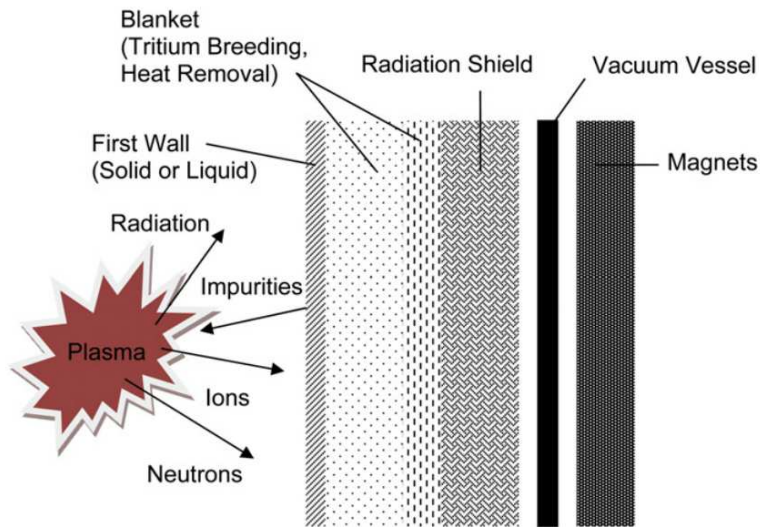


FIGURE 1.3: Deuterium-tritium fusion blanket module, which mainly consists of a plasma facing wall (the first wall), lithium blanket for cooling and breeding tritium purposes and shield for radiation protection. This figure is reproduced from Dobran (2012) with permission from Elsevier.

circular and rectangular ducts, expansions and contractions, single and multi-channel bends, manifolds and 180° U-turns, as depicted in Barleon *et al.* (1996). MHD flows in a constant-area cross-section rectangular duct in transverse uniform magnetic fields have received the most attention to date, both theoretically and experimentally (Kirillov *et al.* 1995; Cuevas *et al.* 1997; Mück *et al.* 2000; Bhuyan & Goswami 2008; Dousset & Pothérat 2008; Kobayashi 2008; Moreau *et al.* 2010; Hussam *et al.* 2012a; Chatterjee & Chatterjee 2013; Chatterjee *et al.* 2013; Kanaris *et al.* 2013; Chatterjee & Gupta 2015). The magnetic field penetrates the blankets and induces electric currents in the ducts. The interaction between the induced electric current and the applied magnetic field results in an electromagnetic Lorentz force. This force has been shown to cause a degradation in the thermal-hydraulic performance of the blanket module (Malang & Tillack 1995). Great attention has been devoted to the aforementioned problems due to their importance in controlling the reactor core temperature. Suggested methods to enhance the performance of the cooling blanket are reviewed in § 2.5 and § 2.6.

Furthermore, the Lorentz force balances the pressure gradient in the core. Consequently, the flow can be split into a quasi-inviscid core flow and thin boundary layers. These layers include Hartmann layers, which adjoin solid walls perpendicular to the magnetic field, and other layers at walls parallel to the magnetic field, known as Shercliff

layers (Shercliff 1953). The thickness of the Hartmann layers is inversely proportional to the intensity of the imposed magnetic field (Shercliff 1953). Under fusion-relevant conditions, these layers are very thin. From a numerical point of view, resolving such a thin layer would indeed incur very large computational costs. Thus, such flows are often treated as quasi-two-dimensional (quasi-2-D). In this approach, the flow quantities in the core and the boundary layers are averaged, yielding an additional term in the two-dimensional momentum equation that accounts for the Hartmann wall friction (Sommeria & Moreau 1982). The details of the approach are described in § 3.1.3.

1.2 Fusion-relevant MHD duct flow governing parameters

MHD duct flows may be characterised by three non-dimensional parameters. The first is the Reynolds number,

$$Re = \frac{uL}{\nu}, \quad (1.1)$$

which quantifies the ratio of inertial to viscous forces. Here u and L denote typical velocity and characteristic length scales for the flow and ν is the kinematic viscosity of the fluid (here liquid metal). In the present study, the length scale is characterised by either the half duct width L or the cylinder diameter d , depending on the configuration of the flow problem being considered. The former is denoted by Re_L , and the latter by Re_d .

The second parameter is the Hartmann number, which is defined as the square root of the ratio of electromagnetic force to viscous force, i.e.

$$Ha = aB\sqrt{\frac{\sigma}{\rho\nu}}, \quad (1.2)$$

where B is the imposed magnetic field, a is the out-of-plane duct depth (in the magnetic field direction), while σ and ρ are electrical conductivity and density of the liquid metal, respectively. This parameter is also sometimes expressed as

$$M = \frac{aB}{2}\sqrt{\frac{\sigma}{\rho\nu}} = \frac{Ha}{2}. \quad (1.3)$$

In the context of quasi-two-dimensional MHD duct flow, the more relevant parameter than the Hartmann number is the friction parameter (Poth erat 2007),

$$H = n \left(\frac{\alpha}{2} \right)^2 Ha, \quad (1.4)$$

where n is the number of Hartmann walls (e.g. $n = 2$ for a closed duct; $n = 1$ for a free-surface channel flow) and $\alpha = 2L/a$ is the aspect ratio of the rectangular duct cross-section.

The ratio of electromagnetic force to inertia force yields the third important parameter in MHD duct flows, the *Stuart* number or interaction parameter,

$$N = \frac{Ha^2}{Re} = \frac{\sigma B^2 a}{\rho u}. \quad (1.5)$$

Two further parameters of importance are the magnetic Reynolds number and the Lundquist number. These characterize the relative importance of magnetic advection to diffusion, and are respectively defined as

$$Rm = \sigma \mu_m u L, \quad (1.6)$$

and

$$S = Ha \sqrt{Pr_m}, \quad (1.7)$$

where μ_m is the magnetic permeability and $Pr_m = Rm/Re$ is the magnetic Prandtl number. Although these numbers do not directly govern the present flow problems, their relevance is demonstrated in § 1.5 and § 3.1.1.

In the present study, the fluid of interest is the eutectic alloy $\text{Ga}^{68}\text{In}^{20}\text{Sn}^{12}$. This low-melting point liquid metal is chosen primarily due to its wide employment in MHD laboratory experiments, e.g. in Frank *et al.* (2001); Morley *et al.* (2008); Klein *et al.* (2009). The relevant physical properties of the $\text{Ga}^{68}\text{In}^{20}\text{Sn}^{12}$ at 20°C (Lyon 1952) are summarised in Table 1.1.

Property	Symbol	Value	Unit
Prandtl number	Pr	0.022	Dimensionless
Density	ρ	6.3632×10^3	kg m^{-3}
Electrical conductivity	σ	3.30737×10^6	$\Omega^{-1}\text{m}^{-1}$
Kinematic viscosity	ν	3.4809×10^{-7}	m^2s^{-1}

TABLE 1.1: Properties of eutectic alloy GaInSn.

1.3 Statement of the problem

The study of MHD duct flows in the presence of a transverse magnetic field has received increased attention owing to its practical applications in MHD generators, pumps, metallurgical processing and magnetic confinement fusion reactors. In coolant blankets of fusion reactors, for example, the fundamental physics of MHD results in Laminarisation of the coolant flow that is used to evacuate the heat generated by the nuclear fusion (Branover & Gershon 1979). This yields substantial reduction in the thermal-hydraulic performance of the blankets. Techniques to promote turbulence or vortical structures include the insertion of bluff bodies or grid bars in a duct and by employing wall protrusions (Kolesnikov & Tsinober 1974; Sukoriansky *et al.* 1989; Branover *et al.* 1995; Huang & Li 2010). However, the heat transfer performance deteriorates with increasing magnetic field strength due to the fact that the wake vortices tend to be suppressed by Hartmann damping force (Mutschke *et al.* 1997). In the case of bluff bodies obstacle, the transition to the steady state wake flow can be delayed by oscillating the bodies (Hussam *et al.* 2012a). However, employing a mechanical actuator for such turbulisers in a duct faces significant technical obstacles to a practical implementation. Furthermore, the placement of solid bodies in a duct means that enhancement in convective heat transfer is obtained at the expense of significant pressure loss (Malang & Tillack 1995).

An alternative vorticity generation mechanism is by the use of inhomogeneous wall conductivity (Bühler 1996) or vortex generation via electric current injection (Sommeria 1988; Pothérat & Klein 2014). The former is achieved through Kelvin–Helmoltz instabilities, which results in the wake resembling that of Kármán vortex street. However, this mechanism acts passively on the flow and lacks a means to control the ensuing vorticity. In the latter, electric current enters the flow through an electrode embedded in one of the Hartmann walls, radiating outward, imparting a rotational forcing around the electrode due to the Lorentz force. The design and implementation of such a system would avoid the complexity of a mechanically actuated turbulence promoter system. Furthermore, the amount and rate of current injection can be actively controlled based on feedback from the flow conditions. Electrical generation of vortices has already been used to generate vortices parallel to the imposed magnetic field by Sommeria (1988); Pothérat & Klein (2014); Pothérat *et al.* (2005) in the study of decaying vortices, flow stability and MHD turbulence, but not yet in a duct arrangement with sidewall heat-

ing. It is therefore important that a rigorous investigation be conducted to explore the potential of current injection for heat transfer enhancement from a heated sidewall of an MHD duct.

As a prelude to the heat transfer analysis, the dynamics and the decay of a vortical structure in an MHD duct under various flow conditions is quantitatively analysed, owing to the fact that relevant studies are rather scarce. In the hydrodynamic counterpart, considerable research has been conducted into the evolution of cylinder wake vortices, particularly the wake behind a circular cylinder. Hence, for this particular investigation, the vortices are generated from a circular cylinder in order to gain a more complete understanding of this important flow phenomenon.

1.4 Aims of the research

The present study investigates the flow of an electrically conducting fluid in a rectangular duct under the influence of a uniform magnetic field. The main aim is to examine the overall heat transfer enhancement under the various current injection parameters. A further subsidiary aim is to gain better understanding on the stability, evolution and kinematics of vortex shedding of an electrically conducting fluid subjected to a uniform magnetic field.

Specifically, the research will investigate the following aspects in order to fulfill the objectives:

1. The effect of different flow parameters on the global properties of cylinder wake flow, such as the vortex formation length, its trajectory, and the Strouhal number.
2. The spatial decay behaviour of wake vortices at different blockage ratio ($\beta = d/2L$), friction parameter (H), and Reynolds number (Re).
3. The wake behaviour and the associated heat transfer enhancement of combined obstacle and electrically driven vortices.
4. The overall thermal-hydraulic performance enhancement due to vortices generated by a point-electrode current injection alone.

1.5 Research delimitations

In the present investigation, the magnetohydrodynamic cases are simulated across $0.1 \leq \beta \leq 0.4$ (for cases with a cylinder placed in the duct), $500 \leq H \leq 5000$ and

$1500 \leq Re_L \leq 8250$. The magnetic Reynolds number of simulated flows is assumed to be low, whereby the magnetic field is diffusive in nature due to the typical low-velocity liquid metal and relatively small length scale (Davidson 2001). The fluctuating induced magnetic field around the externally applied field is negligible, and therefore, the quasi-static approximation is invoked (Hunt 1965, the details of this approximation is discussed in § 3.1.1). Furthermore, the flow is assumed to be quasi-two-dimensional, which is realized through selecting the combinations of H and Re_L that satisfies the quasi-two-dimensionality conditions (the details of these conditions are provided in § 3.1.3).

However, Alfvén waves might be generated when either the Hartmann number is sufficiently high or strong current pulses are injected into the flow. Their propagation along the magnetic field is governed by the Lundquist number S (Lundquist 1949). For liquid metals, the quasi-static approximation holds when $Ha \leq \mathcal{O}(10^3)$ (Pothérat & Kornet 2015). Taking this constraint into consideration, the magnetic field intensity was limited to $H = 5000$ (which corresponds to $Ha = 10^4$ for $n = 2$ and $\alpha = 1$). It should be noted that the bulk of the present numerical simulations was based on the flow at $H = 500$. It is therefore anticipated that the Alfvén waves, if present, will produce rather limited effects due to a strong dissipation. Moreover, current pulses have been used previously to drive quasi-2-D flows (Sommeria 1988) and no such effect was reported.

For the heat transfer analysis, the Prandtl number is fixed at $Pr = 0.022$ throughout. This choice is motivated by the widespread laboratory use of eutectic alloy Ga⁶⁸In²⁰Sn¹² in MHD duct flow research. This relatively small value of Pr implies that the thermal diffusion rate greatly exceeds the momentum diffusion rate.

1.6 Structure of the thesis

This thesis comprises seven chapters, including three results chapters. These are organised as follows: Chapter 1 (the present chapter) presents the general background of the subject of interest, its motivation and objectives. Following this introductory chapter, works on the wake evolution and its associated heat transfer enhancement in duct flows are reviewed in Chapter 2. Chapter 3 details the numerical strategies used to compute the flow problems and its validation. Chapters 4-6 present the results of the study. Chapter 4 is dedicated to the investigation of the spatial evolution of peak vorticity in

a wake behind a cylinder. Chapter 5 explores the heat transfer characteristics of MHD duct flows with electrically-augmented cylinder wake vortices. Following this, Chapter 6 looks into the potential of current injection to drive vortices for thermal performance enhancement. Finally, Chapter 7 is devoted to conclusion and recommendations for future work.

Chapter 2

A review of the literature

This chapter presents a review of hydrodynamic and magnetohydrodynamic duct flows. The review is categorized into two topics; the evolution of wake vortices, and heat transfer in duct flows.

The chapter begins with a review of the wake flows in the absence of a magnetic field, presented in § 2.1. Next, a review of the MHD duct flow characteristics under various conditions are discussed in § 2.2. § 2.3 presents studies pertaining to the cylinder vortex shedding in an MHD duct, particularly on its dynamics and the subsequent decay. Following this, heat transfer characteristics of MHD duct flows are described in § 2.4. This is followed by a review of various mechanisms to enhance convective heat transfer in these flows, such as a bluff body vortex promoter (presented in § 2.5) and electromagnetic promoters (presented in § 2.6).

The chapter culminates with identification of gaps in the literature.

2.1 Cylinder vortex shedding in hydrodynamic flows

At very low Reynolds numbers, flow around a circular cylinder is steady, attached, and nearly symmetrical upstream and downstream due to the dominance of viscous diffusion over inertia. At $Re \approx 6$, the upstream-downstream symmetry breaks as flow around the cylinder separates, creating a wake comprising a counter-rotating pair of vortices attached to the leeward side of the cylinder (Taneda 1956). These eddies elongate as Re increases, ultimately succumbing to the first instability at $Re \approx 47$ (Gaster 1969), where a regular pattern of vortices known as the Kármán vortex street appears. The vortex street generated from two-dimensional bluff body has long been a subject of interest due to its fundamental academic and practical importance in myriad engineering problems. Analysis of such bluff body wakes are typically divided into three

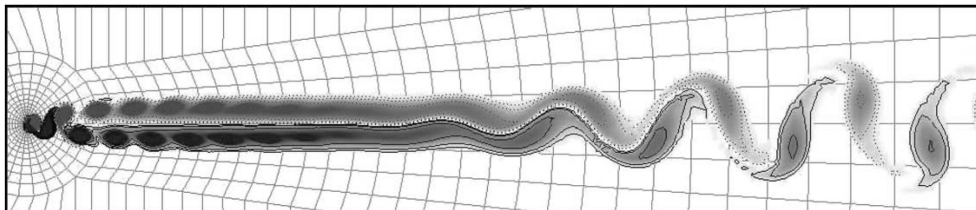


FIGURE 2.1: Vorticity contour of cylinder wake for $Re = 125$. The primary structure (stable Kármán vortex street) breaks down into a nearly parallel shear flow before a secondary vortex street of larger scale appears further downstream. This figure is reproduced from Johnson *et al.* (2004) with permission from Elsevier.

main focus areas: the correlation between drag coefficient, base pressure and shedding frequency; the vortex dynamics, where the formation and re-arrangement process are addressed; and the stability of the mean velocity profile in the wake (Monkewitz & Nguyen 1987).

For Reynolds numbers $50 \lesssim Re \lesssim 150$, wake vortices are stable (Roshko 1954a) and are shed in a half wavelength staggered array (Eisenlohr & Eckelmann 1989). Vortices in viscous fluids are always subjected to a dissipative effect due to viscosity, which results in the gradual decay of their strength. Classically the vortex street within this Reynolds number range has been divided into three distinct regions, namely the formation region immediately behind the cylinder, the stable region, and the unstable region (Schaefer & Eskinazi 1959). Researchers have also identified a distinguishable transition region between the stable and unstable regions (Durgin & Karlsson 1971; Aleksyuk *et al.* 2012). In this region, no velocity fluctuations are measured and the primary vortex street breaks down into an almost parallel shear flow (Zdravkovich 1968; Karasudani & Funakoshi 1994, as depicted in Figure 2.1), where the mean velocity across the wake decreases.

2.1.1 Formation region

The formation region occurs immediately behind the cylinder, where the vorticity dissipates and organises into a coherent structure (Kieft *et al.* 2003) and is laminar for Reynolds number $Re < 300$ (Bloor 1964). The process can be further divided into three stages (Green & Gerrard 1993; Ponta 2006), i.e.

1. The accumulation of vorticity from the separated boundary layers. The vorticity

is accumulated and concentrated as it rolls up around the incipient eddy.

2. The stretching of the vorticity blob. The stretching process which results from the interplay between neighboring vortices is associated with the typical “S” shape of the vorticity.
3. The separation and shedding of this blob from the boundary layer. Following the separation, the vorticity blob that is connected to the incipient vortex is advected into the core which incorporates its vorticity content. At the other end of the vortex, a second vorticity blob is created by the traces of vorticity that fall beyond the confluence point.

Experimental and numerical results revealed that the formation process is essentially two-dimensional, although the ensuing vortices are three-dimensional (Green & Gerrard 1993; Singh & Mittal 2005). The stages are completed within the length L_F , often referred to as the formation length. Several definitions of formation length have been offered, for example:

1. Schaefer & Eskinazi (1959): L_F is defined as a distance between the centre of a cylinder and a point where the minimum spread of paths of vortex centres occurs (i.e. where lateral spacing is minimum. Here the vortex centre is defined as the centre of maximum vorticity). They found that the position of minimum lateral spacing is nearly coincident with the position of maximum downstream velocity fluctuation.
2. Bloor (1964): The formation region is defined as a region of flow inside the wake and the length is taken between the centre of the cylinder and the first appearance of the periodic vortex street, marked by the abrupt decrease in low-frequency irregularities due to three-dimensionalities in the flow. This definition only applies for wakes beyond the stable range, i.e. Re_d greater than $\mathcal{O}(150)$, where the low-frequency irregularities starts to appear.
3. Bearman (1965): L_F is defined as a distance between the rear of a cylinder and the position where the streamwise velocity fluctuation at twice the shedding frequency has maximum amplitude.
4. Gerrard (1978): L_F is the length between centre of a cylinder and a point closest to the cylinder at which irrotational fluid crosses the wake centre line (refer

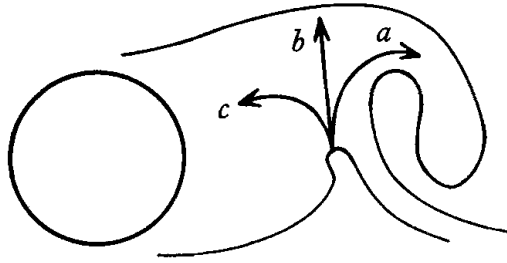


FIGURE 2.2: Vortex shedding formation region at high Re . At low Re , however, the vortices are laminar and the entrainment flow b is negligible compared with entrainment flow a . The fluid enters the region near the rear of the cylinder from the downstream direction at low Re rather than from the side at high Re (Gerrard 1978). This figure is reproduced from Gerrard (1966) with permission from the Cambridge University Press.

Figure 2.2). However, this definition is based purely on flow visualization and becomes less appropriate at lower Re (Green & Gerrard 1993).

5. Green & Gerrard (1993); Kieft (2000): L_F is the distance from the rear of a cylinder to the position of maximum strength of the first shed vortex. They found that this definition is applicable for both low and high Reynolds number.
6. Roshko (1954b): L_F is the distance from a cylinder to the location of minimum mean pressure on the wake axis or centreline.

The formation length plays a significant role in determining the shedding frequency. However, it was proposed that the change in shedding frequency is due to the changes in vorticity transport (Green & Gerrard 1993), which leads to the variation of formation length as a secondary effect. As the level of turbulence increases, the length of the vorticity strand shrinks due to the counter effect of the entrainment rate and the reversed flow. On the other hand, as the Reynolds number increases, the shear layer close to the cylinder tends to dissipate more and the emergence of vorticity blob is delayed, which results in a longer dissipation length. This leads to a higher shedding frequency. However, at a higher Reynolds number, the balancing effect of decreasing formation length and increasing diffusion length makes the shedding frequency tend to a constant (Gerrard 1966).

2.1.2 Stable region

Succeeding the formation region is the stable region, where the longitudinal spacing is constant for a given Reynolds number (Schaefer & Eskinazi 1959; Roshko 1954a). An experimental investigation by Schaefer & Eskinazi (1959) has revealed that in this region, the shedding frequency is preserved and that the advecting velocity of wake vortices is dependant on Reynolds number (its value is about 90% of the free stream velocity). Experimental investigation by Durgin & Karlsson (1971) has also shown that the longitudinal spacing decreases towards the end of the stable region, which extended up to 50 cylinder diameter downstream. The length of the stable region is dependent on the Reynolds number, and the locations where it starts and ends are governed approximately by the empirical relations

$$Re_d \approx \frac{260}{x_d} \quad (2.1)$$

and

$$Re_d \approx \frac{1500}{x_d}, \quad (2.2)$$

respectively (Schaefer & Eskinazi 1959), where Re_d and x_d are respectively the Reynolds number and the streamwise coordinate nondimensionalised with the cylinder diameter. They also found that a complete stable region becomes less visible at $Re \gtrsim 125$.

As the wake vortices advect downstream in a viscous fluid, the lateral spacing between vortex rows tends to widen. Experimentally, measuring them is not a straightforward procedure. Schaefer & Eskinazi (1959) assumed the periphery of a vortex core coincides with the position of maximum velocity fluctuation in order to determine the lateral spacing. However, Durgin & Karlsson (1971) argued that this assumption is not applicable when the vortex is not circular. Instead, the authors have suggested to use the vortex centre, where it coincides with the maximum in the mean vorticity. This assumption has been proven to be applicable for a circular vortex. However, if a non-circular vortex is considered, this assumption overpredicts the lateral spacing of vortices. In general, the trend of the lateral spacing with distance downstream is similar regardless of the Reynolds number. The spacing first decreases to a minimum value in the near-wake region. This is then followed by an increase to a maximum value before decreasing in the far-wake region, as depicted in Figure 2.3.

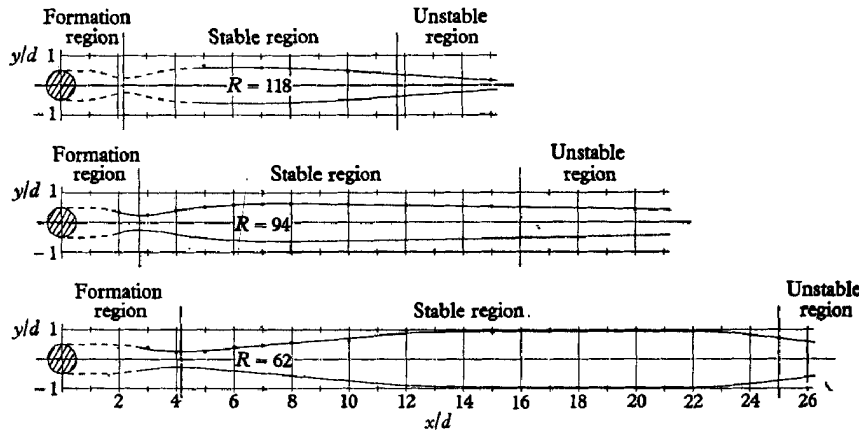


FIGURE 2.3: Lateral spacing of vortex streets behind a circular cylinder for Reynolds numbers as indicated. This figure is reproduced from Schaefer & Eskinazi (1959) with permission from the Cambridge University Press.

Another parameter that is of interest is the spacing ratio, which is defined as the ratio between lateral to longitudinal spacing (h/l) of vortices. This ratio is essential in determining the stability of far-wake vortices (Karasudani & Funakoshi 1994). A value of 0.281 was proposed by von Kármán for the spacing ratio as a wake stability condition (Birkhoff & Zarantonello 1957). This ratio corresponds to $\cosh(\pi h/l) = \sqrt{2}$, a value at which no first-order instability occurs in the equilibrium, i.e. that the relative position of vortices in the wake do not become greatly disturbed. More recently, Kronauer (1964), as cited in Bearman (1966), proposed that the spacing ratio is not constant for the condition of stability, but instead depends on the relative velocity in the wake. The dependency between the spacing ratio and the relative velocity is due to the condition of satisfying the minimum vortex street drag coefficient. By comparing the Strouhal numbers based on the lateral vortex spacing derived from the Kronauer stability condition with the base pressures, Bearman (1966) concluded that the use of the Kronauer stability criterion was partly justified. However, results from previous experimental results revealed that the spacing ratio depends on the Reynolds number (Schaefer & Eskinazi 1959) and the streamwise location of the vortices (Schaefer & Eskinazi 1959; Durgin & Karlsson 1971). Generally, the spacing ratio increases with the distance downstream. However, there is no clear trend in the variation of spacing ratio with Reynolds number.

Furthermore, as the wake vortices are advected downstream, the core of a vortex de-

forms into an elliptic shape. At a critical spacing ratio, the vortex becomes sufficiently slender that it overlaps with its neighboring same-sign vortices to form the aforementioned parallel shear flow (Karasudani & Funakoshi 1994). A theoretical analysis by Durgin & Karlsson (1971) suggested a critical spacing ratio $h/l = 0.366$, where for h/l less than the critical value, the typical vortex street structure is preserved.

Typically, stable wake vortices in the laboratory have the following properties (Chopra & Hubert 1965):

1. spacing ratio $0.28 < l/h < 0.52$,
2. wake advection velocity relative to the bulk flow velocity $0.7 < U_\xi < 0.9$,
3. Lin parameter $10^{-3} < \beta_L < 2.5 \times 10^{-3}$ (the definition of this parameter is introduced in the following chapter),
4. Strouhal number $St \approx 0.2$,

2.1.3 Unstable region

As the vortices advect further downstream, the viscous effect becomes less dominant and this eventually leads to a vortex street breakdown (Durgin & Karlsson 1971). New, larger vortical structures evolve, marking the beginning of the unstable region. This secondary street possesses a lower frequency and a longer wavelength than the primary street. Experimental investigation by Cimbalá *et al.* (1988) found that the formation of the secondary vortex street does not depend directly upon the scale or frequency of the primary shed vortices, but rather it is due to the local hydrodynamic instability of the far wake. They also found that the secondary street possesses a broad frequency spectrum. However, for the case of forced wakes, the pairing of shed vortices has been found to be responsible for the growth of the vortical structures in the far wake (Inoue & Yamazaki 1999).

2.2 MHD duct flow

Magnetohydrodynamic flows in rectangular ducts, amongst many other geometries, have received significant attention in the past due to their wide application (Shercliff 1953; Hunt 1965), especially in the cooling system of poloidal self-cooled blankets (Molokov 1994). The liquid metal flow in the ducts tends to be laminarized due to a strong magnetic field. The stabilizing effect stems from the additional damping in

the form of Hartmann braking due to the interaction between induced electric currents and the applied magnetic field (Sommeria & Moreau 1982; Dellar 2004; Hussain *et al.* 2013). In the limit of high magnetic field strength, a very thin boundary layer on the wall that is perpendicular to the magnetic field direction (the Hartmann layer) dominates the friction in an MHD duct flow (Krasnov *et al.* 2012) and the flow becomes quasi-two-dimensional (with 2D core flow and 3D flow confined in the boundary layers).

An experimental investigation revealed that the transition to a laminar state occurs at $Re/Ha \approx 225$ (with laminar flow at $Re/Ha \lesssim 225$; Brouillette & Lykoudis 1967). However, direct numerical simulations by Krasnov *et al.* (2012) revealed that, in the high-Reynolds number regime ($Re = 10^5$), both the core of the MHD duct flow and the Shercliff layers laminarized due to the imposed magnetic field, while the Shercliff layers remain turbulent (as depicted in Figure 2.4). The Hartmann layer is suppressed strongly by a magnetic field, whereas the sidewall layer is suppressed weakly. This observation supports large-eddy simulations by Kobayashi (2008) for flows of similar configuration. Furthermore, Krasnov *et al.* (2012) concluded that the range of Hartmann number corresponding to such states narrows with decreasing Reynolds number.

2.3 Bluff body wake flow in an MHD duct

The study of bluff body wake flow in an MHD duct is a relatively young area compared to its hydrodynamic counterpart, but has received growing attention from the scientific community due to its practical application including the flows of cooling fluid in fusion power-reactor breeding blankets. Within the blankets, the electrically conducting cooling fluid flows in ducts under a strong plasma-confining magnetic field. The interaction between induced electric currents and the applied magnetic field results in an electromagnetic Lorentz force, which in turn gives a damping effect to the flow and subsequently alters the formation (Yoon *et al.* 2004) and the evolution (Rhoads *et al.* 2014) of the wake vortices. The formation and evolution of wake vortices have been shown to have significant effects on the fluid flow characteristics and heat transfer (Hussam *et al.* 2012a). Thus, an understanding of the dynamics and the subsequent decay of such vortical structures in the wake are crucial in the aspect of real engineering application. The following sections present a review of the dynamics and the decay of wake vortices in these flows.

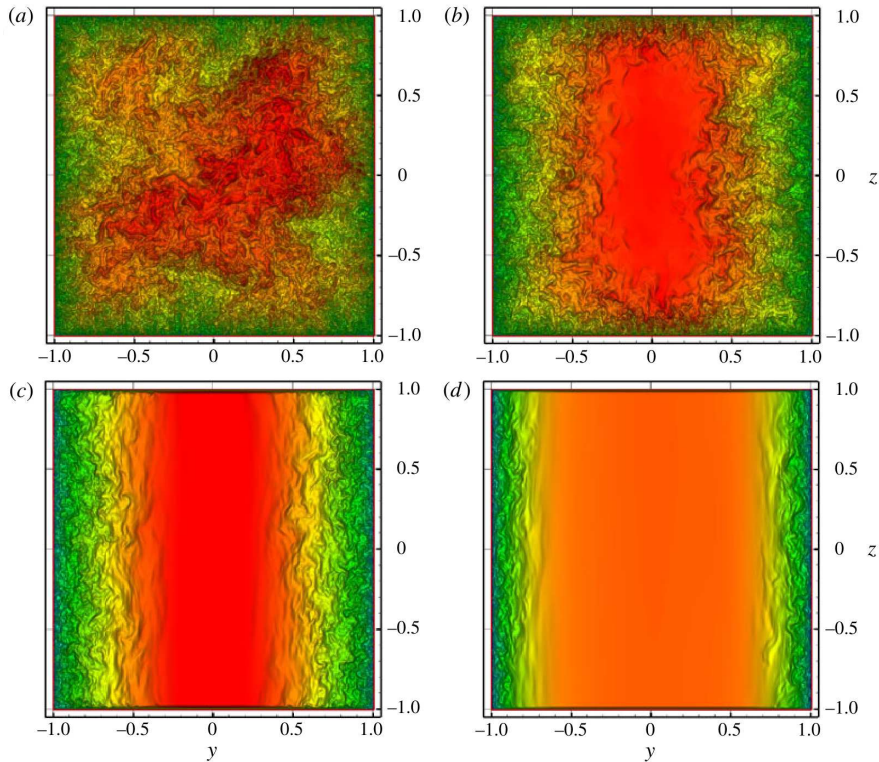


FIGURE 2.4: Instantaneous streamwise velocity of the mid-plane cross-section for Reynolds number $Re = 1 \times 10^5$ and (a) $Ha = 0$ (hydrodynamic flow), (b) $Ha = 100$, (c) $Ha = 200$ and (d) $Ha = 300$. The contour levels range between 0 (blue) and 1.25 (red). Magnetic fields act in the z -direction. In (a), the flow is everywhere turbulent. In (b), both Hartmann and Shercliff layers are turbulent. In (c), only Shercliff layers are turbulent, while the Hartmann layer and the core are laminar. In (d), the Shercliff layer remains turbulent, however its thickness reduces. This figure is reproduced from Krasnov *et al.* (2012) with permission from the Cambridge University Press.

2.3.1 Vortex shedding dynamics

When a strong magnetic field is imposed to an electrically conducting fluid, the resulting cylinder wake possesses a distinct features as compared to the normal hydrodynamic flow. The fundamental difference between the two cases is that in the laminar periodic vortex shedding regime, the rows of counter-rotating vortices in a hydrodynamic flow intersect at the duct centreline and their positions becomes inverted (Camarri & Giannetti 2007), whereas no inversion of the shed vortices is observed when a magnetic field is imposed on the flow. The influence of a magnetic field on the vortex street trajectory has been experimentally investigated by Papailiou (1984), where the vortex street was generated by a cylinder placed in mercury and the magnetic field was aligned

with the cylinder axis. His experiment revealed that the magnetic field tends to reduce the longitudinal and lateral spacing of vortices. However, they found that the magnetic field has a smaller effect on Strouhal number.

Furthermore, in a more recent numerical investigation by Dousset & Poth erat (2008), cylinder wake flows under a homogeneous magnetic field aligned with the cylinder axis have been investigated in the limit of high Hartmann number and high interaction parameter. They found that, for a given Reynolds number, the vortex shedding formation length and shedding frequency increase with decreasing Hartmann number. In their study, the formation length was defined as the distance between the rear of the cylinder and the point of maximum velocity fluctuations, as per Bearman (1965). Similar observation has been made by Yoon *et al.* (2004) for a magnetic field parallel to the streamwise direction.

A more recent three-dimensional direct numerical simulation of liquid metal flow around a circular cylinder by Kanaris *et al.* (2013) revealed a distinct feature of wake formation under the action of the magnetic field. Secondary vortices were formed in the near-wake region as a result of the deformation of the primary vortex core soon after it was shed. This phenomenon occurs for a flow where the inertia and the magnetic damping are relatively significant (i.e. $Ha = 1120$ and $Re_d = 5000$). The resulting wake flow in this regime is rather irregular. A similar observation has been previously reported by Dousset & Poth erat (2008) in their quasi-two-dimensional simulation for the same Reynolds number and Hartmann number. In this regime, which is unique to magnetohydrodynamics, the K arm an vortex street interacts strongly with the Shercliff layers, generating secondary counter-rotating vortices. As these secondary vortices advect downstream, they migrate towards the opposite wall, resulting in an irregular wake pattern that oscillates from one wall to the other (as shown in Figure 2.5).

However, when the magnetic field intensity is decreased for the same Reynolds number (i.e. $Ha = 320$ and $Re_d = 5000$), Kanaris *et al.* (2013) found that the wake is more regular with the lateral spacing between the shed vortices decreasing in the near-wake. They attributed this observation to the fact that at low Hartmann number, the vortex in the formation region exhibits small-scale three-dimensional structures (see Figure 2.6) that cause very strong Joule dissipation. The dissipation extracts energy from the large-scale primary vortex, which makes them less energetic and thus leads to a more regular vortex shedding pattern. This observation has been confirmed by a more

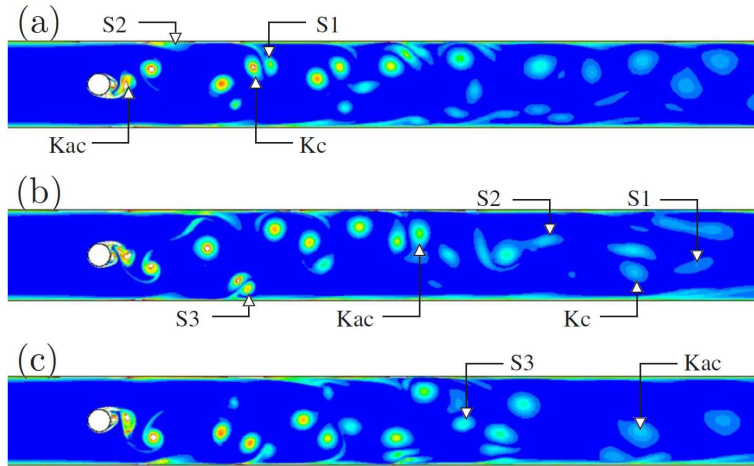


FIGURE 2.5: Absolute vorticity fields of cylinder wakes in an irregular regime ($Ha = 1120$ and $Re_d = 5000$), where secondary vortices are released from the sidewalls (vortices S1 - S3) and interact with the Kármán vortex street (vortices Kac and Kc). Plots in (a), (b) and (c) represent successive stages of the flow at $t = 6.44\tau_H$, $6.67\tau_H$ and $6.90\tau_H$, respectively. τ_H is the Hartmann damping time, a time scale for the damping of two-dimensional vortices in MHD duct flows due to the closing of currents in the Hartmann layer (Sommeria & Moreau 1982). A further discussion on the relevant time scales in MHD flows is presented in § 3.1.3. This figure is adopted from Dousset & Pothérat (2008) with permission from the American Institute of Physics.

recent experimental investigation by Rhoads *et al.* (2014), where small-scale turbulent eddies were present within the vortices when the applied magnetic field is weak.

2.3.2 Decay of wake vortices

The evolution and the decay of vortices in a normal hydrodynamic flow has received considerable attention in previous studies, for example in Lamb (1932); Chopra & Hubert (1965); Holzäpfel (2003); Roushan & Wu (2005); Ponta (2010); Aleksyuk *et al.* (2012). The solution to the vortex strength under the viscous effect is described by the Lamb–Oseen vortex model, where the peak vorticity decreases inversely with time. The dimensional core radius of the wake vortices evolve as $r_c = \sqrt{4\nu t}$, where t is time. The radius of a shed vortex core at an arbitrary time of $t = n_\xi/f$, in which a vortex would have advected to a downstream distance of $n_\xi l$, can be rewritten in terms of the Lin parameter (Chopra & Hubert 1965), i.e.

$$r_c = 2 \left(\frac{U_0}{f} (\beta_L n_\xi)^{1/2} \right), \quad (2.3)$$

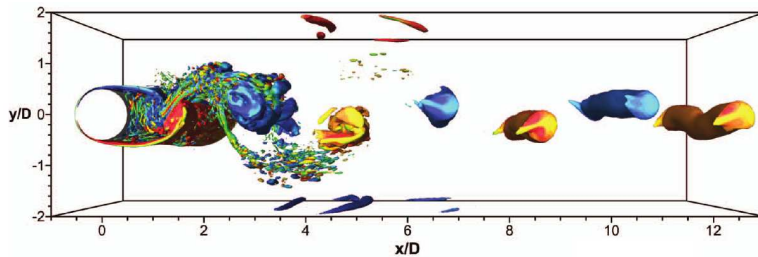


FIGURE 2.6: Instantaneous plots of iso-surfaces of the λ_2 criterion normalised by its absolute minimum for wake flow at $Ha = 320$ and $Re_d = 5000$, depicting small scale three-dimensional structures in the near-wake region. This figure is reproduced from Kanaris *et al.* (2013) with permission from the American Institute of Physics.

where U_0 is the free stream velocity, n_ξ is the number of cycles of shed vortices, f is the shedding frequency, l is the longitudinal spacing between two same-sign vortices and $\beta_L = St/Re$ is the Lin parameter, which is an inherent property of the wake vortices, given the fact that the value is independent of the obstacle size (Chopra & Hubert 1965).

However, when the fluid is electrically conducting and is subjected to a strong magnetic field, the decay of wake vortices perpendicular to the field is accelerated via Joule dissipation (Davidson 1997). However, in the context of fusion applications, the induced currents predominantly reside in the Hartmann layer, and hence Joule dissipation is only important in this layer (Poth rat *et al.* 2000). Furthermore, the liquid metal has a very high electrical conductivity ($\sigma = \mathcal{O}(10^6) \Omega^{-1}\text{m}^{-1}$; Lyon 1952), thus Joule dissipation plays a lesser role in the damping of the vortical structures (Burr *et al.* 2000; M ck *et al.* 2000). Under this condition, the vortices experience an exponential decay due to Hartmann damping (Sommeria 1988). This fact was confirmed by the experimental investigation of Frank *et al.* (2001) and three-dimensional numerical simulations of M ck *et al.* (2000); Kanaris *et al.* (2013). It is interesting that despite the strong electromagnetic damping of time-dependent wake flows, the action of the Lorentz force is highly anisotropic (Burr *et al.* 2000). The Lorentz force suppresses the velocity fluctuations in the field direction rapidly, whereas the vorticity field in a plane perpendicular to the direction of the magnetic field is only weakly damped (Poth rat *et al.* 2000).

Three-dimensional simulations of a magnetohydrodynamic cylinder wake flow by M ck *et al.* (2000) revealed that under a strong imposed magnetic field, the vortices

whose axes are aligned with the magnetic field are elongated in the field direction and persist far downstream, whereas vortices perpendicular to the magnetic field are rapidly damped. At high interaction parameter, these vortices become stretched over the entire duct cross-section (Sukoriansky *et al.* 1989), forming quasi-2-D vortical structures (as depicted in Figure 2.7(a)). This observation is in agreement with the previous experimental investigation by Branover *et al.* (1995) where the intensity of velocity fluctuation is preserved for an extended period of time when the vortices are aligned with the magnetic field but get suppressed when they are perpendicular to the magnetic field.

The rate of vortex damping depends on the strength of the imposed magnetic field and the electrical conductivity of the Hartmann walls. It has been shown analytically that the vorticity dissipation rate is smallest for an insulating duct (Bühler 1996), which makes it a favourable candidate for the fusion blanket applications. In this case, the characteristic decay time of vorticity depends on Hartmann braking with a scale proportional to Re/Ha (Bühler 1996). A numerical investigation by Hussam *et al.* (2011) found that for high Reynolds and Hartmann numbers, viscous diffusion is negligible, and the decay of peak vorticity magnitude of an individual wake vortex is described by the Hartmann friction term only, i.e. Ha/Re , as suggested by theory. Under this condition, the diameter of wake vortices decrease rapidly as they travel downstream (as depicted in Figure 2.7(b)). Frank *et al.* (2001) concluded that the vortex energy in the MHD wake flow was dissipated by Hartmann braking rather than by cascading down towards smaller scales, which is a prominent feature of quasi-2-D MHD flow as compared to pure hydrodynamic flow.

When the Hartmann number is increased above a critical value, the vortex shedding from a bluff body is completely inhibited. Previous research has shown that the inhibition of vortex shedding caused a dramatic reduction in Nusselt number, and the effect becomes more prominent at higher blockage ratio (Hussam *et al.* 2011). Alternatively, one can take advantage of the MHD flow characteristics, i.e. the presence of an imposed magnetic field in an electrically conducting flow, to intensify vortical structures by means of, for example, electric current injection. This method and other alternatives are discussed later in § 2.6.

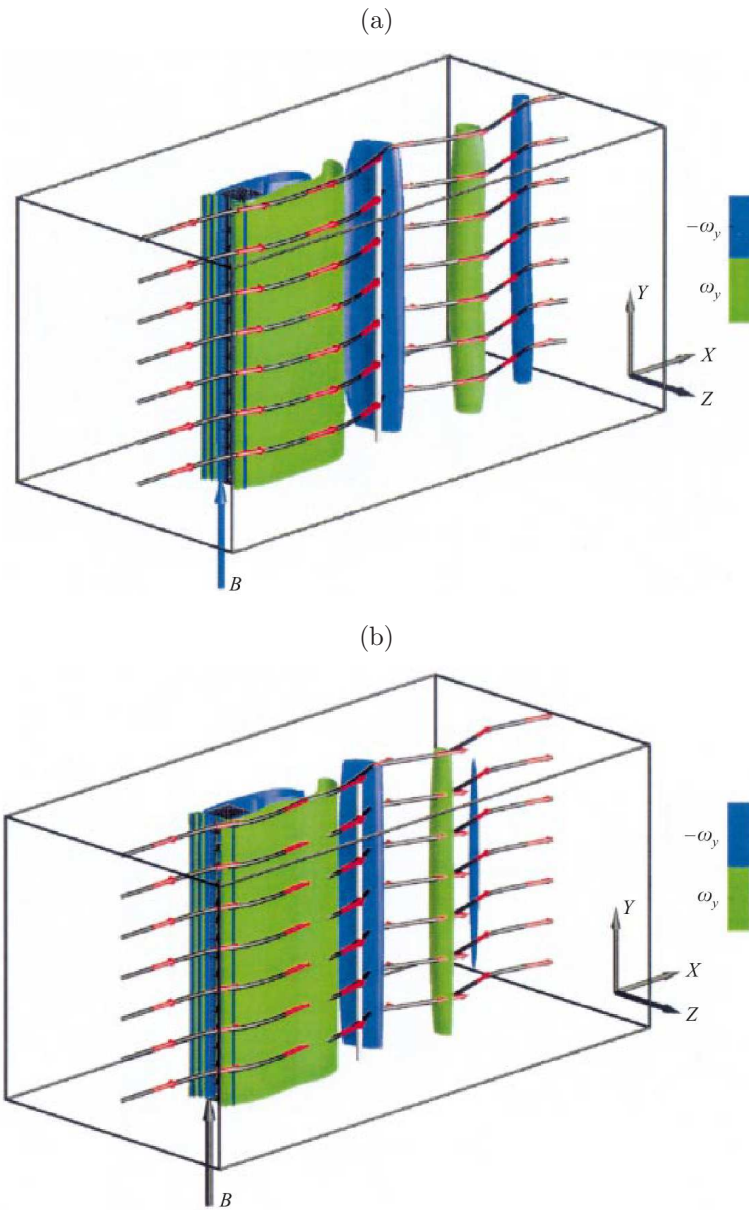


FIGURE 2.7: Iso-surface plot of spanwise vorticity of the three-dimensional MHD flow around a square cylinder with blockage ratio $\beta = 0.1$ at $Re_d = 200$ and (a) $Ha = 200$, and (b) $Ha = 529$. Contour levels range between -6 and 6. This figure is reproduced from Mück *et al.* (2000) with permission from the Cambridge University Press.

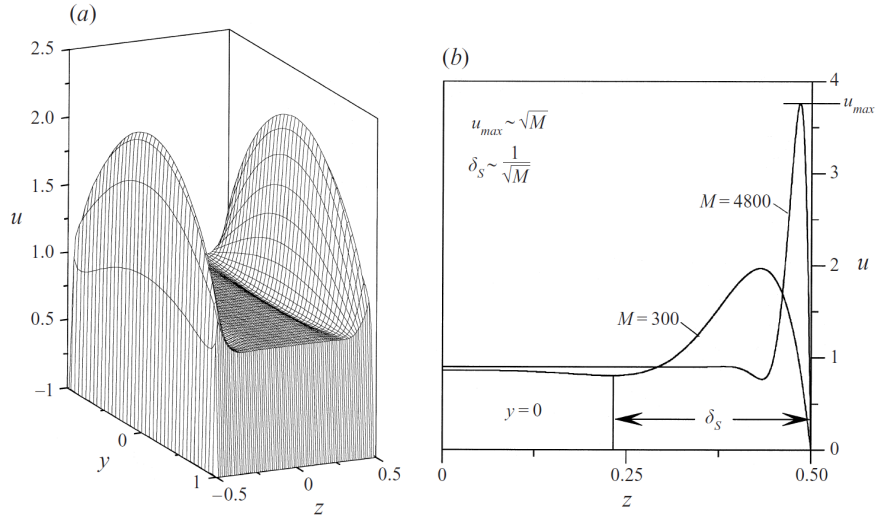


FIGURE 2.8: Normalised streamwise velocity distribution of a fully developed MHD rectangular duct flow with aspect ratio 1:2. Both Hartmann and Shercliff walls are electrically conducting. In this configuration, the side layer jets are weaker than in Hunt’s flow (Moreau 1990). Magnetic field is in the y -direction. (a) Three-dimensional velocity distribution for $M = 600$. (b) Mid-plane velocity distributions for M as indicated. This figure is reproduced from Burr *et al.* (2000) with permission from the Cambridge University Press.

2.4 Heat transfer in MHD duct flows

One of the key factors in efficient fusion energy conversion is high performance liquid-metal cooled fusion reactor blankets. The thermal performance of these blankets has been shown to be influenced by the resulting velocity profile due to the Lorentz force, which in turn depends on the electrical conductivity of the duct wall. When the Hartmann walls are perfectly electrically conducting and the Shercliff walls are electrically insulating (known as Hunt’s flow; Hunt 1965) or both walls are electrically conducting, the flow in the vicinity of the wall is accelerated. In this configuration, the high velocity jet flows near the sidewalls give rise to an M-shaped profile (as depicted in Figure 2.8), and when the shear stress in these jets exceeds a critical value, vortices are formed near the sidewalls (Burr *et al.* 2000). These vortices compensate for the decay of the already existing vortices caused by Hartmann damping (Barleon *et al.* 2000). It has been shown previously that in this configuration, an increase in magnetic field intensity generally leads to an improved heat transfer near the walls (Cuevas *et al.* 1997; Miyazaki *et al.* 1986; Takahashi *et al.* 1998).

On the other hand, when all walls are insulating, the flow presents a flat velocity

profile in the core region, monotonically decreasing to zero through the boundary layers. The flow exhibits thin boundary layers with thickness of order $\mathcal{O}(Ha^{-1})$ and $\mathcal{O}(Ha^{-1/2})$ for the Hartmann and Shercliff layers, respectively. The flow in this configuration generally features a lower heat transfer from the heated sidewall as compared to the conducting Hartmann wall counterpart (Cuevas *et al.* 1997), mainly due to the flow laminarisation. It has been reported that the transverse magnetic field tends to inhibit the convective mechanism of heat transfer in an insulated duct flow by as much as 70% (Gardner & Lykoudis 1971). Despite the low heat transfer characteristic, insulated ducts offer promising application to fusion blankets due to their low pressure drop (Cuevas *et al.* 1997). When the duct walls are insulated, the pressure drop is linearly proportional to the Hartmann number, whereas it increases as Ha^2 for conducting walls (Barleon *et al.* 1991; Bhuyan & Goswami 2008). Hence it has become a particular interest of researchers to enhance the heat transfer in this flow configuration.

Blum (1967); Yamamoto & Kunugi (2011) proposed an empirical correlation for a fully developed turbulent MHD channel flow (interaction parameter $N < 0.04$), flowing in a channel with non-conducting walls, heated from one Hartmann wall and cooled from the opposite wall. The correlation related the normalised Nusselt number to the interaction parameter, i.e. $Nu/Nu_0 = 1 - pN$, where Nu is the Nusselt number, Nu_0 is the Nusselt number under the same flow conditions in the absence of a magnetic field and p is a Prandtl-number-dependent constant. Their correlation suggests that heat transfer decreases monotonically with increasing magnetic field strength. It has been shown previously that the convective transfer of heat can be enhanced by means of a turbulence promoter that generates intensive vortices (Myrum *et al.* 1993). Some of the proposed methods and their associated heat transfer enhancement are reviewed in the following section.

2.5 Heat transfer enhancement using a bluff body

The cooling process in an MHD duct can be assisted by mixing of the flow via turbulence or vortical structures. Several methods have been proposed to improve the convective heat transfer, but generally the mechanism is the same: either by promoting turbulence or by generating vortical velocity fields in the flow. The vortex motion induces a significant velocity component in the transverse direction, thus improving fluid mixing in this direction and reducing thermal boundary layer thickness (Sukoriansky *et al.*

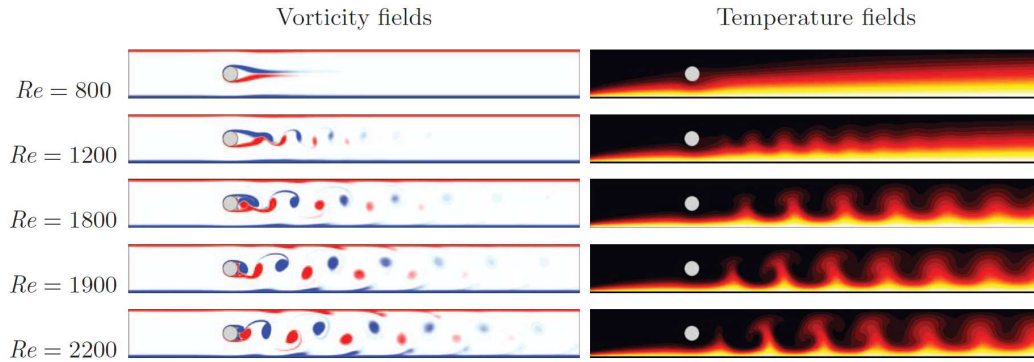


FIGURE 2.9: Contour plots of vorticity (left) and temperature (right) fields of a cylinder wake flows in a duct at $H = 303$ and Reynolds number as indicated. The flow is in a steady-state for $Re_d = 800$, and becomes unsteady at higher Reynolds number with progressively increasing wake vortex strength and wake-boundary layer interaction with increasing Reynolds number. This figure is reproduced from Hussam *et al.* (2012a) with permission from the American Institute of Physics.

1989), as can be seen in Figure 2.9.

Suggested methods to generate these vortices include placement of an obstacle in the duct, such as a cylinder (Malang & Tillack 1995; Mutschke *et al.* 1998; Hussam & Sheard 2013), grid bars (Sukoriansky *et al.* 1989; Branover *et al.* 1995), or a wall protrusion (Kolesnikov & Andreev 1997). Branover *et al.* (1995) used experiments to show that grid bars could achieve up to an almost twofold increase in the Nusselt number relative to the unperturbed flow with the bars oriented parallel to the imposed magnetic field, while no enhancement was produced with perpendicular orientation. A more recent investigation by Hussam & Sheard (2013) revealed a maximum threefold Nusselt number increment when a rather large circular cylinder (with $\beta = 0.4$) was placed at the duct centreline, producing large wake vortices. It should be noted that the enhancement in heat transfer was attained while the wake flow is time-dependent.

However, the state of the wake flow behind a bluff body depends on the intensity of the imposed magnetic field. For a given Reynolds number, high magnetic fields result in a low bulk flow velocity upstream of the obstacle, which then leads to a complete suppression of either wake shedding downstream of the cylinder (Lahjomri *et al.* 1993) or turbulence (Shatrov & Gerbeth 2010). In the case of a cylinder obstacle, the development of wake vortices can be enhanced via an active excitation. Hussam *et al.* (2012b) reported that the optimum perturbations leading to Kármán vortex

shedding are localised in the near-wake region around the cylinder, which can be excited by an imposed cylinder oscillation.

Studies have examined wakes of an oscillating cylinder in a duct for both hydrodynamic and magnetohydrodynamic flows. The cylinder is either rotated about its own axis (Hussam *et al.* 2012a; Beskok *et al.* 2012), oscillated in a transverse direction (Yang 2003; Fu & Tong 2004; Celik *et al.* 2010) or in-line with the incident flow (Griffin & Ramberg 1976). The resulting vorticity fields in all cases are similar, despite the different oscillation mechanisms (Beskok *et al.* 2012). It has been found that increasing oscillation amplitude leads to a higher convective heat transfer from a hot wall (Yang 2003; Beskok *et al.* 2012), though the gains become more modest at larger amplitudes (Hussam *et al.* 2012a). Furthermore, substantial improvement in Nusselt number has been observed when the cylinder oscillates at a frequency within the lock-in regime (Fu & Tong 2004), a region over which the cylinder motion governs the wake shedding frequency. An oscillation frequency beyond this lock-in regime leads to a lower convective heat transport (Celik *et al.* 2010; Yang 2003; Beskok *et al.* 2012). It is also found that higher oscillation amplitude leads to a lower optimum oscillation frequency (Hussam *et al.* 2012a) and broader primary lock-in regime (Mahfouz & Badr 2000).

It should also be noted that the enhancement in convective heat transfer due to the insertion of a bluff body is obtained at the expense of pressure loss. For example, the thermal performance augmentation using a circular cylinder reported by Hussam & Sheard (2013) was accompanied by 30% increase in pressure drop, even at a moderate interaction parameter (i.e. $N \approx 40$). Recently, a similar investigation by Cassells *et al.* (2016) using an inclined rectangular cylinder revealed a maximum increase in pressure drop of more than 50% at a lower interaction parameter of $N = 20$. Furthermore, a maximum twofold increase in pressure gradient of MHD flows in a square insulated duct was reported as a result of the insertion of two rather small circular cylinders (with blockage ratio of 0.15) in tandem arrangement (Malang & Tillack 1995). A previous study (Hussam *et al.* 2011) has also shown a monotonic increase in additional pressure loss for increasing cylinder diameter, and the effect is more pronounced at a higher Hartmann number. This thesis will describe a vortex generation mechanism that carries a negligible cost in duct pressure drop.

2.6 Heat transfer enhancement by electromagnetic promoters

The inherent fundamental physics of MHD flow that result in the inhibition of time-dependent bluff body wakes leads to the quest for an alternative vorticity generation mechanism that avoid the insertion of a physical body. An example is the use of inhomogeneous wall conductivity, as explored by Bühler (1996). In that investigation, a thin conducting strip running parallel to the main flow was added to the otherwise electrically insulating out-of-plane duct wall, as depicted in Figure 2.10(a). The smoothly transitioned wall conductance inhomogeneity leads to the formation of a quasi-2-D shear layer in the duct. Above a critical Hartmann-number-dependent Reynolds number, this shear layer was strong enough to trigger Kelvin–Helmoltz instabilities (Smolentsev *et al.* 2012), which resulted in a feature resembling a Kármán vortex street. A similar observation has been made by Alpher *et al.* (1960) using a copper disk mounted on the bottom wall of an insulating channel. However, with these methods, the ensuing vortices cannot be actively controlled to optimise the heat transfer enhancement depending on the local bulk flow conditions.

An alternative vortex generation method is the use of a localised zone of magnetic field, known as magnetic obstacle (Cuevas *et al.* 2006; Votyakov *et al.* 2008; Kenjereš *et al.* 2011; Kenjereš 2012). When a conducting fluid passes this zone, shear layers around the “obstacle” develop into time periodic vortical structures, as shown in Figure 2.10(b). Cuevas *et al.* (2006) reported vortex shedding frequencies that are relatively much smaller than the vortex street of a bluff body counterpart, despite the similarity in the resulting wakes. Furthermore, they found that the Strouhal number was almost uninfluenced by the variation in Hartmann number. The magnetic obstacle may also be moved along the duct centreline to generate time-dependent wake flows, as has been investigated by Honji (1991). Different flow patterns have been observed, depending on the velocity of the magnet and the strength of the Lorentz force.

Vortices can also be generated by spatially varying the magnetic field (Reed *et al.* 1987; Barleon *et al.* 1991; Müller & Bühler 2001). The intensity of the imposed magnetic field decreases along the streamwise direction over some distance (as depicted in Figure 2.10(c)). As the flow passes the region where the magnetic field varies, the local current density is redistributed, which results in a jet flow near the sidewalls, resembling Hunt’s flow (refer § 2.5). The destabilization of these jets results in the

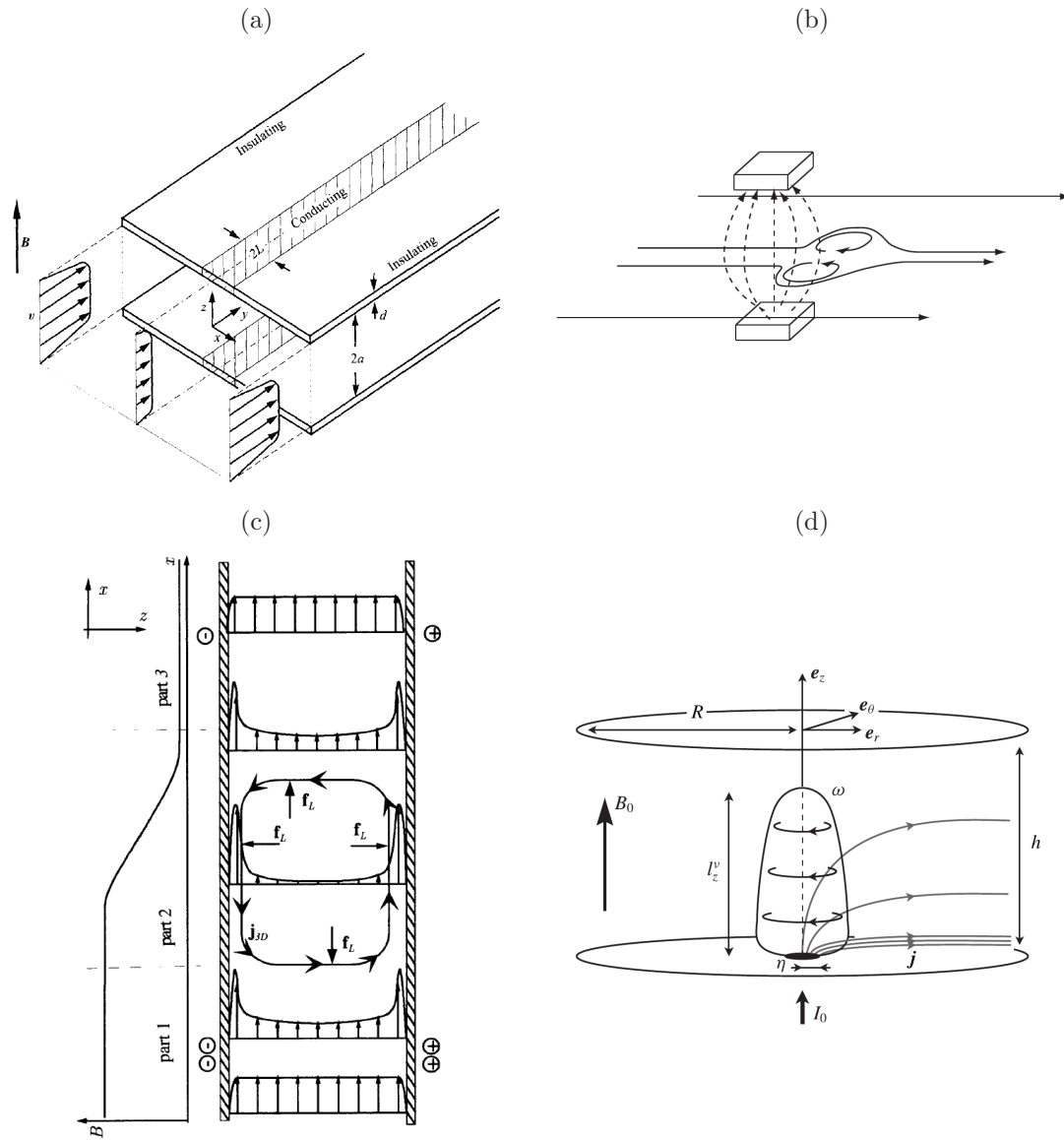


FIGURE 2.10: Various mechanisms of electromagnetic means capable of producing time-dependent wake flows, including (a) the insertion of a conducting strip into the otherwise electrically insulating wall (the figure is reproduced from Bühler (1996) with permission from the Cambridge University Press), (b) imposing a localised zone of magnetic field, known as magnetic obstacle (reproduced from Kenjereš *et al.* (2011) with permission from Dr. Sybren ten Cate), (c) spatially varying the magnetic field along the streamwise direction (reproduced from Müller & Bühler (2001) with permission from Springer), and (d) injection of current through a point electrode embedded in one of the Hartmann walls (reproduced from Baker *et al.* (2015) with permission from the Cambridge University Press).

formation of vortices near the sidewalls, which can result in a large portion of the thermal boundary layer being entrained into the bulk flow, thus improving heat transfer in the transverse direction. In a recent numerical investigation by Gallo *et al.* (2015), the non-uniform magnetic field is generated by electric currents positioned underneath the channel walls, creating a series of localised magnetic obstacles referred to as magnetic ribs. A maximum increase in Nusselt number of 27% has been observed with respect to the unperturbed case, though at the expense of greater than a twofold increase in pressure drop. It should be noted, however, that under fusion-relevant conditions, imposing localised or spatially varying magnetic fields appears to be practically challenging due to the strong external plasma-confining magnetic field.

A promising alternative method is injection of an electrical current through the duct wall (Bühler 1996). This method allows the resulting flow to be precisely controlled via the injected current parameters (Pothérat & Klein 2014); indeed these parameters could even be actively controlled according to feedback from the flow conditions. When uniform magnetic fields are imposed on a conducting fluid in a channel, the direction of injected current determines whether it serves as a force mechanism that drives the flow (as in Moresco & Alboussière (2004); Stelzer *et al.* (2015)) or as a vortex generator (as in Sommeria (1988)). In the latter case, as the injected current moved radially towards the sidewalls, the radial electric current lines induce azimuthal force on the fluid (represented in Figure 2.10(d)). The study of electrically driven vortices has received a considerable attention for their stability (Young *et al.* 2014), dimensionality (Klein & Pothérat 2010; Baker *et al.* 2015), decay behaviour (Sommeria 1988) and turbulence in an MHD flow (Sommeria 1986; Alboussière *et al.* 1999; Messadek & Moreau 2002; Pothérat & Klein 2014).

In an experimental investigation of Klein & Pothérat (2010), a periodic network of alternating vortices in a cubic box are driven by injecting electric current through electrodes mounted flush with the bottom Hartmann wall. They found that the dimensionality of the confined MHD flows was dictated not by the current amplitude, but rather by the intensity of the imposed magnetic fields. For a high magnetic field, the flow tends to two-dimensionality. The transition to three-dimensionality is associated with vortex pairing (Sommeria 1986). The current amplitude and the magnetic field strength dictate the state of the flow, i.e. either steady, periodic or chaotic, although the magnetic field effect is less prominent in the lower range of Hartmann number.

In general, larger current amplitude results in the destabilization of the flow (Klein & Poth erat 2010) and broadening of the vortex core (Sommeria 1988).

A more recent experimental investigation by Poth erat & Klein (2014) revealed that the dimensionality of the vortex structure driven by current injected through an electrode is due to the viscous effect in the core flow, and is governed by the ratio l_{\parallel}/a , i.e.

$$\frac{l_{\parallel}}{a} = \left(\frac{r_e}{a}\right)^2 Ha, \quad (2.4)$$

where l_{\parallel} is the distance over which momentum diffuses under the action of the Lorentz force (Sommeria & Moreau 1982), a is the duct height and r_e is the electrode radius. When the imposed magnetic field is weak, i.e. Ha is finite and $N_t < 1$ (here $N_t = N(r_e/a)^2$ is the true interaction parameter, a more accurate representation of the ratio of the diffusive effect of the Lorentz force to inertial effects than N ; Sreenivasan & Alboussiere 2000; Sreenivasan & Alboussiere 2002), and the inertia is negligible ($N \rightarrow \infty$), the current injected into the domain spreads equally between the core and the bottom Hartmann wall and does not reach the upper Hartmann wall (Figure 2.11(a)). In this case, the diffusive effect of the Lorentz force is balanced by viscous dissipation, and the vortex extended to a height of $l_{\parallel} < a$.

However, when the magnetic field intensity is moderate ($N_t \gtrsim 1$), part of the injected current flows into the top Hartmann layer and the vortex structure is three-dimensional (Figure 2.11(b)). In the limit of $N_t \gg 1$, the Lorentz force dominates and most eddy currents recirculate through both Hartmann layers. The current in the core is Ha times smaller than currents in both Hartmann layers, and the flow structure approaches quasi-two-dimensionality (Figure 2.11(c)). In this regime, the azimuthal velocity in the core of electrically driven vortex from a single point electrode was linearly dependent on the current amplitude (Sommeria 1986). In Figure 2.11(d), the vortex structures are not attached to an injection electrode. The current that loops in the core is equally sourced from both Hartmann layers.

2.7 Review summary

Vortical structures in MHD duct flows are subjected to viscous dissipation and magnetic damping. The formation of these vortices, as well as their dynamics and subsequent decay are not only dependent on the flow conditions (such as the flow velocity and

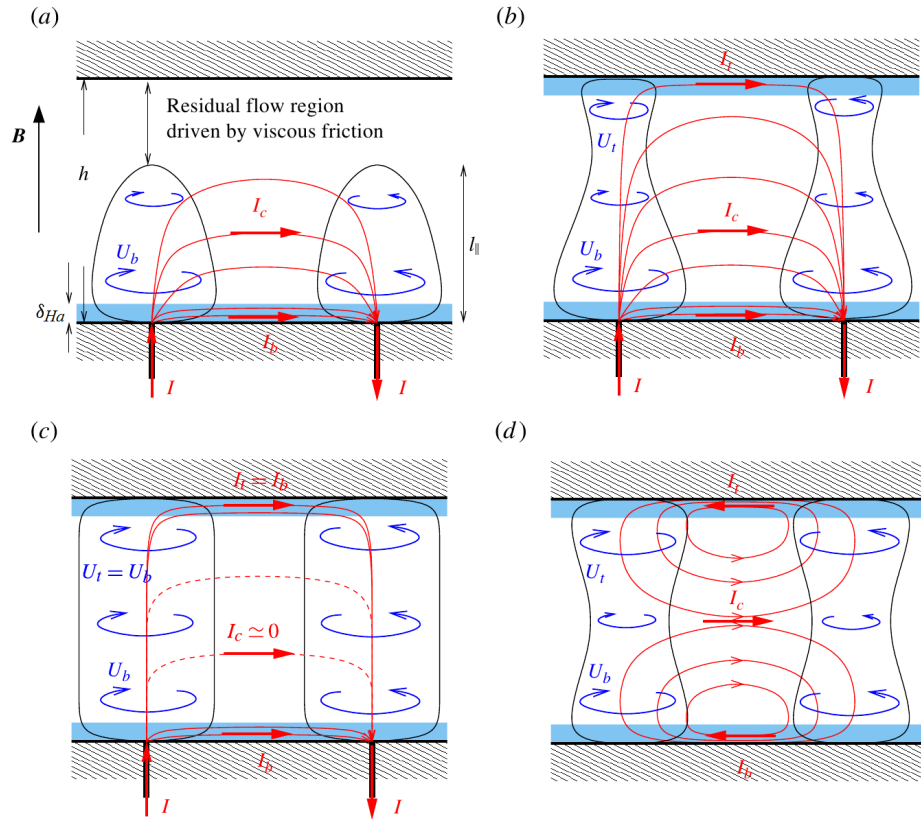


FIGURE 2.11: Schematic representation of vortex structure in a bounded domain. The blue shaded region represents Hartmann layers and the red lines represent electric current paths. This figure is reproduced from Pothérat & Klein (2014) with permission from the Cambridge University Press.

the strength of the imposed magnetic field), but also on the size of the obstacle from which they are produced. While a great deal of attention has been paid to cylinder wake vortices in hydrodynamic flow, less attention has been paid to magnetohydrodynamic counterparts. Furthermore, little is known about the decaying core vorticity behaviour, particularly in MHD flow. This is despite the potential application of bluff body turbulence promoters for enhancement of heat transport in ducts within magnetic confinement fusion reactor blankets (Hussam *et al.* 2011). This motivates the first phase of the research, reported in Chapter 4. In the study of the wake dynamics, particular attention is given to the low- Re regime, motivated by the typical low-velocity operating condition in fusion reactor application (Tagawa *et al.* 2002). Furthermore, in this flow regime, the resulting wake flows in the absence of a magnetic field are laminar and periodic. Hence a direct comparison between the MHD wake flows and the hydrodynamic

counterpart is possible. To the best of the author's knowledge, no such comparison has yet been made.

The wake vortices are, however, subjected to a heavy damping due to the Lorentz force in MHD duct flows under fusion-relevant conditions. Previous studies have shown that these vortices can be kinematically enhanced through cylinder oscillations. The wakes produced by the oscillating cylinder are similar, regardless of the mechanism of oscillation. The resulting heat transfer enhancement has been found to be dependent on the amplitude and frequency of oscillation. Alternative methods have been proposed by taking advantage of the MHD flow characteristics. These methods include the insertion of a thin conducting strip or disk into the insulated duct, imposing localised zone of magnetic field, spatially varying the magnetic field and injecting an electrical current through the duct wall. The current injection method has been used in various studies of confined MHD flows, in the absence of a throughflow, though a similar attention for heat transfer augmentation in a duct flow configuration is rather scarce, despite its potential capability (Bühler 1996). The second results chapter of this thesis (Chapter 5) investigates the potential of current injection to enhance cylinder wake vortices and the associated heat transfer in a heated MHD duct flow. The third results chapter (Chapter 6) extends this investigation to consider the potential of current injection as a sole source of vorticity for MHD duct heat transfer enhancement.

Chapter 3

Methodology

In this chapter, an overview of the relevant MHD governing equations and the numerical strategies used to solve them are presented. § 3.1 details the equations that govern the MHD duct flow subjected to a uniform magnetic field. Equations for an MHD flow with negligible induced magnetic field are presented in § 3.1.1. In § 3.1.2, analytical solutions for the streamwise velocity and induced magnetic field in a rectangular duct are given. § 3.1.3 discusses the quasi-two-dimensional magnetohydrodynamic flow model formulation whereby the electromagnetic force dominates the flow. In § 3.2, the equations governing the flow and heat transfer in the present investigation are given. In the following section, the numerical formulation of the spectral-element method is described, where the spatial and temporal discretisation methods are presented in § 3.3.1 and § 3.3.2, respectively. Finally, a discussion regarding the reliability and the accuracy of the present numerical solver is analysed in § 3.4, including validation against hydrodynamic and magnetohydrodynamic flow cases.

3.1 Magnetohydrodynamic flow equations

Magnetohydrodynamic flows are described by two sets of equations, the fluid dynamic equations and the electromagnetic field equations. In essence, the mutual interactions between the magnetic field and the velocity field can be described as follows (Moreau 1990; Davidson 2001): the relative motion of a conducting liquid and the imposed magnetic field ($\hat{\mathbf{B}}_0$) induces an electromotive force (EMF) according to Faraday's law of induction, which is represented by $\hat{\mathbf{u}} \times \hat{\mathbf{B}}_0$, where $\hat{\mathbf{u}}$ is the velocity vector. The interaction between the EMF and the magnetic field induces an electrical current of order $\sigma(\hat{\mathbf{u}} \times \hat{\mathbf{B}}_0)$, where σ is the electrical conductivity of the liquid metal. According to Ampère's law, a magnetic field ($\hat{\mathbf{B}}_i$) is induced by the induced electrical current. In

the context of fusion blankets, however, this induced magnetic field is negligible relative to the imposed field due to the typical low-velocity liquid metal and relatively small length scale (Davidson 2001); further relevant discussions are presented in § 3.1.1. The total magnetic field (i.e. $\hat{\mathbf{B}} = \hat{\mathbf{B}}_0 + \hat{\mathbf{B}}_i$) interacts with the induced current to give rise to a Lorentz force of order $\hat{\mathbf{j}} \times \hat{\mathbf{B}}$, where $\hat{\mathbf{j}}$ is the current density vector.

For an incompressible, Newtonian and electrically conducting fluid, its flow is governed by the incompressible Navier–Stokes equation with an additional term due to the electromotive force, the conservation of mass (continuity) and energy equations, respectively written as

$$\frac{\partial \hat{\mathbf{u}}}{\partial \hat{t}} = -(\hat{\mathbf{u}} \cdot \hat{\nabla})\hat{\mathbf{u}} - \frac{1}{\rho}\hat{\nabla}\hat{p} + \nu\hat{\nabla}^2\hat{\mathbf{u}} + \frac{1}{\rho}(\hat{\mathbf{j}} \times \hat{\mathbf{B}}), \quad (3.1)$$

$$\hat{\nabla} \cdot \hat{\mathbf{u}} = 0, \quad (3.2)$$

and

$$\rho C_p \frac{\partial \hat{\theta}}{\partial \hat{t}} + \rho C_p (\hat{\mathbf{u}} \cdot \hat{\nabla})\hat{\theta} = k\hat{\nabla}^2\hat{\theta}, \quad (3.3)$$

where \hat{t} is time, $\hat{\nabla}$ the gradient operator, ν , ρ , k and C_p are kinematic viscosity, density, thermal conductivity and constant pressure specific heat of the liquid metal, respectively, \hat{p} is the pressure field and $\hat{\theta}$ is the temperature field.

In equation (3.3), the heat due to the viscous and Joule dissipation is assumed to be negligible. This is possible when the interaction parameter is large and the flow reaches a quasi-2-D state (Burr *et al.* 2000; Pothérat *et al.* 2000). It has been reported previously (Hussam *et al.* 2011) that in the context of MHD flow for fusion blanket applications, their contributions were up to seven orders of magnitude smaller than the other terms in equation (3.3). Furthermore, since no constraint has been imposed on the orientation of the channel, and following Burr *et al.* (2000); Hussam & Sheard (2013), the influence of natural convection on heat transfer is not considered in the present investigation. Previous research has reported that the natural convection effect tends to be inhibited by the strong imposed magnetic field (Gardner & Lykoudis 1971; Morley *et al.* 2000).

As mentioned in the beginning of this section, the MHD equations result from the combination of the fluid dynamics equations, which are Galilean invariant, and the

electromagnetic field equations which in the general case are Lorentz invariant. In order to fuse them and get a complete set of equations with the same (Galilean) invariant properties, it is necessary to invoke the so-called MHD approximation (Shercliff 1965; Roberts 1967). The MHD approximation can be summarized by the following assumptions:

1. The fluid velocity is much less than the velocity of light (i.e. non-relativistic approximation $u/c' \ll 1$, where c' is the velocity of light),
2. Flows take place under quasi-steady or low frequency magnetic fields, which is justified when the time scale of variation in field is long compared with L/c' , where L is the length scale of the system considered,
3. The electric fields are of the order of magnitude of the EMF induced by the fluid motion inside the magnetic field, that is $\mathbf{E} \approx \mathbf{u} \times \mathbf{B}$, where \mathbf{E} is the electrical field.

The implications of the MHD approximation are:

1. the imposed magnetic field remains relatively unperturbed, and hence the convection current can be neglected,
2. the displacement current is negligible (Moreau 1990),
3. the rate of change of the electric charge density is negligible.

Consequently, the electromagnetic field equations that govern an MHD flow within the MHD approximation are described by Ohm's law, Maxwell's equations (i.e. Ampère's law, Gauss's law for magnetism describing the solenoidal nature of the magnetic field and Faraday's law of induction) and the conservation of charge (Shercliff 1965), i.e.

$$\hat{\mathbf{j}} = \sigma(\hat{\mathbf{E}} + \hat{\mathbf{u}} \times \hat{\mathbf{B}}), \quad (3.4)$$

$$\hat{\nabla} \times \hat{\mathbf{B}} = \mu_m \hat{\mathbf{j}}, \quad (3.5)$$

$$\hat{\nabla} \cdot \hat{\mathbf{B}} = 0, \quad (3.6)$$

$$\hat{\nabla} \times \hat{\mathbf{E}} = -\frac{\partial \hat{\mathbf{B}}}{\partial t}, \quad (3.7)$$

$$\hat{\nabla} \cdot \hat{\mathbf{j}} = 0, \quad (3.8)$$

where $\hat{\mathbf{B}}$ is the magnetic field and μ_m is the magnetic permeability.

Equations (3.4-3.8) together with equations (3.1) and (3.3) form a complete formulation of the MHD equations within the MHD approximation. Introducing non-dimensional variables and coordinates which are defined from physical variables as

$$\left. \begin{aligned} \hat{\mathbf{x}} &= L\mathbf{x}, & \hat{\mathbf{u}} &= U_0\mathbf{u}, & \hat{t} &= \frac{L}{U_0}t, \\ \hat{p} &= \rho U_0^2 p, & \hat{\nabla} &= \frac{1}{L}\nabla, & \hat{\theta} &= \theta(\hat{\theta}_w - \hat{\theta}_0) + \hat{\theta}_0, \\ \hat{\mathbf{B}} &= B\mathbf{B}, & \hat{\mathbf{E}} &= U_0 B \mathbf{E}, & \hat{\mathbf{j}} &= \sigma U_0 B \mathbf{j}, \\ Re &= \frac{U_0 L}{\nu}, & Ha &= aB\sqrt{\frac{\sigma}{\rho\nu}}, & N &= \sigma B^2 a / \rho U_0 = \frac{Ha^2}{Re}, \end{aligned} \right\} \quad (3.9)$$

the dimensionless form of equations (3.1-3.3) and (3.4-3.8) are respectively

$$\begin{aligned} \frac{\partial \mathbf{u}}{\partial t} &= -(\mathbf{u} \cdot \nabla)\mathbf{u} - \nabla p + \frac{1}{Re}\nabla^2\mathbf{u} + N(\mathbf{j} \times \mathbf{B}), \\ \nabla \cdot \mathbf{u} &= 0, \\ \frac{\partial \theta}{\partial t} + (\mathbf{u} \cdot \nabla)\theta &= \frac{1}{RePr}\nabla^2\theta = \frac{1}{Pe}\nabla^2\theta, \\ \mathbf{j} &= \mathbf{E} + \mathbf{u} \times \mathbf{B}, \\ \nabla \times \mathbf{B} &= Rm \mathbf{j}, \\ \nabla \cdot \mathbf{B} &= 0, \\ \nabla \times \mathbf{E} &= -\frac{\partial \mathbf{B}}{\partial t}, \\ \nabla \cdot \mathbf{j} &= 0, \end{aligned} \quad (3.10)$$

where L is the half duct width, U_0 is the peak inlet velocity, θ_w and θ_0 are hot and cold reference temperatures, respectively, and $Rm = \sigma\mu_m U_0 L$ is the magnetic Reynolds number, characterising the relative importance of induced magnetic field and externally imposed field (Müller & Bühler 2001).

The following section describes equations that govern the flow when magnetic Reynolds number is negligible, i.e. the induced magnetic field is insignificant compared to the imposed field.

3.1.1 MHD flow at low- Rm

The magnetic field in MHD flows varies with time through its advection and diffusion, and this is described by the induction equation. The equation is derived by first taking the curl of equation (3.4), i.e.

$$\frac{\hat{\nabla} \times \hat{\mathbf{j}}}{\sigma} = \hat{\nabla} \times \hat{\mathbf{E}} + \hat{\nabla} \times (\hat{\mathbf{u}} \times \hat{\mathbf{B}}), \quad (3.11)$$

and using equation (3.5) and (3.7) to substitute for the expressions of $\hat{\mathbf{j}}$ and $\hat{\mathbf{E}}$ as a function of $\hat{\mathbf{B}}$ gives

$$\frac{\hat{\nabla} \times (\hat{\nabla} \times \hat{\mathbf{B}})}{\sigma \mu_m} = -\frac{\partial \hat{\mathbf{B}}}{\partial \hat{t}} + \hat{\nabla} \times (\hat{\mathbf{u}} \times \hat{\mathbf{B}}). \quad (3.12)$$

Noting the vector identity $\hat{\nabla} \times (\hat{\nabla} \times \hat{\mathbf{B}}) = \hat{\nabla}(\hat{\nabla} \cdot \hat{\mathbf{B}}) - \hat{\nabla}^2 \hat{\mathbf{B}}$ and due to equation (3.6),

$$\hat{\nabla} \times (\hat{\nabla} \times \hat{\mathbf{B}}) = -\hat{\nabla}^2 \hat{\mathbf{B}}, \quad (3.13)$$

and hence the induction equation may be expressed as

$$\frac{\partial \hat{\mathbf{B}}}{\partial \hat{t}} = \hat{\nabla} \times (\hat{\mathbf{u}} \times \hat{\mathbf{B}}) + \frac{1}{\sigma \mu_m} \hat{\nabla}^2 \hat{\mathbf{B}}. \quad (3.14)$$

The equation is recast in dimensionless form using the scalings presented in equation (3.9) as

$$\frac{\partial \mathbf{B}}{\partial t} = \nabla \times (\mathbf{u} \times \mathbf{B}) + \frac{1}{Rm} \nabla^2 \mathbf{B}. \quad (3.15)$$

In the context of MHD flows encountered in laboratory setups and industrial flows with liquid metals, electrolytes and molten salts, the magnetic field is diffusive in nature (Poth erat & Dymkou 2010; Cuevas *et al.* 2006), i.e. the magnetic diffusion time is much smaller than any other characteristic time. It follows that the magnetic Reynolds number is very small (typically less than unity; Gallet & Doering 2015). The fluctuating induced magnetic field around the externally applied field is, therefore, negligible (Schumann 1976; M uller & B uhler 2001). Under these conditions, the flow has an insignificant influence on the imposed magnetic field, i.e. the aforementioned two-way interaction between the velocity field and the magnetic field is neglected. Thus the quasi-static approximation is invoked (Roberts 1967).

Within this inductionless approximation, the so-called Alfvén waves are inhibited (Alboussière 2011). Furthermore, the velocity variations along the magnetic field direction is suppressed by the Lorentz force. Consequently, the vortices elongate in this direction and the flow tends towards anisotropy (Pothérat & Dymkou 2010). The inertial effects, however, tend to break up long vortices and the flow becomes more and more isotropic. The relative importance of the electromagnetic to the inertial forces is characterised by the interaction parameter N (also known as the Stuart number).

For a large interaction parameter, the flow tends to two-dimensionality. When a strict two-dimensionality is achieved, the electric currents, and hence the Joule dissipation, vanish. Without electric currents, the Lorentz force vanishes, and the flow recovers the properties of hydrodynamic flow (Pothérat 2012; Mück *et al.* 2000). In the presence of a Hartmann wall, the flow is always three-dimensional, at least in the boundary layer, due to the wall friction (Mück *et al.* 2000), while in the limit of high interaction parameter, the flow becomes quasi-two-dimensional (2D core flow with 3D flow confined to the boundary layers).

A quasi-two-dimensional (quasi-2-D) model has been proposed by Sommeria & Moreau (1982) to describe MHD duct flow subjected to a strong magnetic field, where the flow quantities in the 2D core flow and in the Hartmann layers are averaged in the magnetic field direction. Further discussions regarding this model are presented in § 3.1.3.

3.1.2 Analytical solutions of electrically insulated MHD duct flows

A solution to a fully developed MHD duct flow with insulating walls under a uniform transverse magnetic field was first proposed by Shercliff (1953), hence the name Shercliff flow. In this configuration, the flow is driven by a uniform pressure gradient, $\partial p/\partial x = -\rho P_x$. The walls parallel and perpendicular to the magnetic field are separated by $2L$ and a , respectively (see Figure 3.1).

Under the low- Rm approximation, the non-dimensional velocity and induced magnetic fields for this flow problem can be determined (Moreau 1990) from

$$\Delta u_p + M \frac{\partial b_i}{\partial z} = -1, \quad (3.16)$$

and

$$\Delta b_i + M \frac{\partial u_p}{\partial z} = 0, \quad (3.17)$$

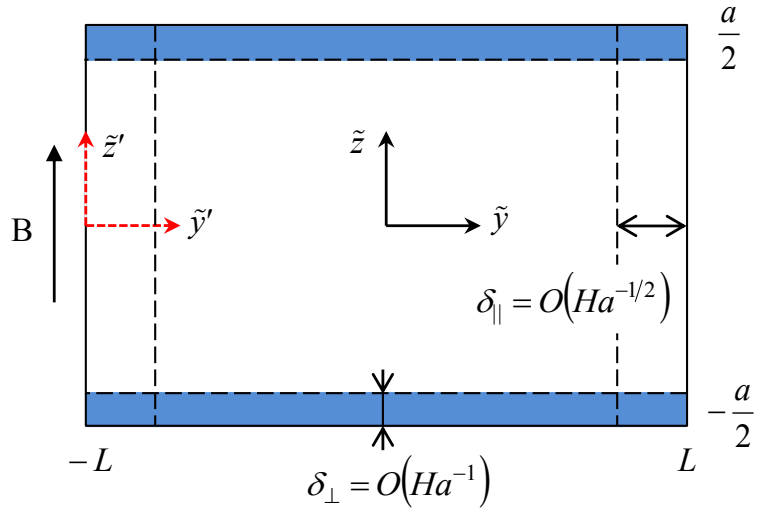


FIGURE 3.1: Cross section of rectangular duct placed in a uniform magnetic field. δ_{\perp} and δ_{\parallel} represents thickness of the Hartmann layers and Shercliff layers, respectively. The blue shaded region represents Hartmann layers.

respectively, where M is the Hartmann number scaled with half duct height, $(x, y, z) = (\tilde{x}, \tilde{y}, \tilde{z})/(a/2)$ are dimensionless coordinates, $u_p = U\nu/((a/2)^2 P_x) = 4\hat{u}\nu/(a^2 P_x)$ is the non-dimensional velocity, \hat{u} a dimensional velocity, $P_x = -(1/\rho)\partial p/\partial x$ the driving pressure gradient, ν the kinematic viscosity of the liquid metal, and a is the duct height. The non-dimensional induced magnetic field $b_i = 4B_i\sqrt{\nu/(\sigma\rho)}/(\mu_m a^2 P_x)$, where B_i is the dimensional induced magnetic field strength, while σ , ρ and μ_m are electrical conductivity, density and magnetic permeability of the liquid metal, respectively.

A no-slip condition is imposed at $z = \pm 1$ and $y = \pm \alpha$ for u_p , where $\alpha = 2L/a$ is the duct aspect ratio. As the duct walls is assumed to be electrically insulated, the induced magnetic field is set to an arbitrary value of zero at $z = \pm 1$ and $y = \pm \alpha$ (Dousset 2009). The governing equations (equations (3.16) and (3.17)) are decoupled with Elsasser variables, written as $A_1 = u_p + b_i$ and $A_2 = u_p - b_i$. Due to the symmetrical condition about the z -axis, only the solution for A_1 is needed to deduce A_2 , u_p and b_i . The solution is obtained by expanding the unknown A_1 into a Fourier series. Alternatively, the velocity and the induced magnetic field in the governing equations can be expanded directly, which yields

$$u_p(y, z) = \sum_{n=1,3,5,\dots}^{\infty} u_n(z)\cos(\lambda_n y), \quad (3.18)$$

and

$$b_i(y, z) = \sum_{n=1,3,5,\dots}^{\infty} b_n(z) \cos(\lambda_n y), \quad (3.19)$$

with

$$\begin{aligned} u_n(z) &= \frac{k_n}{\lambda_n^2} \left[1 - \frac{f_n(y)}{f_n(1)} \right], \\ b_n(z) &= \frac{k_n}{\lambda_n^2} \left[1 - \frac{g_n(y)}{f_n(1)} \right], \\ f_n(y) &= \sinh(p_{n2}) \cosh(p_{n1}z) - \sinh(p_{n1}) \cosh(p_{n2}z), \\ g_n(y) &= \sinh(p_{n2}) \sinh(p_{n1}z) - \sinh(p_{n1}) \sinh(p_{n2}z), \\ p_{n1,2} &= \frac{1}{2} \left(M \mp \sqrt{M^2 + 4\lambda_n^2} \right), \\ k_n &= 2 \frac{\sin(\lambda_n \alpha)}{\lambda_n \alpha}, \\ \lambda_n &= \frac{n\pi}{2\alpha}. \end{aligned}$$

Substituting $Ha = 0$ (i.e. $M = 0$) into equation (3.18) recovers the hydrodynamic velocity profile. Alternatively, the hydrodynamic profile can be obtained using the exact solution for hydrodynamic duct flow (Frank 1991; Shah & London 1972), i.e.

$$u_p(y, z) = \frac{16}{\pi^3} \sum_{n=1,3,5,\dots}^{\infty} (-1)^{\frac{n-1}{2}} \left[1 - \frac{\cosh(m\pi y/2)}{\cosh(m\pi \alpha/2)} \right] \frac{\cos(m\pi z/2)}{n^3}. \quad (3.20)$$

For large Hartmann number $Ha \gg 1$, the evaluation of equations (3.16) and (3.17) may cause numerical issue (Drake & Abu-Sitta 1966; Müller & Bühler 2001). For such cases, both expressions for $u_p(y, z)$ and $b_i(y, z)$ can be evaluated using an asymptotic solution valid for large Ha (Moreau 1990),

$$u_p(y', z) = \frac{1-z}{M} [1 - F(\alpha)], \quad (3.21)$$

where

$$F(\alpha) = (1 + \alpha^2) \left(1 - \operatorname{erf}\left(\frac{\alpha}{\sqrt{2}}\right) \right) - \alpha \sqrt{\frac{2}{\pi}} \exp\left(-\frac{\alpha^2}{2}\right), \quad (3.22)$$

and

$$\alpha(y', z) = \frac{y'}{\sqrt{\frac{2}{M}(1-z)}}. \quad (3.23)$$

Here “erf” is the Gauss error function and y' is the y -axis translated to one of the Hartmann walls (refer Figure 3.1).

Solutions for other configurations such as a duct with perfectly conducting Hartmann walls and insulating Shercliff walls (also known as *Hunt’s flow*) or a duct with all conducting walls can be found in Moreau (1990); Müller & Bühler (2001).

3.1.3 A quasi-two-dimensional MHD duct flow model

A quasi-two-dimensional model proposed by Sommeria & Moreau (1982) (hereafter referred to as the SM82 model) has been employed in the current work. This model is derived by averaging the flow quantities in the 2D core flow and in the Hartmann layers along the magnetic field direction to give a modified two-dimensional Navier-Stokes equation augmented by a linear braking term representing friction in the Hartmann layers. Formally, the quasi-two-dimensional model is accurate to order $\mathcal{O}(Ha^{-1}, N^{-1})$. Under this quasi-two-dimensional model, equation (3.1) reduces to

$$\frac{\partial \hat{\mathbf{u}}_{\perp}}{\partial \hat{t}} = -(\hat{\mathbf{u}}_{\perp} \cdot \hat{\nabla}) \hat{\mathbf{u}}_{\perp} - \frac{1}{\rho} \hat{\nabla} \hat{p} + \nu \hat{\nabla}^2 \hat{\mathbf{u}}_{\perp} - \frac{n}{\tau_H} \hat{\mathbf{u}}_{\perp}, \quad (3.24)$$

where $\hat{\mathbf{u}}_{\perp}$ and \hat{p}_{\perp} are the respective velocity and pressure fields, projected onto a plane orthogonal to the magnetic field, $\tau_H = (a/B) \sqrt{\rho/\sigma\nu}$ is the Hartmann damping time (Pothérat 2007) and n is the number of Hartmann walls ($n = 1$ in the case with a free surface and $n = 2$ for a flow between two Hartmann walls).

Pothérat (2007) explains that quasi-two-dimensionality is achieved when the time scale for the Lorenz force to act to diffuse momentum of a structure of size l_{\perp} along magnetic field lines over length l_{\parallel} , $\tau_{2D} = (\rho/\sigma B^2) l_{\parallel}^2/l_{\perp}^2$, is shorter than any other time scales in the flow. The relevant time scales include the time scales for viscous diffusion in the perpendicular and parallel planes ($\tau_{\nu}^{\perp} = l_{\perp}^2/\nu$ and $\tau_{\nu}^{\parallel} = l_{\parallel}^2/\nu$, respectively), and the inertia time scale $\tau_U = l_{\perp}/U$. These conditions are attained when both Hartmann number $Ha \gg 1$ and interaction parameter $N \gg 1$, in which any velocity variations along the magnetic field direction is suppressed almost instantaneously (Pothérat *et al.* 2000), and the Hartmann layer is laminar (Pothérat & Schweitzer 2011). Furthermore, taking $l_{\parallel} = a$, these three conditions can be used respectively to obtain limiting length scales under the model, $l_{\perp}/a > Ha^{-1/2}$, $l_{\perp}/a > Ha^{-1}$ and $l_{\perp}/a > N^{-1/3}$. The second condition is always satisfied under the first condition for $Ha > 1$. For moderate values of the interaction parameter, Ekman recirculating flows are produced in the Hartmann

layer. A more refined model (i.e. PSM2000) that takes into account the moderate inertial effects was developed by Poth erat *et al.* (2000). More recently, Poth erat & Schweitzer (2011) establish a quasi-2-D model for which turbulent Hartmann layers are present.

At present, generally the SM82 model is understood to be applicable for MHD duct flows under the influence of a strong magnetic field, although some deviation from the quasi-2-D behaviour can be observed in some situations, e.g. in complex geometry ducts. In the case of rectangular duct flows, the SM82 model has been verified against three-dimensional analytical solutions, where the local error in the velocity profile in the sidewall boundary layer is less than 10% (Poth erat *et al.* 2000). Furthermore, 3D simulations of MHD wakes behind a cylinder by M uck *et al.* (2000) verified the accuracy of the quasi-2-D model at high interaction parameter and Hartmann number. This result is further supported by more recent 3D simulations by Kanaris *et al.* (2013), where at the highest Hartmann number investigated, they found maximum errors of the averaged parameters between the quasi-2-D model and the 3D DNS of 6% and 8% for the steady and time-dependent flows, respectively. It is also worth mentioning that a quasi-2-D model proposed by Smolentsev & Moreau (2007) for MHD turbulence based on SM82 has been found to be in excellent agreement with previous experimental results.

3.2 The governing equations

The present investigation is concerned with the flow of electrically conducting fluid in a duct, where a constant homogeneous strong magnetic field with a strength B is imposed in a spanwise direction. Under this condition, the flow is quasi-two-dimensional, and thus, the SM82 model is adopted. Using the scalings presented in equation (3.9), the non-dimensional form of the magnetohydrodynamic equations of continuity, momentum and energy reduce to

$$\nabla \cdot \mathbf{u}_\perp = 0, \quad (3.25)$$

$$\frac{\partial \mathbf{u}_\perp}{\partial t} = -(\mathbf{u}_\perp \cdot \nabla) \mathbf{u}_\perp - \nabla p_\perp + \frac{1}{Re_L} \nabla^2 \mathbf{u}_\perp - \frac{L^2}{a^2} \frac{Ha}{Re_L} (\mathbf{u}_0 - n \mathbf{u}_\perp), \quad (3.26)$$

and

$$\frac{\partial \theta_{\perp}}{\partial t} + (\mathbf{u}_{\perp} \cdot \nabla) \theta_{\perp} = \frac{1}{Pe} \nabla^2 \theta_{\perp}, \quad (3.27)$$

respectively, where \mathbf{u}_0 is the forcing velocity field. In the context of the current study, it is the product of the reaction between the imposed magnetic field and the transverse electric current density imposed at the sidewalls, and will be defined in § 5.2. The dimensionless parameters Reynolds number Re_L , Hartmann number Ha and Peclet number Pe are defined as

$$\left. \begin{aligned} Re_L &= U_0 L / \nu, \\ Ha &= a B \sqrt{\sigma / \rho \nu}, \\ Pe &= U_0 L / \kappa_T = Re_L Pr, \end{aligned} \right\} \quad (3.28)$$

where κ_T is the thermal diffusivity of the liquid metal. Prandtl number $Pr = \nu / \kappa_T$ characterizes the ratio of viscous to thermal diffusion in the fluid, and $Pr = 0.022$ is used throughout, representative of the eutectic alloy GaInSn. Hartmann number is expressed in term of friction parameter $H = n(L/a)^2 Ha$, following Poth erat (2007). All variables are expressed in their dimensionless form hereafter, unless otherwise stated.

The exact solution of equations (3.25) and (3.26) satisfying the no-slip boundary conditions at the sidewalls for fully developed quasi-2-D flow is applied at the duct inlet (Poth erat 2007), i.e.

$$u_{\perp}(y) = \frac{\cosh \sqrt{H}}{\cosh \sqrt{H} - 1} \left(1 - \frac{\cosh(\sqrt{H} y)}{\cosh \sqrt{H}} \right). \quad (3.29)$$

Solutions for velocity at different Hartmann numbers are depicted in Figure 3.2. It can be seen from the figure that the velocity distribution becomes flatter in the core flow with increasing Hartmann number. This is attributed to the fact that the magnitude of the induced current, and thus the Lorentz force, are linearly dependent on the fluid velocity (M uller & B uhler 2001). In the core region, where the velocity is higher than in the regions near the walls, the damping by the Lorentz force is stronger. This results in the counterbalancing effect between the damping force and the driving pressure gradient, and thus the uniform velocity profile in the core region.

It is also evident from the figure that both Hartmann and Shercliff boundary layers become thinner with increasing Hartmann number, and that the Hartmann boundary layer (as shown in Figure 3.2(b)) are significantly thinner compared to the Shercliff boundary layer (Figure 3.2(a)). In the limit of high Hartmann number, the core region

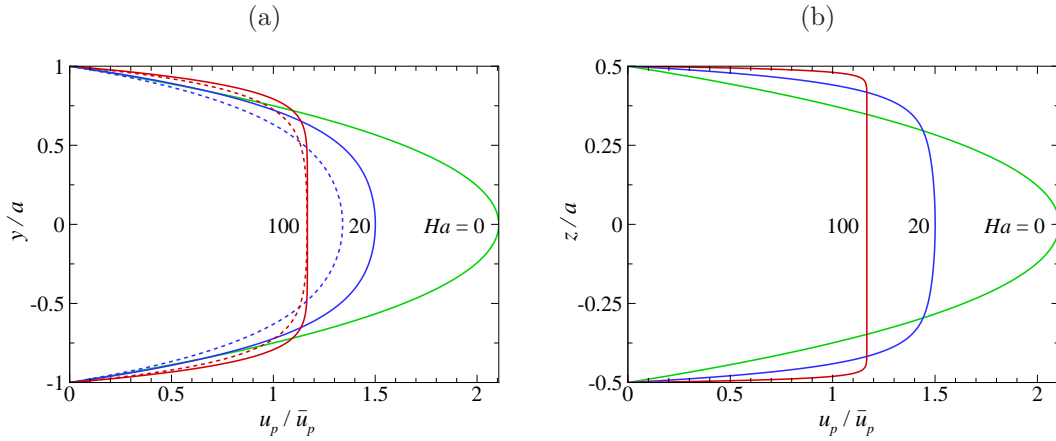


FIGURE 3.2: Streamwise component of velocity profiles of MHD rectangular duct (i.e. $\alpha = 2$) flow with electrically insulating walls along the symmetry axes (a) $z = 0$ and (b) $y = 0$. Solid and dashed lines represent velocity profiles calculated from three-dimensional analytical solution in equation (3.18) and a prediction from quasi-two-dimensional model (SM82 model) as in equation (3.29). The velocity is normalised with the bulk flow velocity. $Ha = 0$ correspond to hydrodynamic flow profile in a duct, calculated from an exact solution of equation (3.20).

dominates over the entire duct cross section. This argument is supported by the asymptotic decrease in the normalised velocity towards unity as Hartmann number approaches infinity, as can be seen in Figure 3.3(a). The peak velocity, however, decreases asymptotically towards zero with increasing Hartmann number, as shown in Figure 3.3(b). This demonstrates the substantial additional pumping power required to maintain the prescribed flowrate in an MHD duct flow under a strong imposed magnetic field.

It is also interesting to note from Figures 3.2 and 3.3 that the discrepancy between the quasi-2-D and 3D velocity profile becomes smaller at higher Hartmann numbers, which further supports the validity of the SM82 model for stronger magnetic field strength applications.

3.3 Numerical scheme

The present work employs a nodal spectral-element method to discretise the governing flow and energy equations (equations (3.25)-(3.27)) in space. This method combines the attractive exponential convergence property of spectral methods with the geometric flexibility of the finite element method. The domain space is discretised into a mesh of individual elements, which are then further discretised into $N_p \times N_p$ nodes through

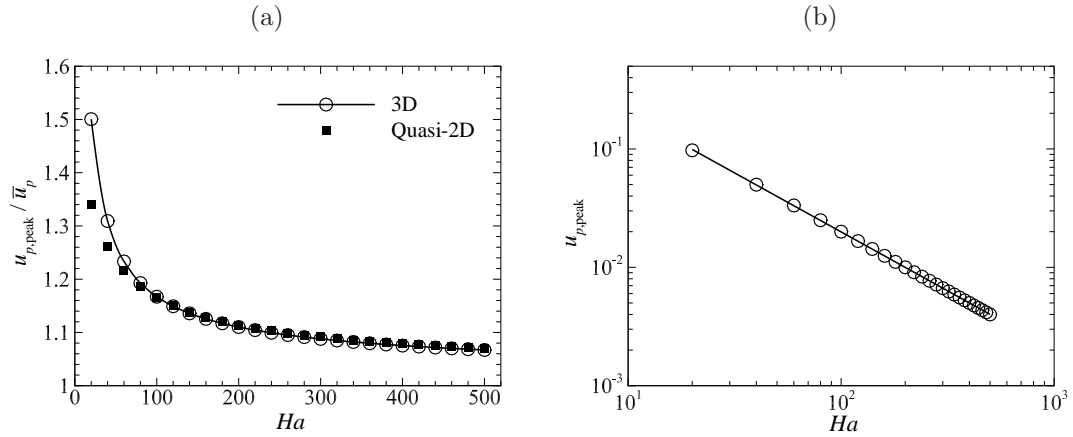


FIGURE 3.3: Peak velocity of MHD duct flow with $\alpha = 1$ plotted against Hartmann number. In (a), velocity is normalised by the bulk flow velocity, while in (b), the velocity is non-dimensionalised by $(a^2 P_x)/4\nu$. The solid lines in (a) and (b) are a power-law fit and a spline fit, respectively, to the 3D data. For both figures, circle and square symbols represent 3D solution (equation (3.18)) and quasi-2-D solution (equation (3.29)), respectively.

a high-order polynomial basis. A tensor product of Lagrangian polynomials is used within each element, with the node points correspond to the Gauss–Legendre–Lobatto (GLL) quadrature integration points, which results in a diagonal mass matrix of the system. This numerical integration is employed to enforce boundary conditions and inter-element continuity by including the end points of the integration interval among the quadrature nodes. A third-order scheme based on backwards differentiation is employed for time integration.

3.3.1 Spatial discretisation

The computational domain is decomposed into a mesh of quadrilateral elements. Within each element, Gauss–Legendre–Lobatto quadrature is employed for integration. The GLL quadrature nodes tend to cluster near the end points of the integration interval. The quadrature rule is defined by Q nodes of ϱ_i and weights w_i , and by convention, the domain of integration for P -nodes Gaussian quadrature rule is taken as $[-1,1]$, so its taking a form (Karniadakis & Sherwin 2013)

$$\int_{-1}^1 p(\varrho) d\varrho = \sum_{i=0}^{Q-1} w_i p(\varrho_i) + \varepsilon(p), \quad (3.30)$$

for all polynomials p , where ϱ is the real variable in the equation solved to find Gauss–Legendre–Lobatto quadrature points, w_i and ϱ_i are the i^{th} Gauss–Legendre–Lobatto

weighting coefficient and quadrature points, respectively, and $\varepsilon(p)$ is the approximation error, which is zero if $p(\varrho)$ is a polynomial of degree $2Q - 3$ or less (Karniadakis & Sherwin 2013). In the GLL quadrature rule, the end points (i.e. $\varrho = \pm 1$) of the integration interval are forced to be among the quadrature nodes which reduces the accuracy from the optimal exactness for polynomial of degree $2Q - 1$ of Gaussian quadrature. The Q quadrature nodes are determined from the roots of the equation

$$(1 - \varrho^2)P_{Q-1}(\varrho) = 0 \quad \text{with} \quad -1 \leq \varrho \leq 1, \quad (3.31)$$

and the weighting coefficients are given by

$$w_i = \frac{2}{Q(Q-1)[P_{Q-1}(\varrho_i)]^2} \quad \text{with} \quad i = 0, 1, \dots, Q-1, \quad (3.32)$$

where P_{Q-1} is the Legendre polynomial of order $Q - 1$. By using Rodriguez's formula, the Legendre polynomial can be expressed as

$$P_{Q-1} = \frac{1}{2^{Q-1}(Q-1)!} \frac{d^{Q-1}}{d\varrho^{Q-1}} (\varrho^2 - 1)^{Q-1} \quad \text{where} \quad Q = 1, 2, \dots \quad (3.33)$$

The weighting coefficients and the quadrature points allow the integrals to be approximated swiftly using Gauss–Legendre–Lobatto quadrature.

3.3.2 Temporal discretisation

The present solver employs a high-order three-step splitting scheme for temporal discretisation following Karniadakis *et al.* (1991). In this scheme, an operator splitting treatment of the Navier–Stokes equations is applied, separating the advection, pressure and diffusion terms, and integrating these in three separate substeps. Taking the order of integration for the advection, pressure and diffusion terms to be J_e , J_p and J_i , respectively, the semi-discrete system is written as (Karniadakis & Sherwin 2013)

$$\frac{\mathbf{u}^* - \sum_{q=0}^{J_i-1} \alpha_q \mathbf{u}^{n-q}}{\Delta t} = - \sum_{q=0}^{J_e-1} \beta_q \left\{ [(\mathbf{u} \cdot \nabla) \mathbf{u}]^{n-q} + \frac{H}{Re} \mathbf{u}^{n-q} \right\}, \quad (3.34)$$

$$\frac{\mathbf{u}^{**} - \mathbf{u}^*}{\Delta t} = -\nabla p^{n+1}, \quad (3.35)$$

$$\frac{\gamma_0 \mathbf{u}^{n+1} - \mathbf{u}^{**}}{\Delta t} = \frac{1}{Re} \nabla^2 \mathbf{u}^{n+1}, \quad (3.36)$$

where the term H/Re represents the Hartmann friction term and \mathbf{u}^* and \mathbf{u}^{**} represent the intermediate velocity fields.

The first substep involves an evaluation of an intermediate velocity field \mathbf{u}^* from equation (3.34) using an explicit projection of the velocity field to the future time $(n+1)$ for evaluation of the right-hand side of equation (3.34).

In the second substep, equation (3.35) is solved by first taking the divergence of this equation to obtain a Poisson equation for pressure. Assuming the intermediate velocity field is divergence-free (i.e. $\nabla \cdot \mathbf{u}^{**} = 0$), the Poisson equation is written as

$$\nabla^2 p^{n+1} = \nabla \cdot \left(\frac{\mathbf{u}^*}{\Delta t} \right). \quad (3.37)$$

This is solved with the appropriate high-order Neumann boundary conditions for pressure (Karniadakis *et al.* 1991), i.e.

$$\frac{\partial p^{n+1}}{\partial n} = - \left[\frac{\partial \mathbf{u}^{n+1}}{\partial t} + \frac{1}{Re} \sum_{q=0}^{J_p-1} \beta_q (\nabla \times \boldsymbol{\xi})^{n-q} + \sum_{q=0}^{J_e-1} \beta_q [(\mathbf{u} \cdot \nabla) \mathbf{u}]^{n-q} \right] \cdot \mathbf{n}, \quad (3.38)$$

where $\boldsymbol{\xi}$ is vorticity. The evaluated pressure is then used to determine the second intermediate velocity field \mathbf{u}^{**} from equation (3.35).

In the third substep, the velocity field \mathbf{u}^{n+1} is evaluated by solving an implicit Helmholtz equation (equation (3.36)). In overall, the splitting scheme achieves a second-order time-accuracy when first-order pressure boundary conditions are imposed (Karniadakis *et al.* 1991).

The energy equation is solved using the same third-order backwards differentiation scheme as used for the velocity field, expressed as

$$\frac{\theta^* - \sum_{q=0}^{J_i-1} \alpha_q \theta^{n-q}}{\Delta t} = - \sum_{q=0}^{J_e-1} \beta_q \{(\mathbf{u}^{n-q} \cdot \nabla) \theta^{n-q}\}, \quad (3.39)$$

and

$$\frac{\gamma_0 \theta^{n+1} - \theta^*}{\Delta t} = \frac{1}{Pe} \nabla^2 \theta^{n+1}. \quad (3.40)$$

3.4 Numerical solver validation

The accuracy of the present numerical solver was validated against published experimental results and analytical solutions for fully developed laminar flows in rectangular

ducts with transverse magnetic fields. The numerical scheme was first tested for hydrodynamic flows, followed by tests against magnetohydrodynamic cases.

3.4.1 Hydrodynamic validation tests

The first test concerns the dimensionless frequency parameter, known as Roshko number $Ro = fd^2/\nu$. This parameter is the product of Strouhal number and the Reynolds number, and was first introduced by Roshko (1954a) for the study of bluff body wakes (Kohan & Schwarz 1973). Roshko number measures the importance of the diffusion of vorticity in oscillating flows at low Reynolds number (Gerrard 1978). Roshko numbers for a circular cylinder within the laminar periodic shedding regime digitised from Roshko (1954a) were compared with results obtained from the present code, and the results are shown in Figure 3.4(a). The agreement with the experimental data is pleasing. In order to quantify the comparison, the mean absolute percentage deviation M was evaluated, which is defined as

$$M = \frac{1}{n} \sum_{i=1}^n \frac{|y_{\text{present}} - y_{\text{published}}|}{y_{\text{published}}}. \quad (3.41)$$

The mean absolute percentage deviation for the comparison in Figure 3.4(a) is 2.67%. In general, $M < 10\%$ is regarded as a very good correlation (Lewis 1997). Following this, the $St - Re$ relationship data reported in Williamson (1989) was compared with data from the present solver. The comparison was made for a Reynolds number range between 60 and 180 (refer Figure 3.4(b)) and revealed an excellent agreement between the two sets of data (with $M = 0.83\%$), particularly at higher Reynolds numbers.

The solver was further validated by comparing the critical Reynolds number for the onset of vortex shedding in a confined flow past a cylinder from numerical data of Sahin & Owens (2004) with the results from the present computations, as shown in Figure 3.5. The comparison was made for blockage ratios $\beta = 0.1, 0.2$ and 0.3 , and an excellent agreement with published data is found (i.e. $M = 0.66\%$).

3.4.2 Magnetohydrodynamic validation tests

The capabilities of the present solver for magnetohydrodynamic cases were validated by comparing the critical Reynolds number at the onset of vortex shedding from experimental data from Frank *et al.* (2001) with the results from the present computations, as shown in Figure 3.6. The comparison was made for friction parameters range from

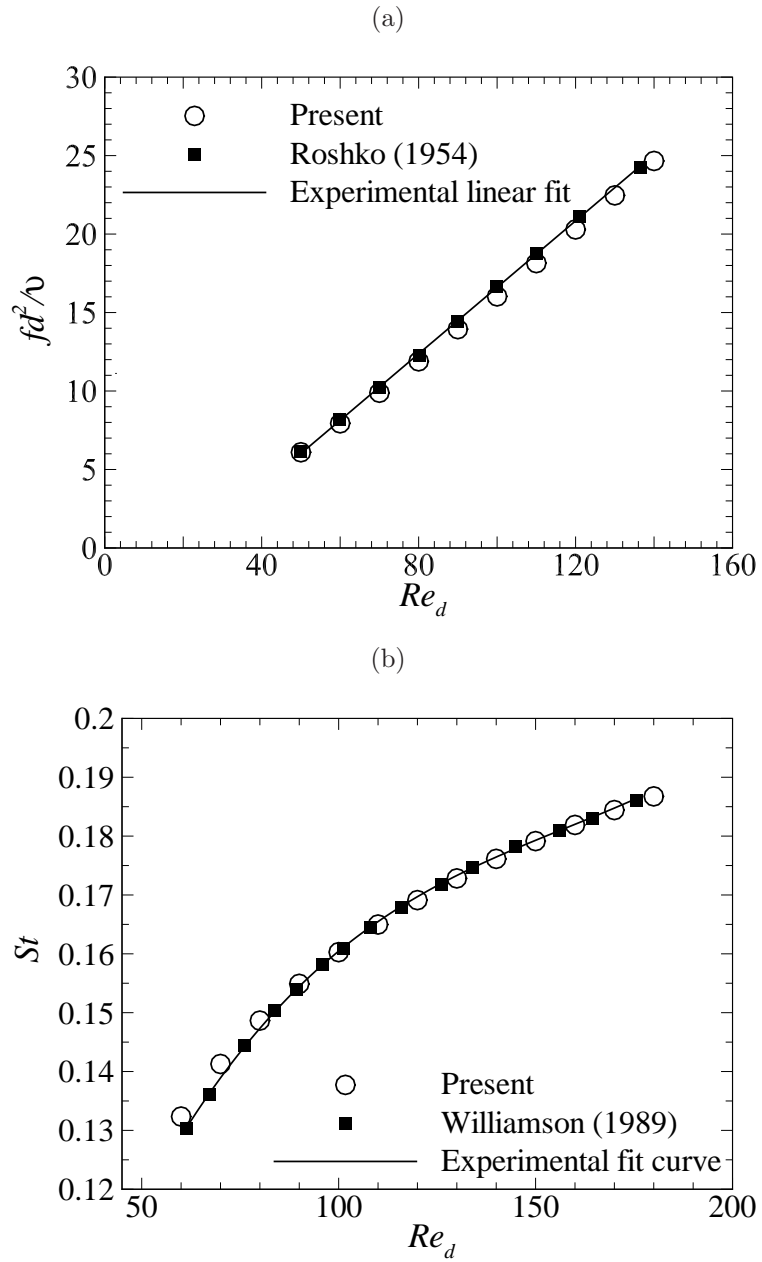


FIGURE 3.4: Circular cylinder wake shedding frequency plotted against Reynolds number. Open symbols represent the present data, while solid symbols and lines represent experimental results from (a)Roshko (1954a) and (b)Williamson (1989).

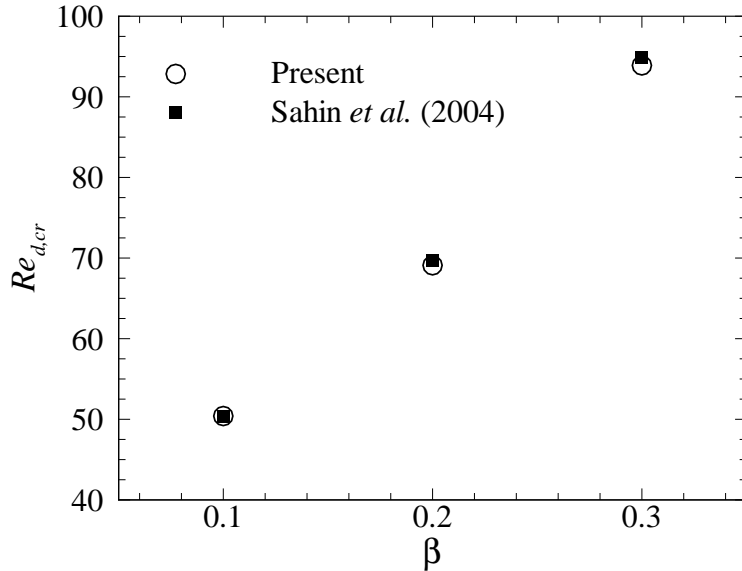


FIGURE 3.5: Critical Re at the onset of vortex shedding for hydrodynamic cases at different blockage ratios. Open symbols represent the present data, while solid symbols represent data published in Sahin & Owens (2004).

$H = 500$ to $H = 3000$, and a good agreement with published data is found. A correlation evaluation yields a mean absolute percentage deviation of $M = 7.12\%$.

The solver was further validated by comparing the peak vorticity time history of a decaying quasi-2-D vortex obtained from the present simulations with the analytical solution derived in § 4.5.1 (i.e. equation (4.17)). Simulations were based on a Lamb–Oseen vortex model and were carried out at various Hartmann number, circulation, and initial core radius. A 50 by 50 unit length domain was considered, with a fine grid concentrated at the centre of the domain to resolve the high vorticity gradients within the vortex core. This is important to isolate computations error arising due to a lack of spatial resolution. A comparison of vorticity maxima obtained from the numerical computations and the analytical solution is shown in Figure 3.7. It should be noted that the curves shown in Figure 3.7 are not fits to the data, but instead are the analytical peak vorticity time histories calculated from equation (4.17). An excellent agreement is consistently seen between the analytical and numerical results (with $\max(M) = 0.002\%$). This strongly confirms the validity of the analytical solution obtained in Section 4.5.1 and the implementation of the SM82 model in the code.

In order to further investigate the capability of the code, vorticity profiles of quasi-2-D MHD duct flows obtained from the numerical computations are compared with the

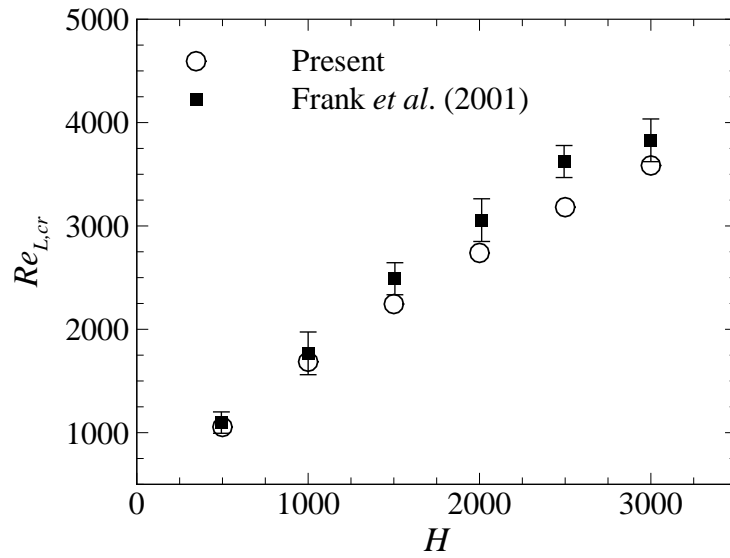


FIGURE 3.6: Critical Re at the onset of vortex shedding for $\beta = 0.1$ and various magnetic field strength. Circle symbols show the experimental results from Frank *et al.* (2001), and square symbols show the present results.

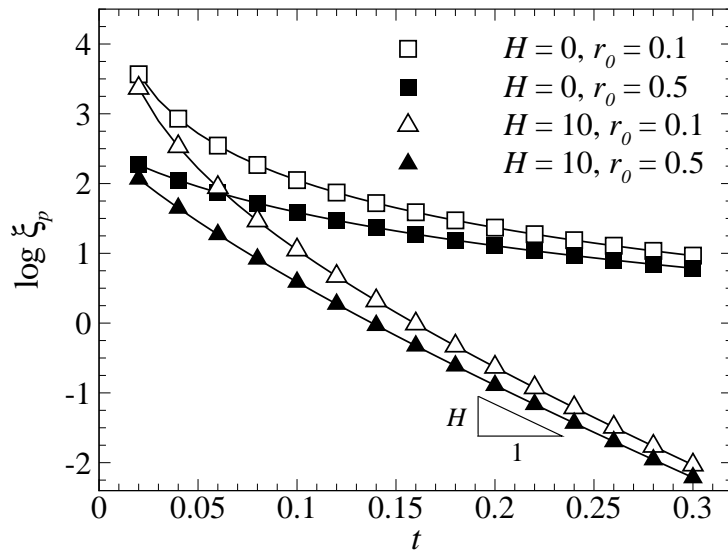


FIGURE 3.7: Natural logarithm of peak vorticity plotted against time, for a decaying quasi-2-D vortex in an open hydrodynamic flow (square symbols) and an open quasi-two-dimensional MHD flow (triangles). Open symbols show initial core radius $r_0 = 0.1$ and solid symbols show $r_0 = 0.5$. $\Gamma = 10$ for all cases. The slope of the quasi-2-D curves approaches $-H$ at larger times ($t > 0.2$).

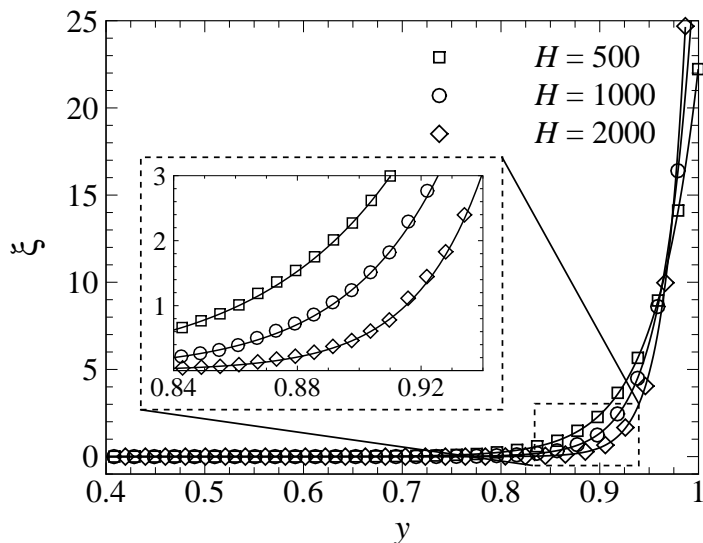


FIGURE 3.8: Vorticity profiles of fully developed quasi-2-D duct flows in the vicinity of the sidewall for $Re = 3000$ and $H = 500$ (square symbols), $H = 1000$ (circle symbols) and $H = 2000$ (diamond symbols). Symbols show results from present computations, while solid lines represent the analytical solution of SM82 model.

analytical solution, which is given by

$$\begin{aligned} \xi &= \frac{\partial v}{\partial x} - \frac{\partial u}{\partial y}, \\ &= \frac{\sqrt{H} \sinh(\sqrt{H}y)}{\cosh(\sqrt{H}) - 1}, \end{aligned} \quad (3.42)$$

where the exact solution for $u(y)$ is given in equation (3.29). The numerically obtained vorticity profiles were computed using a mesh with polynomial degree $N_p = 4$. Figure 3.8 demonstrates that the results from the numerical computations are in excellent agreement with the analytical solutions. Since the data contain zero values, the measure of mean absolute percentage deviation is irrelevant. Instead, relative standard errors (RSEs) are evaluated. The RSE evaluates the residuals relative to the predicted value and is calculated as follows (Goodarzi *et al.* 2009; Asadpour-Zeynali & Manafi-Khoshmanesh 2014):

$$\text{RSE} = \sqrt{\frac{\sum (y_{\text{numerical}} - y_{\text{predicted}})^2}{\sum y_{\text{numerical}}^2}}. \quad (3.43)$$

In general, estimates are considered statistically reliable if the RSE of the estimate is less than 30% (Klein *et al.* 2002). Regression analysis of the data reveal RSEs of

0.41%, 0.55% and 0.83% for $H = 500, 1000$ and 2000 , respectively. Since the Shercliff layer thickness is inversely proportional to the square root of Hartmann number, i.e. $\delta_S = aHa^{-1/2}$, the increased RSE with increasing friction parameter is expected due to the demand for finer resolution at higher H .

The numerical system has also been validated in previous published studies, including for confined hydrodynamic flows (Neild *et al.* 2010) and for heat transfer of stationary and oscillating cylinders in ducts (Cassells *et al.* 2016; Hussam & Sheard 2013; Hussam *et al.* 2012a).

3.5 Chapter summary

In the beginning of this chapter, equations that govern the magnetohydrodynamic flow and their analytical solutions have been presented. This was followed by a brief explanation on the computation scheme employed to solve the quasi-2-D MHD fluid flow. A high-order in-house solver based on the spectral-element method is employed to solve the magnetohydrodynamics equations under investigation. The solver has been validated against both published experimental results and analytical solutions, and the comparisons demonstrate excellent agreement. The specific problem setup and grid-resolution independence studies are discussed in each of the results chapters to follow.

Chapter 4

Spatial evolution of quasi-2-D Kármán vortex street

This chapter deals with the evolution of wake vortices behind a circular cylinder. First, the effects of Reynolds number and friction parameter on the dynamics of the wake are examined, with a focus on the shedding frequency and the distribution of the wake vortices. These two parameters are of primary interest as they play an important role in determining the mixing and heat transfer properties of the downstream flow.

This is followed by a stability analysis to predict the critical Reynolds number at which vortex shedding occurs. This is the first 2-D flow transition, from a steady to a time periodic wake, and is referred to as the Benard–von Kármán instability. The analysis provides a mapping of $Re_{cr}-H-\beta$, which is necessary to determine the combinations of these parameters that will produce laminar periodic flow for the subsequent analysis. Subsets of this parameter space has been reported previously by Frank (1991); Dousset & Pothérat (2008); Hussam *et al.* (2011). The present stability analysis extends the mapping regime to higher Hartmann numbers than reported in the aforementioned references.

Finally, a vortex decay model for predicting a decay of wake vortices is developed. An analogy of the Lamb–Oseen solution (for time decay of a vortex under viscosity) is obtained for a quasi-two-dimensional vortex, where both viscosity and Hartmann braking contribute. This solution is then used as the basis for the wake vortex decay model. The aim is to devise a model describing the decay behaviour of the peak vorticity within wake vortices behind a cylinder under the influence of a strong magnetic field. The obtained model is intended to inform the employment of cylinders as a vortex promoter, e.g. the most favourable location of an auxiliary cylinder, a down-

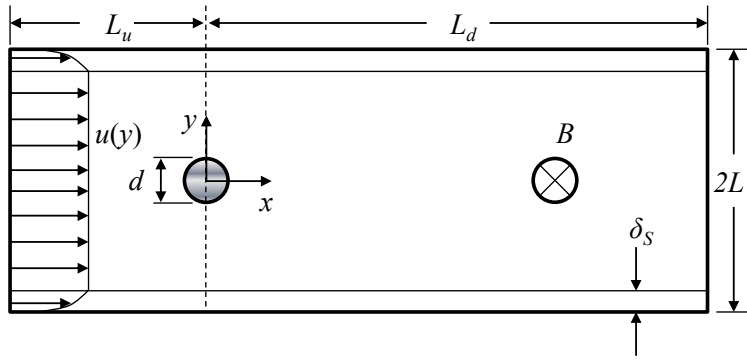


FIGURE 4.1: Schematic diagram of the numerical domain. The shaded area indicates a cylinder of infinite extension along the out-of-plane z -axis with diameter d .

stream cylinder which acts to sustain the dying vortices by means of proximity-induced interference effects. Furthermore, physical interpretations deduced from the findings are expected to furnish valuable information for the design of efficient heat transport systems in high-magnetic-field applications.

Results reported in this chapter have been published in Hamid *et al.* (2014a,b, 2015c).

4.1 Problem setup

The system of interest is a circular cylinder confined by a rectangular duct, as shown in Figure 4.1. The geometry has been non-dimensionalised using the half channel width, L as the reference length. The computational geometry is defined by a rectangle with scaled dimensions summarised in Table 4.1. The streamwise and transverse coordinates were designated by x and y , respectively, and the origin of the coordinate system was located at the cylinder plane section origin. The axis of the cylinder is parallel to the spanwise direction and perpendicular to the flow direction. A constant homogeneous magnetic field with a strength B is imposed parallel to the cylinder axis.

β	d/L	L_u/L	L_d/L
0.1	0.2	1.6	5
0.2	0.4	3.2	10
0.3	0.6	4.8	15
0.4	0.8	6.4	20

TABLE 4.1: Dimensions of computational domain, normalised by the length scale, L .

All boundaries are assumed to be electrically insulated. The flow enters the computational domain with a fully established velocity profile. With the origin of coordinates located at the centre of cylinder, the profiles for quasi-2-D MHD and HD cases are (Poth erat 2007)

$$u(y) = \frac{\cosh \sqrt{H}}{\cosh \sqrt{H} - 1} \left(1 - \frac{\cosh \sqrt{H}y}{\cosh \sqrt{H}} \right), \quad (4.1)$$

and

$$u(y) = 1 - y^2, \quad (4.2)$$

respectively. On the sidewalls and the cylinder surface, a no-slip condition is to maintain a velocity on these surfaces. A constant reference pressure boundary condition is imposed at the outlet, and a high-order Neumann pressure boundary condition is imposed on the Dirichlet velocity boundaries to preserve the third-order time accuracy of the scheme (Karniadakis *et al.* 1991).

4.2 Grid resolution study

A grid independence study has been performed by varying the element polynomial degree from 4 to 10, while keeping the macro element distribution unchanged. Meshes near the walls and the cylinder were refined to resolve the expected high gradients, especially for high-Hartmann-number cases (Poth erat *et al.* 2002). Figure 4.2 shows the spectral element discretisation of the computational domain. The pressure and viscous components of the time-averaged drag coefficient ($C_{D,p}, C_{D,visc}$) and the Strouhal frequency of vortex shedding (St) were monitored, as these are known to be sensitive to the domain size and resolution (Camarri & Giannetti 2007). Percentage errors relative to the case with highest resolution, $\varepsilon_P = |1 - P_{N_i}/P_{N=10}| \times 100$, was used as a monitor for each case, where P is the monitored parameter. A demanding MHD case with $Re_L = 8000$ and $H = 3750$ was chosen for this test. The results are presented in Table 4.2, and show rapid convergence when the polynomial order increases. A mesh with polynomial degree 7 achieved at most a 0.1% error while incurring an acceptable computational cost, and is therefore used hereafter.

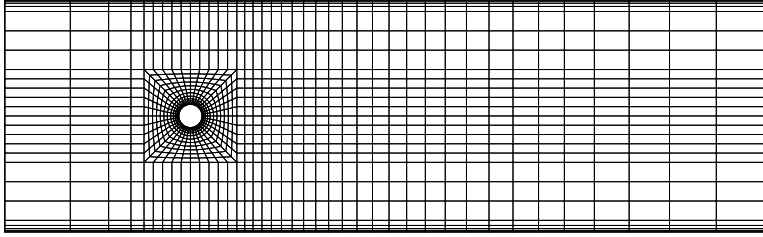


FIGURE 4.2: Macro-element distribution. Fine resolution was placed at the proximity of cylinder surface and walls to ensure accurate representation of the thin boundary layers and the expected wake structures.

TABLE 4.2: Grid independence study at $\beta = 0.1$, $Re_L = 8000$ and $H = 3750$

N_p	4	5	6	7	8	9
$\varepsilon_{C_{D,p}}$	1.6358	0.0987	0.0169	0.0238	0.0152	0.0350
$\varepsilon_{C_{D,visc}}$	3.9082	0.2370	0.2323	0.0997	0.0084	0.0027
ε_{St}	0.3603	0.3362	0.0272	0.0218	0.0089	0.0034

4.3 Stability analysis

A series of computations has been performed to investigate the effect of cylinder size and magnetic field strength on the onset of vortex shedding. The onset of the instability leading from a steady to a periodic wake flow, which is a Hopf bifurcation, can be described by the Stuart–Landau equation (Sohankar *et al.* 1998), i.e.

$$\frac{dA}{dt} = (\sigma_r + i\sigma_i)A - l_r(1 + ic)|A|^2A + \dots, \quad (4.3)$$

where $A(t)$ is a characteristic complex amplitude associated with the fundamental frequency component, σ_r is the linear growth rate of the perturbation, σ_i is the angular oscillation frequency during the linear growth phase, which is non-zero for a Hopf bifurcation, c is the Landau constant and l_r is a dimensional quantity that classifies the hysteretic nature in the vicinity of the critical transition.

Introducing the modulus and phase of A as $A = |A|e^{i\phi}$, the real (amplitude, i.e. the instantaneous growth rate at $Re > Re_{cr}$) and the imaginary (phase) parts of equation (4.3) are given by

$$\frac{1}{|A|} \frac{d|A|}{dt} = \sigma_r - l_r|A|^2 + \dots = \sigma_r \left(1 - \frac{|A|^2}{|A|_{\text{sat}}^2}\right) + \dots, \quad (4.4)$$

and

$$\frac{d\phi}{dt} = \sigma_i - l_r c |A|^2 + \dots = \sigma_i - \sigma_r c \frac{|A|^2}{|A|_{\text{sat}}^2} + \dots, \quad (4.5)$$

respectively, where $|A|_{\text{sat}} = (\sigma_r/l_r)^{1/2}$ is the saturation amplitude for $Re > Re_{cr}$, arising from the condition of saturation, i.e. $d|A|/dt = 0$ in equation (4.4). In this case, $l_r > 0$, whereby the non-linear term saturates the instability and the transition is said to be supercritical (i.e. non-hysteretic). If $l_r < 0$, the second term on the right-hand side of equation (4.4) accelerates the growth of the perturbation, where higher-order terms are required to describe saturation of the flow. There is a possibility of bi-stability (hysteresis) in the vicinity of the transition, whereby $|A| = 0$ or $|A| > 0$ are possible for some $\sigma_r < 0$, which corresponds to subcritical behaviour. In the linear regime, however, the second term on the right-hand side of equation (4.4) is negligible, it follows that A will grow in the exponential manner predicted by linear stability analysis at a rate that depends on the magnitude of σ_r . At the transition point, its value changes from negative to positive. The term in the left-hand side of equation (4.5) becomes the constant angular frequency of oscillation $\sigma_{i,\text{sat}}$ if the flow reaches a periodic state at saturation, and the term $\sigma_r c$ determines the shift from the oscillation frequency in the linear regime.

Equation (4.4) can be rewritten as

$$\frac{d \log |A|}{dt} = \sigma_r - l_r |A|^2 + \dots \quad (4.6)$$

According to equation (4.6), the real parameters in the Stuart–Landau equation can be determined from numerical computations by plotting $d \log |A| / dt$ against $|A|^2$. In the present investigation, the lift coefficient is adopted as the signal to determine the amplitude. A fully-saturated time-dependent solution was first developed for a given Reynolds number, from which Re was decreased to a value close to the onset of vortex shedding, and the flow was evolved until steadiness is recovered (the typical time history of lift coefficient is shown in Figure 4.3(a)).

The time derivative of mode amplitude logarithm $d \log |A| / dt$ was then determined using the central difference method from the lift coefficient time history, and plotted against $|A|^2$. The vertical axis intercept on this plot corresponds to the linear growth rate of the instability and the gradient for small amplitudes near $|A|^2 = 0$ corresponds to $-l_r$. It is noted from Figure 4.3(b) that the plot is linear near the vertical axis, indicating the suitability of the Stuart–Landau model in describing the transition, and

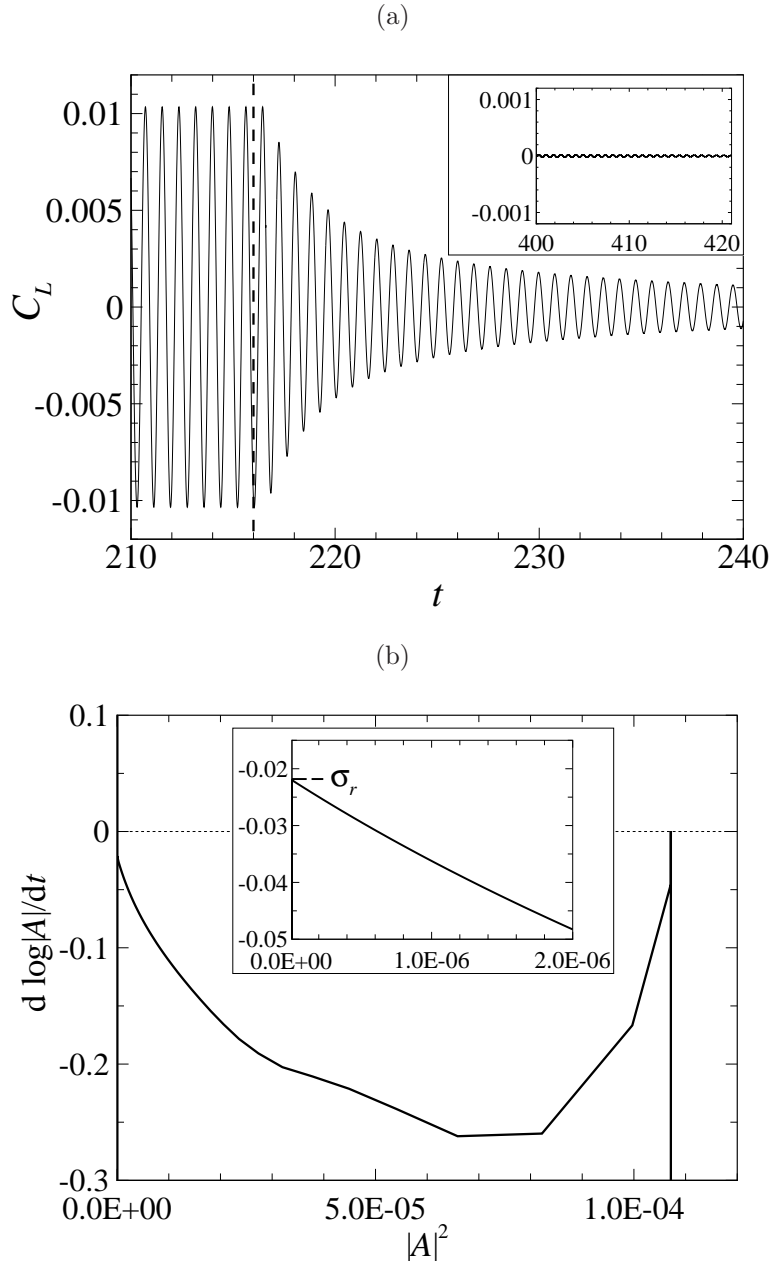


FIGURE 4.3: (a) Time evolution of lift coefficient for case with $\beta = 0.1$ and $H = 1000$. On the left-hand side of the dashed line is the saturated lift coefficient history for $Re_L = 2000$, while the right-hand side part represents the history when Reynolds number is impulsively reduced to $Re_L = 1670$. (b) Instantaneous growth rate plotted against the square of the amplitudes for case in (a). The linear behaviour and negative slope near the vertical axis demonstrate supercritical transition.

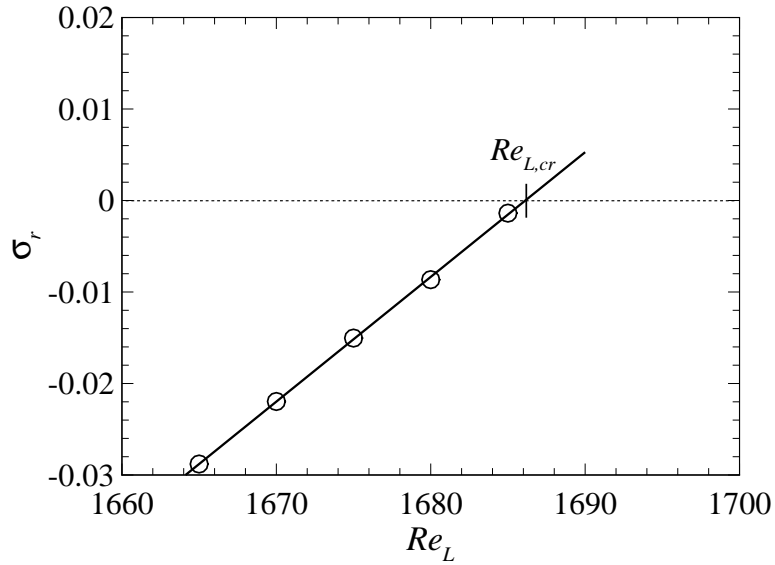


FIGURE 4.4: Linear global growth rate plotted against Reynolds number for $\beta = 0.1$ and $H = 1000$. The solid line is a linear regression of the growth rate data.

that the slope is negative, demonstrating that the transition is non-hysteretic. This observation is in agreement with the previously reported experimental finding (Frank *et al.* 2001), where no evidence of hysteresis was observed for a circular cylinder wake flow. It is also noted that the line intersects the horizontal axis due to the initial fully-developed periodic state of the signal. The method was repeated for several Re close to the onset of vortex shedding, and the corresponding values of σ_r is then plotted against Re_L , as shown in Figure 4.4. The critical Reynolds number is determined by extrapolating a linear fit to the data to zero growth rate. The linear nature of the data demonstrates that it is well described by Stuart–Landau model.

The plot of the resulting $Re_{d,cr}$ against β and H is presented in Figure 4.5. It is important to note that the Reynolds number in this particular plot is scaled with the diameter of the cylinder rather than the duct geometry as the cylinder size characterizes the structure of the two-dimensional flow (Frank 1991). The main conclusion inferred from Figure 4.5 is that the magnetic field delays the onset vortex shedding. The results revealed a monotonic increase in the critical Reynolds number with the Hartmann friction parameter and blockage ratio. This is attributed to the fact that strong magnetic field acts to dampen transverse fluctuations in the channel and confinement effect tends to delay the transition from steady to periodic flow (Birkhoff &

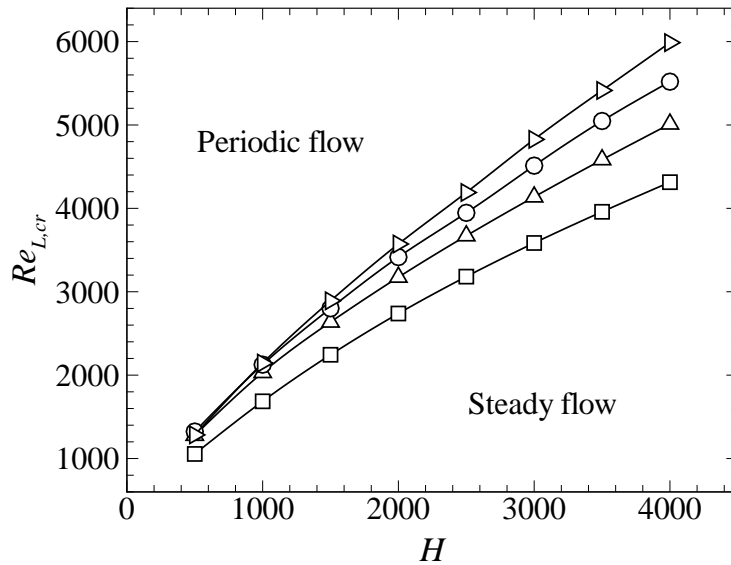


FIGURE 4.5: Stuart–Landau model predictions of critical Reynolds number Re_{cr} plotted against friction parameter H at various blockage ratios, with a closed-up in small H regime. Square, triangle, circle and right triangle symbols represent $\beta = 0.1, 0.2, 0.3$ and 0.4 , respectively. The solid lines are spline fits of the present data (indicated by the open symbols). Closed symbols are numerical data from Hussam *et al.* (2011).

Zarantonello 1957), resulting in a higher Re being required for the onset of instability. Furthermore, Re_{cr} becomes almost proportional to H at higher range of H .

At a given Hartmann number, the critical Reynolds number increases as the blockage ratio is increased. At higher blockage ratio, however, the change in Re_{cr} is less significant. This observation can be explained as follows; as the gap between the cylinder and the confining wall is reduced, the flow at the vicinity of the cylinder is locally accelerated and hence experience a locally high- Re flow. The increase in the level of instability offsets the damping effect caused by the increase in blockage ratio.

4.4 Dynamics of the wake flow

In the following sections, the analysis of vortex shedding frequency and distributions are presented. For this particular investigation, the ratio of cylinder diameter to the duct height is fixed at 0.1.

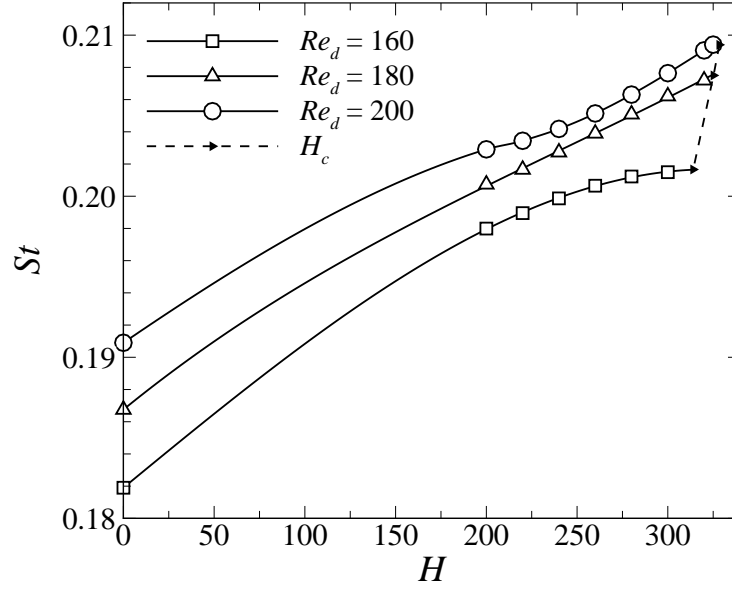


FIGURE 4.6: Variation of the Strouhal number. The symbols connected by the dashed line indicate the critical H , beyond which results in a complete suppression of vortex shedding due to Hartmann damping.

4.4.1 Shedding frequency analysis

The frequency of vortex shedding from a cylinder in hydrodynamic flows has been shown to be dependent on Reynolds number (Roshko 1954a). However, in magnetohydrodynamic flows, the presence of the magnetic field is expected to modify the frequency of vortex shedding. The present study seeks to investigate the effect of axial magnetic field on the vortex shedding frequency. The dependencies of H and Re on the shedding frequency are illustrated in Figure 4.6. The dimensionless frequency is represented by the Strouhal number, $St = fd/U_0$, where f is the shedding frequency, calculated from the fluctuating lift force imparted on the cylinder due to the near-wake flow unsteadiness.

As Figure 4.6 indicates, the Strouhal number is dependent on both H and Re . In the range of the H and Re considered in this study, St increases with increasing H at a given Re . This observation can be attributed to the fact that the imposed magnetic field tends to stretch the shear layer at the near wake, and hence mass conservation requires that the wake advection velocity, U_ξ is increased. It can be seen in Figure 4.7(b-d) that stronger magnetic field intensity produces a narrower wake, thus extending the formation region behind the cylinder before the shear layer rolls up into a vortex street.

Increasing H beyond a critical value results in complete suppression of vortex shedding due to Hartmann damping (as seen in Figure 4.7(e)). Also to be noted is that the boundary layer thickness is modified by the magnetic field, where higher H leads to thinner boundary layer.

The accelerating effect of the magnetic field on the wake advection is illustrated in Figure 4.8. The increase in U_ξ as H is increased explains the increase in St . It is also interesting to note that at a given H , St increases but U_ξ decreases with increasing Re . In this case, the increase in St cannot be associated with an increase of U_ξ , but rather to the increased vorticity production rate as Re is increased. At high Re , the vorticity attached to the cylinder quickly organises into a coherent structure due to the high rate of vorticity supply, thus the duration associated with the formation of vortex shedding becomes shorter, leading to a shorter formation length and a higher St .

In order to verify this argument, the formation length, L_F , has been measured and the results are presented in Table 4.3. The formation length is defined as a distance from the rear of the cylinder to the position of first shed vortex peak strength (Green & Gerrard 1993; Kieft *et al.* 2003). The measurement error, ϵ_{L_F}/λ presented in Table 4.3 is associated with the phase gap between two consecutive snapshots, i.e. 0.25π (which corresponds to nine snapshots per shedding cycle). The maximum error per wavelength is 11%, where the wavelength is calculated by employing the Taylor's hypothesis (which is valid since the present case is in laminar flow regime), i.e. $\lambda = U_\xi/f$. The hypothesis states that, for incompressible plane channel flow with relatively small turbulence fluctuations, the temporal response of some instantaneous quantity at a fixed point in space is proportional to its derivative in the streamwise direction (Taylor 1938). It is found that the distance taken for the vorticity to complete its formation decreases as Re is increased, which supports the aforementioned statement. This trend is also in agreement with the experimental results of the HD counterpart (Green & Gerrard 1993; Nishioka & Sato 1978; Schaefer & Eskinazi 1959; Szepessy & Bearman 1992). Furthermore, the decrease in the formation length is more prominent at higher H values.

This argument also explains the contradicting trend of St at the higher- Re regime as reported by Dousset & Poth erat (2008). They found that at a given Re , St decreases with increasing H . At a higher Re , the rate of vorticity production is increased, thus reducing the acceleration effect due to the near wake contraction. At this point, as H increases, the opposing Lorentz force becomes dominant and hence the St is decreased.

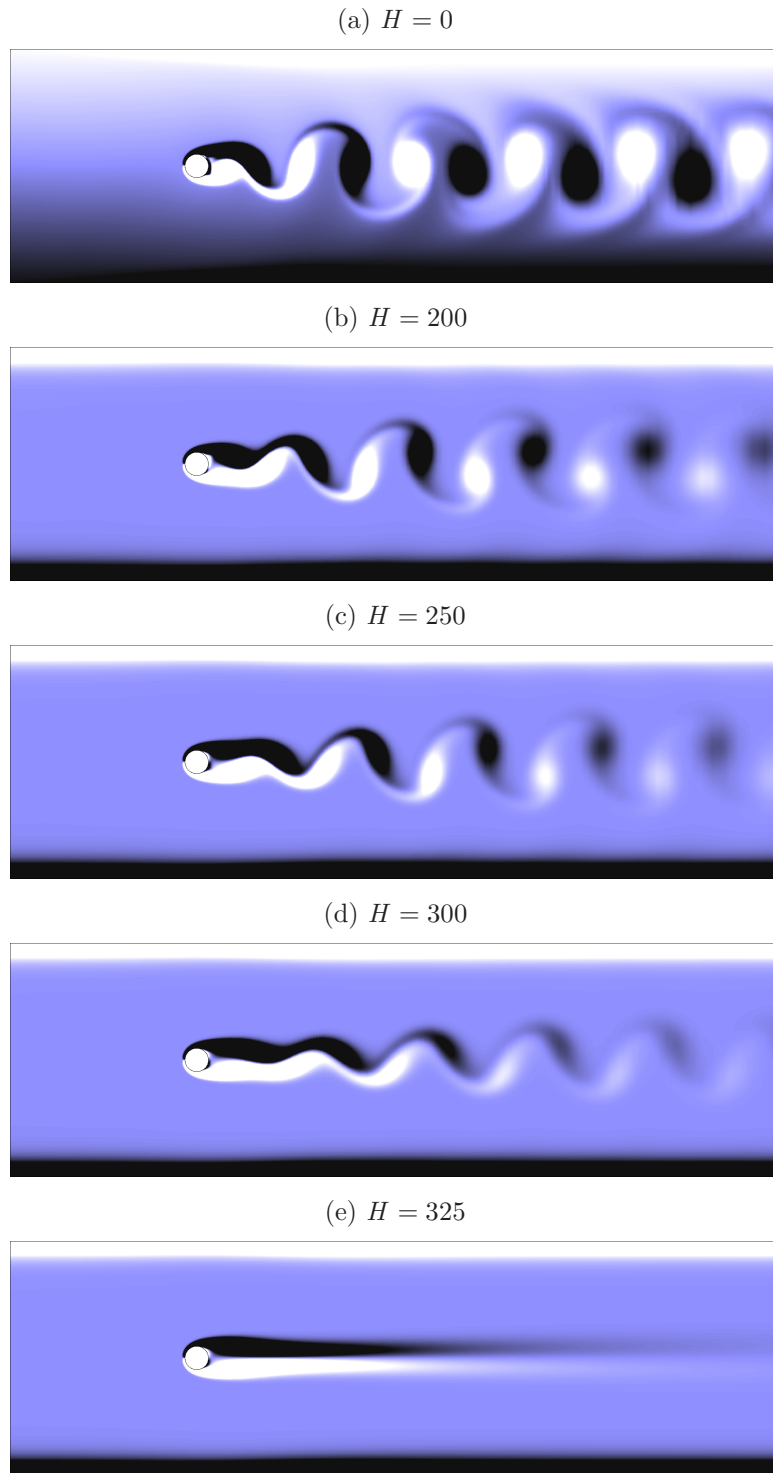


FIGURE 4.7: Contour plots of vorticity snapshot at $Re_d = 160$ and at Hartmann numbers as indicated. Contour levels ranges between -2 and 2, with light and dark countours representing positive and negative vorticity, respectively.

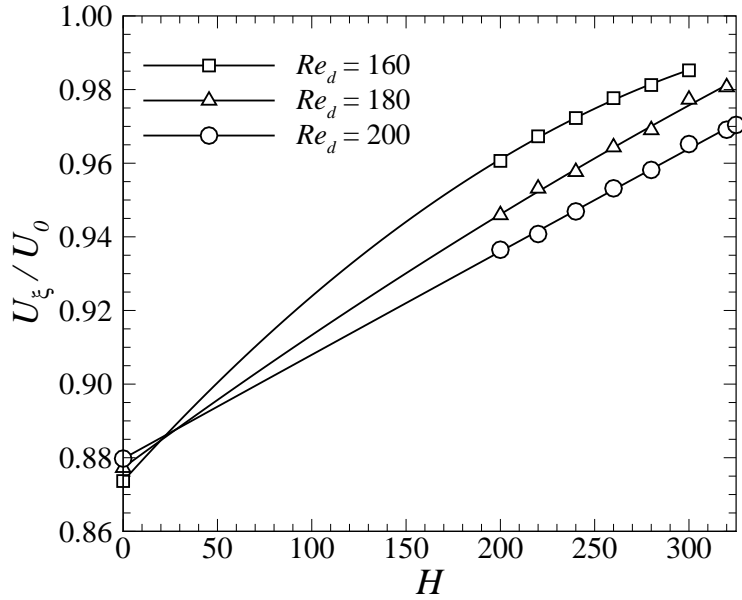


FIGURE 4.8: Advection velocity of wake vortices. The velocities are calculated at the stable region of the wake, where the vortices advected downstream at almost constant velocity. The line is a 2nd order polynomial fit of the data.

It is important to note that in the current simulations, the magnetic field was imposed in the axial direction. However, when the magnetic field is transverse to the cylinder, a previous investigation (Singha & Sinhamahapatra 2011) has found that St is not influenced by the change in H for a fixed Re .

4.4.2 Vortex distributions

Vortex trajectories through the computed domain have been recorded by tracking the locations of local maxima and minima in the vorticity fields. The locations and values of vorticity extrema within a single wake vortex as it advects downstream of a body are determined by searching within each spectral element for collocation points having a locally maximum vorticity magnitude, and then iterating using a Newton–Raphson method to converge on the accurate position. This approach preserves the spectral accuracy of the peak vorticity. In all cases, the trajectories of positive and negative vorticity show a symmetric profile with respect to the wake axis. From these trajectories, lateral spacing (h) and longitudinal spacing (l) of the vortices have been extracted and normalised by the cylinder diameter. The lateral spacing is defined as the vertical distance between peak vorticity of adjacent opposite-sign vortices, or twice the distance

H	Re_d	L_F	ϵ_{L_F}	λ	ϵ_{L_F}/λ (%)	l_{avg}
0	160	0.80	0.17	4.80	3.6	4.80
	180	0.78	0.14	4.70	3.0	4.69
	200	0.68	0.12	4.61	2.7	4.61
200	160	1.48	0.26	4.85	5.5	4.86
	180	1.18	0.18	4.71	3.9	4.72
	200	0.94	0.19	4.62	4.1	4.62
250	160	1.81	0.29	4.87	6.0	4.87
	180	1.45	0.22	4.72	4.6	4.73
	200	1.13	0.20	4.64	4.3	4.64
300	160	2.69	0.52	4.89	10.6	4.91
	180	1.67	0.35	4.74	7.4	4.74
	200	1.33	0.20	4.65	4.4	4.65

TABLE 4.3: Vortex shedding formation length and longitudinal length. The formation length is measured from the rear of the cylinder and both length are non-dimensionalised by the cylinder diameter.

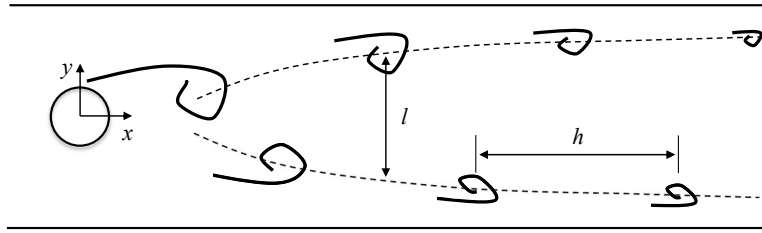


FIGURE 4.9: Schematic definition of vortex street longitudinal (h) and lateral (l) spacings. Dashed lines indicate vortex trajectories.

between peak vorticity of either a positive or a negative-signed vortex and the wake centreline (for a symmetric vortex shedding), while the longitudinal spacing is defined as the distance between successive vortices of the same sign (refer Figure 4.9).

The spatial evolution of lateral spacing is presented in Figure 4.10. For brevity, only cases with $H = 0$ and cases with highest H , i.e. $H = 300$ are shown. A very distinctive wake pattern was observed between the two classes of flows. When the magnetic field is absent, the lateral spacing first decreases to zero at a distance about 130-160% of its respective wavelength (shown by the dotted lines). At this position, an inversion of the wake takes place, where vortices cross the wake centreline to the side opposite to that on which they formed. Beyond the inversion point, the lateral spacing increases along the computed domain. By referring to Figure 4.7(a), it is apparent that the inversion mechanism is the entrainment of vorticity from the free stream into the wake, which tends to push the vortex towards the inverted position. It is also important to

note that the distance at which the wake inverts from the cylinder decreases when Re is increased, which is in agreement with the previous findings (Camarri & Giannetti 2007). However, in the presence of magnetic fields, no wake inversion takes place, at least along the length of the computed domain.

By inspecting the decay of the wake vortices, it is expected that inversion will never takes place for MHD flow for this particular blockage ratio as the vortex dies away before the inversion takes place. In contrast, wake inversion will eventually occur in hydrodynamic flow even for low blockage ratio (Camarri & Giannetti 2007). This can be explained due to the fact that in the presence of magnetic fields, the Lorentz force tends to flatten the incoming flow velocity profile, which eliminates vorticity from the core flow. As a result, the wake vortices advect downstream in an almost parallel manner (as indicated by the small gradient of the MHD data in Figure 4.10). While there is no appreciable difference in h for all Re amongst the hydrodynamic flow cases, h decreases with increasing Re for the MHD cases. As Re is increased, the rate of vorticity supply to the shear layer attached to the cylinder increases. As a result, the tip of the shear layer tends to roll up further towards the wake axis, narrowing the wake. Furthermore, it can be seen that the wake is wider under the influence of a magnetic field than the corresponding non-MHD wake across all of these Reynolds number. This observed widening is supported by the previous 3D simulation by Kanaris *et al.* (2013).

On the other hand, the longitudinal spacing was found to be almost constant for a given H and Re , except in the formation region, where l increases until the vortex stabilizes. Here, the local value of l is not important, and therefore only its mean values are presented in Table 4.3. It is important to note that the local l was determined from the phase diagram, and that the average value was calculated over the stable region. These average values are comparable with the wavelength calculated previously, which strengthens the previous argument that the wake flow is laminar. Also to be noted is that l_{avg} increases with increasing H and decreasing Re , and that l_{avg} is more sensitive to changes in Re than H . This may be understood as follows: the non-dimensional shedding frequency is given by $St = U_{\xi}d/U_0l$ (Roshko 1954a). This relation indicates that the longitudinal spacing is proportional to the wake advection velocity and inversely proportional to the Strouhal number. Although both St and U_{ξ} increase with increasing H , the increment of U_{ξ} is more prominent compared to St , which explains the increase in l for increased H . A similar argument applies to the

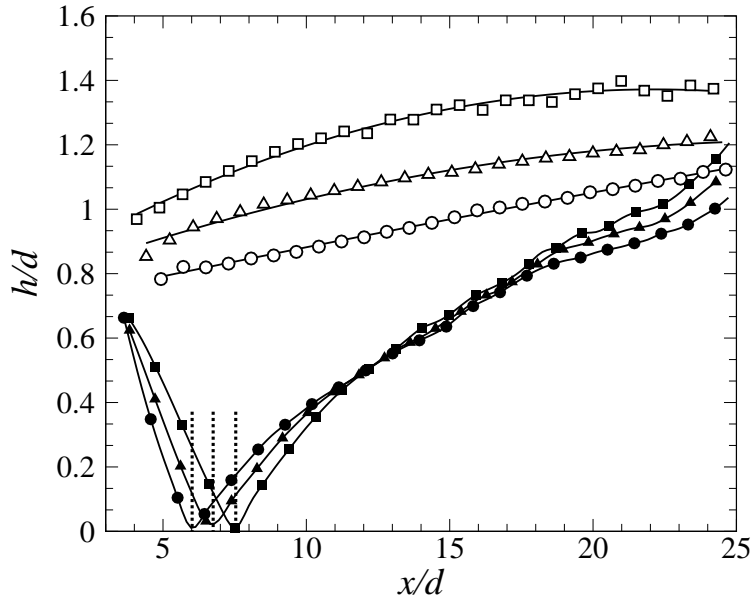


FIGURE 4.10: Spatial variation of vortex lateral spacing. Solid symbols show $H = 0$ and open symbols show $H = 300$. Square, delta and circle symbols represent $Re_d = 160, 180$ and 200 , respectively.

hydrodynamic flows, where the reduction in St is more significant compared to the reduction in U_ξ when Re is decreased, which results in increasing l_{avg} with decreasing Re . The explanation for the increased l as Re is decreased in MHD flows is more straightforward: reduction in Re leads to lower St and higher U_ξ .

4.5 Decay of wake vortices

4.5.1 Analytical solution for vortex decay in a quasi-2-D flow

In this section, the analytical solution for the decaying line vortex is devised to gain fundamental understanding of the behaviour of an isolated vortex in a quasi-two-dimensional flow, which will serve as the basis for a regression fit describing the evolution of cylinder wake peak vorticity in a rectangular duct. From Hussam *et al.* (2011), the curl of quasi-two-dimensional magnetohydrodynamic momentum equation (i.e. equation (3.24)) yields the quasi-two-dimensional vorticity transport equation for an incompressible flow of an electrically conducting fluid between two plates subjected to a uniform strong magnetic field in the out-of-plane direction, given in dimensional form as

$$\frac{D\hat{\xi}_{\perp}}{D\hat{t}} = \nu\hat{\nabla}^2\hat{\xi}_{\perp} - \frac{2}{t_H}\hat{\xi}_{\perp}, \quad (4.7)$$

where $\hat{\xi}_{\perp}$ is vorticity and $D/D\hat{t}$ the material derivative. Therefore, an advecting packet of vorticity will be subjected to both a diffusion process acting to smooth out the vorticity field, and an exponential damping due to the quasi-two-dimensional friction term. By scaling the length by a , the time by a^2/ν and the vorticity by ν/a^2 , the transport equation can be written as

$$\frac{D\xi_{\perp}}{Dt} = \nabla^2\xi_{\perp} - 2Ha\xi_{\perp}, \quad (4.8)$$

where ξ_{\perp} , t and ∇ are dimensionless counterparts to $\hat{\xi}_{\perp}$, \hat{t} and $\hat{\nabla}$, respectively. Consideration is first given to a solution for the decay of a quasi-2-D vortex located at the frame origin, maintaining a solely exponential decay of circulation through Hartmann braking far from the vortex, in an open quasi-two-dimensional flow. For convenience, equation (4.8) is expressed for an axisymmetric ($\partial/\partial\theta = 0$) flow in cylindrical coordinates as

$$\frac{D\xi_{\perp}}{Dt} = \frac{\partial^2\xi_{\perp}}{\partial r^2} + \frac{1}{r}\frac{\partial\xi_{\perp}}{\partial r} - 2Ha\xi_{\perp}, \quad (4.9)$$

where r is the radial coordinate and the vortex is located at $r = 0$. Recognising that radial velocity $u_r = 0$ and $\partial\xi_{\perp}/\partial\theta = 0$ for decaying quasi-2-D vortex flow, the material derivative reduces to $\partial\xi_{\perp}/\partial t$, and equation (4.9) can be transformed (Polyanin 2001) using

$$\xi_{\perp}(r, t) = e^{(-2Hat)}\xi(r, t), \quad (4.10)$$

to give

$$\frac{\partial\xi}{\partial t} = \frac{\partial^2\xi}{\partial r^2} + \frac{1}{r}\frac{\partial\xi}{\partial r}. \quad (4.11)$$

This is precisely the vorticity transport equation for an azimuthal axisymmetric hydrodynamic flow about $r = 0$. For the case of the temporal decay of a quasi-2-D vortex, conserving circulation as $r \rightarrow \infty$, the solution to this equation is exactly the Lamb–Oseen vortex solution, where the vorticity field is given by

$$\xi = \frac{\Gamma}{\pi r_c^2} e^{(-r^2/r_c^2)}. \quad (4.12)$$

Note that this solution is indeed independent of θ , and it can readily be shown that $u_r = 0$. Γ represents the initial amount of circulation contained in the elementary quasi-2-D vortex. The vortex evolves over time $\tau = t - t_0$, where t_0 is an arbitrary initial time. Applying the transformation in equation (4.10) yields

$$\xi_{\perp} = \frac{\Gamma}{\pi r_c^2} e^{-r^2/r_c^2} e^{-2Ha\tau}, \quad (4.13)$$

and the peak vorticity is expressed by solving for $r = 0$, giving

$$\xi_{\perp,p} = \frac{\Gamma}{\pi r_c^2} e^{-2Ha\tau}. \quad (4.14)$$

The dimensionless core radius evolves as $r_c = \sqrt{4\tau}$ (note the absence of ν from the argument of the square root due to the non-dimensionalisation, compared to the dimensional solution) (Saffman 1992). Substituting to eliminate r_c and taking the time derivative yields

$$\frac{\partial \xi_{\perp,p}}{\partial \tau} = -\frac{\Gamma}{4\pi\tau} e^{-2Ha\tau} \left[2Ha + \frac{1}{\tau} \right]. \quad (4.15)$$

The terms in the square brackets constitute the Hartman braking and viscous contributions to the vortex decay, respectively. Equating these, substituting τ in terms of r_c and solving gives a threshold core radius below which viscosity exceeds Hartman friction in reducing the peak vortex strength, $r_{c1} = \sqrt{2}Ha^{-1/2}$. The vortex core diameter is then given by $d_{c1} = 2^{3/2}Ha^{-1/2} \approx 3Ha^{-1/2}$, i.e. approximately three times the limiting scale on perpendicular flow structures under the quasi-two-dimensional model, $l_{\perp}/l_{\parallel} = Ha^{-1/2}$. Therefore vortices whose decay is contributed to significantly by viscous diffusion can exist in a quasi-two-dimensional flow under the SM82 model.

Substituting $Ha = 0$ into equation (4.14) recovers the peak vortex time history for a Lamb–Oseen vortex written here in terms of time,

$$\xi_p = \frac{\Gamma}{4\pi(t - t_0)}, \quad (4.16)$$

and finally the corresponding expression for a vortex in quasi-two-dimensional flow is

$$\xi_{\perp,p} = \frac{\Gamma}{4\pi(t - t_0)} e^{-2Ha(t-t_0)}. \quad (4.17)$$

Equation (4.17) will serve as a basis for the form of the correlation function developed in this chapter. It is important to note that real wake vortices experience different effects to an isolated Lamb–Oseen vortex due to the fact that wake vortices are being advected downstream and there is interaction between neighbouring vortices, which

leads to mutual straining and merging among the vortices (Durgin & Karlsson 1971; McWilliams 1990). Furthermore, wake vortices experience a confinement effect due to the duct wall, where in high-blockage cases the vortices shed from the wall can cause dramatic changes in the global flow behaviour and modification of the flow structure (Sahin & Owens 2004). On the other hand, an isolated vortex possesses a general structure of monotonic decrease of vorticity with radial distance from a central extremum (McWilliams 1990). Hence, it is expected that the model being developed will be more complicated than the solutions in equations (4.16) and (4.17).

Before proceeding with the analytical model, the scaling condition arising from the inertial time scale is briefly explored,

$$l_{\perp}/a > N^{-1/3}, \quad (4.18)$$

in the context of a quasi-two-dimensional vortex. The tangential velocity profile for the vortex can be adapted from the known Lamb–Oseen solution (e.g. see Devenport *et al.* (1996)) written in terms of initial circulation as

$$u_{\theta}(r, t) = \frac{\Gamma}{2\pi r} \left(1 - e^{-r^2/r_c^2}\right) e^{-2Ha\tau}, \quad (4.19)$$

and maximum tangential velocity $u_{\theta, \max}$ as

$$u_{\theta}(r, t) = u_{\theta, \max} \left(1 + \frac{1}{2\alpha_{LO}}\right) \frac{r_{\max}}{r} \left[1 - e^{-\alpha_{LO}r^2/r_{\max}^2}\right] e^{-2Ha\tau}, \quad (4.20)$$

where $r_{\max} = \sqrt{\alpha_{LO}}r_c(t)$ is the radius at which the tangential velocity is maximum and $\alpha_{LO} = 1.25643$ is the Lamb–Oseen constant. Given the requirement that $N \gg 1$, the dependence of N on the reciprocal of U means that considering the maximum tangential velocity as the reference velocity is equivalent to finding the minimum local interaction parameter for a vortex. Substituting $u_{\theta, \max} = U$ and solving equations (4.19) and (4.20) for U yields

$$U = \frac{\hat{\Gamma}}{\sqrt{\nu \hat{t}}} \frac{\sqrt{\alpha_{LO}}}{4\pi(2\alpha_{LO} + 1)}. \quad (4.21)$$

The interaction parameter can then be expressed as

$$N = Ha^2 \left[\frac{2\pi(2\alpha_{LO} + 1)}{\sqrt{\alpha_{LO}}} \right] \frac{r_c}{\Gamma}. \quad (4.22)$$

For a Lamb–Oseen vortex, a Reynolds number based on circulation is conventionally defined as $Re_{\Gamma} = \hat{\Gamma}/2\pi\nu = \Gamma/2\pi$. Taking the core radius to represent the scale of

a quasi-two-dimensional structure, i.e. $r_c = l_\perp/l_\parallel$, using equation (4.22) to express equation (4.18) in terms of r_c ultimately produces

$$r_c > \left[\frac{\sqrt{\alpha_{LO}}}{2\alpha_{LO} + 1} \right]^{1/4} N_\Gamma^{-1/4}, \quad (4.23)$$

where an interaction parameter based on vortex circulation, $N_\Gamma = Ha^2/Re_\Gamma$, has been introduced. The dissipation of a quasi-two-dimensional vortex through Hartman braking will reduce Re_Γ over time, in turn increasing N_Γ , thus reducing the minimum allowable scale satisfying the quasi-two-dimensional model through equation (4.23). It follows then that if a vortex initially satisfies the quasi-two-dimensional model, it will do so throughout its lifetime.

4.5.2 Analytical model for the decay of wake vortices

4.5.2.1 Derivation

It is observed from previous studies (and follows from the Hartmann braking term in the quasi-two-dimensional model) that increasing Hartmann number generally acts to increase the decay rate of vortices (Hussam *et al.* 2011). To quantify these observations, the peak vortex strength of wake vortices behind a cylinder has been recorded at different blockage ratios and a broad range of Hartmann and Reynolds numbers. The model is derived by assuming that wake vortices decay according to a law of the same form as isolated vortices, on the basis that Hartmann friction remains the dominant mechanism and that non-linear interactions act too slowly to strongly affect the vortex profile during the decay. This assumption is expected to remain valid at high N , and provided the influence of the walls remains limited (i.e. smaller blockage ratios), ξ_p and $\xi_{\perp,p}$ are assumed to take the form

$$\xi_p = \frac{a'}{t - t_0}, \quad (4.24)$$

and

$$\xi_{\perp,p} = \frac{a'}{t - t_0} e^{-b'(t-t_0)}, \quad (4.25)$$

for pure hydrodynamic and magnetohydrodynamic cases, respectively. The values of constants in these equations are evaluated by means of a regression analysis. Since the advection velocity U_ξ for the wake vortices is approximately constant (Ponta 2010), it is possible to write $t - t_0 = (x - x_0)/U_\xi$, where the cylinder is located at $x = 0$, and

x_0 is the streamwise location of the virtual point vortex that the wake vortices project from. Hence, equations (4.24) and (4.25) can be recast in terms of streamwise position of a wake vortex as

$$\xi_p = \frac{a}{x - x_0}, \quad (4.26)$$

and

$$\xi_{\perp,p} = \frac{a}{x - x_0} e^{-b(x-x_0)} = \frac{a}{x - x_0} e^{-bx+c}. \quad (4.27)$$

While a , x_0 , b and c are constant for the Lamb–Oseen and quasi-two-dimensional vortex decay solutions (equations (4.16) and (4.17), respectively), it is anticipated that these will exhibit a dependence on one or more of the control parameters (i.e. Re , H and β) when applied to describe the decay of a transported wake vortex. At $H \gg 1$, the area-averaged velocity, U_{avg} , across the duct approaches the peak velocity U_0 (in contrast, for Poiseuille flow in a channel, $H = 0$, $U_0 = 3/2U_{\text{avg}}$). It is also convenient to define a Reynolds number based on the cylinder diameter, $Re_d = U_0 d / \nu$, and an effective Reynolds number based on mean velocity through the gaps either side of the cylinder ($2L - d$), which simplifies to $Re'_d = 2\beta Re_L / (1 - \beta)$, where $\beta = d/2L$ is the blockage ratio. The definition of Re'_d assumes that the change in peak velocity due to cylinder blockage is consistent with the change in area-averaged velocity. The use of different length scales in MHD cylinder wake flows is inevitable: the two-dimensional linear braking term is governed by Ha and L , whereas the structure of the cylinder wake is governed by d (Frank *et al.* 2001).

The expressions for parameters a and x_0 are obtained from simulations of hydrodynamic flow within the parameter space $0.1 \leq \beta \leq 0.4$ and $300 \leq Re_L \leq 900$. The values of a and x_0 were determined by curve-fitting the spatial decay of peak vortex strength for each hydrodynamic case ($H = 0$) into equation (4.26). A typical time history of peak vorticity is presented in Figure 4.11.

Inspection of the data for a range of parameters revealed that a and x_0 are dependent on Reynolds numbers relating to the cylinder diameter and the blockage ratio (refer Figure 4.12). It can be seen from Figure 4.12(a) that parameter a increases linearly with increasing effective Reynolds number Re'_d , and with increasing blockage ratio the gradient decreases. Figure 4.12(b) shows that parameter x_0 decreases linearly with

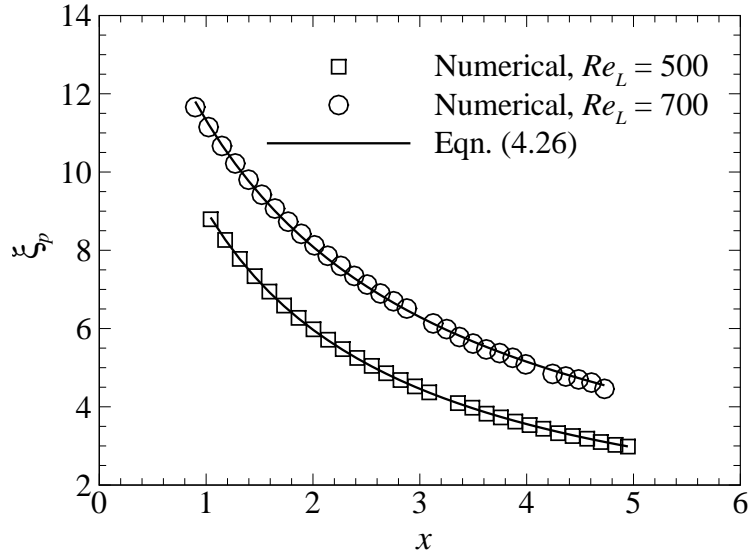


FIGURE 4.11: Spatial evolution of peak vorticity decay for $\beta = 0.1$ and $Ha = 0$, at Reynolds numbers as indicated in the legend. Lines are least-squares fits of the data to equation (4.26).

$Re_d(1-\beta)$, and an increase in blockage ratio produces an increase in gradient magnitude of the linear trends. The least-squares linear fits for coefficients a and x_0 take the form

$$a = M_a Re_d' - C_a, \quad (4.28)$$

and

$$x_0 = M_{x_0} Re_d(1-\beta) - C_{x_0}, \quad (4.29)$$

respectively. The slope (M) and the intercept (C) of these fits are plotted against blockage ratio in Figure 4.13. Both M and C are found to vary almost linearly with β (producing coefficients of determination in the range $0.990 < r^2 < 0.994$), and the resulting relations are given in equation (4.30).

Using the same approach as per the development for expressions for a and x_0 for pure hydrodynamic flow, parameters b and c are derived from the peak vorticity time history of magnetohydrodynamic cases across $0.1 \leq \beta \leq 0.4$, $500 \leq H \leq 5000$ and $1500 \leq Re_L \leq 8250$, where a laminar periodic shedding regime is captured throughout this parameter range. The valid upper range of Re_L is determined by both the assumptions of the SM82 model, i.e. the flow has sufficiently large perpendicular scales, in such a way that the condition of $N \gg (a/l_\perp)^3$ and $H \gg (a/l_\perp)^2$ are satisfied (Pothérat *et al.* 2000;

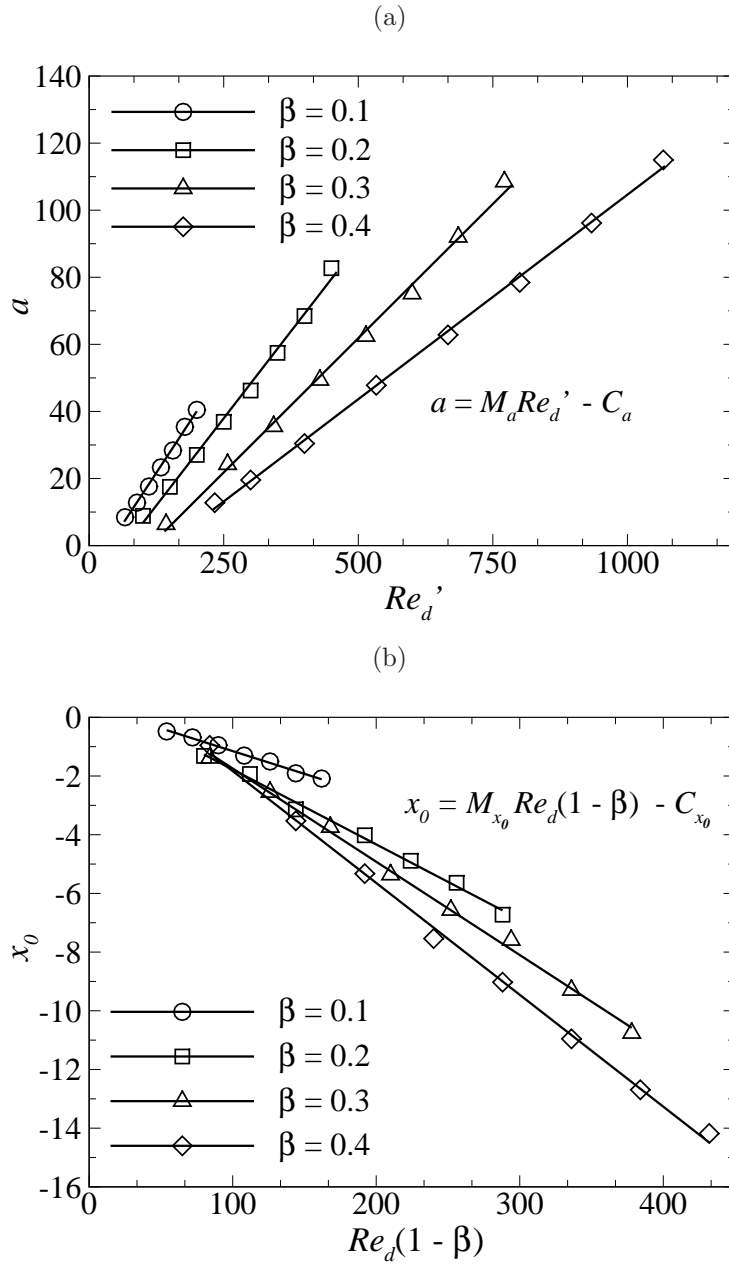


FIGURE 4.12: Variations of parameters a and x_0 with respect to different cylinder Re and blockage ratio.

Poth erat 2007), and the Hartmann layers must be laminar, i.e. the Reynolds number based on the Hartmann layer thickness $Re/H < 250$ (Sommeria & Moreau 1982). The former criterion is stricter than the latter, and by taking $N > 10$ as an indicative threshold for the applicable range of interaction parameters and $H = 500$, the model will break down at a Reynolds number of order $Re_L < H^2/N = 500^2/10 = 25000$, which is well above the maximum Re_L studied, i.e. $Re_L = 8250$. Dousset & Poth erat

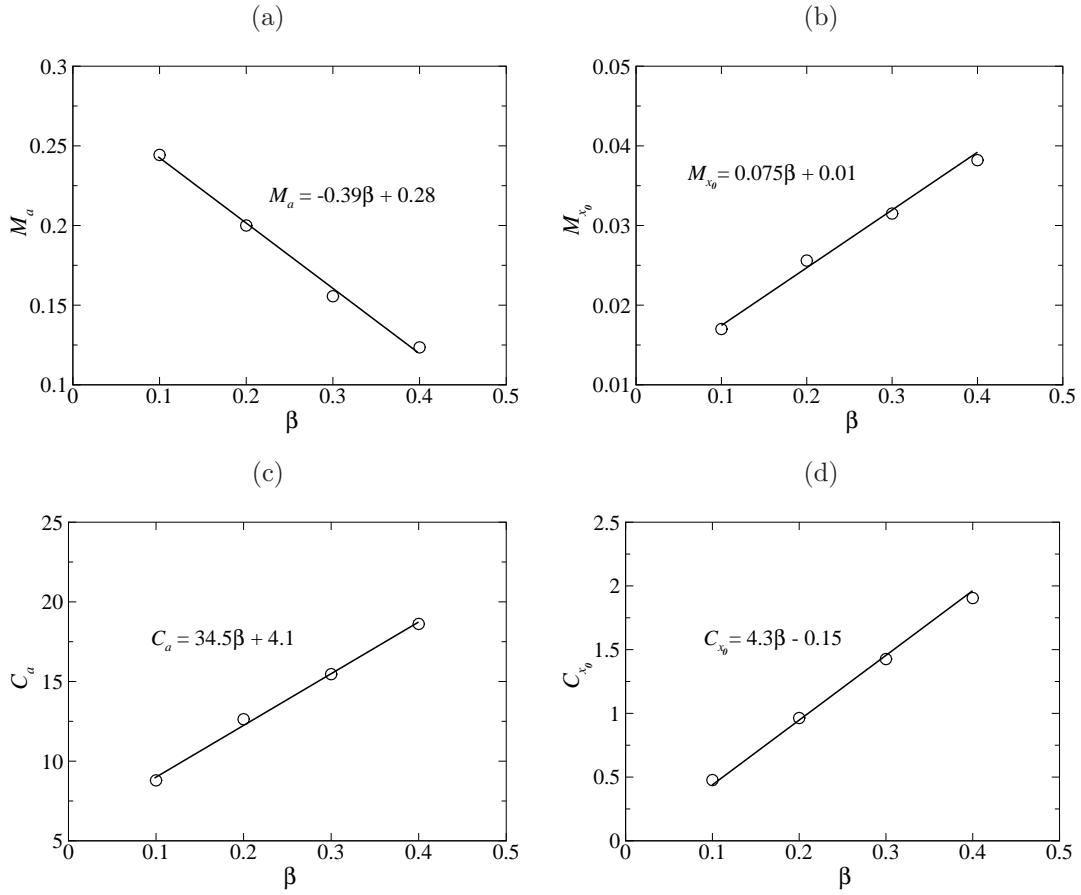


FIGURE 4.13: (a-b) Gradients, M_a and M_{x_0} , and (c-d) vertical axis intercepts, C_a and C_{x_0} , for the linear fits to a and x_0 , respectively, from Figure 4.12, plotted against β .

(2008) showed that transition to a chaotic wake occurred at a critical Reynolds number in the range $6000 < Re_L < 10000$ for $150 < H < 1250$. While the SM82 model is well capable of reproducing the dynamics of turbulent flows as long as they remain quasi-two-dimensional and the Hartmann layer remains laminar, it breaks down if any of these assumptions are violated. If the Hartmann layer becomes turbulent, the flow may still remain quasi-two-dimensional but boundary layer friction is altered. Poth rat & Schweitzer (2011) developed an alternative shallow water model which is valid in these conditions.

Regression analysis revealed that b/H exhibits a power-law dependence on Re_L , and the data exhibits a pleasingly collapse to a positive b/H shift curve of Hartmann friction term (refer Figure 4.14(a)). A non-linear optimization of parameter c yields a collapse of data into a linear trend when $c/H^{0.02}$ is plotted against $\beta^{0.36} Re_L^{0.67}$, as shown in Figure 4.14(b). Collecting these results, the evolution of peak vortex strength

is therefore found to be given by

$$\xi_{\perp,p} = \frac{a}{x - x_0} e^{-bx+c}, \quad (4.30)$$

where

$$\begin{aligned} a &= (-0.39\beta + 0.28)Re'_d - (34.5\beta + 4.1), \\ x_0 &= -(0.075\beta + 0.01)Re_d(1 - \beta) + (4.3\beta - 0.15), \\ b &= 0.90 \frac{H}{Re_L^{0.974}}, \\ c &= H^{0.02}(0.004\beta^{0.36} Re_L^{0.67} - 0.1). \end{aligned}$$

Equation (4.30) may be used to predict peak vorticity time history for confined hydrodynamic flows by substituting $H = 0$, which yields

$$\xi_p = \frac{(-0.39\beta + 0.28)Re'_d - (34.5\beta + 4.1)}{x + (0.075\beta + 0.01)Re_d(1 - \beta) - (4.3\beta - 0.15)}. \quad (4.31)$$

Further, when unbounded flow is considered, i.e. $\beta = 0$, equation (4.31) recovers the reciprocal relationship to time expected from the Lamb–Oseen vortex solution (noting that at $\beta = 0$, Re'_d reduces to Re_d), i.e.

$$\xi_p = \frac{0.28Re_d - 4.1}{x + 0.01Re_d + 0.15} = \frac{0.28Re_d - 4.1}{U_\xi \tau}. \quad (4.32)$$

Comparing equation (4.32) with the peak vorticity of the Lamb–Oseen vortex solution, i.e. $\xi_p = \Gamma/(4\pi\tau)$, yields

$$\Gamma = \frac{4\pi}{U_\xi} \left(0.28 - \frac{4.1}{Re_d} \right). \quad (4.33)$$

This equation suggests that circulation is a function of Reynolds number. Substituting $Re_d = 75$ and $U_\xi = 0.89$ (a typical wake advection velocity at this particular Reynolds number) results in $\Gamma = 3.18$. This value which agrees very well with the values obtained from previous numerical simulations of hydrodynamic flow past a cylinder, and is very close to values from experimental data of Kieft (2000). Their study obtained $\Gamma = 3.17$ and $\Gamma = 2.81$ from numerical and experimental data, respectively, at $Re_d = 75$. The small discrepancy between their numerical and experimental values may be due to the error in measuring velocity vectors in the experiment (Kieft 2000).

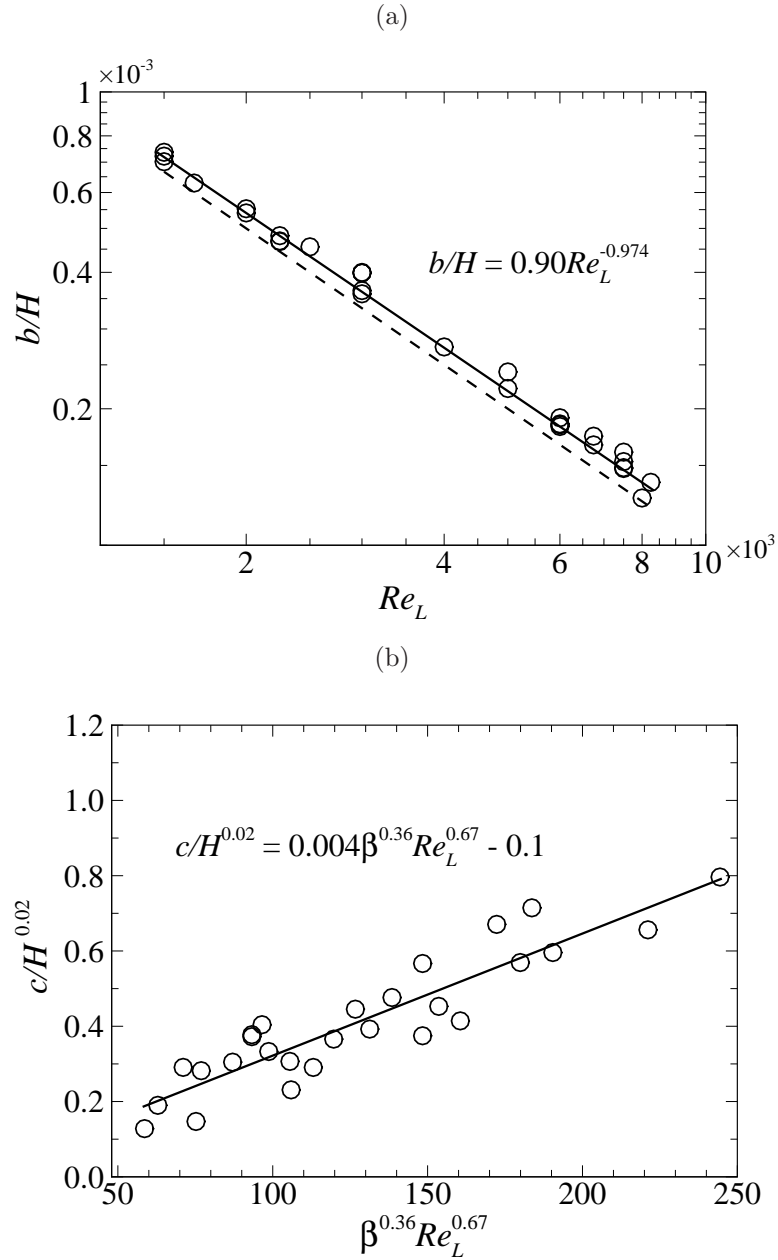


FIGURE 4.14: (a) A plot of b/H against Re_L and (b) $c/H^{0.02}$ against $\beta^{0.36} Re_L^{0.67}$ measurements (symbols). The solid lines in (a) and (b) are a power-law fit and a linear fit, respectively, to the data adopting the equations shown, and the dashed line is the behaviour described by the Hartmann friction term (H/Re_L) for comparison.

4.5.2.2 Validation of the model

The validity of the proposed model, equation (4.31) and equation (4.30) for HD flow and MHD flow, respectively, is examined using all the computed cases, and relative standard errors (RSEs) are compared to assess the reliability of estimates. The RSE, which was defined earlier in § 3.4.2, is calculated in the present section as follows

$$\text{RSE}(\xi) = \sqrt{\frac{\sum(\xi_{p,\text{numerical}} - \xi_{p,\text{predicted}})^2}{\sum \xi_{p,\text{numerical}}^2}}, \quad (4.34)$$

where $\xi_{p,\text{numerical}}$ and $\xi_{p,\text{predicted}}$ are the peak vorticity from numerical simulations and the model predictions, respectively. The summation was performed for vortices transported over the downstream part of the domain. Applying the model developed in this chapter across the computed parameter space ($0.1 \leq \beta \leq 0.4$, $500 \leq H \leq 5000$ and $300 \leq Re_L \leq 8250$) results in an overall relative standard error (RSE) of less than 25%, with more than 80% of the samples having an RSE of less than 15%. Figure 4.15 and Figure 4.16 represent a typical comparison of MHD cases at a range of Reynolds numbers and blockage ratios, providing a comparison between predicted and numerically calculated peak vorticity, respectively. These figures verify that the agreement between model predictions and computed data is very good.

It should be noted that the wake vortices in the laminar flow regime are generally stable, i.e. the longitudinal spacing between two successive vortices, l , is constant (Schaefer & Eskinazi 1958; Roshko 1954a; Bearman 1967), except at the formation region, within the parameter range currently investigated. The spacing was determined by plotting the phase-downstream distance relationships along the wake, where a typical plot is shown in Figure 4.17. Here, 17 instantaneous snapshots of vorticity were taken for two shedding periods, where snapshot sequences begin at an arbitrary phase and this is set to zero for comparison purposes.

The slope of the curve at any position corresponds to the reciprocal of the longitudinal spacing of the vortices at that position. The plot shows that the longitudinal spacing becomes constant within two or three diameters downstream of the cylinder. Upstream of the stable region is the formation region, where the vorticity dissipates and organises into a coherent structure in the vicinity of the cylinder (Kieft 2000). This process can be further divided into three stages, namely the accumulation of vorticity from the separated boundary layers ('vortex A' in Figure 4.18(a)), the stretching

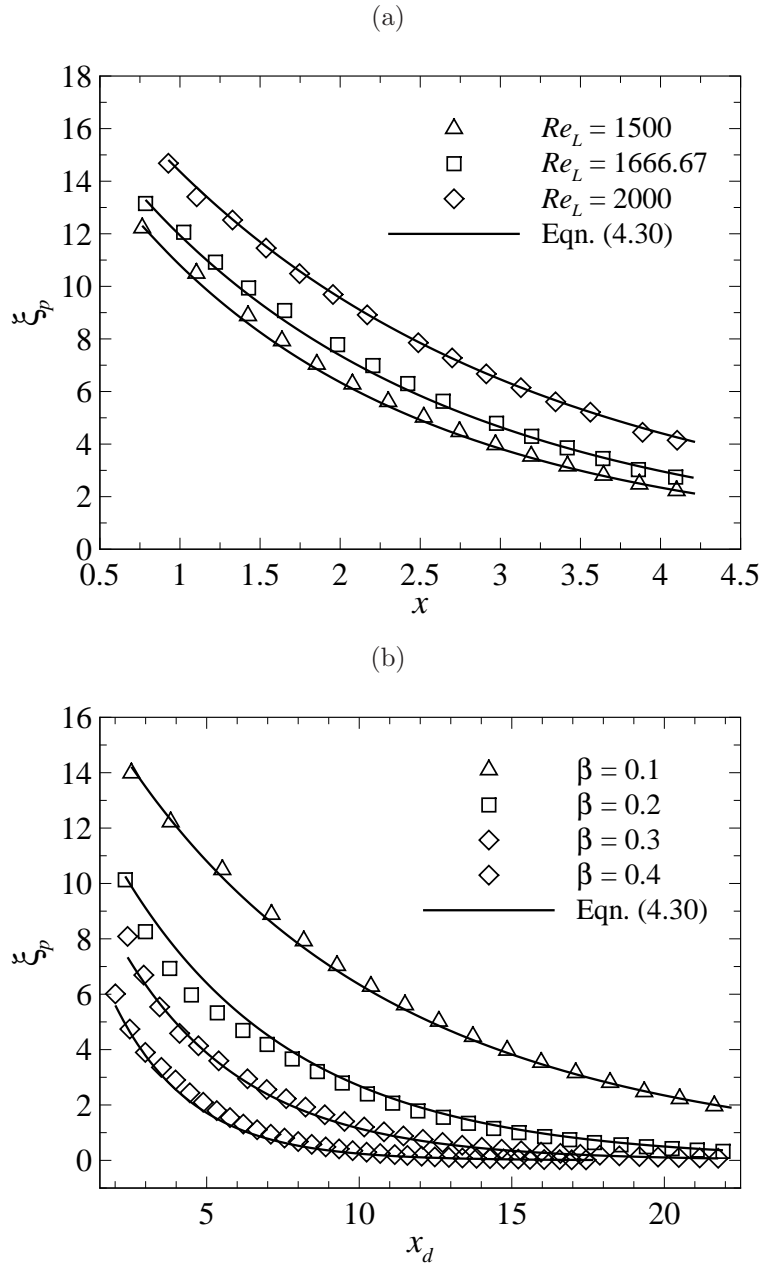


FIGURE 4.15: Decaying peak vorticity from numerical results and prediction by equation (4.30) for (a) $H = 500$ and $\beta = 0.1$, and (b) $H = 500$ and $Re_L = 1500$.

of vorticity (Figure 4.18(b)), and the separation of this vorticity from the boundary layer (Figure 4.18(d)). The subsequent vortex ('vortex B') is also formed during the stretching of vortex A, as shown in Figure 4.18(c).

Beyond the stable region, the viscous effect has become less dominant and eventually leads to vortex street breakup (Durgin & Karlsson 1971). This unstable secondary street possesses a longer wavelength than the primary street and contains more than

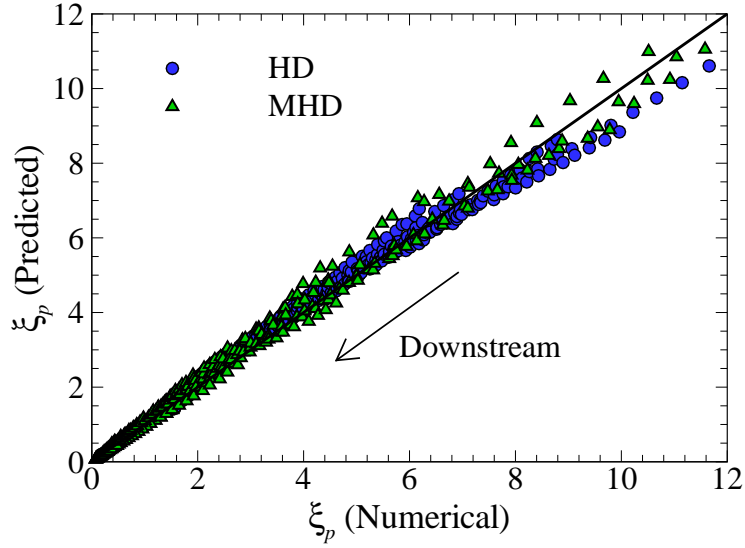


FIGURE 4.16: Overall comparison between numerical and predicted peak vorticity. The solid line $\xi_{p,\text{predicted}} = \xi_{p,\text{numerical}}$ denotes the ideal scenario where predictions perfectly match the simulated values.

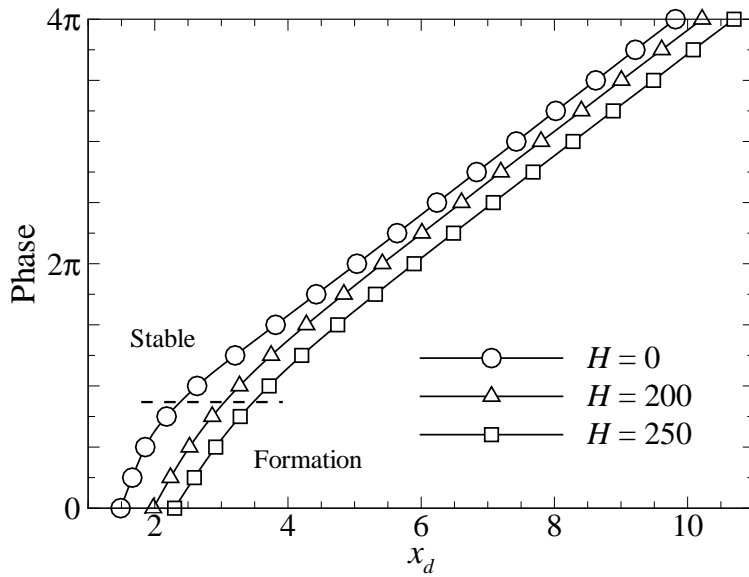


FIGURE 4.17: Phase relationships along the wake for $\beta = 0.1$ and $Re_L = 800$. The dashed line separates the regions of vortex formation and stable wake.

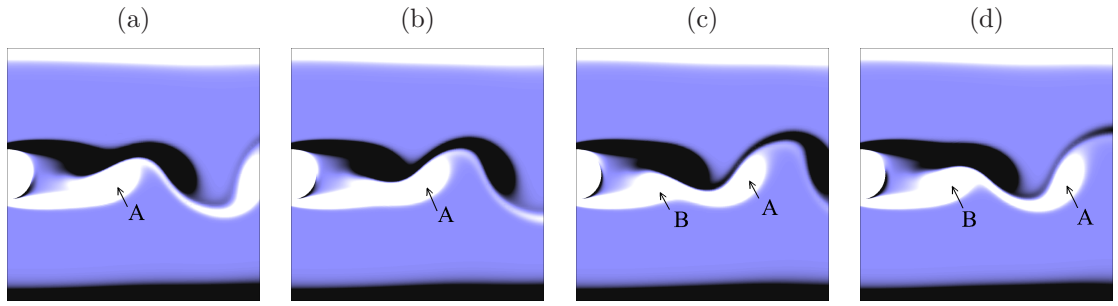


FIGURE 4.18: Typical formation of vortex shedding of a cylinder for $\beta = 0.2$, $H = 500$ and $Re_L = 1500$. Non-dimensional time increment $\Delta t = 0.25T \approx 0.36$ between each subfigure, where T_0 is period. Vorticity contour levels range uniformly from $\xi = -2$ (black) through to 2 (white).

one dominant frequency (Bühler 1996). These two regions (the formation and unstable regions) exhibit complex vortex geometries and behaviour and hence are not considered in the development of equation (4.30). In some cases, a distinct vortex formation behaviour in the near wake is observed. Figure 4.19(a) shows a complex formation of vortex shedding at $\beta = 0.4$, $H = 2500$ and $Re_L = 7500$, where the free shear layer separated from the cylinder surface rolls up towards the cylinder. Due to the relatively high free stream velocity, the vorticity is concentrated into vortex sheets on the surface of the vortex, which leads to the development of the irrotational core. Another interesting feature of the flow is the appearance of a secondary vortex within the recirculation zone. During the vortex sheet roll-up, the primary shed vortex deforms and is eventually torn apart, giving rise to the secondary vortex. As the vortex propagates downward, the irrotational core shrinks and eventually disappears. Beyond this point of disappearance, the vortex street becomes more coherent and stable. Comparison of the decaying peak vorticity from the current numerical data along with the prediction from equation (4.30) (refer Figure 4.19(b)) reveals overprediction towards the cylinder, but becoming more predictable further downstream. The overprediction at the beginning of the vortex shedding is expected due to the fact that part of the fed vorticity is supplied to the secondary vortex. This explains the scatter of data towards the stronger vorticity region seen in Figure 4.16. As vortices move further downstream, the wake stabilizes and hence equation (4.30) becomes more capable of predicting the peak vorticity, which produces the excellent collapse of data to a straight line of unit gradient as data approaches the origin.

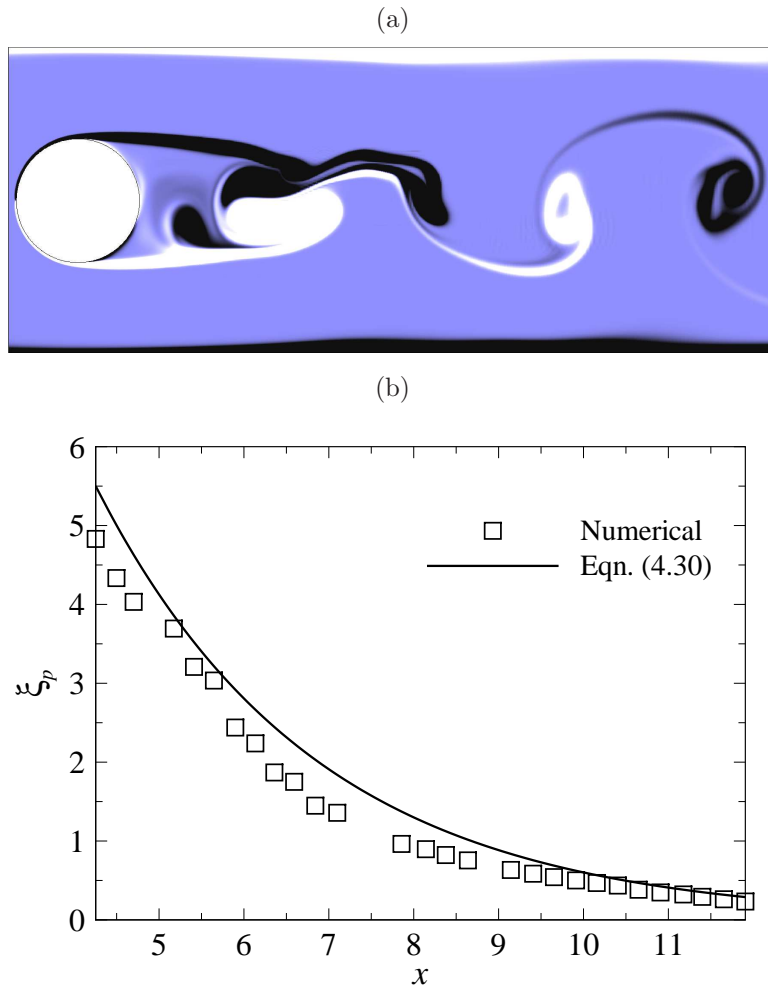


FIGURE 4.19: (a) Instantaneous vorticity contour plots at the formation region and (b) decaying peak vorticity spatial history for the case of $\beta = 0.4$, $H = 2500$ and $Re_L = 7500$. In (a), contour levels are as per Figure 4.18. In (b), square symbols represent numerical data and solid line represent prediction by equation (4.30).

The accuracy of the devised model was further assessed by comparing the experimental and numerical results from Kieft *et al.* (2003) and Ponta (2010) of unbounded channel flows ($\beta = 0$) along with the predictions from equation (4.32), and is plotted in Figure 4.20. The predictions compare very well with the numerical results, however deviation further downstream is seen in the experimental results. Kieft *et al.* (2003) attributes this discrepancy to the lower spatial resolution and noise in the experimental measurements.

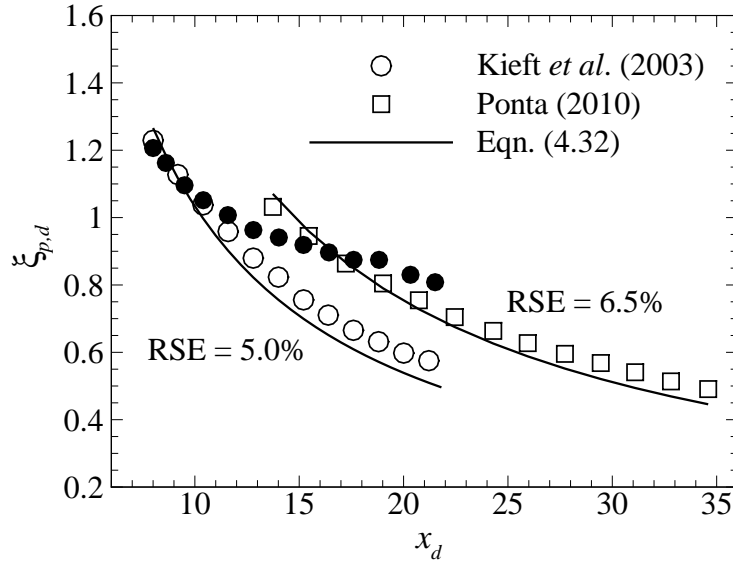


FIGURE 4.20: Comparison of predicted peak vorticity spatial evolution with the previous experimental data (Kieft *et al.* 2003) and numerical data (Kieft *et al.* 2003; Ponta 2010). Open and solid symbols represent numerical data and experimental data, respectively, while lines represent predicted values.

4.5.3 Suggestions for the spacing in periodic arrays of cylindrical vortex promoters

Fluid flow past an array of cylinders has received considerable attention due to its importance in the design of heat transfer equipments. The estimation of the spacing between adjacent cylinders is crucial for the sustainment of the shed vortices, and thus the heat transfer augmentation. In the present investigation, the ideal spacing between two adjacent cylinders is defined as the distance between the upstream primary cylinder and the downstream auxiliary cylinder, which is placed at a location where the vortex strength has decayed to $p\%$ of its initial peak vorticity when it is first shed, i.e.

$$s \approx \{x_2 : \xi_{p,2}(x_2) = p\xi_{p,1}(x_1)\}, \quad (4.35)$$

where s is the ideal spacing between two adjacent cylinders and subscripts 1 and 2 represent the location of the primary and secondary cylinders, respectively. By taking the initial location at the rear of the cylinder, i.e. $x_1 = d/2 = \beta L$, the solution to the spacing yields

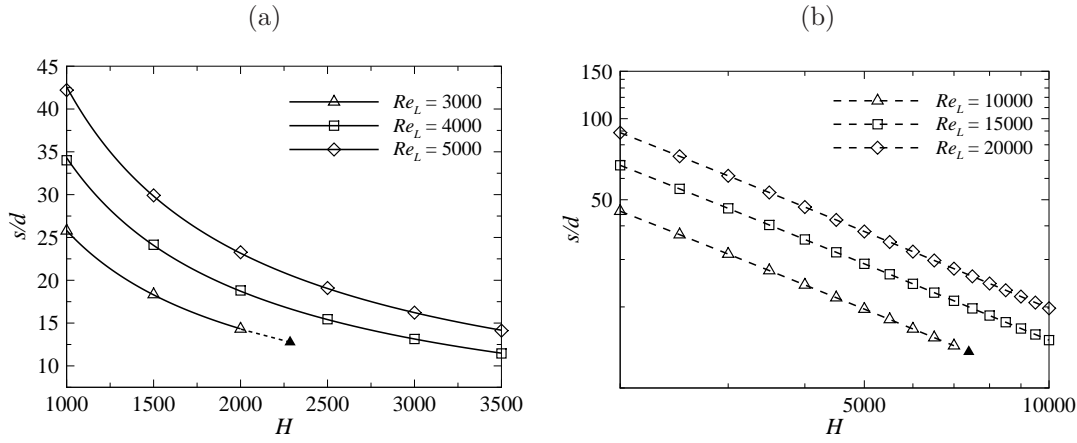


FIGURE 4.21: Ideal cylinder spacing s/d , where s is the centre to centre distance between adjacent cylinders, for $\beta = 0.1$ and $p = 10\%$ plotted against friction parameter for Re_L as indicated. Lines are power-law fits of the data for the respective Re_L . Solid symbol represents critical friction parameter for (a) $Re_L = 3000$ (estimated from the stability curve presented in Figure 4.5) and (b) $Re_L = 10000$ (estimated from a linear extrapolation of $H - Re_{cr}$ relation in Frank *et al.* (2001)), above which vortex shedding is completely inhibited.

$$\begin{aligned} \xi_{p,2} &= p\xi_{p,1}, \\ \frac{a}{x_2 - x_0} e^{-bx_2+c} &= p \frac{a}{x_1 - x_0} e^{-bx_1+c}, \\ x_2 &= \frac{1}{b} W \left(\frac{b(\beta L - x_0) e^{b(\beta L - x_0)}}{p} \right) + x_0 \approx s, \end{aligned} \quad (4.36)$$

where b and x_0 are as defined in equation (4.30), s is the cylinder spacing, p is the fraction of the vortex strength at the auxiliary cylinder location relative to its initial peak vorticity and W is the Lambert W function (Corless *et al.* 1996). This equation is plotted in Figure 4.21(a) for various Hartmann numbers and Reynolds numbers where a vortex strength fraction of $p = 10\%$ is selected by way of example.

The figure shows that the spacing between adjacent cylinders decreases monotonically with increasing friction parameter and decreasing Reynolds number. Considering the typical high-magnetic-field fusion-relevant condition, this leads to a requirement of closely-spaced cylinder arrays in the cooling ducts. Such a configuration is expected to incur higher pressure losses, and will thus require greater pumping power. A plot of equation (4.36) on a log-log scale with an extended range of friction parameters and Reynolds number to include fusion-relevant parameters (Kirillov *et al.* 1995) is shown in Figure 4.21(b). The plot exhibits a linear trend, indicating power law relation between

s and H . Furthermore, the figure reveals that the required cylinder spacing decreases to approximately 10 – 15 cylinder diameter with increasing friction parameter, before the vortex shedding is completely inhibited by the strong Hartmann damping. It is important to note that the spacing estimated by equation (4.36) ignores the effect of cylinder-cylinder proximity. The interference between two adjacent cylinders at close proximity results in a modified downstream flow pattern and in some cases, suppression of vortex shedding (Zdravkovich & Pridden 1977). These factors motivate the investigation of the potential for electric current injection to enhance cylinder wake vortices, which is the subject of Chapter 5. Nevertheless, the proposed model (equation (4.30)) provides numerous other insights into the spatial evolution of the wake vortices, and these are discussed in the following section.

4.5.4 Interpretation of the model

Equation (4.30) can be used to predict the spatial decay rate of peak vorticity. In a similar fashion to the conventional approach for analysing mode evolution using the Stuart–Landau equation (Sheard *et al.* 2004a,b), a model that provides a tool for the study of the non-linear behaviour near the critical Reynolds number, an “instantaneous” spatial decay rate may be defined as the spatial derivative of the natural logarithm of peak vorticity, which evaluates to

$$\frac{\partial(\log_e \xi_{\perp,p})}{\partial x} = -\frac{1}{x + (0.075\beta + 0.01)Re_d(1 - \beta) - (4.3\beta - 0.15)} - 0.90\frac{H}{Re_L^{0.974}}. \quad (4.37)$$

As x approaches infinity, the first term on the RHS vanishes, and the instantaneous decay rate reaches an asymptote of $-0.9H/Re_L^{0.974}$. This closely resembles the decay described by the Hartmann friction term in the governing equation (i.e. $-H/Re_L$). This implies that viscosity only contributes to the dissipation of vortices in the near wake; far downstream only Hartmann friction is significant.

A plot of H against Re_L is given in Figure 4.22. It can be seen in this plot that the decay rate is strongly dependent on friction parameter and Reynolds number at their higher and lower ranges, respectively. This can be attributed to the fact that at these ranges, viscous decay becomes less significant and the Hartmann braking effect becomes more prominent. Hence, the decay rate becomes sensitive to the changes in friction parameter. Figure 4.22 also implies that lower blockage ratio leads to faster decay of vorticity.

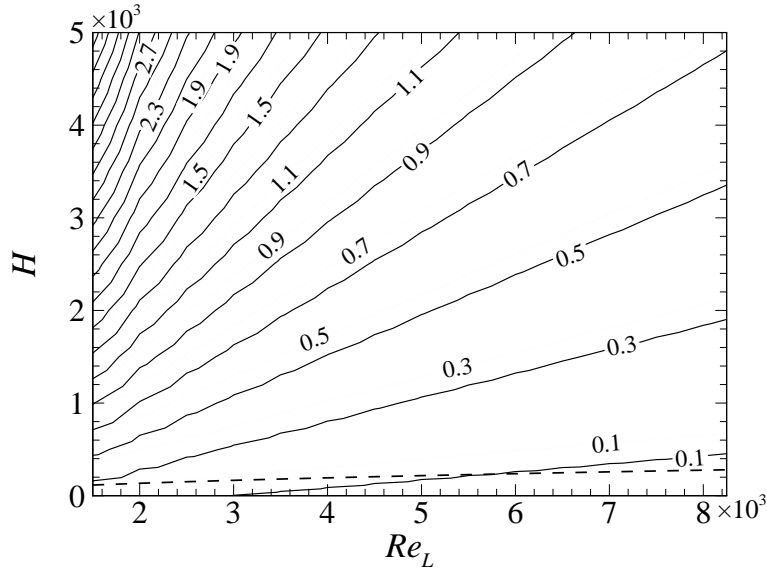


FIGURE 4.22: Countours of the absolute value of the instantaneous spatial decay rate of vorticity against Re_L and H at $x = 1$, determined from equation (4.37). Solid and dotted lines indicate $\beta = 0.1$ and $\beta = 0.4$, respectively. The dashed line indicates the $N = 10$ curve, above which the assumption of SM82 model ($N \gg 1$) is applicable.

Furthermore, recalling the form of the quasi-two-dimensional analogue of the Lamb–Oseen vortex, the right-hand-side terms of equation (4.37) are derived from the hyperbolic and exponential decay components arising from viscous diffusion ($\xi_{p,\text{visc}}$) and Hartmann braking ($\xi_{p,H}$), respectively. For any given flow parameters, both terms will always be negative, i.e. both terms are acting to reduce the intensity of the vortex. To express the relative contributions of each component to the decay of vorticity, the ratio of these terms is evaluated, i.e.

$$\frac{\partial(\log_e \xi_{p,\text{visc}})}{\partial x} \bigg/ \frac{\partial(\log_e \xi_{p,H})}{\partial x} = \frac{1}{b(x - x_0)}, \quad (4.38)$$

and this quantity is depicted in Figure 4.23. A ratio of gradients greater (less) than unity indicates region dominated by viscous dissipation (magnetic damping). It is interesting to note that at low friction parameter, the decay of the wake vortices is first dominated by viscous dissipation, and beyond some critical distance downstream will be dominated by the magnetic damping, which corroborates the aforementioned discussion. It should be qualified that this analysis is derived from quasi-2-D simulations, and it is likely that at least some of the predicted viscous-dominated region would see a deviation between assumed quasi-2-D and actual 3D vortex decay as the scale of the vortex impinges on

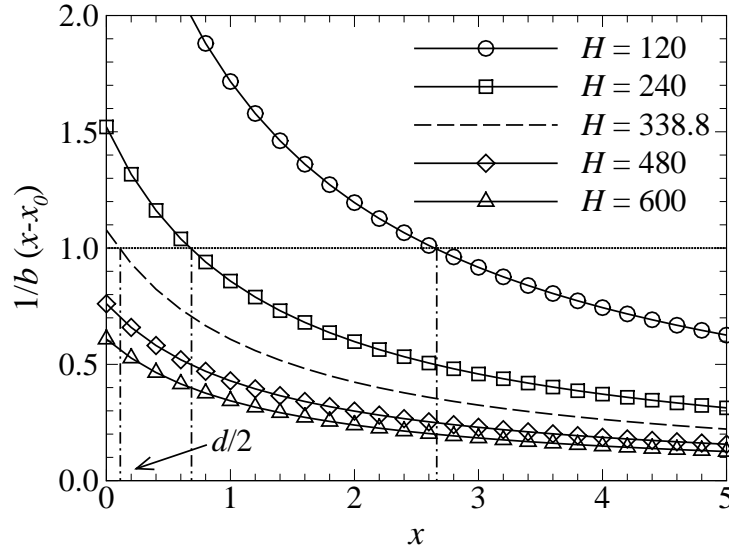


FIGURE 4.23: Spatial distribution of viscous-to-magnetic damping gradients ratio for $\beta = 0.1$ and $Re_L = 500$. The dotted line indicates the border of magnetic damping dominated region, and the corresponding locations at different Ha is shown by the dash-dotted lines. The dashed curve indicates the critical H above which Hartmann braking dominates for the entire wake. The expression for parameters b and x_0 are given in equation (4.30), and $d/2$ is the cylinder radius.

the limits for quasi-two-dimensionality discussed in § 4.5.1.

The region for this transition is located where both viscous dissipation and magnetic damping contribute equally to the decay of peak vorticity. It (i.e. the critical location) is found by setting equation (4.38) equal to unity and solving for x , which yields

$$\begin{aligned}
 x_{cr} &\approx \left\{ x : \frac{1}{b(x-x_0)} = 1 \right\} \\
 &= \frac{Re_L^{0.974}}{0.90H} - (0.075\beta + 0.01)Re_d(1-\beta) + (4.3\beta - 0.15). \quad (4.39)
 \end{aligned}$$

Equation (4.39) states that for a given Reynolds number, the turning point advances upstream as the friction parameter increases, indicative of a shorter viscous dissipation dominated region (which is also shown in Figure 4.23). At a critical friction parameter, the magnetic damping effect already prevails from the beginning of the decay process. In order to validate these model predictions against quasi-two-dimensional simulations, simulations were carried out for hydrodynamic and magnetohydrodynamic cases. In both cases, simulations are started with the wake at a fully saturated state and under the

influence of magnetic field. The flows were then evolved over a very short time interval, and the change in vortex strength of each wake vortex was then used to calculate the local instantaneous decay rate of peak vorticity. The process was repeated for initial conditions at several different phases over a shedding period. The Hartmann braking contribution to the rate of vortex decay was estimated by taking the difference in the rates of decay obtained from both the hydrodynamic (due to viscous dissipation only) and magnetohydrodynamic (due to viscous dissipation and Hartmann braking) cases. It turns out that the data are systematically scattered (as seen in Figure 4.24). The data were then fitted to a power law and a linear trend for viscous dissipation and Hartmann braking contributions, respectively. The choice of fitting function follows from the form of equation (4.37). The intersection of these curves indicates the critical location at which the viscous dissipation and magnetic damping contribute equally to the wake vortex decay. Figs. 4.24(a) and 4.24(b) reveal that the critical locations compare very well with the predictions from equation (4.39), where higher friction parameters tend to move the critical location further upstream. It is also observed in Figure 4.24(c) that at a friction parameter above the critical value, the fitted curves do not intersect downstream of the cylinder, consistent with Hartmann braking dominating throughout the wake. The model therefore not only predicts the overall quasi-two-dimensional wake vortex decay, but also accurately describes the physical contributions of Hartmann braking and viscous dissipation towards the decay process.

The critical friction parameter (i.e. the minimum friction parameter at which the decay is dominated by the magnetic damping only) is evaluated by solving $x_{cr} = x_{decay}$ for H , where x_{decay} is the location of the beginning of the decay process. If the decay of vorticity is taken to begin at the rear of the cylinder, i.e. at $x = d/2 = \beta L$, and noting that $Re_d = 2\beta Re_L$, then the critical friction parameter is given by

$$H_{cr} = \frac{Re_L^{0.974}}{0.90(\beta L + 2\beta(0.075\beta + 0.01)Re_L(1 - \beta) - (4.3\beta - 0.15))}. \quad (4.40)$$

This critical friction parameter is mapped against Reynolds number and blockage ratio in Figure 4.25. The main observation inferred from Figure 4.25 is that Hartmann braking dominates the decay of vorticity at higher blockage ratio and higher Reynolds number, which is in agreement with the previous findings (Hussam *et al.* 2011). The effect of blockage ratio and Reynolds number on the predominancy of Hartmann braking is more prominent at their lower ranges (i.e. $\beta \lesssim 0.2$ and $Re_L \lesssim 1000$). Furthermore,

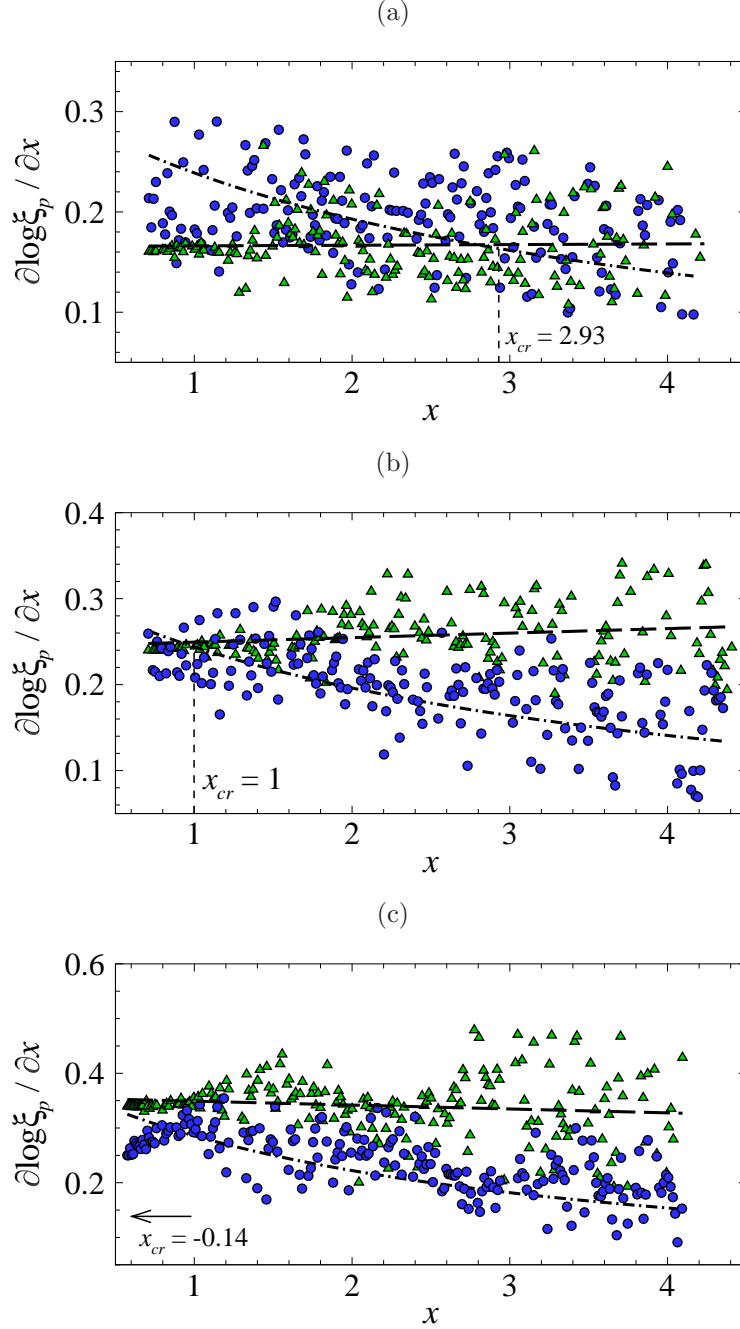


FIGURE 4.24: Local instantaneous rate of peak vortex decay for the case of $\beta = 0.1$, $Re = 1000$ and (a) $H = 160$, (b) $H = 240$ and (c) $H = 340$. Circle and triangle symbols represent decay rate due to viscous dissipation and Hartmann braking, respectively. Dashed and dash-dotted lines show the regression fits for each data set. Vertical dashed lines in (a) and (b) indicate the crossover locations predicted by equation (4.39).

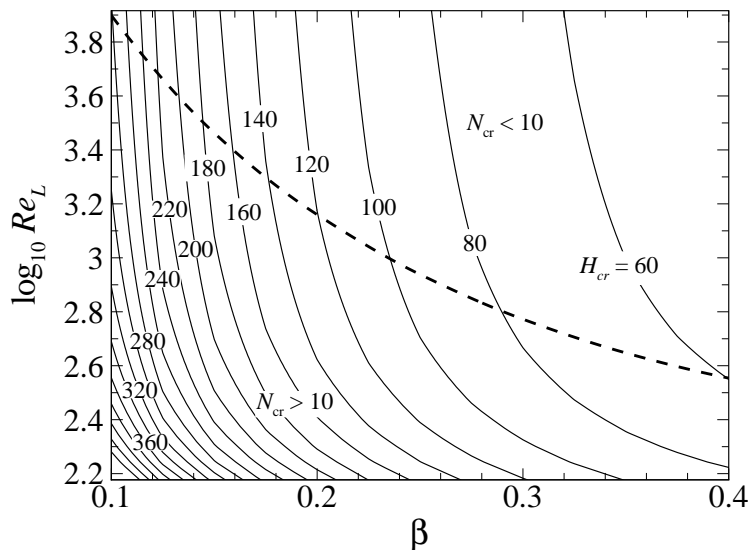


FIGURE 4.25: Contour mapping of H_{cr} over the β - $\log_{10} Re_L$ parameter space. The dashed line shows a curve of $N_{cr} = H_{cr}^2/Re_L = 10$. If N_{cr} exceeds the interaction parameter required for validity of the SM82 model (here taken representatively as $N = 10$), then it may be possible that a quasi-2-D wake vortex experiencing viscous-dominated decay for some of its lifetime.

at higher Re_L , the critical friction parameter becomes almost independent of Reynolds number for any given blockage ratio. This observation is attributed to the asymptotic behaviour of equation (4.38) for large values of Reynolds number, i.e. $1/b(x - x_0) \approx H^{-1} Re / (x + Re) \sim H^{-1}$ for $x \ll Re$.

As mentioned in the previous section, the SM82 model is valid when $N \gg (a/l_{\perp})^3$ and $H \gg (a/l_{\perp})^2$. Figure 4.25 suggests that for cases where the combination of β and Re_L lies in the $N_{cr} > 10$ region, it is possible to have quasi-two-dimensional MHD flow with vortices dominated by viscous decay for part of their lifetime in the wake provided that restriction on the perpendicular length scale is still satisfied. However, under the SM82 model, the momentum at the vicinity of the Hartmann layer is assumed to diffuse immediately due to the two-dimensionalisation time τ_{2D} being much less than the time scales for viscous diffusion in the perpendicular plane, τ_{ν}^{\perp} (Pothérat 2007; Dousset 2009). As a result, the SM82 model breaks down locally when the effect of viscosity is relevant, i.e. when $Ha \sim l_{\parallel}/l_{\perp}$, or when the transverse length scale l_{\perp} is of the order of the Shercliff layers thickness, $\delta_S = aHa^{-1/2}$. Despite the inherent limitations of the SM82 model, it has nevertheless been shown to predict the Shercliff layers thickness

and an isolated vortex profile to high accuracy when compared to three-dimensional (3D) solutions, (Poth erat *et al.* 2000) where the reported errors are less than 10% (Dousset & Poth erat 2008; Poth erat 2007). The model has also been tested for flows in a duct with a cylinder obstacle, where the critical Reynolds number at the onset of vortex shedding in Dousset & Poth erat (2008); Hussam *et al.* (2011) compares well with the 3D direct numerical simulation results (Kanaris *et al.* 2013) and experimental results (Frank *et al.* 2001). Furthermore, Kanaris *et al.* (2013) found that the critical Reynolds number decreases as Ha is increased at a low Hartmann number (i.e. $Ha \lesssim 35$, corresponding to $N \lesssim 2$). However, critical Reynolds number varies almost linearly with Hartmann number for higher Hartmann number, which is in agreement with the previous findings (Dousset & Poth erat 2008; Frank *et al.* 2001; Hussam *et al.* 2011; Kanaris *et al.* 2013). Surprisingly, this non-monotonic trend is also observed in a wake-type vortex using the SM82 model (B uhler 1996). This observation is supported by more recent findings (M uck *et al.* 2000), where the transition to two-dimensionality of wake vortices occurs at relatively low interaction parameter ($1 < N < 5$). It is hence anticipated that the SM82 model will be able to provide some trustworthy insights into the two-dimensional wake behaviour beyond the parameter ranges where it is formally applicable. Moreover, the requirement for the analytical threshold vortex size presented in Section 4.5.1 is stricter than that of perpendicular scales. This suggest that at least some of the wakes produced for $H < H_{cr}$ will formally satisfy the SM82 model. These arguments support the application of the wake vortex decay model developed in this study to wakes across a wide range of Re and H , including cases where viscous diffusion contributes more significantly than Hartman braking to the vortex decay for at least part of their lifetime. Figure 4.25 also suggest that at higher Reynolds numbers (where the combination of β and Re_L lies in the $N_{cr} < 10$ region), the decay of quasi-two-dimensional MHD wake vortices must always be dominated by Hartmann braking for the entire wake. This is because in this region, H_{cr} is lower than the friction parameter required to produce interaction parameter satisfying quasi-two-dimensionality. This supports the conjecture that quasi-2-D MHD turbulence is dominated by Hartmann braking in this region (Poth erat 2012).

4.5.5 Comparison with three-dimensional data at low and moderate interaction parameter

In this section, predictions from the current model are compared with the recent three-dimensional direct numerical simulations of MHD duct flow past a cylinder computed by Kanaris *et al.* (2013). Three cases are compared, referred to as cases $U1$, $U2$ and $U3$, having interaction parameters $N_d \approx 3.2$, $N_d \approx 1.3$ and $N_d \approx 15.7$, respectively. N_d is the interaction parameter based on cylinder diameter, and these correspond to the present interaction parameter based on duct height with values $N = H^2/Re_L \approx 6.4$, $N \approx 2.6$ and $N \approx 31.4$ for cases $U1$, $U2$ and $U3$, respectively. The aim here is to compare the decay rate of wake vortices in quasi-2-D MHD flows against the corresponding three-dimensional flows at low and moderate interaction parameters.

Firstly a comparison of case $U1$ is considered. Figure 4.26(a) compares the spatial evolution of peak vortex strength from 3D data of Kanaris *et al.* (Kanaris *et al.* 2013), taken at the middle plane, present quasi-2-D simulations and present model predictions, noting that the peak vorticity is potentially a very sensitive measure of a vortex strength. A normalization of the 3D data is also plotted to provide a better comparison in terms of the rate of vortex decay with the model predictions. The predictions compare very well with the 3D data in the near wake region, but the wake decays faster further downstream in the presence of three-dimensionality. However, inspection of vortex profiles at arbitrary locations reveals that the breadth of the vortex from both quasi-2-D and 3D simulations are comparable, as shown in Figure 4.26(bi) to (ciii). It is also interesting to note from Figure 4.26(bi) and (ci) that the Shercliff layer thicknesses in the quasi-2-D and 3D simulations are in very good agreement, confirming previous findings (Poth erat 2007).

In case $U2$, there is poor agreement between quasi-2-D and 3D peak vorticity spatial history, as shown in Figure 4.27(a). This is expected because at this low interaction parameter, the near wake is highly three-dimensional (Kanaris *et al.* 2013), and the SM82 model is certainly inaccurate. Furthermore, a recent experimental investigation by Rhoads *et al.* (2014) found that at low interaction parameter, the evolution of wake vortices were significantly altered due to the prevalence of small-scale turbulent eddies, which corroborates the aforementioned argument. Inspection of Figure 4.27(bi) to (biii) reveals that the vorticity profile from 3D simulations is almost uniform, most likely due to diffusion of vorticity in the magnetic field direction. However, the rate of

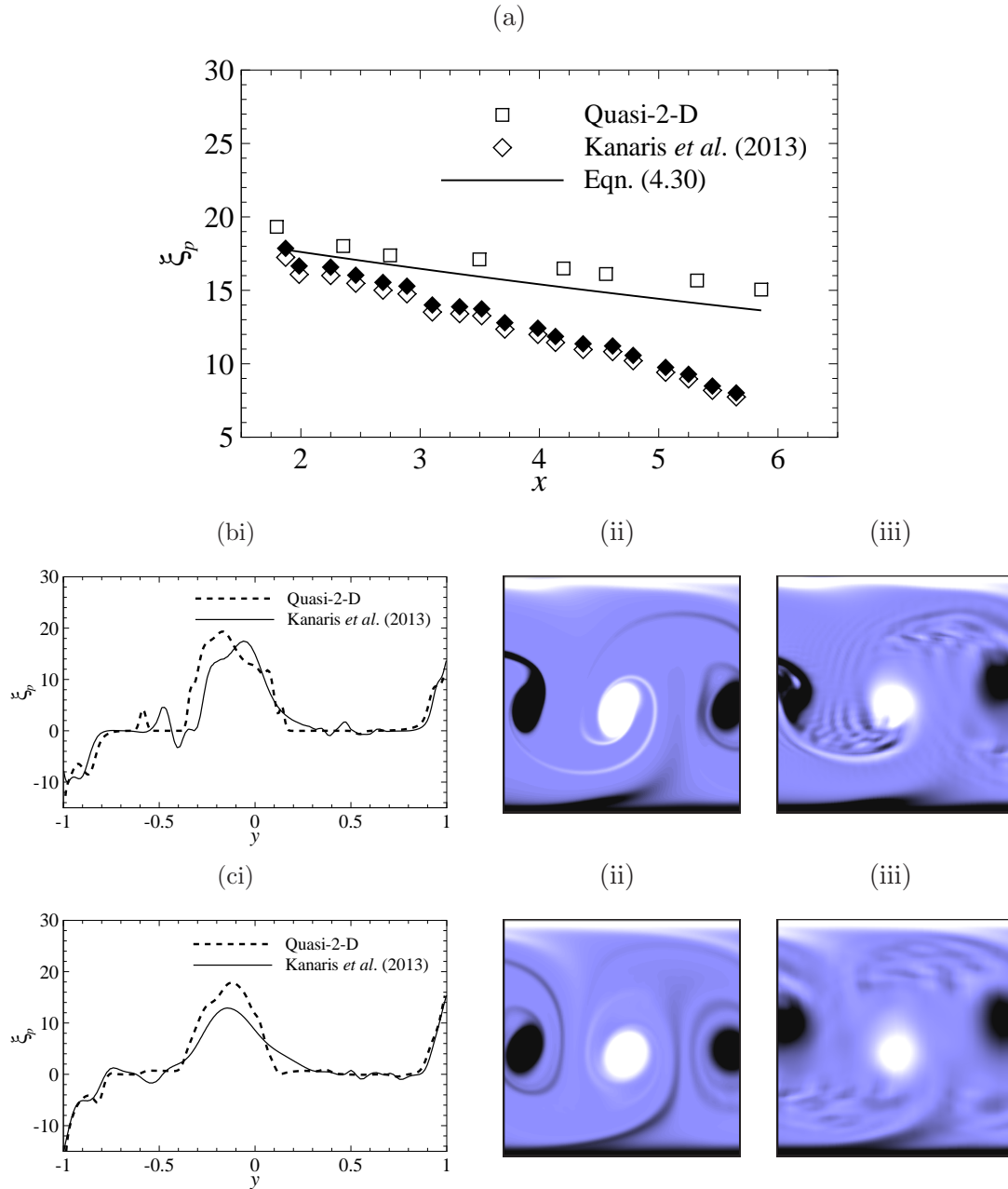


FIGURE 4.26: Case $U1$: $\beta = 0.25$, $H = 160$, $Re_L = 4000$ and $N = 6.4$. (a) Peak vorticity spatial evolution. Square and diamond (open) symbols represent data from present quasi-2-D simulations and previous 3D numerical results (Kanaris *et al.* 2013). Solid symbols are 3D data normalised to the equation (4.30) prediction at the first vortex location and solid line represent predicted values. (b) Vorticity profiles in the transverse direction, at $x = 1.8$. (bii) and (biii) Instantaneous vorticity contour plot from the present quasi-2-D and previous 3D simulations (Kanaris *et al.* 2013), respectively. Contour levels are as per Figure 4.18. (c)-(ciii) Captions as per (b)-(bii), respectively, at $x = 3.6$

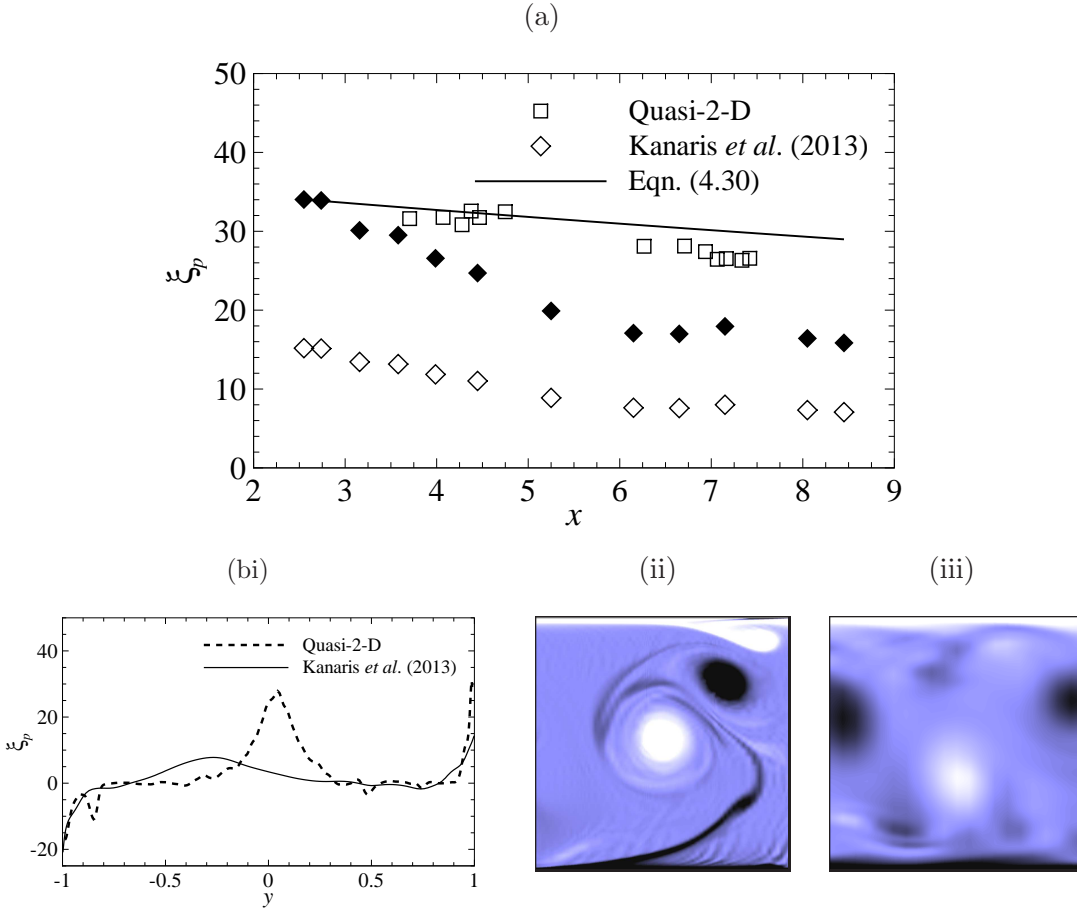


FIGURE 4.27: Case $U2$: $\beta = 0.25$, $H = 160$, $Re_L = 10000$ and $N = 2.6$. Captions are as per Figure 4.26, (bi)-(biii) $x = 6.7$.

peak vorticity decay is in good agreement further downstream. This observation can be attributed to the transition to a two-dimensional state, as discussed by Mück *et al.* (2000) In their 3D simulations at a low interaction parameter ($N_d = 1$), they observed that the spanwise velocity fluctuation tend to zero farther from the cylinder and that the vorticity diffuses along the magnetic field lines, an evidence of two-dimensionality.

Comparisons of decaying peak vorticity for case $U3$ is shown in Figure 4.28(a). Having the highest N , this case is expected to produce the best agreement. It can be seen that quasi-2-D model tends to overpredict the intensity of wake vortices, seemingly due to different wake vortex profiles. As depicted in Figure 4.28(bi), the vortex produced by the 3D simulations resemble a Rankine vortex with solid body rotation in the core region, whereas the vortex in the quasi-2-D model exhibit a Lamb–Oseen vortex. The corresponding contour plots of these vortices are shown in Figure 4.28(bii) and (biii). Figure 4.28(ci) to (ciii) shows vorticity profiles and the corresponding contour plots

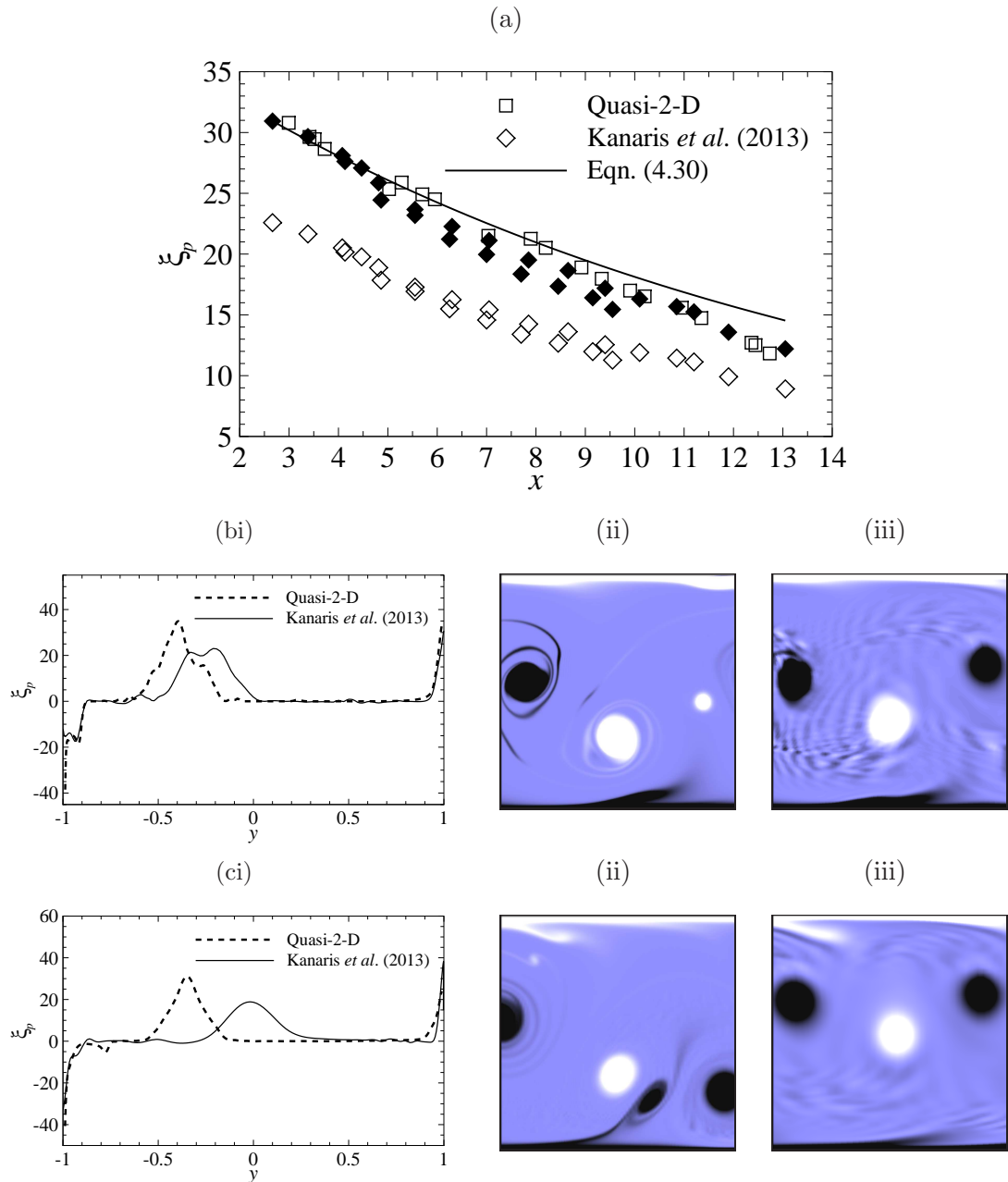


FIGURE 4.28: Case $U3$: $\beta = 0.25$, $H = 560$, $Re_L = 10000$ and $N = 31.4$. Captions are as per Figure 4.26, (bi)-(biii) $x = 2.2$ and (ci)-(ciii) $x = 4.5$.

at a further downstream location. Despite the overprediction of the vortex strength, the proposed model seems to perform very well at predicting the rate of vorticity decay, where the normalised 3D data almost coincides with the predicted line plot (refer Figure 4.28(a)).

4.6 Chapter summary

In this chapter, the dynamics and decay behaviour of vortices in a stable wake behind a circular cylinder under the influence of a strong magnetic field parallel to the cylinder axis has been examined. Under these conditions, the velocity field becomes almost independent of the spanwise direction in the bulk, and hence is treated as a quasi-two-dimensional flow. The Stuart–Landau model has been employed to estimate the critical Reynolds number for the transition from steady to time-dependent flow in a cylinder wake. In general, the effect of the magnetic field and cylinder diameter are significant, where small increments of Hartmann number and blockage ratio lead to a large increase in the critical Reynolds number. The output from this analysis is then used to predict the combinations of β , H and Re that will produce time-periodic wake flows for the subsequent analysis.

The analysis of cylinder wake dynamics revealed that the formation of vortex shedding plays significant roles in determining the shedding frequency. An axial magnetic field tends to appreciably increase the shedding frequency, regardless of flow Reynolds number. Furthermore, the advection velocity of wake vortices was found to be greatly dependent on both friction parameter and Reynolds number. However, it was only weakly dependent on Reynolds number for hydrodynamic flows. An increase in H leads to higher wake advection velocity relative to the free stream. It follows then that the longitudinal spacing of wake vortices is also affected since the wake parameters are interdependent. In addition, the incoming flow vorticity plays an important role in the lateral dispersion of wake vortices and thus the wake inversion phenomenon. In the absence of a magnetic field, the wake inverted at about 6 - 8 diameter downstream from the centre of the cylinder. However, in the presence of a magnetic field, two nearly parallel rows of vortices in a staggered arrangement resembling an ideal Kármán vortex street were observed.

The analysis is followed by the investigation of the decay of wake vortices. Numerical simulations have been performed over the range of blockage ratios $0.1 \leq \beta \leq 0.4$, friction parameter $500 \leq H \leq 5000$ and Reynolds numbers $300 \leq Re_L \leq 8250$. The analytical solution for the decay of a quasi-two-dimensional MHD vortex is obtained, and this forms the basis for a regression fit to describe the decay of stable wake vortices behind an idealized vortex promoter (i.e. a circular cylinder) in a rectangular duct. The devised model proposes that the decay rate varies with blockage ratio, imposed magnetic field

intensity and Reynolds number. This model can further describe hydrodynamic vortex decay ($H = 0$) and decay of wake vortices in an open flow ($\beta = 0$). The instantaneous spatial decay rate becomes sensitive to the change in friction parameter and Reynolds number at their higher and lower ranges, respectively. As vortices are advected far downstream, the decay rate approaches an approximate Hartmann friction term (i.e. $-H/Re_L$).

The model also predicts that quasi-two-dimensional vortices can be dominated by viscous decay in the near wake, if the friction parameter remains below a critical value. Friction parameters lower than this critical value imply that there are two distinct regions of dominant decay forcing, i.e. viscous dissipation in the near wake, and Hartmann braking further downstream. Otherwise, Hartman braking dominates the decay for the entire wake. The region for the transition from a viscous dissipation dominated regime to a magnetic damping dominated regime was approximated by solving the model for spatial location where the both viscous dissipation and magnetic damping contribute equally to the decay of peak vorticity. This region was confirmed with further analysis from additional simulations.

The critical friction parameter is dependent on Reynolds number and blockage ratio, where higher Re_L and β leads to lower H_{cr} . However, the critical friction parameter becomes almost constant for a higher level of flow turbulence due to the counterbalancing effects of both viscous dissipation and Hartmann braking. Under this condition, the quasi-two-dimensional MHD vortex decay is dominated by Hartmann braking. Furthermore, this dependency becomes more apparent at lower Re_L and β .

A comparison between the model predictions and published 3D MHD simulation data at different interaction parameters confirms the capability of the proposed model in predicting the rate of peak vorticity decay within an advecting vortex at high interaction parameters.

In the next chapter, the results examining the effect of electrically-enhanced cylinder wake vortices on the duct wall heat transfer is presented.

Chapter 5

Electrically augmented cylinder wake vortices

In this chapter, the potential of electrically-augmented cylinder wake vortices for heat transfer enhancement from a heated sidewall of an MHD duct is explored. The electromagnetic effects on the quasi-two-dimensional flows are in the form of Hartmann friction and the forcing due to the injected electric current from an electrode embedded in the duct wall. Influences of vortex dynamics on heat transfer, pressure drop and efficiency enhancement are examined over a wide range of current injection amplitudes, frequencies and pulse width, cylinder gap ratios and electrode positions. The investigation focuses on a flow with Reynolds number $1500 \leq Re \leq 3000$ and friction parameter $200 \leq H \leq 5000$ in a duct with a blockage ratio $\beta = 0.2$. These parameter ranges correspond to $50 \lesssim N \lesssim 6.7 \times 10^4$ for $n = 2$ and $\alpha = 1$, which justifies the employment of the SM82 model. Furthermore, these parameters are chosen as they produce time periodic flows at each gap ratio, permitting investigation of the interaction between the forcing current injection and the natural vortex shedding behind the cylinder. This investigation builds on a recommendation from previous work (Bühler 1996), dedicated to understanding the flow stability in a similar configuration.

Some of the results in this chapter have previously been published in Hamid *et al.* (2015a,b, 2016a).

5.1 Problem setup

In this investigation a flow of electrically conducting fluid passing over a circular cylinder in a rectangular duct is considered (as depicted in figure 4.1). The bottom wall of the duct (grey shaded region in figure 5.1) is maintained at a constant hot temperature of

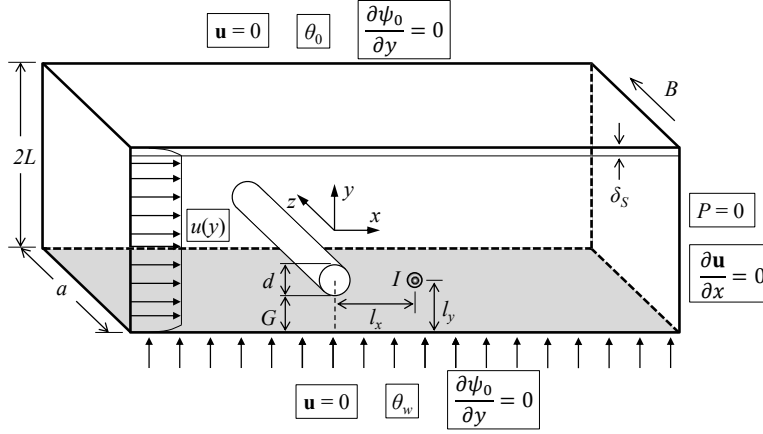


FIGURE 5.1: Schematic diagram of the system under investigation. The cylinder spans the duct, with diameter d and axis parallel to z -direction, and the small circle indicates a point electrode embedded in one of the Hartmann walls.

θ_w , while the top wall and inflow have a constant cold temperature of θ_0 . The cylinder is thermally insulated, while the duct sidewalls and the cylinder are each electrically insulated. On the duct walls and the cylinder surface, a non-slip condition is imposed. A fully developed quasi-2-D MHD duct flow is applied at the duct inlet (as given in equation (4.1)), while at the outlet, a constant reference pressure is imposed and a zero streamwise gradient of velocity is weakly imposed. The transverse distance between the cylinder and the heated wall is characterised by the gap ratio G/d . This study considers gap ratios $G/d = 0.5, 1$ and 2 , with $G/d = 2$ corresponding to the duct centreline. The wake flow is modified by means of current injection through an electrode embedded at various locations in the otherwise electrically insulating out-of-plane duct wall. The ratio of cylinder diameter to the duct width (i.e. blockage ratio, $\beta = d/2L$) is fixed at 0.2 throughout this study. A uniform magnetic field B is imposed in the axial direction (z -axis).

5.2 Electrical forcing velocity field

The electric current is injected in alternating-sign pulses with amplitude I , and angular frequency $\omega_f = 2\pi f_f$, where f_f is the forcing frequency, and pulse width, τ/T , where $T = 2\pi/\omega_f$ is the period of the current oscillation (refer Figure 5.4). The non-dimensional forcing velocity field \mathbf{u}_0 is defined as

$$\mathbf{u}_0 = \mathbf{j} \times \mathbf{e}_z = \nabla\psi_0 \times \mathbf{e}_z, \quad (5.1)$$

where \mathbf{j} is the electric current density, \mathbf{e}_z is the unit vector in the z -direction and ψ_0 is the scalar potential. The electric current density and the electrical potential are scaled by $\sigma BU_0/Ha = U_0\sqrt{\rho\nu\sigma}/a$ and aBU_0 , respectively. In a high magnetic field application, the change in the field due to the currents induced by the flow can be neglected. Under this condition, the equations governing continuity of electric current and incompressibility are also linear, so they may be averaged to give $\nabla \cdot \mathbf{j} = -j_w$, $\mathbf{j} = Ha(\mathbf{E} + \mathbf{u} \times \mathbf{e}_z)$ and $\nabla \cdot \mathbf{u} = 0$. Here j_w is the current density injected at one or both of the confining planes, and \mathbf{E} is a dimensionless electrical field. The z -averaged current can be expressed as the gradient of a scalar field ψ_0 satisfying a Poisson equation with the source term being j_w , i.e. $\mathbf{j} = \nabla\psi_0$, obtained from $\nabla^2\psi_0 = -j_w$ (Poth erat *et al.* 2005). This Poisson equation is first solved (Polyanin 2001) for a source term at the current injection point that is a Dirac function located at $(0, l_y)$, i.e. $j_w(x, y) = I\delta(x, y - l_y)$, on a domain extending infinitely in streamwise direction and bounded by duct sidewalls at $y = \pm 1$. In a physical implementation, it is conceived that the current circuit would be completed far upstream and downstream of the electrode. Imposing zero Neumann conditions on the electrical potential field at the boundaries due to the insulating Shercliff walls (Poth erat *et al.* 2000), i.e. $\partial\psi_0/\partial y = 0$ at $y = \pm 1$, leads to

$$\psi_0(x, y) = \frac{I}{4\pi} \left[\log \left(\frac{1}{\cosh(\pi x/2) - \cos[\pi(y + 1 + l_y)/2]} \right) + \log \left(\frac{1}{\cosh(\pi x/2) - \cos[\pi(y + 1 - l_y)/2]} \right) \right]. \quad (5.2)$$

I is the non-dimensional current amplitude, which is defined as

$$I = \frac{\hat{I}}{aU_0\sqrt{\rho\nu\sigma}}. \quad (5.3)$$

Substituting equation (5.2) into equation (5.1), the forcing velocity field becomes

$$\mathbf{u}_0 = \nabla\psi_0 \times \mathbf{e}_z = \left\langle \frac{\partial\psi_0}{\partial x}, \frac{\partial\psi_0}{\partial y}, 0 \right\rangle \times \mathbf{e}_z. \quad (5.4)$$

Evaluating equation (5.4) for electrode positioned at $(l_x, 1 - l_y)$ yields \mathbf{u}_0 components

$$u_0 = \frac{I}{8} \left(\frac{\sin[\pi(y + 1 + l_y)/2]}{\cos[\pi(y + 1 + l_y)/2] - \cosh[\pi(x - l_x)/2]} + \frac{\sin[\pi(y + 1 - l_y)/2]}{\cos[\pi(y + 1 - l_y)/2] - \cosh[\pi(x - l_x)/2]} \right), \quad (5.5)$$

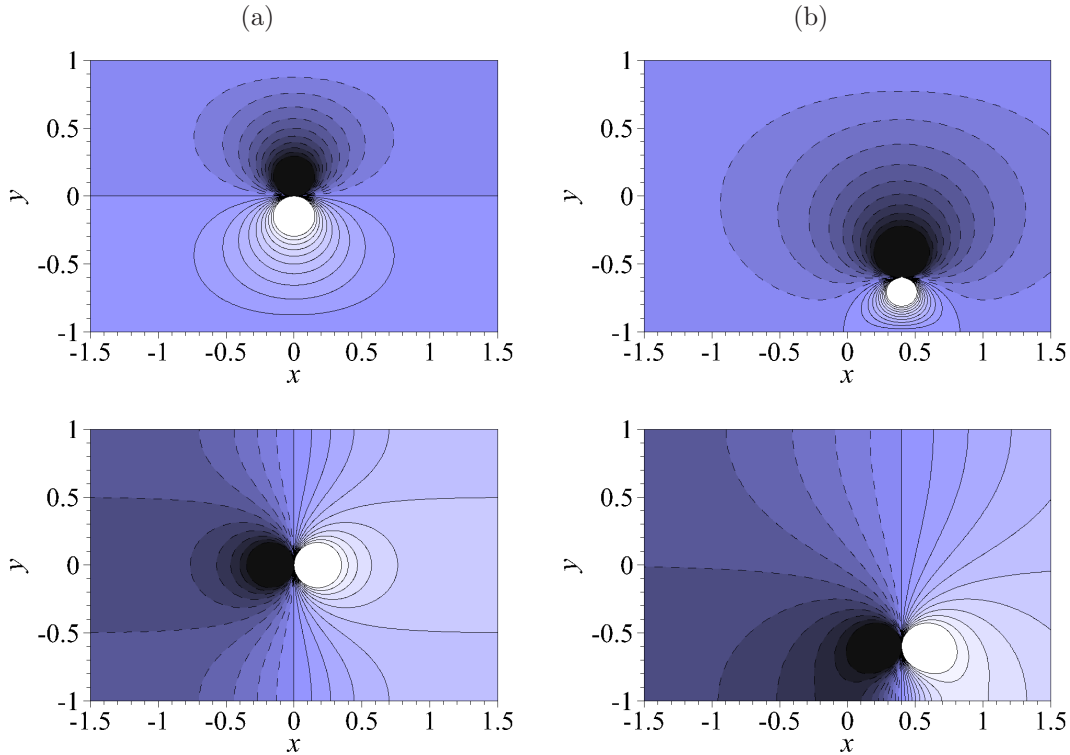


FIGURE 5.2: Contour plots of the horizontal (top) and vertical (bottom) components of \mathbf{u}_0 for $I = 60$, $H = 500$, $Re_L = 1500$ and electrode locations (a) $(x,y) = (0,0)$ and (b) $(x,y) = (0.4,-0.6)$. Contour levels range between -5 and 5 , with light and dark contours representing positive and negative velocity, respectively.

and

$$v_0 = \frac{I}{8} \left(-\frac{\sinh[\pi(x-l_x)/2]}{\cos[\pi(y+1+l_y)/2] - \cosh[\pi(x-l_x)/2]} - \frac{\sinh[\pi(x-l_x)/2]}{\cos[\pi(y+1-l_y)/2] - \cosh[\pi(x-l_x)/2]} \right). \quad (5.6)$$

The contours of the resulting horizontal and vertical components of the forcing velocity fields for a representative case with $I = 60$, $H = 500$ and $Re_L = 1500$ are depicted in Figure 5.2. Unless otherwise mentioned, the current injection amplitude is expressed nondimensionally hereafter as in equation (5.3).

In the present investigation, the current is either injected from the base of the cylinder or from an electrode located away from the cylinder. In the former arrangement, the physical realisation of this setup is likely from a ring of electrodes around the base of the cylinder (as depicted in Figure 5.3). In the limit of high Hartmann number and high interaction parameter, most of the electric current flow is through the Hartmann layers

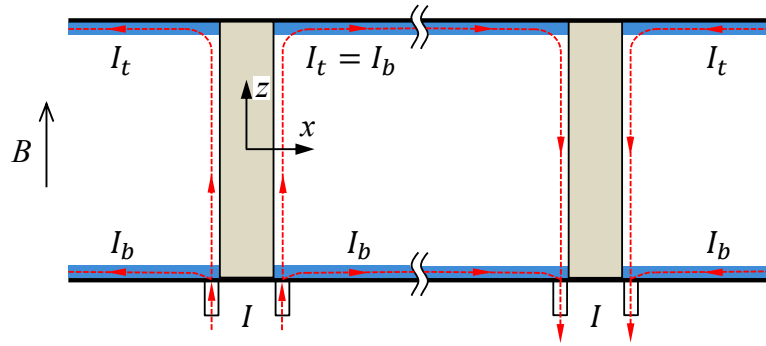


FIGURE 5.3: Schematic representation of the electric current paths (dotted lines) from a ring of electrodes around the base of the cylinder (the cylinder is represented by a grey shading) in the limit of high Hartmann number and interaction parameter. The electrode is embedded into one of the Hartmann walls and made flush with the surface to avoid disturbance of the flow. The Hartmann layers are shaded blue, which contain most of the current paths in for quasi-2-D flow.

(Poth erat & Klein 2014). The currents are equally divided into each Hartmann layer (i.e. $I_t = I_b$, where subscripts t and b correspond to the top and bottom boundaries, respectively), which results in an axisymmetric two-dimensional vortex in the core flow. The current also interacts with the Shercliff layer only within the very thin top and bottom Hartmann layers. It is anticipated that such an interaction will be relatively insignificant to affect the core flow and thus neglected in the present formulation. For a thorough description of electric current path in the latter arrangement, the reader is referred to Poth erat & Klein (2014).

It is noted that these solutions are obtained for a duct with no cylinder present. While the cylinder diameter is small relative to the duct width, it is not negligible, and so this forcing solution inexactly approximates the true forcing field. In order to justify the validity of these solutions, evaluation of the errors associated with the approximation has been performed by comparing the electrical potential field calculated from the analytical solution with the field that is solved numerically in the presence of the electrically insulating cylinder.

The results (as shown in Figure 5.5) reveal that the errors are isolated to the vicinity of the cylinder. For a case where the electrode is coincident with the cylinder, the largest discrepancies were three orders of magnitude below the overall variations in the electrical potential field within the domain. When the electrode was positioned downstream of the cylinder, errors were again isolated to the vicinity of the cylinder,

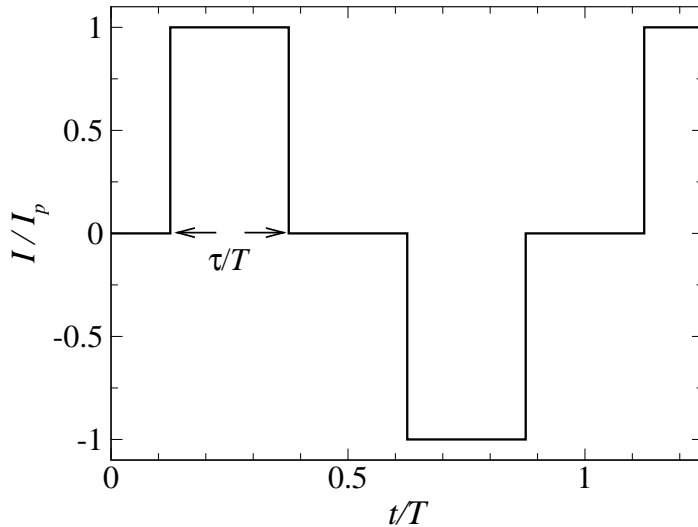


FIGURE 5.4: Typical electric current injection profile, represented by modified square waveform with pulse width $0 < \tau/T < 0.5$. In the limit of $\tau/T = 0.5$, the current injection profile takes a square waveform. The amplitude of current is normalised by its peak amplitude, I_p , and the time is normalised by signal period, T .

and were at least an order of magnitude below the overall field variations. It is therefore expected that the resulting electrically generated vortices will closely resemble the true vortices.

5.3 Validity of the forcing field in a quasi-2-D domain

It is important to ensure that the time scale at which the current forcing is imposed is much larger than the two-dimensionalisation time so that the induced vortex shedding is quasi-two-dimensional and satisfies the SM82 model assumptions. The condition for the forcing time scale is justified as follows: in this chapter, the forcing frequency is varied between $\omega_f = 0.5$ and 10, which corresponds to a non-dimensional forcing time scale between $\tau_f = 2\pi/\omega_f \approx 13$ and 0.6, respectively. Following the scalings used in this study, the non-dimensional two-dimensionalisation time is expressed as $\tau_{2D} = \hat{\tau}_{2D}U_0/L = \rho U_o \lambda^2 / \sigma L \hat{B}^2$. For $H = 500$ (a friction parameter at which the highest forcing frequency is simulated in this study; low friction parameter and high forcing frequency impose demanding requirements for the time scales), and taking $n = 2$, $\alpha = 1$, and the properties of low-melting eutectic alloy Ga⁶⁸In²⁰Sn¹² at 20°C (density $\rho = 6.3632 \times 10^3 \text{ kg m}^{-3}$, electrical conductivity $\sigma = 3.30737 \times 10^6 \text{ } \Omega^{-1}\text{m}^{-1}$, and

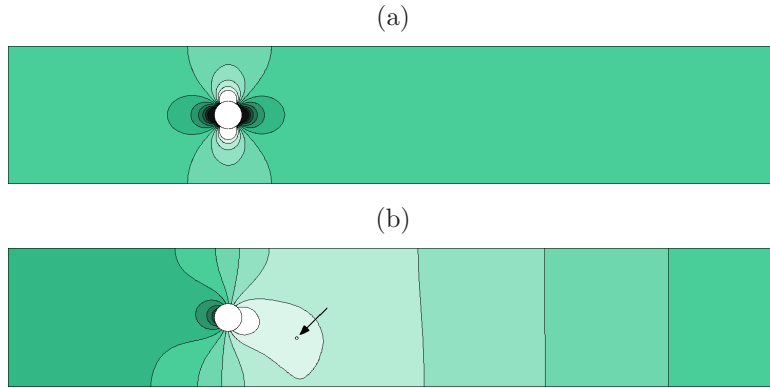


FIGURE 5.5: Contour plots of the difference in electrical potential field calculated from the analytical solution and the field that is solved numerically in the presence of the electrically insulating cylinder. In (a), current is injected from the base of the cylinder and contour levels range between -0.001 and 0.001, and in (b), current is injected from an electrode placed at $l_x = 1$ and $l_y = 0.7$ (indicated by the arrow), and contour levels range between -0.04 and 0.06. Light and dark contours represent positive and negative difference in electrical potential, respectively.

kinematic viscosity $\nu = 3.4809 \times 10^{-7} \text{ m}^2\text{s}^{-1}$; Lyon 1952), the imposed magnetic field is $B = (Ha/a)\sqrt{\rho\nu/\sigma} = 4H\sqrt{\rho\nu/\sigma}/(n\alpha^2a) \approx 0.26 \text{ T}$. Taking the typical bulk flow velocity in the blanket as $U_0 = 0.015 \text{ m s}^{-1}$ (Smolentsev *et al.* 2010), $l_\perp = L$ and $l_\parallel = a$ so that $\lambda = 2$, along with the typical length scale for the fusion blanket application $a = 0.1 \text{ m}$ (Smolentsev *et al.* 2010), the two-dimensionalisation time is then $\tau_{2D} \approx 0.03$. This time scale is at least an order of magnitude smaller than the forcing time scale, which justifies the quasi-two-dimensionality assumption.

While the most demanding forcing case considered in this study has a time period approximately 20 times the two-dimensionalisation time, the square or modified square forcing current waveforms introduce higher frequencies that may not be resolvable under the SM82 model. For instance, a modified square waveform with $\tau/T = 0.25$ may be described by a Fourier series with coefficients of the form (see Appendix A for derivation)

$$\sum_{n=1}^{\infty} \frac{2}{n\pi} \left[\cos\left(\frac{n\pi}{4}\right) - \cos\left(\frac{3n\pi}{4}\right) \right]. \quad (5.7)$$

Even-numbered coefficients are identically zero, and it can be seen that the odd-numbered harmonic coefficients scale with $1/n$. It would be expected therefore that the SM82 model will resolve up to the order of the 19th harmonic in the aforemen-

Included harmonic	ε_{Nu}	ε_{C_D}	$\varepsilon_{\mathcal{L}^2}$
1 st	0.0389	0.5790	0.0909
3 rd	0.0031	0.0761	0.0087
5 th	0.0031	0.0016	0.0027
7 th	0.0024	0.0003	0.0016
9 th	0.0023	0.0027	0.0017
11 th	0.0024	0.0046	0.0015
13 th	0.0029	0.0009	0.0015

TABLE 5.1: Percent absolute deviations as a function of the number of harmonics included in the Fourier representation of the imposed current pulses. The deviations were calculated relative to the ideal modified square waveform with $\tau/T = 0.25$. The 1st harmonic represents a perfect sinusoidal waveform, where all the energy in the current signal is contained at the fundamental frequency.

tioned most demanding current forcing case, or components of the pulse waveform with magnitudes down to approximately 5% of the first Fourier mode. In order to evaluate the sensitivity of the resulting flow to the number of included modes in the Fourier series representation of the ideal modified square waveform, simulations were performed at $H = 500$, $Re_L = 1500$, $I = 60$, $\omega_f = 10$ and $\tau/T = 0.25$. The effect is quantified by the deviations of the flow parameters (time-averaged Nusselt number Nu , total drag coefficient C_D , and integral of velocity magnitude throughout the domain \mathcal{L}^2) obtained with pulses represented by the truncated Fourier series from the ideal square waveform. The results are presented in Table 5.1, which shows that the deviations are small ($< 1\%$) even for a sinusoidal (single-harmonic) approximation to the square wave, quickly becoming insignificant ($< 0.005\%$) when including the first three or more non-zero harmonics (frequencies that are well within the valid range of the SM82 model). It is therefore expected that no artefacts will be present in the solutions due to high-frequency components of the modified square wave current forcing violating the SM82 model.

It is also important to ensure that the electrically driven vortices are well resolved by the SM82 model, particularly their scale in the perpendicular plane, i.e. the vortex core. Here, the scale is defined as the radius of the electrode (Hunt & Malcolm 1968). The smallest quasi-2-D structure that can be satisfactorily resolved by the model arises from the condition that $\tau_{2D} \sim \tau_\nu^\perp$, which yields $l_\perp \sim a/\sqrt{Ha}$. The bulk of the present numerical simulations was based on the flow at $H = 500$, which corresponds to $Ha = 1000$ for $n = 2$ and $\alpha = 1$. This then yields the smallest resolved scale of $l_\perp \sim a/30$. For

a typical duct length scale $a = \mathcal{O}(10^{-1} \text{ m})$, the electrode size must be at least in the order of millimetres, which is typical in MHD experiments (Hunt & Malcolm 1968; Sommeria 1988). Furthermore, findings obtained in Chapter 4 demonstrate the capability of the SM82 model in predicting the evolution of quasi-2-D vortices even at rather moderate interaction parameters (i.e. $N \approx 31$). For the sake of comparison, the interaction parameter is varied between $N = 50$ and 67000 in the present investigation, and hence justifies the implementation of the SM82 model. It may therefore be asserted that the present results are representative of the actual physical behaviour, at least within the correct order of magnitude.

5.4 Quantification of duct flows thermal-hydraulic performance

The instantaneous Nusselt number variation along the heated duct walls is quantified by

$$Nu_w(x, t) = \frac{2L}{\theta_f - \theta_w} \frac{\partial \theta}{\partial y} \Big|_{wall}, \quad (5.8)$$

where θ_f is the bulk fluid temperature, which is calculated using the velocity and temperature distribution as

$$\theta_f(x, t) = \int_{-L}^L u \theta \, dy / \int_{-L}^L u \, dy. \quad (5.9)$$

For a periodic flow, the instantaneous wall Nusselt number calculated from equation (5.8) is also periodic. The time-averaged local Nusselt number at each x -station is represented by $\overline{Nu_x}(x)$. Integrating over the downstream length of the heated bottom wall, L_d , gives the time-averaged Nusselt number

$$Nu = \frac{1}{L_d} \int_0^{L_d} \overline{Nu_x}(x) \, dx. \quad (5.10)$$

To quantify the efficiency of the current injection on the heat transfer, the efficiency index is adopted (Walsh & Weinstein 1979), defined as

$$\eta = \frac{HR}{PR}, \quad (5.11)$$

where HR and PR are the heat transfer enhancement ratio and pressure penalty ratio, given respectively by $HR = Nu/Nu_0$ and $PR = \Delta p/\Delta p_0$. Nu_0 is the time-averaged Nusselt number of the heated region of the duct without any current injection, and Δp and Δp_0 are the time-averaged pressure drop across the duct, with and without current injection, respectively (with the cylinder present).

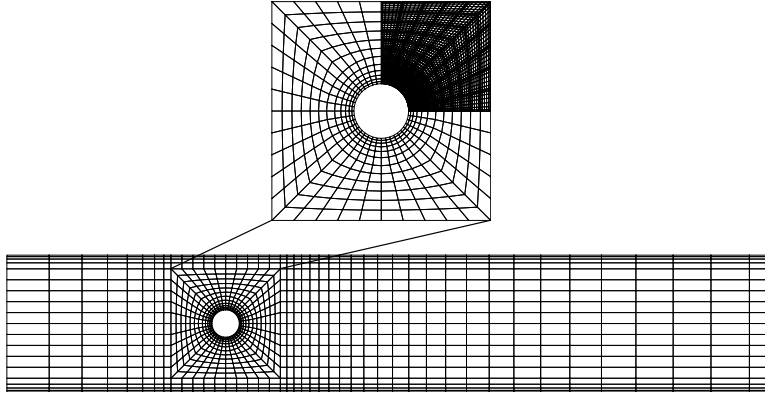


FIGURE 5.6: Macro-element distribution of the computational domain, and magnified mesh in the vicinity of the cylinder, with the upper right quadrant representing the distribution of collocation points within elements with $N_p = 8$. The mesh extends $3.2L$ upstream and $8L$ downstream.

5.5 Domain size study

Meshes were constructed consisting of four regions: two regions near the transverse walls, a core region, and a region in the vicinity of the cylinder. Elements are concentrated near the walls and the cylinder (as shown in Figure 5.6) to resolve the expected high gradients in MHD flows (Poth erat *et al.* 2002) and to capture the crucial characteristics of the boundary layer (e.g. boundary layer separation) (Ali *et al.* 2009). The grid is also compressed in the horizontal direction towards the cylinder.

To test the domain independence of the meshes constructed for this study, the dependence of Nusselt number on downstream domain length was investigated. A case with $H = 500$, $Re_L = 1500$, $I = 60$, $\omega_f = 1.75$ and $\tau/T = 0.25$ was considered. The results are summarised in Table 5.2, and the variation of time-averaged Nusselt number along the duct is given in Figure 5.7. The result reveals that truncating the downstream length from $16L$ to $8L$ or $12L$ causes negligible errors of less than 0.09% or 0.08%, respectively, in the time-averaged Nusselt number calculated up to $L_d = 8L$. Hence, the M1 mesh sizing was used hereafter.

5.6 Grid resolution study

As in the previous chapter, a grid independence study was performed by varying the element polynomial degree, while keeping the macro element distribution unchanged. The time-averaged Strouhal number $St = fd/U_0$, total drag coefficient $C_D = 2F_D/\rho U_0^2 d$,

Mesh	M1	M2	M3
L_d/L	8	12	16
N_{el}	1292	1425	1558
Nu	2.9097	2.9094	2.9073
ε_{Nu}	0.0822	0.0712	0

TABLE 5.2: Domain length L_d/L and number of elements N_{el} of different meshes. $\varepsilon_{Nu} = |1 - Nu_{M_i}/Nu_{M_3}|$ is the error in time-averaged Nusselt number relative to the case with longest domain for $H = 500$, $Re_L = 1500$, $I = 60$, $\omega_f = 1.75$ and $\tau/T = 0.25$.

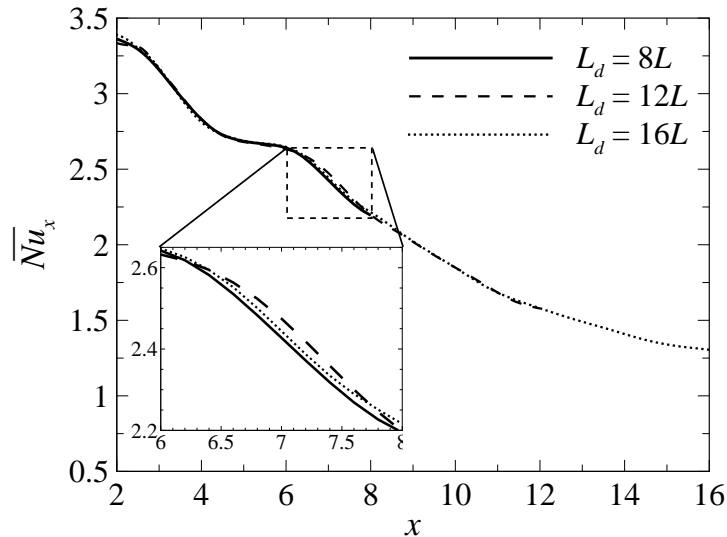


FIGURE 5.7: Time-averaged local Nusselt number in the downstream of cylinder for $H = 500$, $Re_L = 1500$, $I = 60$, $\omega_f = 1.75$ and $\tau/T = 0.25$. Solid, dashed and dotted lines represent domains with respective downstream lengths $L_d = 8L$, $12L$ and $16L$.

where F_D is the drag force exerted by the fluid per unit length of the cylinder, the integral of velocity magnitude throughout the domain (\mathcal{L}^2 norm) and Nusselt number (Nu) were monitored, as they are known to be sensitive to the domain size and resolution. Errors relative to the case with highest resolution, $\varepsilon_P = |1 - P_{N_i}/P_{N=11}| \times 100\%$, were defined as a monitor for each case, where P is the monitored parameter. A demanding MHD case with $H = 500$, $Re_L = 1500$, $I = 60$, $\omega_f = 4$ and $\tau/T = 0.25$ was chosen for the test. The results are presented in Table 5.3, and show rapid convergence with increasing polynomial order. The case with polynomial degree 8 achieved at worst a 0.9% error, and is used hereafter.

N_p	ε_{St}	ε_{C_D}	$\varepsilon_{\mathcal{L}^2}$	ε_{Nu}
3	0.2813	4.4134	0.5788	5.0943
4	0.4048	0.2138	0.0296	3.4334
5	0.3903	0.6136	0.1104	2.5580
6	0.2714	1.1087	0.1812	1.9540
7	0.2624	1.0248	0.1763	1.5904
8	0.1884	0.5990	0.1040	0.8984
9	0.1698	0.9263	0.1095	0.5187
10	0.0882	0.8289	0.0446	0.2656

TABLE 5.3: Percent uncertainties as a function of element polynomial degree arising from the grid independence study at $H = 500$, $Re_L = 1500$, $I = 60$, $\omega_f = 4$ and $\tau/T = 0.25$. A polynomial degree of $N_p = 8$ was ultimately chosen for the simulations reported in this chapter.

5.7 Results

5.7.1 Base cases

Three base cases, each having $Re_L = 1500$, $H = 500$ and $\beta = 0.2$, are constructed, with cylinder gap heights $G/d = 0.5, 1$ and 2 , as well as a fourth case comprising the same duct but with the cylinder removed at the same flow conditions. The instantaneous vorticity contours for these cases are shown in Figure 5.8, along with a plot of the streamwise distribution of the local time-averaged Nusselt number. With no cylinder, the flow is steady (see Figure 5.8(a)) and the local Nusselt number decreases monotonically as the thermal boundary layer grows with distance from the inlet towards the fully developed value (see Figure 5.9). Figure 5.8(b-d) shows that the wall proximity affects the dynamics of the cylinder wake. Figures 5.8(b) and (c) illustrate a typical Kármán vortex shedding, whereas Figure 5.8(d) shows a vortex pairing pattern in the wake. A strong entrainment of vorticity into the wake in the near wake region occurs as the cylinder gap ratio is decreased, and this increases the local thermal boundary layer thickness (while temperature fields are not shown, they may be inferred from the vorticity field since they are correlated; Celik *et al.* 2010). This explains the abrupt decrease in local Nusselt number immediately downstream of the cylinder for the small gap ratio case, as shown in Figure 5.9. This is then followed by an appreciable increase in Nusselt number due to the vortex shedding at the end of the formation region ($2 \lesssim x \lesssim 3$).

Furthermore, when the cylinder is positioned at the centre of the duct, it was observed from Figure 5.8(b) that the interaction between the wake and the walls is

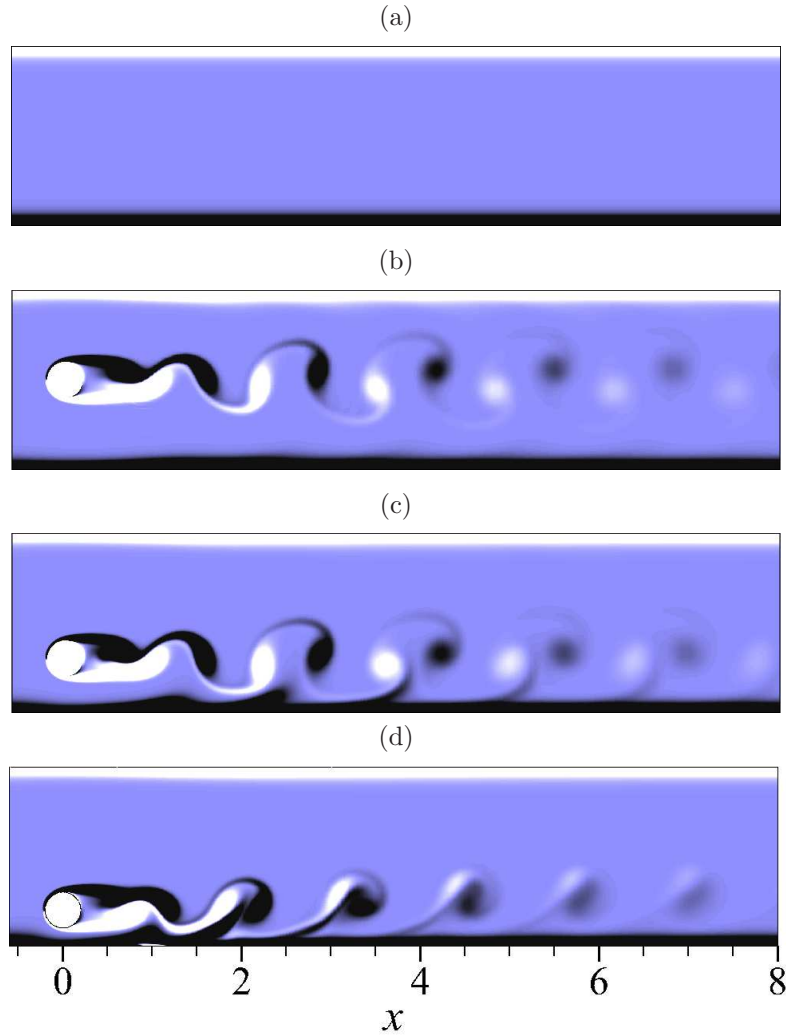


FIGURE 5.8: Instantaneous vorticity contour plots of base cases for (a) empty duct, (b) $G/d = 2$, (c) $G/d = 1$ and (d) $G/d = 0.5$. Contour levels range between -2 and 2, with light and dark contours representing positive and negative vorticity, respectively.

relatively weak, thus the trend of local Nusselt number resembles that of the empty duct case. The results of time-averaged Nusselt number along the heated wall reveal that cylinder placement with gap ratio $G/d = 1$ performed best, achieving heat transfer increment $HI = (Nu - Nu_e)/Nu_e = 8.6\%$, where Nu_e is the Nusselt number of an empty duct. This is followed by the case with $G/d = 2$ ($HI = 3.9\%$), and the poorest performance being the cylinder placed nearest to the wall with $G/d = 0.5$ ($HI = -1\%$). A similar trend is observed for the efficiency index (refer Table 5.4). This finding confirms a previous observation (Hussam & Sheard 2013), whereby an optimal gap between the cylinder and the heated wall for maximising the rate of heat

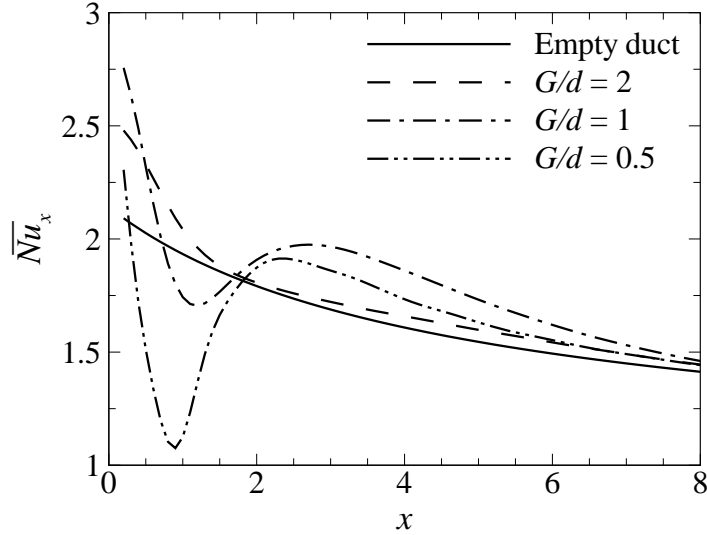


FIGURE 5.9: Time-averaged local Nusselt number in the downstream of cylinder of base cases.

G/d	Nu	ΔP	η	f_0
Empty duct	1.647	7.467	-	-
2	1.711	7.805	0.994	0.743
1	1.789	7.817	1.037	0.717
0.5	1.630	7.833	0.944	0.798

TABLE 5.4: Time-averaged flow quantities at $\beta = 0.2$, $H = 500$, $Re_L = 1500$ for the base cases.

transfer was found to lie within $0.8 \lesssim G/d \lesssim 1.4$. The trend of increasing pressure drop with increased gap ratio is also in agreement with the findings from that study.

5.7.2 Effects of the current injection frequency and amplitude on heat transfer

In this section, overall enhancement in heat transfer for various forcing frequency ω_f and forcing amplitude I are presented. The current is injected from the cylinder, and ω_f is varied between 0.5 and 10 for $I = 12, 30$ and 60 . For all cases, $H = 500$, $\tau/T = 0.25$ and $G/d = 2$. The results are presented in Figure 5.10(a). It can be observed that higher current amplitude leads to a higher peak heat transfer. Furthermore, HR reaches its maximum value at $1.3 \lesssim \omega_f \lesssim 1.7$, which corresponds to normalised forcing frequencies $0.28 \lesssim F = f_f/f_0 \lesssim 0.36$ within the investigated current amplitudes, where f_0 is the natural shedding frequency. Spectral analysis of the cylinder lift coefficient $C_L =$

$2F_L/\rho U_0^2 d$, where F_L is the lift force exerted by the fluid per unit length of the cylinder, reveals that this frequency range is appreciably lower than the lock-in frequency range (a state where the vortex shedding is synchronised with the forcing frequency), as shown in Figure 5.10(b). There are three distinct regimes of wake response, and further discussion on the frequency response analysis is presented in § 5.7.2.1. This observation contrasts previous studies of heat transfer from a heated channel wall in the presence of a cylinder oscillating either rotationally (Beskok *et al.* 2012) or transversely (Celik *et al.* 2010), where maximum heat transfer was observed at the lower range of the lock-in frequency. The observed discrepancy between the present results and the previous observations is attributed to the different mechanism of vorticity supply in both cases. In the oscillating cylinder case, the wake vortices are derived (or enhanced) through the relative motion between the cylinder and the free stream. This type of flow is governed by the relative size of the time scales of vortex dynamics and of cylinder oscillation. When the time scale of oscillation is comparable to that of vorticity, the vortex shedding is synchronised with the cylinder oscillation (the oscillation frequency is said to be in the lock-in regime). This leads to a generation of high intensity vortices and a substantial interaction between the vortices and the channel walls (Beskok *et al.* 2012). On the other hand, if the time scale of the oscillation is much smaller or much larger than the vortex dynamics (i.e. forcing frequencies outside the lock-in regime), the rate at which vorticity is shed into a wake is governed by the natural frequency irrespective of the oscillation frequency. The downstream wake in this state is similar to that for a fixed cylinder (Mahfouz & Badr 2000), and therefore inherit its poorer heat transfer characteristic.

In the present case, the wake vortices are governed by the forcing current injection, which is indicated by the presence of strong narrow peaks at the forcing frequency and its harmonics in the spectra of lift coefficient (which will be discussed further in § 5.7.2.1). For a low forcing frequency, the amount of vorticity supplied to each shed vortex is large, which leads to large wake vortical structure (as shown in Figure 5.11). This in turn would generally enhance the wake-boundary layer interaction, and thus the heat transfer from the sidewall. However, a lower forcing frequency also means fewer shed vortices for a given time duration, which may not be beneficial for heat transfer enhancement. The competition between the size and number of shed vortices results in a non-monotonic trend in the $HR-\omega_f$ relation.

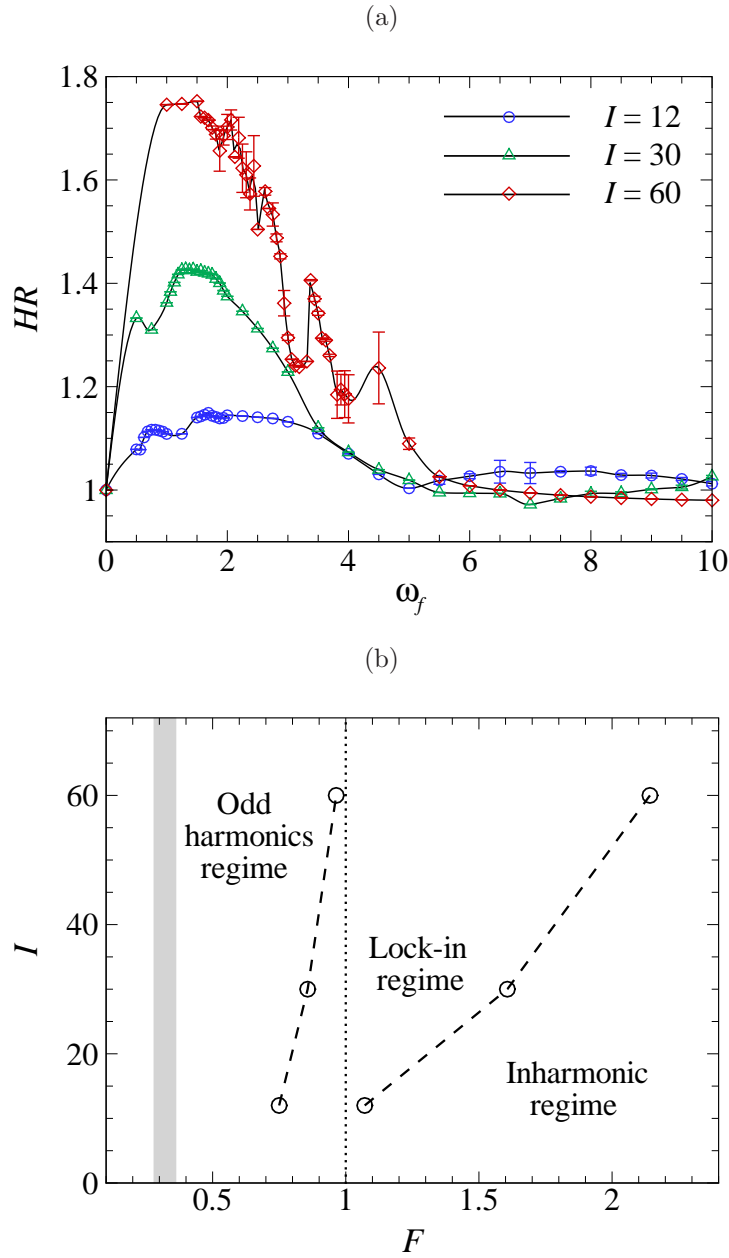


FIGURE 5.10: (a) Time-averaged heat transfer enhancement plotted against forcing frequency ω_f at non-dimensional current amplitudes I as indicated for $\tau/T = 0.25$ and $G/d = 2$. The current is injected from the cylinder. Error bars represent standard deviations of the mean Nusselt number within a shedding cycle evaluated at various shedding phases. (b) Limits of the lock-in regime as a function of forcing amplitude and normalised forcing frequency $F = f_f/f_0$. Regime to the left (right) of the lower (upper) bound represent wakes with odd harmonics (inharmonic) in cylinder lift force. The dotted line represent $F = f_f/f_0 = 1$, and the shaded region highlights the zone where HR is maximum.

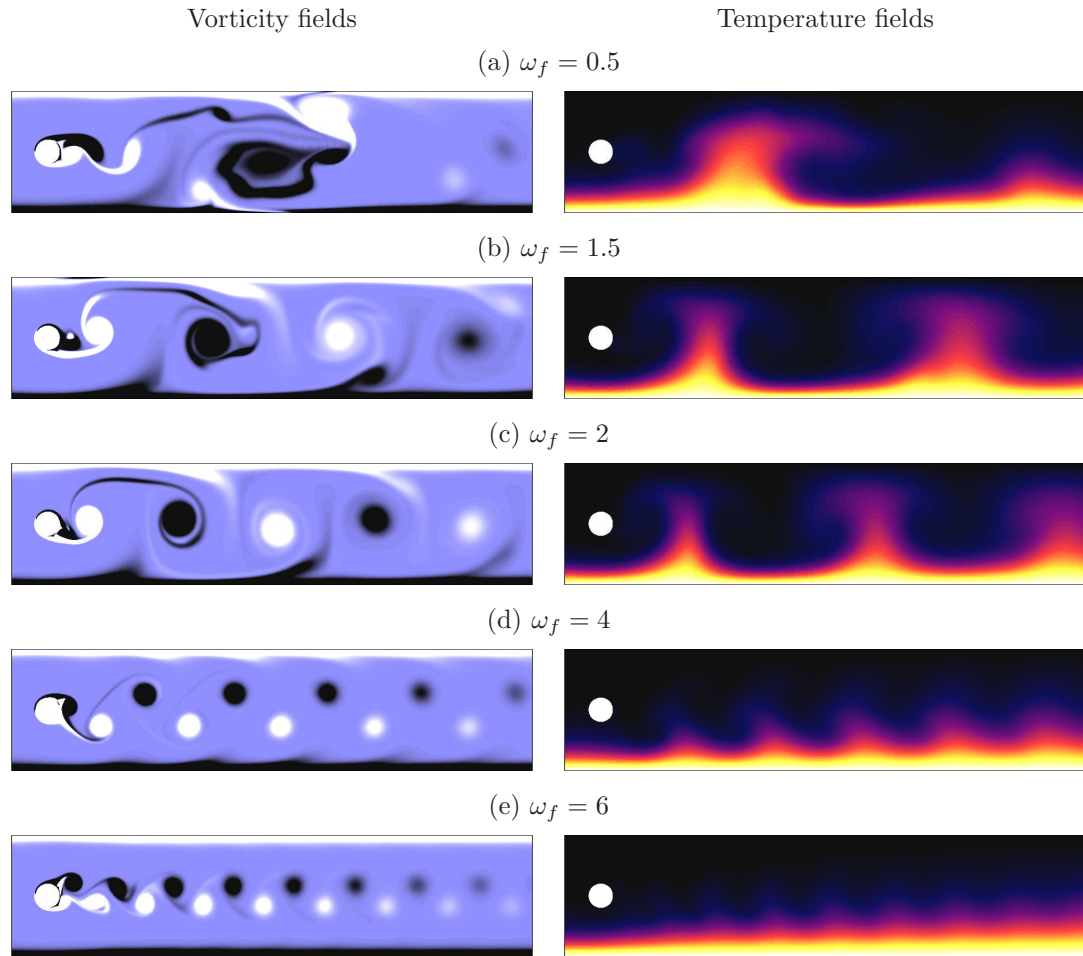


FIGURE 5.11: Contour plots of instantaneous vorticity (left) and temperature (right) fields for current injection amplitude $I = 30$ and forcing frequencies as indicated. Vorticity fields: contour levels are as per Figure 5.8. Temperature fields: dark and light contours show cold and hot fluid, respectively.

It is also interesting to observe that at higher forcing frequencies, the Nusselt number tends to asymptote towards the value obtained for the non-forced case (i.e. without current injection). Similar observations have been reported previously for a rotationally oscillating circular cylinder (Hussam *et al.* 2012a) and a transversely oscillating square cylinder (Yang 2003). This observation is attributed to the fact that for a high forcing frequency, the amount of vorticity feeding into the wake per shedding cycle decreases. This leads to a more coherent and smaller wake structure, resembling the unperturbed Kármán vortex shedding. The vortices therefore align closer to the duct centreline, which diminishes the interaction between wake vortices and thermal boundary layers (as can be seen in Figure 5.11). Figure 5.10(a) showed for $I = 12$ a noticeable enhancement

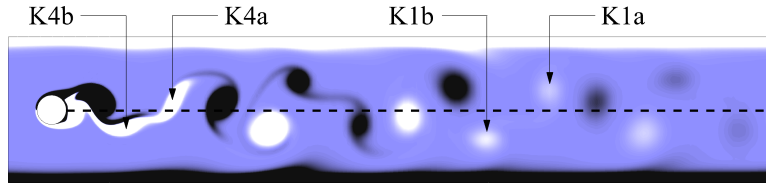


FIGURE 5.12: Instantaneous vorticity contour plots for $I = 12$ and $\omega_f = 6$. The dashed line represents the duct centreline. Contour levels ranges between -1 and 1 , with light and dark contours represent positive and negative vorticity, respectively.

in heat transfer at higher forcing frequencies ($6 \lesssim \omega_f \lesssim 9$). The local Nusselt number variation along the duct was found to exhibit a relatively higher convective heat transfer further downstream of the cylinder at higher forcing frequency. This is generated by the enhanced wake-boundary layer interaction due to the development of vortex splitting in the downstream wake, as depicted in Figure 5.12. The mechanism of this phenomenon is as follows: as an attached shear layer rolls up halfway from the cylinder in the formation region, an incipient eddy of opposite sign crosses the wake centreline, causing the shear layer to stretch and finally split into two (i.e. vortices K1a and K1b) at approximately four diameters downstream of the cylinder. This process is repeated in the third successive phases (which results in the birth of vortices K4a and K4b), and the vortex sheds in the form of a regular Kármán vortex shedding between these two phases.

It is also worth mentioning that the fluctuations in the trend in Nusselt number for a higher forcing amplitude are due to the different modes of response of the wake at different forcing frequencies. For example, at $\omega_f = 3.375$, HR is 13% higher than at $\omega_f = 3.3125$ for $I = 60$, despite the frequencies differing by less than 2%. Vorticity contours for the marginally higher $\omega_f = 3.375$ (as shown in Figure 5.13(a)) reveal that there is a substantial interaction between wake vortices and the heated wall due to the broadening of the width of the wake. There is clear evidence of boundary layer entrainment from the heated wall into the wake, as well as strong mixing between the high-temperature fluid near the heated region with the low-temperature core flow. In the case with $\omega_f = 3.3125$, however, almost no boundary layer entrainment from the heated wall into the wake was observed (as can be seen in Figure 5.13(b)). This results in poor mixing between the hot fluid near the boundary and cold fluid in the core flow, which explains the abrupt increase in Nusselt number at this particular forcing

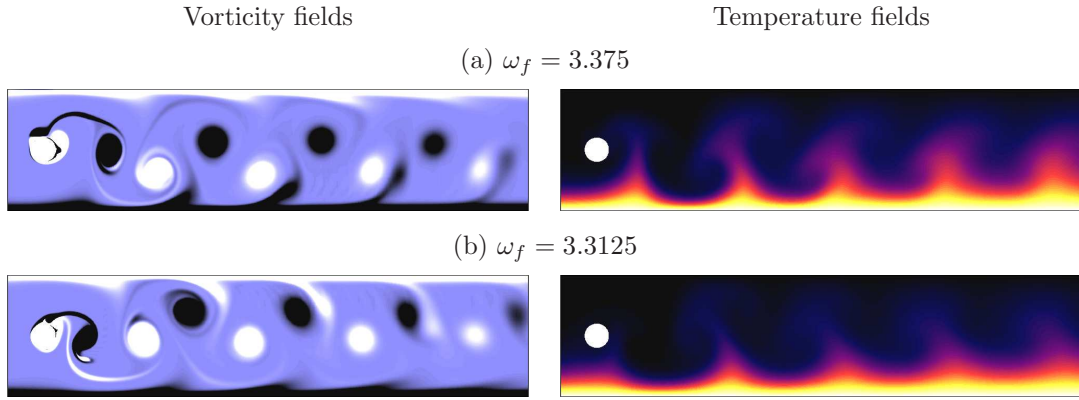


FIGURE 5.13: Instantaneous vorticity contour plots for $I = 60$ and (a) $\omega_f = 3.375$ and (b) $\omega_f = 3.3125$. Contour levels are as per Figure 5.8.

frequency.

Inspection of instantaneous vorticity fields for these two frequencies reveals that the wakes are almost perfectly reflectively symmetric about the wake centreline. It has been shown previously that similar deflections of wake vortex shedding from the centreline is triggered by introducing local disturbances into the boundary layer on the cylinder by either heating the cylinder (Kieft *et al.* 2003) or by rotating the cylinder (Lam 2009). In the present case, however, the current injection perturbation is in a modified square waveform with an alternating polarity, and the boundary and forcing conditions are symmetrical about the duct centreline. To test the robustness of this bi-stable behaviour to asymmetry in the system, simulations were conducted with the cylinder shifted transversely by 5% of the duct width, corresponding to $G/d = 2.25$ and $G/d = 1.75$. No clear trend concerning the cylinder position and the mode of wake response was found. The wake was biased upwards, downwards, or was symmetric with respect to the duct centreline. The resulting heat transfer enhancement ratio data are presented in Figure 5.14. For a given forcing frequency, HR was found to vary within a narrow range, indicated by the shaded region, due to the aforementioned uncertainty in the mode of wake response. Nevertheless, the overall trend remains: increasing forcing frequency leads to a lower heat transfer enhancement.

5.7.2.1 Shedding frequency analysis

In this section, analysis of the lift coefficient time histories and the vorticity time series is presented in order to investigate the response in the wake of the circular cylinder to

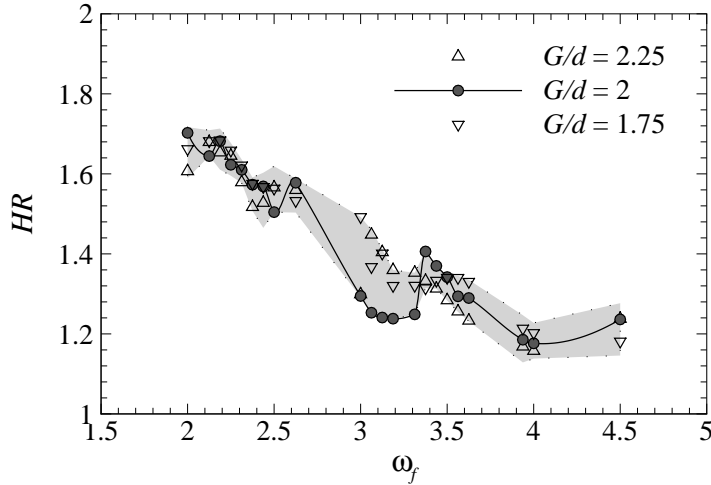


FIGURE 5.14: Time-averaged heat transfer enhancement plotted against forcing frequency for $I = 60$, $\tau/T = 0.25$, and ω_f and G/d as indicated. The current is injected from the cylinder. The shaded region highlights the zone bounded by $\max(HR + \sigma_{HR})$ and $\min(HR - \sigma_{HR})$, where σ_{HR} is the standard deviation of mean HR .

the current injection. The analysis was conducted on data recorded after the transient startup phase of the simulations had completed. The peaks in the resulting spectra are interpreted in terms of the natural shedding frequency, forcing frequency, and their harmonics. The analysis reveals three distinct regimes of wake response: the odd harmonics regime, lock-in regime and inharmonic regime.

In the lock-in regime, the wake shedding frequency is governed only by the forcing current. In general, the synchronisation of vortex shedding (lock-in state) occurred over $0.8 < F < 2$ within the investigated forcing amplitude (refer Figure 5.10(b)). This compares quite well with the range of synchronisation $1.2 < F < 2.5$ for a circular cylinder oscillating in-line with an incident flow of air observed by Griffin & Ramberg (1976). It should be noted that in the case of a transversely oscillating cylinder, a synchronisation range of $0.75 < F < 1.25$ was reported by Koopmann (1967). Despite these observed disparities, the qualitative trend is consistent across these systems: the domain of the lock-in regime increases with increasing forcing amplitude.

In the present cases, a distinct spectrum was observed outside the lock-in regime compared to the oscillating and vibrating cylinder cases. A typical lift force history is shown in Figure 5.15(a) for a case with $I = 12$ and $\omega_f = 1$ and 6, where the inharmonic case with $\omega_f = 1$ resembles a distorted waveform. When the forcing frequency

is below the lock-in frequency threshold (i.e. in the region to the left of the lower bound shown in Figure 5.10(b)), the spectrum is composed of the forcing frequency and its odd harmonics (as shown in Figure 5.16 for $\omega_f = 1$), which corresponds to the forcing response. Beyond the lock-in regime (i.e. the inharmonic regime shown in Figure 5.10(b)), the forcing frequency, its harmonic(s), and fraction of the natural shedding frequency (i.e. $f = nf_0/4$, where n are odd integers) are present in the spectrum (as shown in Figure 5.16 for $\omega_f = 6$). The presence of multiple peaks may be the result of nonlinear interaction between the electrically generated vortices and the naturally shed vortices. Similar nonlinear interactions were reported by Karniadakis & Triantafyllou (1989) for a cylinder vibrating beyond the lock-in regime. Furthermore, the observed spectral peaks at frequencies lower than the forcing frequency can be explained by the aforementioned split vortex that misses the measurement “probe” located at the duct centreline. It has previously been shown that only the natural shedding frequency or forcing frequency are dominant outside the lock-in regime for an oscillating cylinder (Celik *et al.* 2008), while only the natural shedding frequency is dominant outside the lock-in regime for a vibrating cylinder (Karniadakis & Triantafyllou 1989), although the presence of several other frequencies have been reported for some of these cases. Here, the spectrum in the lock-in regime is typical; the lift force fluctuation synchronises with the forcing frequency (shown by the strong narrow peak at $f/f_f = 1$ in Figure 5.16 for $\omega_f = 3.5$) and with nearly uniform amplitude (as shown in Figure 5.15(b)).

The wake response was further assessed via spectral analysis of the vorticity time series recorded at the duct centreline and at different streamwise positions (five, ten and fifteen diameters downstream of the cylinder, corresponding to $x = 2, 4$ and 6 , respectively). It was found that, irrespective of the position where the signal was acquired, the wake exhibits a similar response (i.e. the spectrum peak is located at the same dominant frequency) for a given forcing amplitude and frequency. It was also observed that these signals have a similar response to the cylinder lift coefficient, except in the lock-in regime, where the frequency spectra exhibit peaks at odd harmonics. The appearance of these odd harmonic peaks in the spectrum is due to the absence of vorticity between two consecutive vortices of opposite sign, which results in an imperfect sinusoidal but symmetric waveform of vorticity time series (as shown in Figure 5.17). For comparison, the corresponding cylinder lift coefficient time histories are shown in Figure 5.15(b).

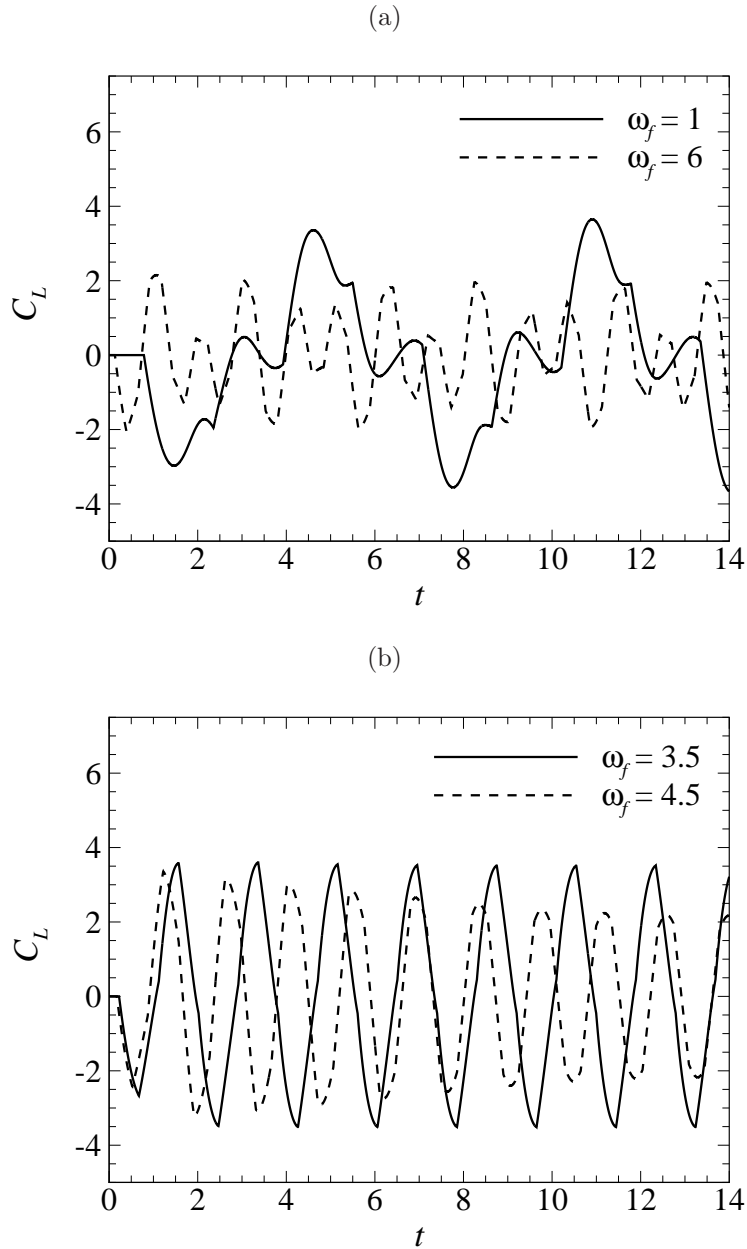


FIGURE 5.15: A typical time variation of the cylinder lift coefficient for $I = 12$ and ω_f as indicated within (a) unlock-in regimes and (b) lock-in regimes.

5.7.3 Effects of the current injection amplitude and gap ratio on heat transfer

This section examines the variation of HR as a function of forcing amplitude and transverse cylinder position. A typical plot is shown in Figure 5.18. In general, HR increases with increasing forcing amplitude, with $HR_{\max} \approx 1.9$ across the computed parameters. The increment is relatively substantial compared to the gain observed for oscillating

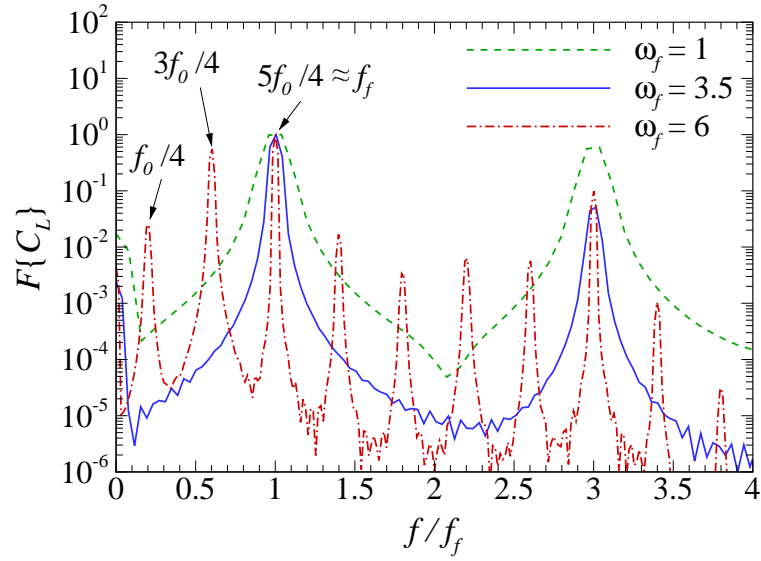


FIGURE 5.16: Respective Fourier spectra of the lift coefficient signals in Figure 5.15(a) and (b).

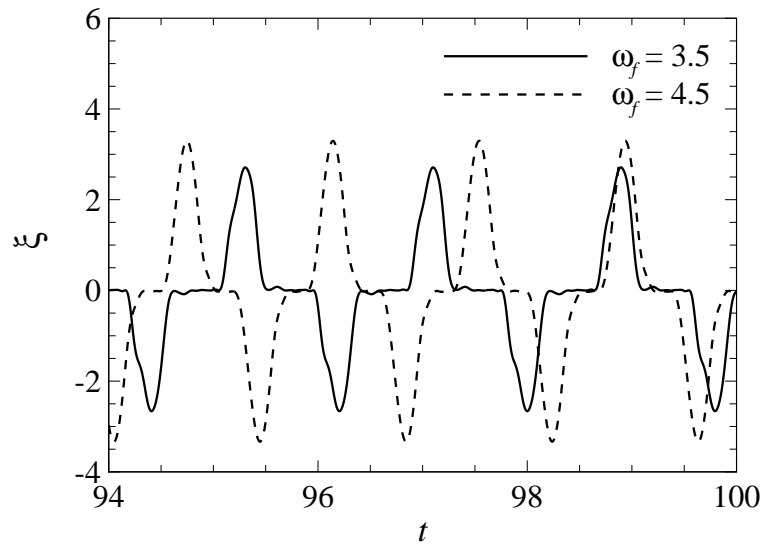


FIGURE 5.17: Time history of vorticity signal taken at $(x, y) = (0, 5d)$ for $I = 12$ and ω_f as indicated.

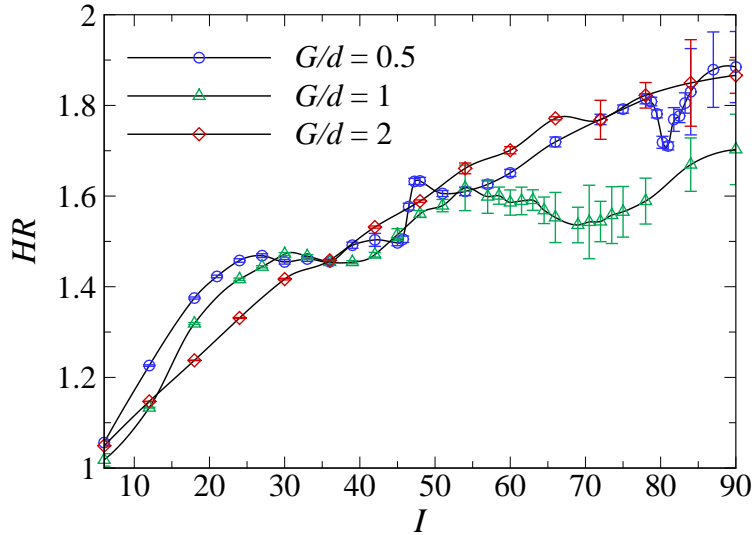


FIGURE 5.18: Heat transfer enhancement ratio plotted against current injection amplitude I at gap ratios G/d as indicated for $H = 500$, $\tau/T = 0.25$ and $\omega_f = 1.75$. The current is injected from the cylinder.

cylinder cases, e.g. in Hussam *et al.* (2012a), where $HR_{\max} \approx 1.2$ was reported for a case with maximum oscillation amplitude (i.e. $A = 3$), at optimum frequency, $Re_L \approx 1800$ and $H \approx 210$. It is noted that at a lower range of I (i.e. $I \lesssim 30$), the forcing current injection has a more profound effect on the heat transfer enhancement when the cylinder is placed closest to the heated side of the duct wall (i.e. $G/d = 0.5$) as compared to the other positions investigated. The reason for this is that when the cylinder is placed close to the wall, the shed vortices interact strongly with the thermal boundary layer in the vicinity of the cylinder, reducing its thickness and therefore increasing the local Nusselt number abruptly within the formation region (as shown by the sharp peak of the time-averaged local Nusselt number for the case of $G/d = 0.5$ and $I = 18$ in Figure 5.19(a)). On the other hand, the interaction between the wake and the thermal boundary layer becomes weaker as the cylinder is placed further away from the wall, which results in relatively lower HR and more consistent local Nu along the duct (as shown by the almost uniform local Nu profile for the case of $G/d = 2$ and $I = 18$ in Figure 5.19(a)).

However, for a large forcing amplitude, the duct with a cylinder placed on the centreline exhibits the highest enhancement in heat transfer. This occurs because for increasing I , the vortex becomes larger (as seen in Figure 5.20(a-c)) and there is a

consistently strong interaction between the heated wall and the cylinder wake along the duct. Furthermore, the local Nu is progressively increased over a downstream region up to $I = 54$ (as shown in Figure 5.19(b)). Beyond $I = 54$, the local Nu exhibits a wavy pattern due to the complex interactions between the wake vortices and the thermal boundary layer (as shown in Figure 5.20(c)). Nevertheless, Nu increases steadily with I , as shown by the almost linear trend in the $HR-I$ plot. For the asymmetric cases, on the other hand, the strong wake-boundary layer interaction remains only in the vicinity of the cylinder even for high I , which spans only approximately 20% of the duct length, whereby a rapid decrease in local Nu downstream of the local maxima was observed (as shown in Figure 5.19(a) for cases with $I = 84$). The reason for this observation is that the paired vortices are deflected away from the heated wall toward the opposite wall as they advect downstream (as shown in Figure 5.20(d)).

Note also that the HR for cases with $G/d = 1$ tend to level off for $54 \lesssim I \lesssim 78$. A similar tendency was also observed for $G/d = 0.5$ cases, except that for $I \geq 60$, there is another relatively smaller peak of local Nusselt number downstream of the first one, as shown in Figure 5.19(a) for $I = 84$. This second peak emerges due to the strong wall vorticity entrainment into the wake, induced by the paired vortices that have effectively shed (refer vorticity contours in Figure 5.20(d)), and is attributed to the increase of HR with increasing I at a high forcing amplitude range. A similar observation was reported for transversely (Celik *et al.* 2010) and rotationally (Beskok *et al.* 2012) oscillating cylinders in duct arrangements, whereby the second peak of a local wall Nusselt number has a significant contribution to the spatial-averaged heat transfer. It is also found that as I increases, the magnitude of the second peak increases and its distance from the cylinder decreases.

5.7.4 Effects of the current injection pulse width and frequency on heat transfer

Here the variation of Nusselt number with different forcing pulse width and frequency is examined. Figure 5.21 reveals that the heat transfer enhancement ratio increases monotonically with increasing forcing pulse width. This may be explained as for a given forcing frequency, the wake vortex size is larger for a longer forcing pulse width (as shown in Figure 5.22). As a result, the wake-boundary layer interaction is enhanced, thinning the thermal boundary layer at the heated wall and thus improving the convective heat transport.

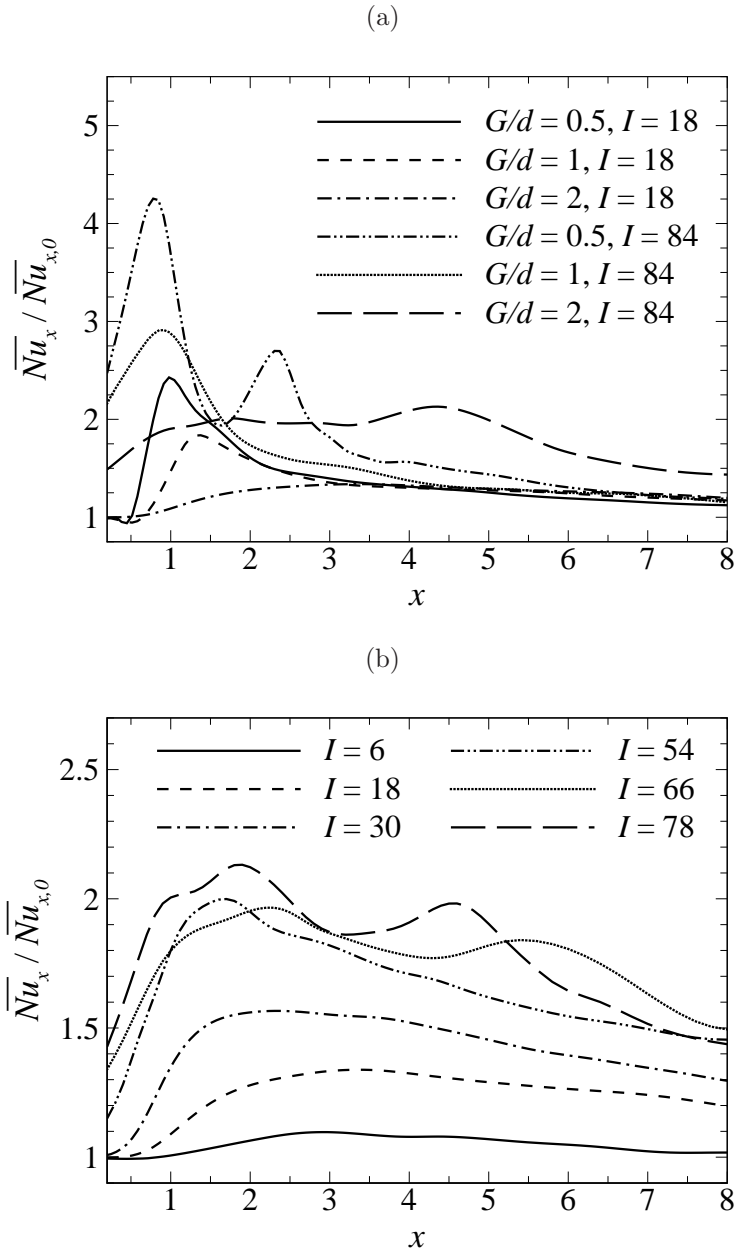


FIGURE 5.19: Normalised time-averaged local Nusselt number along the downstream of the heated wall for $\tau/T = 0.25$, $\omega_f = 1.75$ and (a) I and G/d as indicated, and (b) $G/d = 2$ and I as indicated.

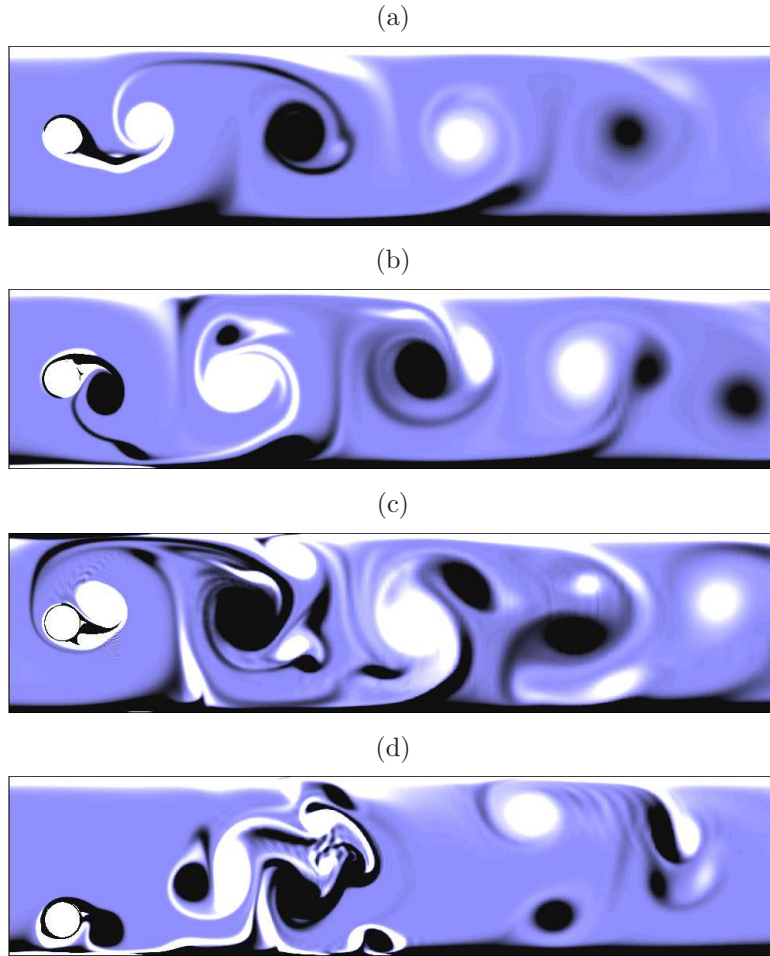


FIGURE 5.20: Instantaneous vorticity contour plots for (a) $I = 30$ and $G/d = 2$, (b) $I = 54$ and $G/d = 2$, (c) $I = 78$ and $G/d = 2$ and (d) $I = 84$ and $G/d = 0.5$. Contour levels are as per Figure 5.8.

Furthermore, cases with $\omega_f = 1.75$ show a better heat transfer enhancement than the cases with $\omega_f = 3.5$. This observation is in agreement with the findings presented in § 5.7.2, where the Nusselt number reaches its maximum value at $1 \lesssim \omega_f \lesssim 2$ for $I = 30$. However, at the lowest forcing pulse width (i.e. $\tau/T = 0.05$), the enhancement in heat transfer is almost similar for both forcing frequencies. This is due to the fact that for low τ/T , the resultant wake vortices are relatively small, regardless of the forcing frequency. This in turn results in almost no interaction between the wake and the boundary layer (as shown in Figure 5.22 for $\tau/T = 0.05$), which results in only an approximately 6% enhancement in heat transfer.

For cases with $\tau/T = 0.5$, although the forcing current injection is in the form of a square wave (as shown in Figure 5.4), the resulting wake resembles that of a Kármán

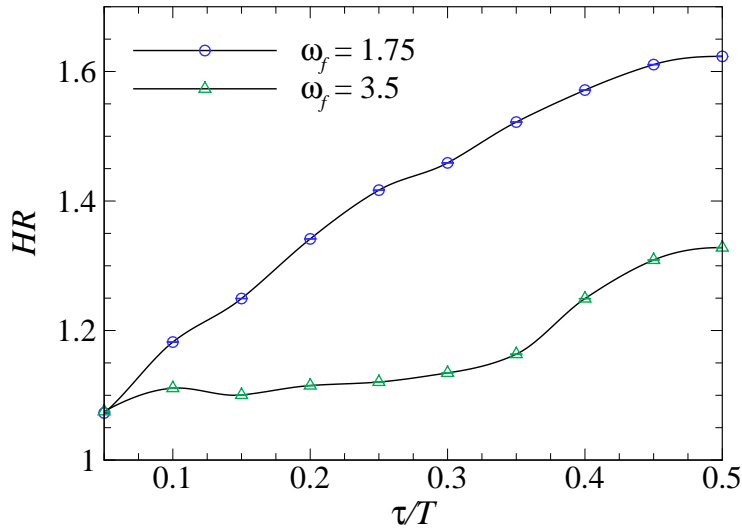


FIGURE 5.21: Heat transfer enhancement ratio plotted against current injection pulse width τ/T at frequencies ω_f as indicated for $H = 500$, $I = 30$ and $G/d = 2$. The current is injected from the cylinder.

vortex shedding, where there is a finite spacing between two consecutive shed vortices of opposite sign. This may be understood as follows: as the vortex rolls up, it is advected downstream and is effectively “shed” before the forcing current switches to the opposite sign, forming a long tail that connects to the succeeding shed vortex of opposite sign (as can be seen in Figure 5.22(aii) and (bii)). From these figures, it was also observed that the tail of the counter-clockwise (positive) vortices have a greater influence on thinning the thermal boundary layer than do the clockwise vortices. It may therefore be anticipated that for a given pulse duty cycle D , the efficiency index may be further increased by injecting current which produces positive vorticity that has a longer pulse width relative to the negative vorticity. Here, $D = 2\tau/T$ for a modified square wave, which represent a fraction of one period in which the signal is active. This would be an interesting avenue for future study.

5.7.5 Effects of the electrode position relative to the cylinder on heat transfer

The effect of electrode position on the heat transfer enhancement ratio is now considered. The electrode was placed at 18 different positions in the vicinity of the cylinder and the heated wall, in order to investigate the effect of complex interactions between

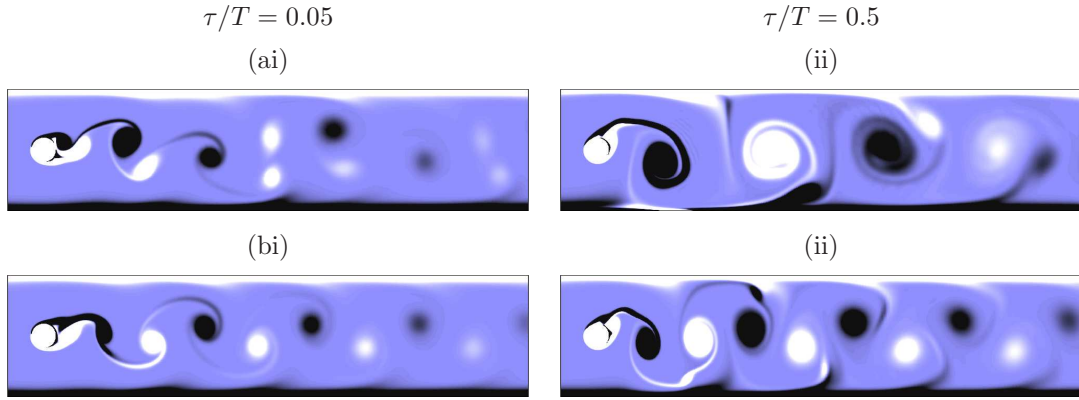


FIGURE 5.22: Instantaneous vorticity contour plots for $I = 30$ and (a) $\omega_f = 1.75$ and (b) $\omega_f = 3.5$. Contour levels are as per Figure 5.8.

the shear layers on the global heat transfer. Other parameters are fixed at $H = 500$, $I = 12$, $\omega_f = 1.75$, $\tau/T = 0.25$ and $G/d = 2$, and the results are shown in Figure 5.23. The figure reveals that the enhancement in heat transfer is almost independent of the streamwise electrode position. The reason for this observation is due to the counterbalancing effect of the relative “surplus” and “deficit” in the streamwise distribution of local Nu (as depicted by the shaded regions in Figure 5.24(a)); increased heat transfer downstream of the electrode as it is placed further downstream is offset by the larger region upstream of the electrode exhibiting low heat transfer. This happens because the heat transfer enhancement is found to occur only downstream of the electrode (i.e. there was almost no enhancement at $x \lesssim l_x$), and due to the variations in the magnitude and/or location of the local Nu peaks with l_x .

Figure 5.23 also reveals that the heat transfer is significantly more sensitive to transverse electrode position. Inspection of the normalised local Nusselt number reveals that, for a given l_x , the peaks for cases with $l_y = 0.4$ are consistently higher than for the cases with $l_y = 0.6$ (as shown in Figure 5.24(b)). The magnitude, however, decreased abruptly downstream of the electrode, due to the aforementioned deflection of shed vortices away from the heated wall toward the opposite wall for the offset cylinder cases. This leads to a lower overall heat transfer enhancement than for cases with electrode placed at $l_y = 0.6$.

For a given l_y , the magnitude of the peaks were almost invariant with respect to l_x (with the coefficient of variation, $0.015 \leq CV \leq 0.046$ for all l_x), indicating that the magnitude of the peaks is governed by the electrode-wall proximity. However, at

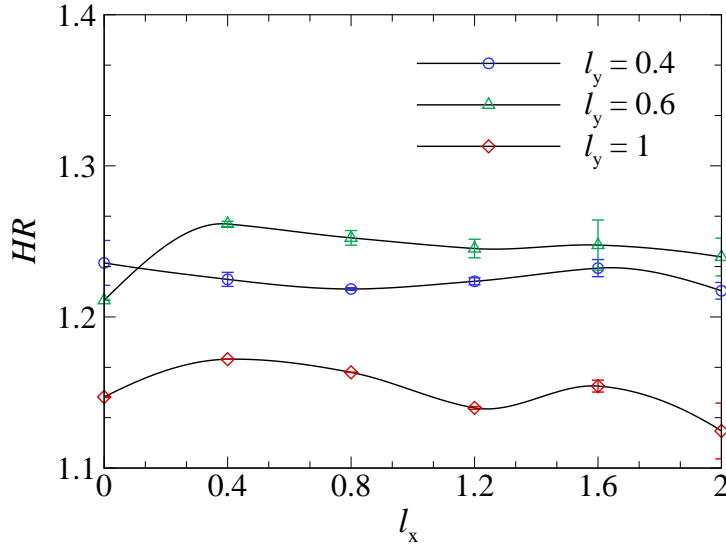


FIGURE 5.23: Heat transfer enhancement ratio plotted against horizontal distance l_x at vertical distance l_y as indicated for $I = 12$, $\omega_f = 1.75$, $\tau/T = 0.25$ and $G/d = 2$.

$l_y = 0.6$, the peak of time-averaged $Nu_x/Nu_{x,0}$ for $l_x = 0$ is significantly lower than the peaks for other l_x (as can be seen in Figure 5.24(a)), which results in HR lower than the case for $l_y = 0.4$ for the same l_x (as shown in Figure 5.23). This observation is consistent with the results presented in Figure 5.18, where at a lower range of I , HR is higher when the cylinder is placed closest to the heated wall.

For the cases with electrode placed at the duct centreline, the wake-boundary layer interaction is weak throughout the duct, and there were no strong peaks observed in the local $Nu-x$ plot. The peaks are consistently lower than for the offset electrode counterparts, which leads to a lower HR for any given l_x .

5.7.6 Effects of friction parameter and Reynolds number on heat transfer

This section reports the influence of magnetic field strength (quantified by friction parameter H) and Reynolds number. Other parameters are fixed at $I = 30$, $\omega_f = 1.75$, $\tau/T = 0.25$, $G/d = 2$. The results are shown in Figure 5.25 for $200 \leq H \leq 5000$ and $Re_L = 1500$ and 3000 . The figure shows that for a given Reynolds number, the enhancement in heat transfer due to the imposed current exhibits a non-monotonic relation with friction parameter. At low H , HR increases with increasing H and reaches a peak, before decreasing steadily with further increases in H and eventually reaching

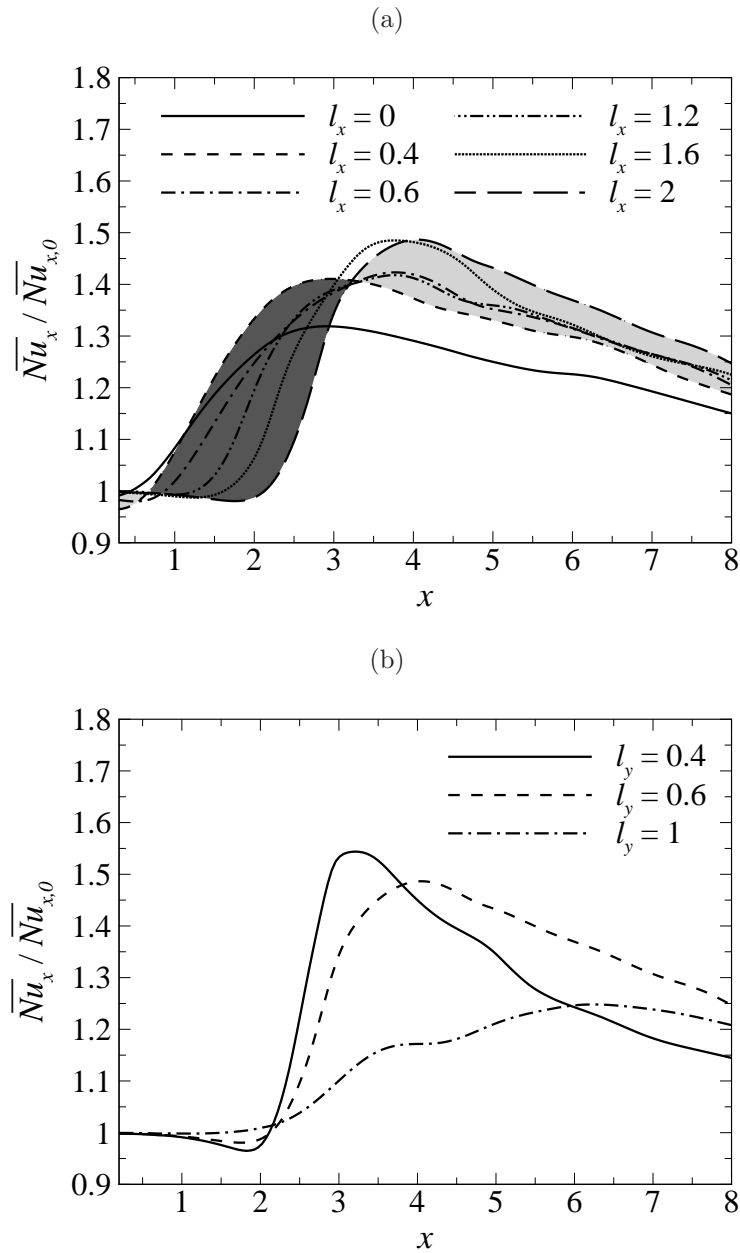


FIGURE 5.24: Normalised time-averaged local Nusselt number along the downstream of the heated wall. (a) The electrode is placed at $l_y = 0.6$ and at l_x as indicated. The dark (lighter) region correspond to a deficit (surplus) in heat transfer enhancement of case with $l_x = 2$ relative to the case with $l_x = 0.4$. (b) The electrode is placed at $l_x = 2$ and at l_y as indicated.

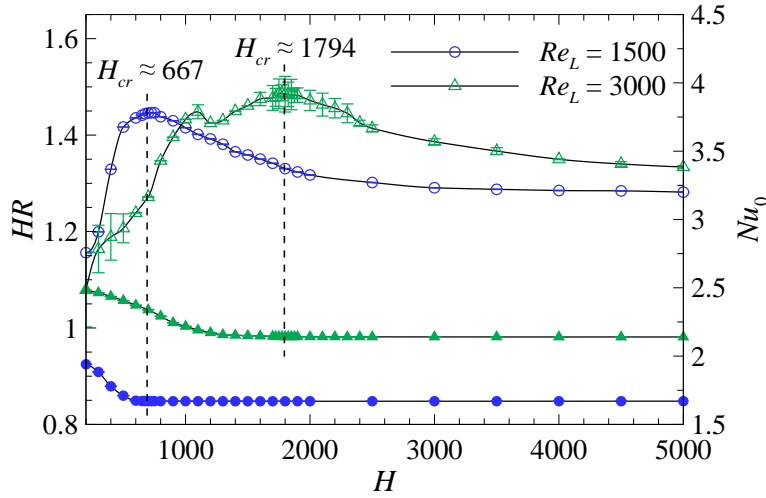


FIGURE 5.25: (Primary vertical axis) Heat transfer enhancement ratio and (secondary vertical axis) base flows time-averaged Nusselt number plotted against friction parameter H for Reynolds numbers $Re_L = 1500$ and 3000 . Open symbols represent HR and solid symbols represent Nu_0 . The dashed lines indicate a critical value of the friction parameter, above which the cylinder vortex shedding is completely suppressed.

an asymptotic value.

This observation is attributed to the competition between inertia and Hartmann damping, i.e. $(a^2/nL^2)Re_L/Ha$ (Sommeria 1986). In the low- H regime, the inertially shed and electrically driven vortices dominate over the damping force, which results in shed vortices being sustained to greater downstream distances. There is a consistently strong interaction between the heated wall and the cylinder wake along the duct, visible in the vorticity field plot in Figure 5.26(ai). Consequently, the enhancement in the local Nusselt number is nearly uniform throughout the domain (as shown by the almost horizontal profile for $H = 200$ in Figure 5.26(b)). In the high- H regime, however, Hartmann damping dominates over the driving force. The strength of the shed vortices is relatively high in the near wake due to the strong interaction between the magnetic field and the imposed current forcing, but is damped rapidly after they are shed (as indicated in the plot of vorticity contour in Figure 5.26(aii)). As a result, the strong wake-boundary layer interaction occurs only in the near wake region, which is reflected by the strong peak of local Nusselt number in the vicinity of the cylinder, followed by a rapid decline further downstream (as shown in Figure 5.26(b) for friction parameters in the high- H regime). With H increasing further, the flow field is dominated by the

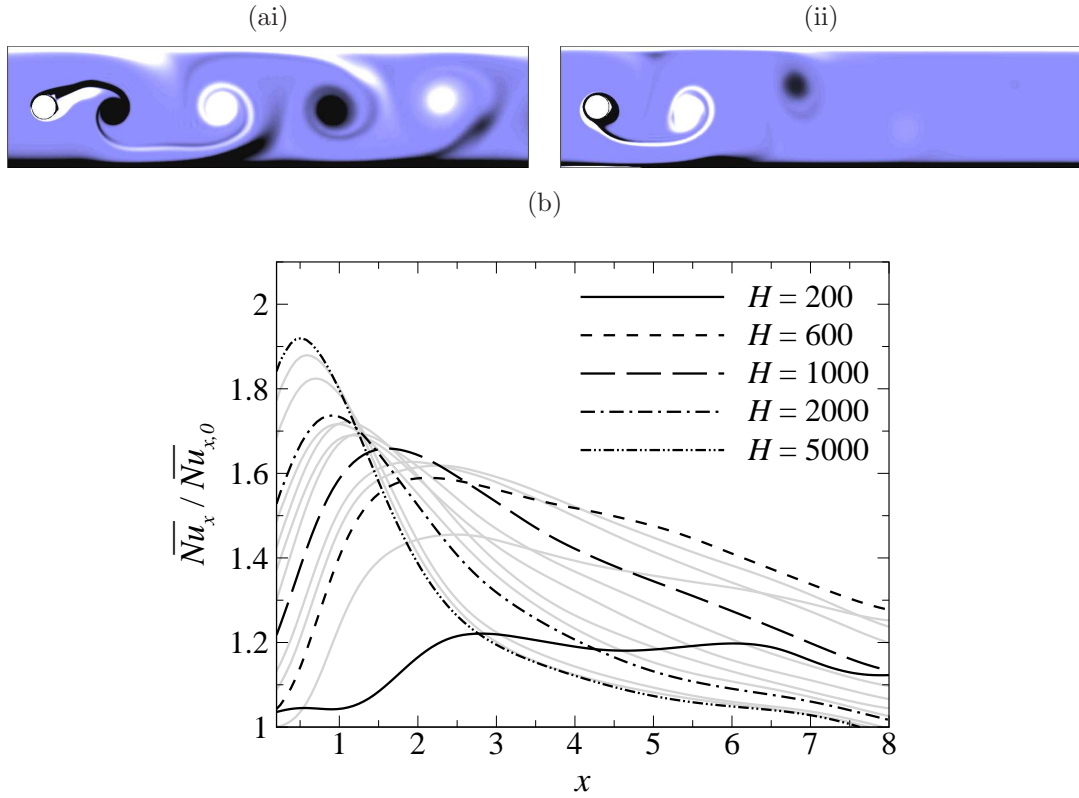


FIGURE 5.26: (a) Instantaneous vorticity contour plots for $Re_L = 1500$ and (ai) $H = 300$ and (aii) $H = 1500$. Contour levels are as per Figure 5.8. (b) Normalised time-averaged local Nusselt number along the downstream of the heated wall for $Re_L = 1500$ and H as indicated.

forcing current. However, due to very strong damping, the shedding is completely suppressed and the heat transfer eventually becomes asymptotically independent of H .

HR reaches its maximum value at a friction parameter close to the critical value H_{cr} at which a transition between time-dependent and steady state flows occurs in the base flows. The Nusselt number for the base flows, however, reaches an asymptote beyond the critical friction parameter due to laminarisation (as can be seen in Figure 5.25). This observation is in contrast to cases where the duct walls are conducting, where Nu increased with increasing Ha due to high velocity gradient near the heated wall (Takahashi *et al.* 1998; Cuevas *et al.* 1997). Furthermore, the flow with higher Re_L reached a higher asymptote in the steady state regime due to the increased level of turbulence, which is favourable for effective heat dissipation (Sukoriansky *et al.* 1989). Noting the Hartmann friction term in equation (4.9), the heat transfer enhancement ratio is plotted against H/Re_L in Figure 5.27. The figure shows that the HR data for both Reynolds numbers nearly collapses into a single curve, suggesting that the

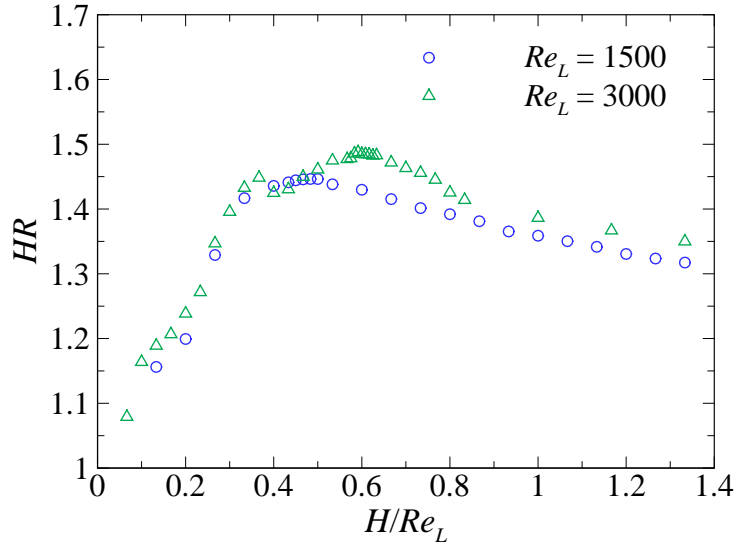


FIGURE 5.27: Heat transfer enhancement ratio and plotted against H/Re_L for Re_L as indicated. Circle and delta symbols represent $Re_L = 1500$ and 3000 , respectively.

enhancement of heat transfer is governed by the H/Re_L . This observation is perhaps not surprising, given that the stability (Sommeria 1986) and the decay of vortices (Sommeria 1988; Hamid *et al.* 2015c) in quasi-two-dimensional MHD duct flows are controlled by the H/Re_L parameter.

5.7.7 Power and efficiency analysis

In this section, the characteristics of pumping power requirement (expressed in terms of pressure penalty ratio), overall system efficiency resulting from the employment of current injection as a turbulence enhancer, and the current injection power input are reported. The pressure penalty ratio PR in this study is the ratio of pressure drop across identical ducts with and without current injection. Inspection of PR across all cases in this study (not shown for brevity) reveals that the pressure drop induced by the imposed current injection is almost negligible, with the maximum pressure increment of 13% (i.e. $PR_{\max} = 1.13$). It was also observed that the position of the electrode and magnetic field strength have almost no effect on PR , where the mean (and standard deviation in parentheses) of PR for various investigated electrode positions and Hartmann numbers are respectively 1.004 (0.0032) and 1.012 (0.0067). Furthermore, it was found that cases with the cylinder at the duct centreline show a relatively higher increment in pressure drop as compared to the cases with an offset cylinder, and this

becomes more apparent at a higher current amplitude. In some cases, the imposed current injection has a desirable effect by reducing the pressure drop with respect to the base cases, with a maximum reduction of 4% (i.e. $PR_{\min} = 0.96$). Since PR is almost unity for all cases, it follows then that the system efficiency (quantified by the efficiency index η as in equation (5.11)) and the heat transfer enhancement ratio HR have a similar dependency on all varying parameters (as presented in the previous sections). The maximum efficiency index was found to be $\eta = 1.91$ for the case with highest current amplitude, which produces the highest heat transfer enhancement ratio of $HR = 1.89$. This enhancement in heat transfer is 55% more than what has been reported for rotationally oscillating cylinder rotating at maximum amplitude and optimum frequency (i.e. $HR \approx 1.22$) (Hussam *et al.* 2012a).

In their numerical study, the flow condition was fixed at $Re_L \approx 1774$ and $H = 825$. For the sake of comparison, the Nusselt number enhancement due to the current perturbation described in § 5.7.6 is roughly estimated for the same flow condition. The estimation is made using linear interpolation between $Re_L = 1500$ and $Re_L = 3000$, and between $H = 800$ and $H = 900$, as presented in Figure 5.25. The enhancement was estimated to be $HR \approx 1.42$, which is about 16% more than the enhancement due to the cylinder oscillation. It is important to note that the estimated gain in HR was obtained with the cylinder diameter being relatively smaller than in Hussam *et al.* (2012a) (i.e. $\beta = 0.2$ against $\beta = 0.303$). It has been shown previously (Hussam *et al.* 2011) that a larger cylinder generally leads to an improved heat transfer, hence it is expected that the gain would be higher for larger cylinder. Furthermore, the estimation is performed for $I = 30$ and $\tau/T = 0.25$; the HR can be further improved by increasing current amplitude and pulse width, as shown by the monotonically increasing trend of HR with I and τ/T in figures 5.18 and 5.21, respectively. In the hydrodynamic counterpart, maximum enhancement of $HR \approx 1.55$ has been reported when the cylinder with $\beta = 1/3$ rotationally oscillates with maximum amplitude and within the lock-in regime (Beskok *et al.* 2012).

It is important to mention that the effect of inertially driven recirculation in the parallel planes on the heat transfer is assumed to be negligible in the present work. A recent investigation by Baker *et al.* (2015) has shown that in the limit of quasi-2-D base flow, the local fluid rotation above the Hartmann layer induces secondary counter-rotating 3D recirculations which correspond to Ekman pumping. The emergence of

these recirculations drives an inward radial flow within the Hartmann layers, and thus can potentially transport a fraction of heat towards the core flow and alter the heat transfer characteristics of the flow. However, it has been reported (Alboussière *et al.* 1999) that the 3D recirculation is weakened under a strong magnetic field. It is then anticipated that this weak recirculation becomes less effective in transferring heat relative to the primary vortex flow, justifying the aforementioned assumption.

The average power supply due to current injection is proportional to I_{rms}^2 , where I_{rms} is the root mean square of injected current. Since the dimensional current amplitude

$$\hat{I} = IaU_0\sqrt{\rho\nu\sigma} = \frac{2IRe_L}{\alpha}\sqrt{\rho\nu^3\sigma}, \quad (5.12)$$

and taking, for example, the properties of low-melting eutectic alloy Ga⁶⁸In²⁰Sn¹² at 20°C (as presented in § 1.2) and $\alpha = 1$, the dimensional current injection amplitude is given by

$$\hat{I} \approx 5.96 \times 10^{-5} IRe_L \text{ ampere.} \quad (5.13)$$

In the present investigation, the bulk of the numerical simulations were computed at $Re_L = 1500$, while the dimensionless current injection amplitude was varied between 6 and 90. This then corresponds to a dimensional current of $\hat{I} \approx 0.5$ and 8 ampere, respectively. For the sake of comparison, this current supply is three orders of magnitude lower than that required to induce the confining magnetic fields for fusion blanket MHD research in the MEKKA experimental facility (Barleon *et al.* 1996). The use of electrically generated quasi-two-dimensional vortices for heat transfer augmentation therefore appears to be viable, at least in principle. There are, however, significant technical challenges in realizing controlled current injection through electrodes that are embedded in a Hartmann wall. These include ensuring a good contact between the electrode surface and the liquid metal, as poor contact can lead to overheating, and the effect on the fluid rotation above the electrode may be significant. Furthermore, the electrode-liquid metal interface is also susceptible to varying resistance, where erratic variation in contact resistance can lead to an irregular electric current distribution over multiple electrodes. This effect can be avoided by incorporating ohmic resistance of orders of magnitudes higher than any other resistance in the electric circuit of each electrode (Pothérat & Klein 2014). This solution would, however, result in energy consumption significantly higher than previously estimated. Furthermore, it has been shown previously that the electrical resistance increases monotonically with increas-

ing imposed magnetic field (Sommeria 1988). The technological challenges toward the implementation of such system are outside the scope of the present study.

5.8 Chapter summary

This chapter study has investigated the characteristics of electrically generated quasi-two-dimensional vortices to enhance sidewall heat transfer in MHD ducts containing a circular cylinder vortex promoter under a strong transverse magnetic field. A solution to the current injection forcing field was first derived for a domain extending infinitely in streamwise direction and bounded by duct sidewalls, and was imposed as a forcing field in simulations of the quasi-two-dimensional flows. It was found that the heat transfer enhancement is closely associated with the resulting wake dynamics and its interaction with the heated wall. The results indicate a maximum Nusselt number improvement of about 90% for ducts with current injection, which is highly dependent on the imposed forcing current parameters. Non-monotonic relationships between the heat transfer enhancement ratio HR and the forcing frequency and magnetic field strength were observed. The HR , however, increased almost linearly with forcing amplitude and pulse width. It is also significantly influenced by the electrode position in the transverse direction.

An examination of the local Nusselt number variation along the duct revealed a general trend wherein a sudden jump was followed by an abrupt decrease in the local Nu , due to the deflection of the wake vortices away from the heated wall. In some cases, the appearance of a secondary peak in the local Nusselt number plots has a significant contribution to the overall heat transfer enhancement. Despite the different mechanism of vortex generation in the present MHD duct flow, the heat transfer enhancement exhibits similar characteristics to the hydrodynamic counterpart, whereby the local Nusselt number distribution is closely associated with the strength of the wake-boundary layer interaction and the entrainment of fluid from the boundary layer into the wake. The factors determining the interaction and entrainment are the size, pattern/mode and frequency of shedding of the wake vortex.

Spectral analysis of the cylinder lift coefficient revealed broadening of lock-in regime with increasing forcing amplitude. The analysis also revealed a distinct spectrum of cylinder lift coefficient in the unlock-in regime. Nonlinear coupling of the cylinder vortex shedding with the forcing current injection can account for distinct spectral

peaks beyond the lock-in regime.

The analysis of the pressure drop indicates that the employment of current injection as turbuliser does not significantly alter the hydraulic losses due to the presence of the cylinder. This yields an efficiency index ranging between 97% and 191%.

In the next chapter, the capacity for electrically generated vortices alone to enhance heat transfer in quasi-2-D MHD duct flows will be investigated.

Chapter 6

Convective heat transfer enhancement via electrically driven vortices

This chapter considers current injection from a point electrode as the sole source of vorticity, apart from the friction due to the presence of the lateral walls. The magnetic field strength, Reynolds number, electrode position, electric current injection amplitude, pulse width, frequency and its profile are systematically varied to explore their influences on the convective heat transport phenomenon. First, the thermal performance of a current injection vortex promoter without a cylinder is compared to heat transfer data for the cases with a cylinder from Chapter 5. Analysis of the trajectory and decay of these vortices is conducted to further elucidate their relationships to the observed thermal enhancement.

This is followed by analysis of heat transfer enhancement for current injection parameters that are beyond the scope of the previous chapter. Computations are made over a wider range of Reynolds numbers and electrode transverse positions. Furthermore, the current injection profile is varied to investigate whether the efficiency index may be further increased. Finally, the overall efficiency and power enhancement of the current vortex promoter across all cases are analysed. These results will combine to reveal that the vortices generated by current injection alone generally induce a greater thermal-hydraulic performance with a significantly smaller additional pressure loss than configurations featuring a physical obstacle.

Various results in this chapter are currently under considerations for publication in *Numer. Heat Tr. A-Appl.* (Hamid *et al.* 2016b).

6.1 Problem setup

The flow geometry in this investigation is similar to that presented in Figure 5.1, except that the cylinder is now removed from the duct. In the physical realization of the current injection system, the electrode is mounted flush to one of the out-of-plane walls. The parameter range covers Hartmann numbers between 200 and 5000, Reynolds numbers between 200 and 4000, current amplitudes between 12 and 60, current frequencies between 0.5 and 10, pulse widths between 0.05 and 0.5, electrode transverse position between 0.4 and 1, and injection profile of range ± 5 . The current amplitude and frequency are normalised respectively by $aU_0\sqrt{\rho\nu\sigma}$ and U_0/L , while the pulse width and injection profile are both normalised by the signal period T .

6.2 Grid resolution study

The optimum fineness of the mesh required for the current problems was evaluated by conducting a grid independence study whereby the element polynomial degree was varied from 4 to 10, while keeping the macro element distribution unchanged. The grid consists of four regions: two regions near the transverse walls, a region centered at the electrode location and a core region. Smaller cells were distributed near the walls to resolve the aforementioned expected high gradients in MHD flows (Poth erat *et al.* 2002) and in the vicinity of the electrode, extending towards domain boundary in the transverse and streamwise directions, while the grid in the core sparsely but uniformly distributed (as shown in Figure 6.1). Convergence is assessed using quantities as in § 5.6, i.e. St , C_D , \mathcal{L}^2 and Nu .

Results, presented in Table 6.1, reveal that a mesh with $N_p = 8$ has a numerical convergence that is better than 0.1%, and thus was chosen for the analysis to follow in this chapter.

6.3 Results

6.3.1 Base cases

In this section, both Nusselt number and pressure drop are normalised by reference quantities, i.e. $HR^* = Nu/Nu_0^*$ and $PR^* = \Delta p/\Delta p_0^*$, respectively, where Nu_0^* and Δp_0^* are the time-averaged Nusselt number and pressure drop of an empty duct in the absence of current injection. Figure 6.2 shows the typical vorticity contour plots of the base flows

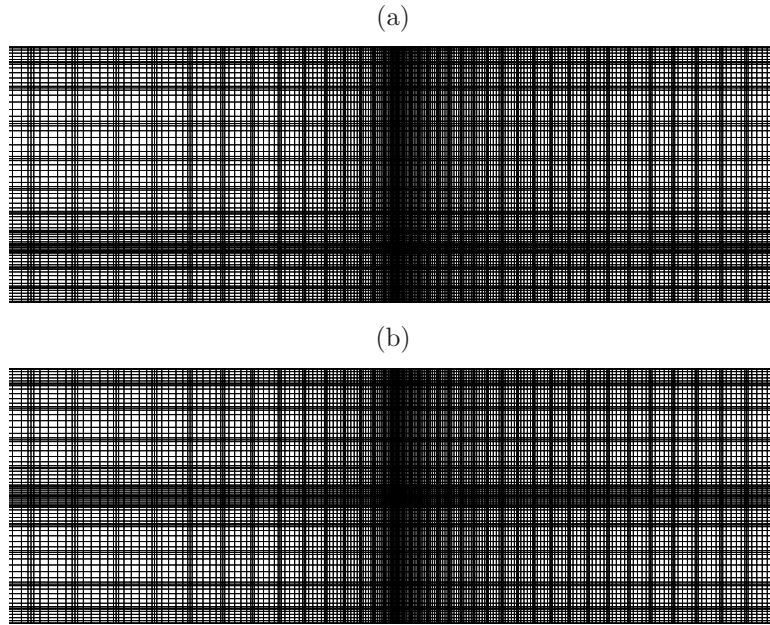


FIGURE 6.1: Close-up of the spectrally discretised domain using an 8th order polynomial shape function. The mesh in the vicinity of the electrode is shown ($\approx 20\%$ of the full-size domain) for (a) $l_y = 0.4$ and (b) $l_y = 1$. The full mesh extends $3.2L$ upstream and $8L$ downstream.

N_p	ε_{St}	ε_{C_D}	$\varepsilon_{\mathcal{L}^2}$	ε_{Nu}
4	0.3813	6.6498	0.4100	0.4072
5	0.1259	0.4469	0.0562	0.1220
6	0.0495	0.1388	0.0232	0.1185
7	0.0193	0.4423	0.0338	0.2748
8	0.0193	0.0971	0.0200	0.0337
9	0.0443	0.2343	0.0192	0.0698

TABLE 6.1: Grid independence study at $H = 500$, $Re_L = 1500$, $l_y = 0.6$, $I = 24$, $\omega_f = 5$ and $\tau/T = 0.25$. A polynomial degree of $N_p = 8$ was chosen for the simulations reported in this chapter.

at different friction parameter values. It is noted from this figure that the flow exhibits a uniform velocity profile (zero vorticity) in the core with boundary layers that become progressively thinner with increasing friction parameter. The velocity drops sharply towards the wall in order to satisfy the kinematic no-slip boundary condition. This leads to a steeper velocity gradient within the boundary layers that in turn generates a thinner thermal boundary layer, and thus a higher Nusselt number is produced (as shown in Figure 6.3). Furthermore, the results also show that as the friction parameter increases, the Nusselt number increases until a near saturation is reached for the heat

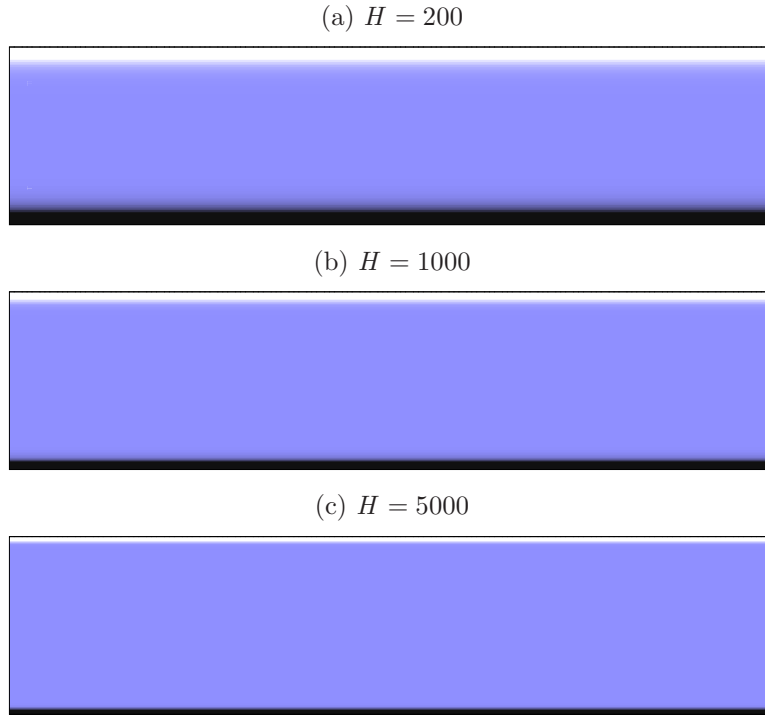


FIGURE 6.2: Instantaneous vorticity contour plots for $Re_L = 1500$ and (a) $H = 200$, (b) $H = 1000$ and (c) $H = 5000$. Contour levels ranges between -2 and 2 , with light and dark contours represent positive and negative vorticity, respectively.

transfer, for which the magnetic field has a minimum effect on the local distribution of Nusselt number. This observation is consistent with the experimental findings of Sukoriansky *et al.* (1989) for a non-conducting duct and a constant Reynolds number, and is likely due to the nature of the velocity profile near the boundary. In the limit of infinite friction parameter, the velocity asymptotically approaches a uniform profile. Thus, the growth of thermal boundary layer is almost uninfluenced by the variation in friction parameter.

Furthermore, the Hartmann damping results in an appreciable increase in pressure drop, as depicted in Figure 6.3. It is also found that the pressure drop agreed well with the quasi-two-dimensional solution for an empty duct pressure drop, which is given by $\Delta p_0^*/L_w = H/Re_L$ (Cassells *et al.* 2016).

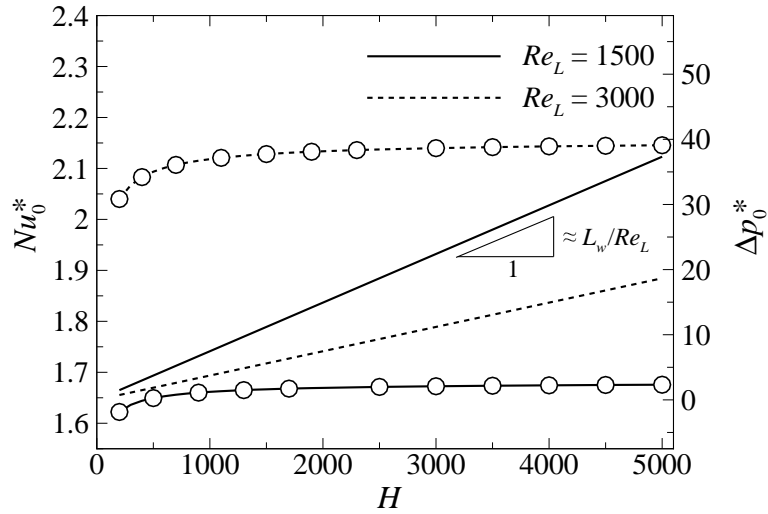


FIGURE 6.3: Primary vertical axis) Local Nusselt number and (secondary vertical axis) pressure drop of base flows plotted against friction parameter H for Reynolds number $Re_L = 1500$ and 3000. Lines with (without) symbols represent local Nusselt number (pressure drop).

6.3.2 Comparisons with the obstructed duct flow cases

6.3.2.1 Thermal performance

In this section, the thermal performance of current injection vortex promotion with and without a cylinder in a duct is compared. The results of heat transfer enhancement ratio HR^* for cases when a cylinder is present are obtained from Chapter 5. To facilitate a direct comparison, these results are renormalised with respect to the base flows in the absence of both current injection and cylinder vortex promoters (given the symbol Nu_0^*), hence the label asterisk. In general, the overall trend of heat transfer is independent of whether the cylinder is present or not, as can be seen in Figures. 6.4, 6.7 and 6.9. Hence, the present chapter will discuss only briefly the dependencies of current injection parameters on the enhancement of heat transfer presented in these figures. The reader is referred to Chapter 5 for further discussions.

The dependencies of the current injection frequency and amplitude on the heat transfer enhancement are presented in Figure 6.4. The heat transfer enhancement ratio HR^* exhibits a non-monotonic relation with forcing frequency. This trend is attributed to the competition between the size and the separation distance of the shed vortices. When the forcing frequency is low, the vorticity supply to each shed vortex is large. The vorticity rolls up to form a large vortex structure in the wake, which then

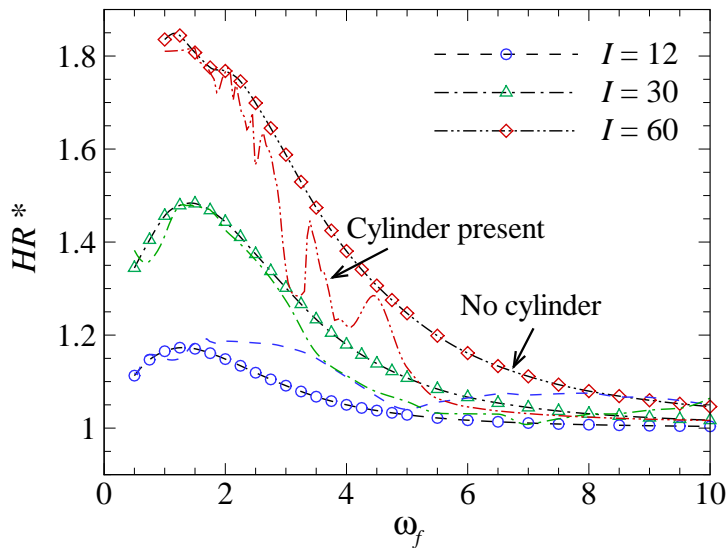


FIGURE 6.4: Time-averaged heat transfer enhancement plotted against forcing frequency ω_f at non-dimensional current amplitudes I as indicated for $H = 500$, $Re_L = 1500$ and $\tau/T = 0.25$. Lines with (without) symbols represent cases without (with) a cylinder in the duct.

interacts efficiently with the heated wall thermal boundary layer. Thermal plumes rise due to the entrainment of heat within the boundary layer by the counter-rotating vortices, reaching the cold wall and rolling up in both sides of the streamwise direction to generate mushroom-like plumes (as can be seen in Figure 6.5(b)). The formation of these structures leads to a thermal boundary layer thinning, and thus to an effective transverse heat transfer. Recall that the diffuse nature of the thermal structures relative to the vorticity structures is due to the small Prandtl number, $Pr = 0.022$.

However, when the forcing frequency is either too low ($\omega_f \lesssim 1.5$) or too high ($\omega_f \gtrsim 6$), the duct thermal performance is poor. In the former condition, the wake loses its coherence as a result of interactions with the Shercliff layers, as depicted in Figure 6.5(a). There is no entrainment of hot fluid into the bulk flow due to the large separation distance between successive counter-rotating vortices, and thus leads to a poor transport of heat. The latter condition results in a wake exhibiting a row of small counter-rotating vortices align to the duct centreline, (refer Figure 6.5(c)). The thermal plumes no longer reach the top wall due to the weak entrainment generated by the small and weak vortices, which also results to a low convective heat transfer.

It is also noted that in the higher current amplitude regime ($I \gtrsim 30$), the empty duct

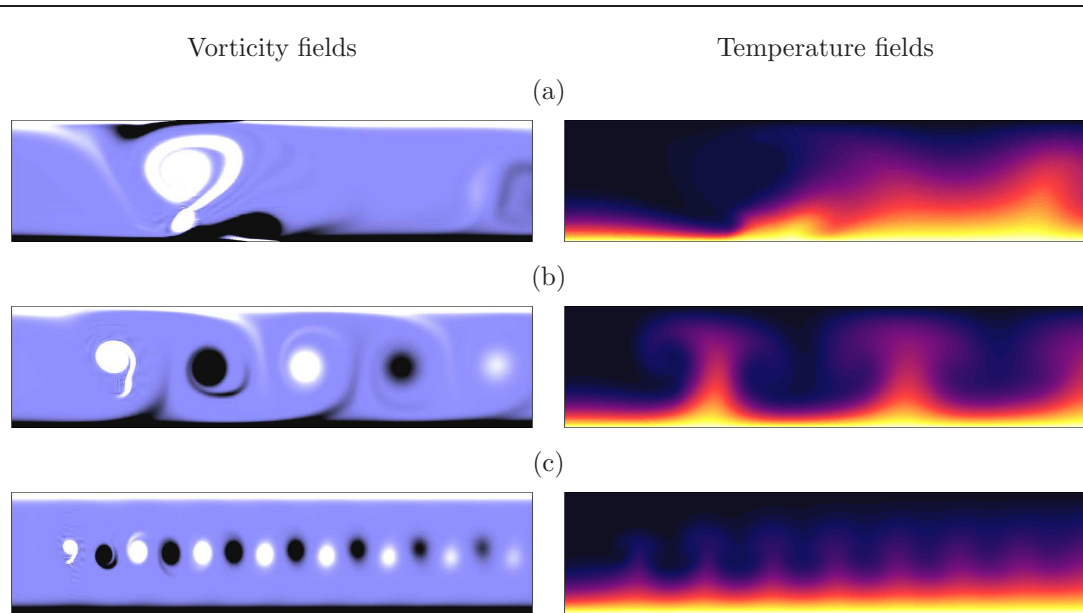


FIGURE 6.5: Plot of vorticity (left) and temperature (right) contours for $H = 500$, $Re_L = 1500$, $I = 30$, $\tau/T = 0.25$ and (a) $\omega_f = 0.5$, (b) $\omega_f = 2$ and (c) $\omega_f = 6$. Vorticity fields: contour levels are as per Figure 6.2. Temperature fields: contour levels ranges between θ_0 and θ_w , with dark and light contours represent cold and hot fluid, respectively.

with current injection alone generally achieves greater thermal performance relative to the duct with a cylinder, while the opposite is true in the lower current amplitude regime. The discussion to follow explains the latter observation. Inspection of vorticity contours for both cases (as shown in Figure 6.6) revealed an apparent difference in the trajectory of the wake vortices. The electrically augmented wake (with a cylinder) tends to be wider than the electrically generated wake (without a cylinder). The wider wake generally leads to a stronger vortex-boundary layer interaction, which results in a thinner thermal boundary layer and thus superior heat transfer.

However, for a high forcing amplitude, although the wake-boundary layer interaction appears to be stronger in the obstructed duct due to the aforementioned wider wake, the enhancement in heat transfer in the unobstructed duct is greater. This is attributed to the fact that the vortices that are generated solely by a current injection are more intense than the vortices generated by both a current injection and a cylinder, which is likely due to the counteractions between the electrically driven vortices and the vortices generated by the cylinder during their formation. The more intense pair of counter-rotating vortices entrains larger amount of hot fluid in the vicinity of the heated wall into the bulk flow, resulting in taller plume structures in the thermal field (as visualised

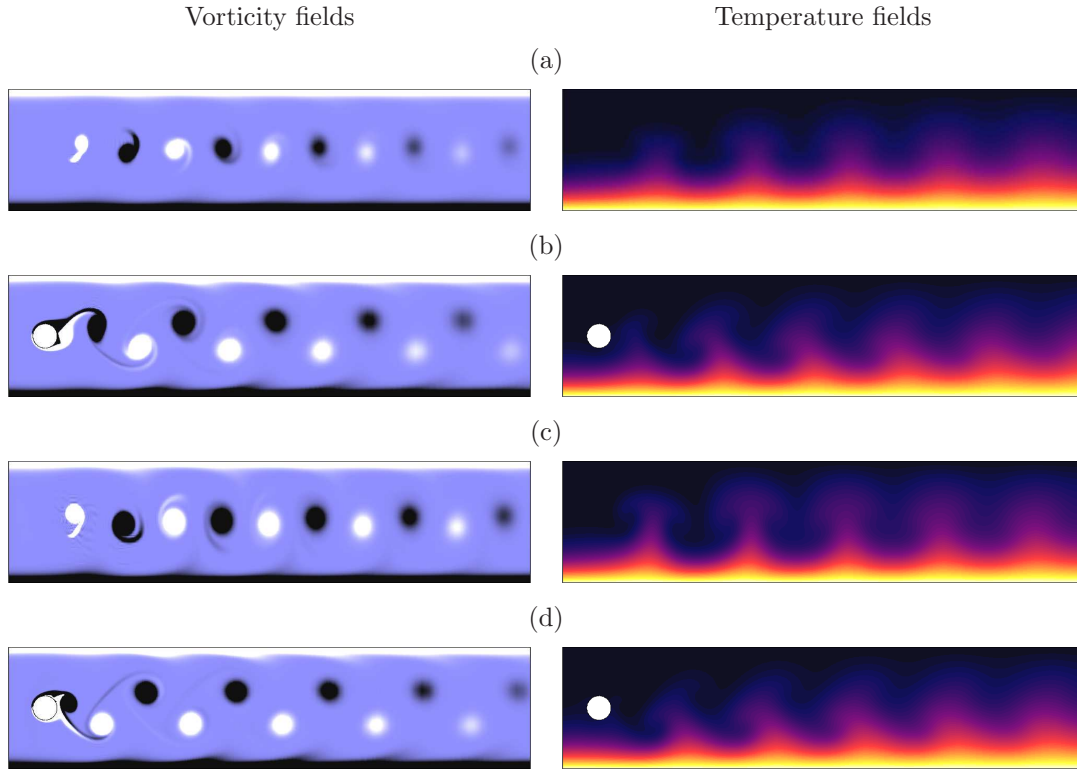


FIGURE 6.6: Plot of vorticity (left) and temperature (right) contours for $H = 500$, $Re_L = 1500$, $\omega_f = 4$, $\tau/T = 0.25$ and (a-b) $I = 12$ and (c-d) $I = 30$. In (b) and (d), a circular cylinder with a diameter of 20% of the duct width is placed at the duct centerline. Vorticity fields: contour levels are as per Figure 6.2. Temperature fields: contour levels are as per Figure 6.5.

in Figure 6.6(c) relative to Figure 6.6(d)) and thus an improved heat transfer. Further discussions concerning the wake vortices dynamics and their decay are presented in Section 6.3.2.2.

Figure 6.7 presents the variation of HR^* with current injection pulse width, which are varied between 0.05 and 0.5 for $\omega_f = 1.75$ and $\omega_f = 3.5$, while other parameters are kept constant. In general, the enhancement in heat transfer progressively increases for increasing current injection pulse width. The reason for this is that for a given forcing frequency, longer injection pulse width means that the vortex rolls up with greater number of rotations as they advect downstream, as can be seen in Figure 6.8. This leads to a larger vortical structure in the wake and thus leading to an improved heat transport enhancement.

Figure 6.7 also reveals that, when the pulse width is short, the duct with a cylinder outperforms the empty duct. In the absence of the cylinder, shorter current pulses

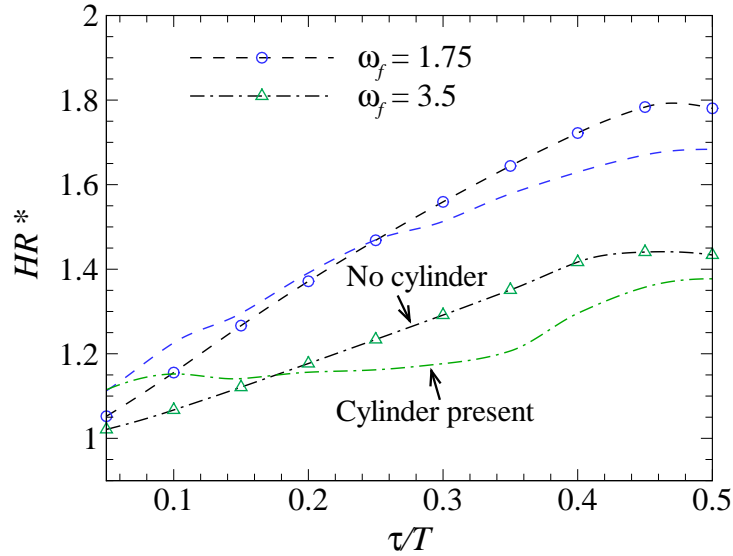


FIGURE 6.7: Time-averaged heat transfer enhancement plotted against current injection pulse width τ/T at frequencies ω_f as indicated for $H = 500$, $Re_L = 1500$ and $I = 30$. Lines with symbols are the no-cylinder cases, lines with no symbols are the cases with the cylinder present.

generate relatively smaller vortices (the sizes are evidenced by comparing Figure 6.8(a) and (c)). When the cylinder is present, the wake is wider and the generated vortices are larger due to the reinforcement by shear layers separating from the cylinder, as can be seen in Figure 6.8(b). However, the vortices are weaker (e.g. the vortex is approximately 50% weaker than the corresponding case without a cylinder at $x/d \approx 3$). Hence, in the regime of shorter pulse width, the strength of wake-boundary layer interaction plays a greater role in the enhancement of heat transfer than the vortex intensity, due to the fact that the entrainment mechanism is rather weak for small vortices. The presence of the cylinder, however, becomes less beneficial when the current pulses are longer due to the aforementioned detrimental interaction between the cylinder and the electrically driven vortices. In this case, the wake vortices are smaller than the empty duct case, as shown in Figure 6.8(d) in comparison with Figure 6.8(c).

The effect of friction parameter and Reynolds number on the heat transfer enhancement ratio is demonstrated in Figure 6.9. The figure shows a non-monotonic relation between the enhancement of heat transfer and the friction parameter due to the aforementioned competing effect between inertia and Hartmann damping. In the low- H regime, the increasing intensity of the imposed magnetic field results in stronger

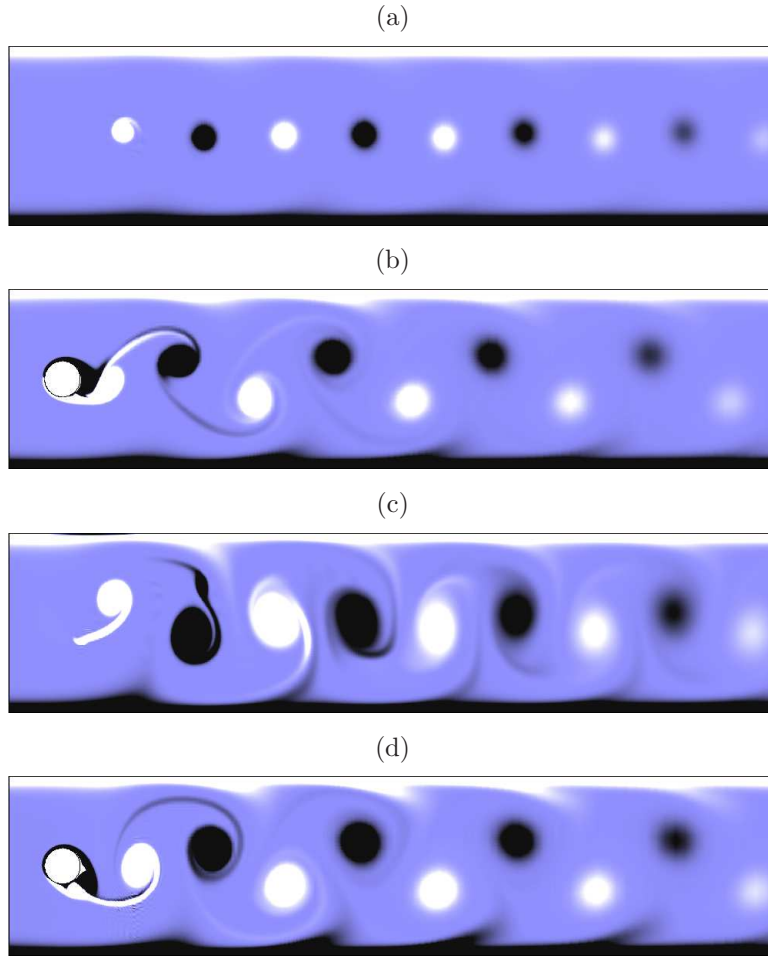


FIGURE 6.8: Instantaneous vorticity contour plots for $H = 500$, $Re_L = 1500$, $I = 30$, $\omega_f = 3.5$ and (a-b) $\tau/T = 0.1$ and (c-d) $\tau/T = 0.4$. In (b) and (d), a circular cylinder with a diameter of 20% of the duct width is placed at the duct centerline. Contour levels are as per Figure 6.2.

electrically driven vortices. Furthermore, the Hartmann damping is relatively low, permitting these coherent vortices to advect to a greater downstream distance while interacting with the thermal boundary layer (as shown in Figure 6.10(a)), thus leading to an increased heat transfer enhancement.

It is interesting to note that, in this regime, the presence of a cylinder improves the heat transfer characteristic of the duct, particularly for the higher Reynolds number case. This is due to mutual interaction of the current driving force and the inertia that leads to a substantial loss of wake coherence, visible in both vorticity and temperature field plots in Figure 6.10(b). The bulk vortices interact with the Shercliff layers, causing its destabilization and formation of secondary vortices that results in a consistent en-

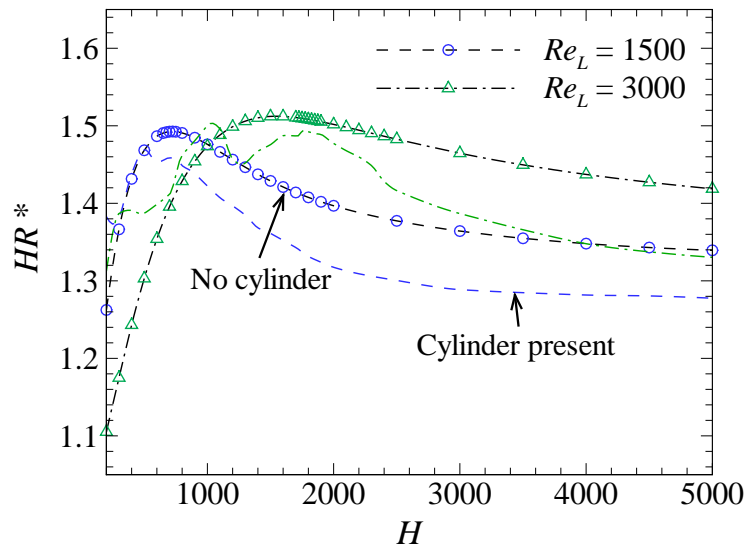


FIGURE 6.9: Time-averaged heat transfer enhancement plotted against friction parameter H at Reynolds numbers Re_L as indicated for $I = 30$, $\omega_f = 1.75$ and $\tau/T = 0.25$. Lines with symbols are the no-cylinder cases, lines with no symbols are the cases with the cylinder present.

hancement in the local Nusselt number along the downstream of the duct (as evidenced in Figure 6.11).

In the high- H regime, however, the action of Hartmann damping is more prominent than the driving Lorentz force, leading to a strong vortex only in the vicinity of the injection point due to the magnetic field-imposed current interaction, and decays abruptly after its formation. As a result, a substantial enhancement in heat transfer which is localised only in this region was observed, as indicated by a strong peak in the local Nusselt number plot in Figure 6.11. The peak is followed by a rapid decline further downstream due to the damping of vortices.

Furthermore, it was found that, in the high- H regime, the enhancement in heat transfer is higher for the empty duct than the obstructed duct. Inspection of local Nusselt number shown in Figure 6.11 reveals a consistently higher local Nu in the downstream of the heated wall for the empty duct. This observation is again attributed to the generation of stronger vortices in the absence of the cylinder, leading to a stronger thermal layer entrainment towards the opposite relatively colder wall and thus better heat transfer. Figure 6.11 also reveals a higher local Nusselt number in the near-wake region of the obstructed duct, which is due to the high velocity jet flow through the

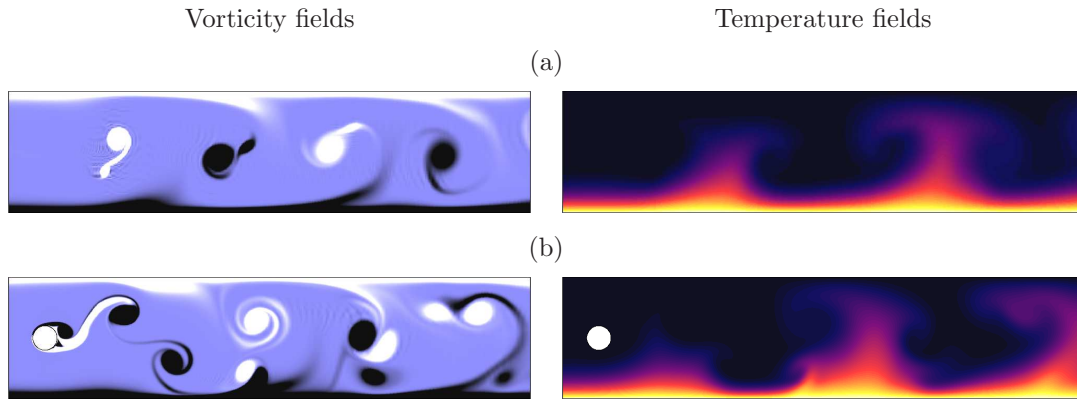


FIGURE 6.10: Instantaneous vorticity and temperature contour plots for $H = 400$, $Re_L = 3000$, $I = 30$, $\omega_f = 1.75$ and $\tau/T = 0.25$ in the (a) absence and (b) presence of a cylinder. Vorticity fields: contour levels are as per Figure 6.2. Temperature fields: contour levels are as per Figure 6.5.

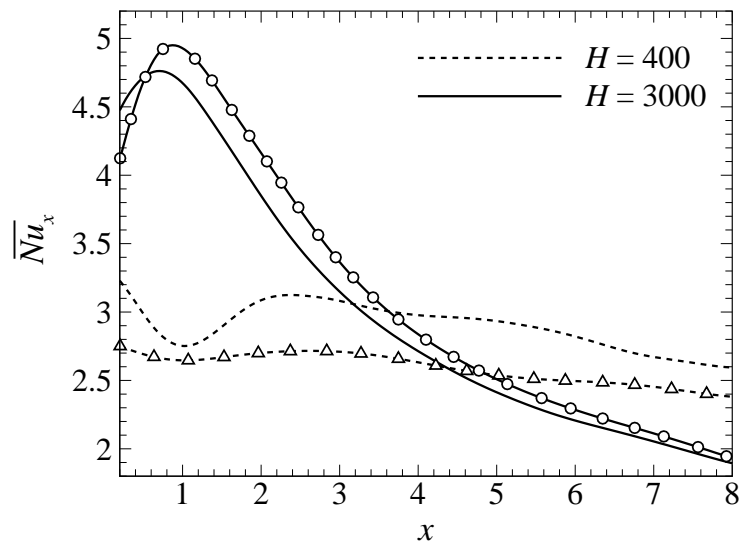


FIGURE 6.11: Time-averaged local Nusselt number along the downstream of the heated wall for $Re_L = 3000$, $I = 30$, $\omega_f = 1.75$, $\tau/T = 0.25$ and $H = 400$ (dashed lines) and 3000 (solid lines). Lines with symbols are the no-cylinder cases, lines with no symbols are the cases with the cylinder present. Symbols are skipped in order to make lines more visible.

gap between the cylinder and the heated wall.

6.3.2.2 Vortex trajectory and decay

This section is dedicated to the quantitative comparison of vortex trajectories and decay behaviours for both obstructed and unobstructed ducts. As outlined in § 4.4.2, vortex trajectories through the computed domain have been recorded by tracking the locations of local maxima and minima in the vorticity. From these trajectories, lateral spacing (h) and longitudinal spacing (l) of the vortices have been extracted and normalised by the cylinder diameter.

For this particular analysis, the vortex trajectory and decay of cases where the vorticity contour plots are presented in Figure 6.6 are compared. The results for lateral spacings are shown in Figure 6.12. The wakes of these cases exhibit a symmetric pattern, and thus the trajectories of both positive and negative vorticity show a symmetric profile with respect to the wake centreline. It is observed from Figure 6.12 that current injection significantly widens the cylinder wake (by more than 100% through the downstream of the computed domain). However, in the absence of the cylinder, vortices of both signs that are generated by the current injection organize into a nearly single row which coincide with the duct centreline, with lateral spacings of less than half of the cylinder diameter. It is interesting to note that the negative (positive) vortices are formed in the upper (lower) half of the wake, but their trajectories intersect at a certain distance along the wake and their position with respect to the duct centreline is inverted, which explains the spacing of zero at approximately $x/d = 5.8$ downstream of the electrode. Beyond the intersection region, vortices of both sign are deflected away equally from the wake axis. Furthermore, it is also observed from Figure 6.12 that higher current amplitude results in the vortices being cast further away from the wake centreline, and that the rate of widening is higher for the unobstructed cases. The reason for the latter observation is that the tandem arrangement of the opposite sign vortices induces a significant transverse velocity component between the vortices, which then feeds energy into the vortices and consequently causes them to expand. Larger current amplitude induces stronger entrainment in the transverse direction, thus explaining the observed wider wake.

The current injection also significantly alters the longitudinal spacing of the vortex street, as shown in Figure 6.13. Here, the longitudinal spacing is measured in the stable

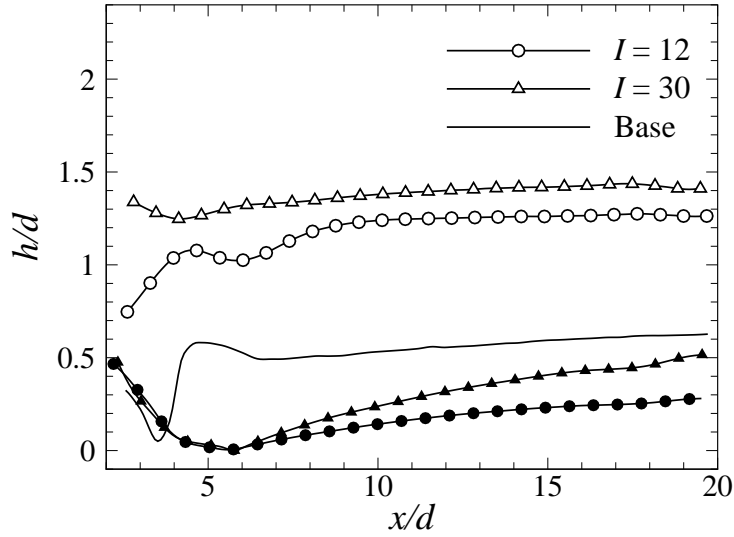


FIGURE 6.12: Spatial variation of vortex lateral spacing for $H = 500$, $Re_L = 1500$, $\omega_f = 4$, $\tau/T = 0.25$ and current amplitudes as indicated. Open and solid symbols represent duct cases with and without a cylinder, respectively. Line without symbols represent duct cases with a cylinder in the absence of current injection.

wake region in which the longitudinal spacing is ideally constant (Schaefer & Eskinazi 1959), i.e. $10 \lesssim x/d \lesssim 16$. Upstream of this region is the formation region, where there is no clear trend in the longitudinal spacings.

In the presence of the current injection, the longitudinal spacing is approximately 17% higher than those with a cylinder only. This is attributed to the fact that the longitudinal spacing is proportional to the wake advection velocity and inversely proportional to the shedding frequency, i.e. $l/d = U_\xi/(fd)$ (Roshko 1954a). The analysis of vortex spatio-temporal evolution revealed that the wake advection velocity is almost identical across the investigated cases, which ranges between 0.98 and 1 relative to peak inlet velocity. This suggest that the longitudinal spacing is strongly influenced by the shedding frequency. It has been observed in the previous chapter that the shedding frequency of an electrically augmented cylinder wake vortices is governed by the electrical forcing frequency. It follows then that for a given forcing frequency, the longitudinal length is constant, which is in agreement with the results shown in Figure 6.13. Spectral analysis of the cylinder lift coefficient reveals a natural cylinder vortex shedding frequency (in the absence of current forcing) for $H = 500$ and $Re_L = 1500$ of $f_0 \approx 0.742$. This frequency is 16.6% higher than the forcing shedding frequency (i.e. $f_f = \omega_f/2\pi = 0.637$),

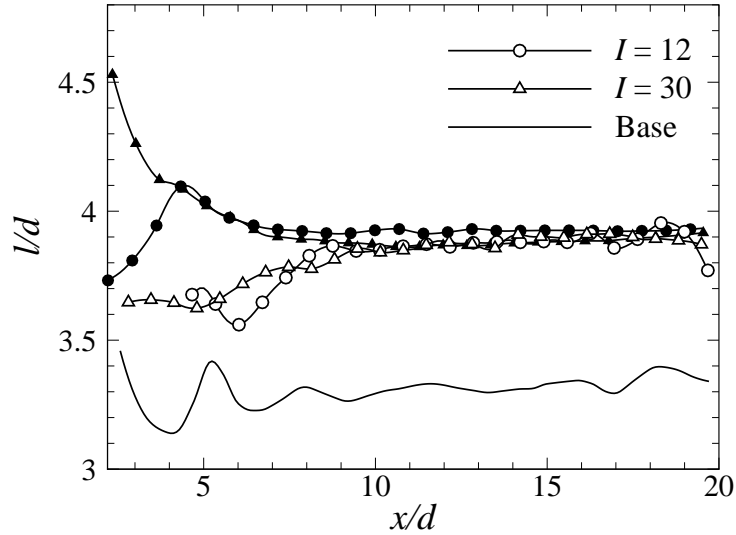


FIGURE 6.13: Spatial variation of vortex longitudinal spacing for $H = 500$, $Re_L = 1500$, $\omega_f = 4$, $\tau/T = 0.25$ and current amplitudes as indicated. Description for symbols and lines are as per Figure 6.12.

which expectedly matches the aforementioned percentage increase in the longitudinal spacing due to the forcing current.

A further analysis on the strength and decay of the shed vortices are performed through the measured local peak vorticity and the results are shown in Figure 6.14. It is observed that the current injection significantly enhances the strength of the cylinder wake vortices, where the peak vorticity increases averagely (calculated along the downstream of the cylinder or electrode) by 90% and 160% relative to the base case, respectively, for $I = 12$ and $I = 30$. It is also observed that for a higher current amplitude ($I = 30$), the presence of a cylinder tends to inhibit the growth of the shed vortices likely due to the aforementioned counteractions of the vorticity generation mechanisms. The peak vorticity in the vortices generated solely by the current injection is on average approximately 30% stronger than in the corresponding obstructed wake flow. However, for $I = 12$, the average strength of shed vortices in the presence of a cylinder is approximately 20% higher relative to the unobstructed case.

It is found that the vortices exhibit very close to an exponential decay, and the rate of decay is similar for all cases (as shown by the almost linear and consistent gradient in the semilog plot of Figure 6.14). This behaviour is attributed to the strong Hartmann damping in the flow. For $\beta = 0.2$ and $Re_L = 1500$, the estimated critical friction

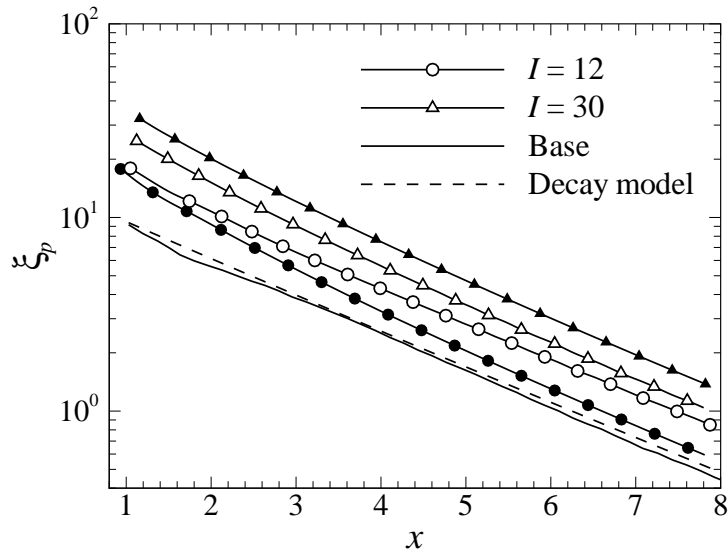


FIGURE 6.14: Spatial evolution of peak vorticity for $H = 500$, $Re_L = 1500$, $\omega_f = 4$, $\tau/T = 0.25$ and current amplitudes as indicated. Dashed line represents peak vorticity predicted using the vortex decay model developed in Chapter 4. Symbols and lines are as per Figure 6.12.

parameter (a friction parameter at which the decay is dominated by the Hartmann damping only) is $H_{cr} = Re_L^{0.974} / (0.90(\beta L + 2\beta(0.075\beta + 0.01)Re_L(1 - \beta) - (4.3\beta - 0.15))) \approx 120$ (see equation (4.40)). The friction parameter imposed to the flow ($H = 500$) is considerably higher than the critical value, which implies that the decay of vortices is governed by the Hartmann friction term and that the magnitude of the decay rate is constant for a given friction parameter and Reynolds number.

In the following sections, the analysis of various parameters on the enhancement of heat transfer are restricted to the case where the cylinder is absent, unless otherwise mentioned.

6.3.3 Reynolds number dependence

In this section, additional consideration is given to the dependence of Reynolds number on the heat transfer. The Reynolds number is varied between $Re_L = 200$ and 4000 for friction parameters of $H = 500$ and $H = 1000$. The resulting Nusselt number variation is plotted against the ratio of friction parameter to Reynolds number H/Re_L ; following Figure 4 of Sukoriansky *et al.* (1989), and is presented here in Figure 6.15.

The Nusselt number for cases with friction parameter being fixed exhibit a distinct

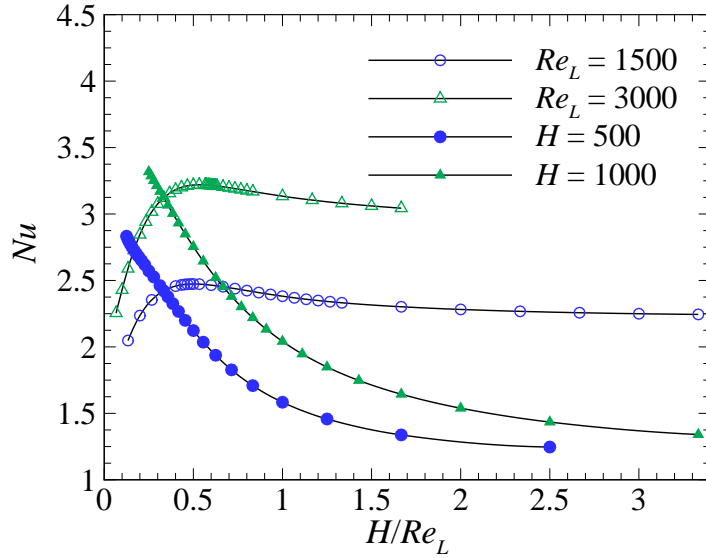


FIGURE 6.15: Variation of Nusselt number with respect to H/Re_L at Reynolds numbers and friction parameters as indicated for $I = 30$, $\omega_f = 1.75$ and $\tau/T = 0.25$. Open and solid symbols represent cases with a fixed Reynolds number and friction parameter, respectively.

trend compared to the cases of constant Reynolds number. In the former case, the Nusselt number increases monotonically with increasing Reynolds number due to the convectively dominated heat transport. The Nusselt number variation for the latter case is also plotted in Figure 6.15 for the sake of comparison (the HR^* data have already been presented in Figure 6.9). The Nusselt number for this case exhibit a similar trend to that of the heat transfer enhancement ratio, which is expected since the Nusselt number for the base case is almost uninfluenced by the friction parameter (as depicted in Figure 6.3). Interestingly, the heat transfer enhancement ratio for the cases with a constant friction parameter also exhibit a non-monotonic trend, as shown in Figure 6.16.

This observed trend may be explained as follows: although the Nusselt numbers for these cases are progressively increasing with an increased Reynolds number, the Nusselt number for the respective base cases are also following a similar trend (as indicated by the consistently increasing local downstream Nusselt number with increasing Reynolds number shown in Figure 6.17). This results in the normalised local Nusselt number variations as shown in Figure 6.18. Figure 6.16 shows that in the low- H/Re_L regime (a regime where $H/Re_L < (H/Re_L)_{cr}$, where $(H/Re_L)_{cr}$ is the critical value corresponding to the peak of HR^* for the respective constant Reynolds number or friction parameter

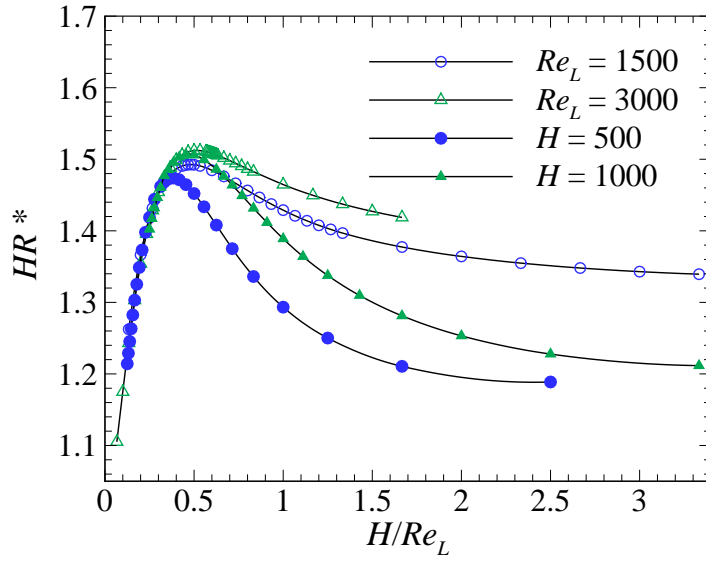


FIGURE 6.16: Time-averaged heat transfer enhancement ratio plotted against H/Re_L at Reynolds numbers and friction parameters as indicated for $I = 30$, $\omega_f = 1.75$ and $\tau/T = 0.25$. Symbols are as per Figure 6.15.

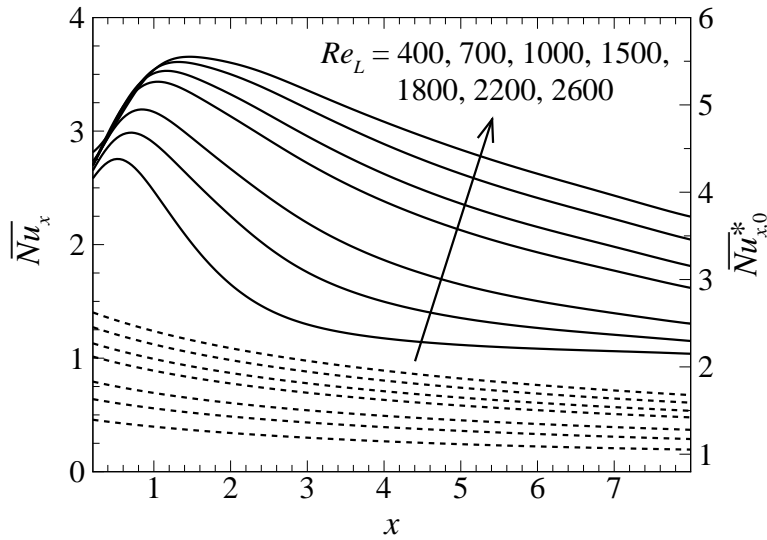


FIGURE 6.17: Local Nusselt number for (primary vertical axis, solid lines) cases with $H = 1000$, $I = 30$, $\omega_f = 1.75$ and $\tau/T = 0.25$ and (secondary vertical axis, dashed lines) the respective base cases. The Reynolds numbers are progressively increasing for lines from bottom to top as indicated, for both solid and dashed lines.

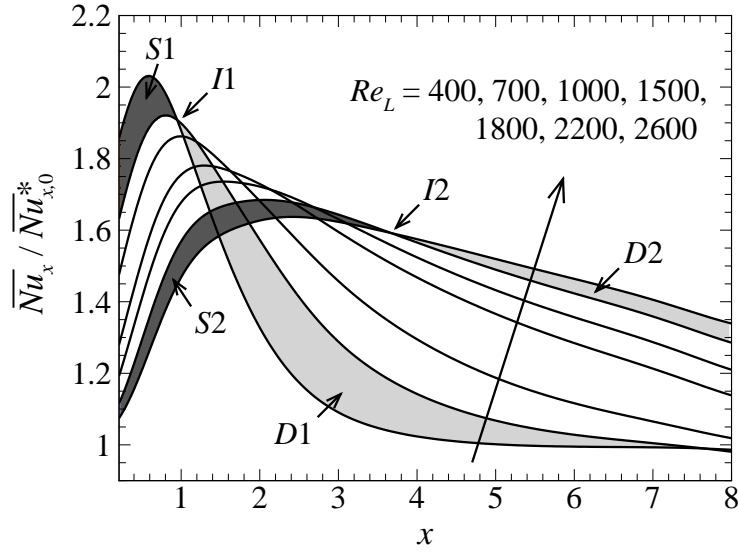


FIGURE 6.18: Normalised time-averaged local Nusselt number along the downstream of the heated wall for $H = 1000$, $I = 30$, $\omega_f = 1.75$ and $\tau/T = 0.25$. The dark (lighter) region correspond to a deficit (surplus) in heat transfer enhancement of a higher Reynolds number case relative to the lower one. $I1$ and $I2$ are intersection points of local Nusselt number lines at different Reynolds number.

lines), an increase in H/Re_L leads to an increase in the heat transfer enhancement ratio. This is due to the enhancement in the local Nusselt number in the region closer to the electrode (as indicated by region $S2$ in Figure 6.18) being greater than its diminution further downstream (as represented by region $D2$), which results in a net increase in HR^* . However, the opposite is true in the high- H/Re_L regime. This is due to the shifting of the intersection point towards the upstream with increasing H/Re_L (e.g. from points $I2$ to $I1$ as shown in Figure 6.18), resulting in a simultaneous shrinking and growing of the “surplus” $S1$ and “deficit” $D1$ regions, respectively, and leading to a net decrease in HR^* .

Unlike the cases with a fixed friction parameter, the base local Nusselt number for cases with a constant Reynolds number are almost independent of the friction parameter. Furthermore, the local Nusselt number for these cases follows a similar trend to that of the normalised local Nusselt number for a fixed friction parameter cases as presented in Figure 6.18, which also explains the non-monotonic behaviour of its heat transfer enhancement.

It is also interesting to note from Figure 6.15 that the HR^* nearly collapses in the

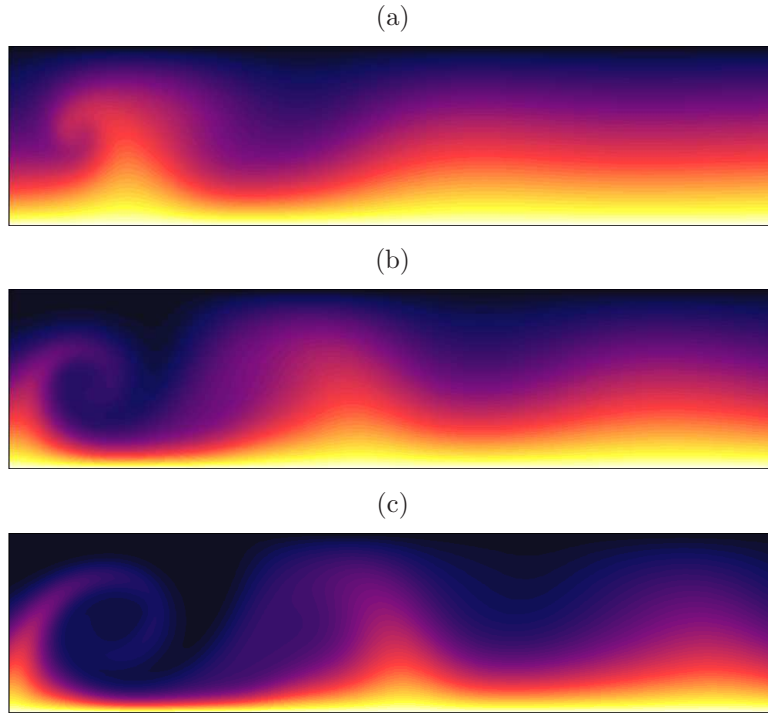


FIGURE 6.19: Instantaneous vorticity contour plots for $H/Re_L = 1.667$, $I = 30$, $\omega_f = 1.75$, $\tau/T = 0.25$ and (a) $Re_L = 300$, (b) $Re_L = 600$ and (c) $Re_L = 1500$. Contour levels are as per Figure 6.5.

low- H/Re_L regime, but not in the higher range of H/Re_L . This is despite the fact that, in the limit of high magnetic field strength and for a given H/Re_L , the resultant vortex pattern and strength are similar regardless of both the Reynolds number and the friction parameter (which is expected since the birth of the vortices and their subsequent decay are governed by the ratio of H/Re_L , as indicated by the respective forcing terms in equation (3.26)). In the high- H/Re_L regime, the magnetic damping effect on the bulk flow is relatively significant (i.e. the heat transport is conductively dominated), thus an increase in Reynolds number yields an appreciable thinning in the thermal boundary layer (as evidenced in Figure 6.19) and as a result an increase in the heat transfer enhancement ratio. In the low- H/Re_L regime, however, the flow is already convectively dominated and thus is less sensitive to Reynolds number variations (as shown by the almost constant thermal boundary layer thicknesses in Figure 6.20).

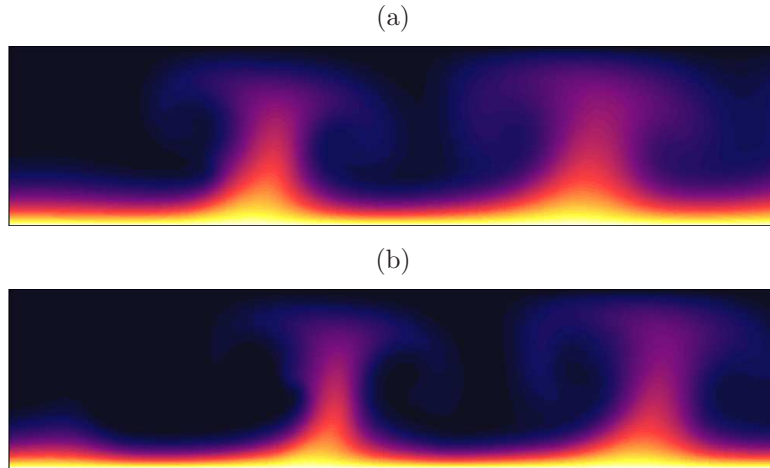


FIGURE 6.20: Instantaneous vorticity contour plots for $H/Re_L = 0.25$, $I = 30$, $\omega_f = 1.75$, $\tau/T = 0.25$ and (a) $Re_L = 2000$ and (b) $Re_L = 4000$. Contour levels are as per Figure 6.5.

6.3.4 Effects of the current injection profile and frequency on heat transfer

In this section, the effect of asymmetric current injection profile on the heat transfer enhancement ratio is investigated. The injection duty cycle is fixed (at $D = 2\tau/T = 0.5$), so that the total current power input is maintained regardless of the imposed current profile. A duty cycle of $D = 0.5$ means that the current injection is active for half of the period. The profile of the asymmetric current pulses are represented by the difference between the positive and negative signal pulse width, i.e. $\Delta\tau/T$, as depicted in Figure 6.21. A positive $\Delta\tau/T$ produces positive vorticity that has a longer pulse width relative to the negative vorticity and vice versa. In the limit of $\Delta\tau/T = \pm 0.5$, the current injection profile takes a square waveform, where only either positive or negative vorticity is produced. Furthermore, $\Delta\tau/T = 0$ represents a symmetric alternating current pulse waveform.

The heat transfer enhancement results are presented in Figure 6.22. In general, it was observed that, for a given injection frequency and duty cycle, the efficiency of the current injection vortex promoter can be further increased by injecting the current pulses asymmetrically; thus confirming the conjecture made in § 5.7.4. The results imply that the action of the counter-clockwise (positive) vortex tail in thinning the thermal boundary layer is more pronounced than the corresponding action of the clockwise vortex, and that the thermal efficiency can be further improved by injecting an asymmetric

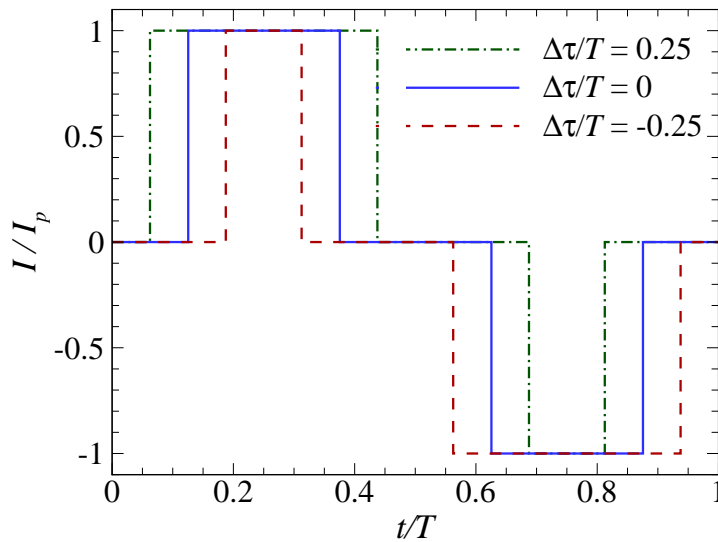


FIGURE 6.21: Electric current injection profiles, represented by an asymmetric modified square waveform with pulse width $\tau/T = 0.5$. The amplitude of current is normalised by its peak amplitude, I_p , and the time is normalised by signal period, T .

current pulse.

The strong positive vortex-boundary layer interaction can readily be seen in Figure 6.23(a) for a positive $\Delta\tau/T$ at a relatively high forcing frequency (e.g. $\omega_f = 3.5$), which results in a higher heat transfer enhancement ratio relative to the symmetric and negative $\Delta\tau/T$ current pulses. It is noted that the vortex pattern resulting from a negative $\Delta\tau/T$ is a flipped to that from the positive $\Delta\tau/T$. As such, the vorticity field of a negative/positive $\Delta\tau/T$ may be inferred from the respective opposite sign field.

The flipped vortex pattern yields an almost opposite trend in the local Nusselt number for both current injection polarities, as shown in Figure 6.24. Furthermore, the symmetric injection pulses produce alternating counter-rotating vortices that interact with the boundary layer in an almost consistent manner (the vorticity field is similar to the one presented in Figure 6.6(c)), which results in a nearly uniform enhancement in the local Nusselt number throughout the domain, which is also shown in Figure 6.24. However, at a low forcing frequency (e.g. $\omega_f = 0.5$), the enhancement in heat transfer is almost uninfluenced by the current injection profile, as indicated in Figure 6.22. This observation is attributed to the fact that at a low forcing frequency, the size of the resulting vortices are relatively large (as depicted in Figs. 6.23(b) and 6.5(a) for asymmetric and symmetric current injection, respectively), thus the integral strength

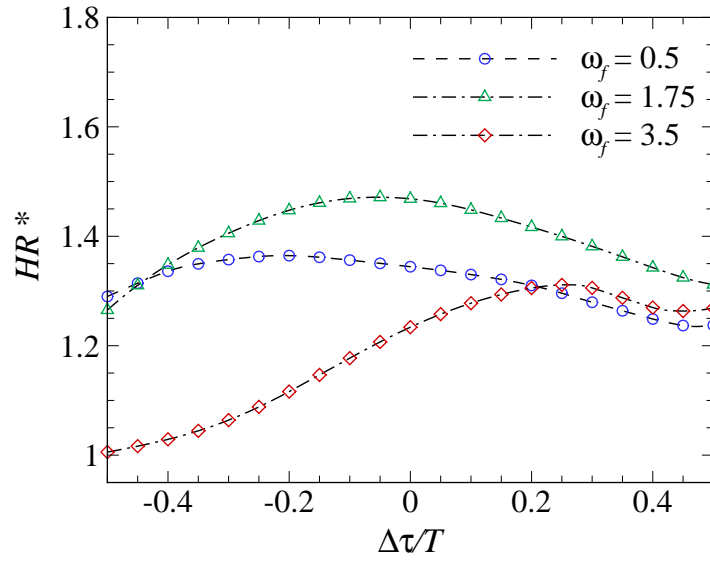


FIGURE 6.22: Time-averaged heat transfer enhancement ratio plotted against pulse width difference at frequencies as indicated for $H = 500$, $Re_L = 1500$, $I = 30$, $\tau/T = 0.5$ and $l_y = 1$.

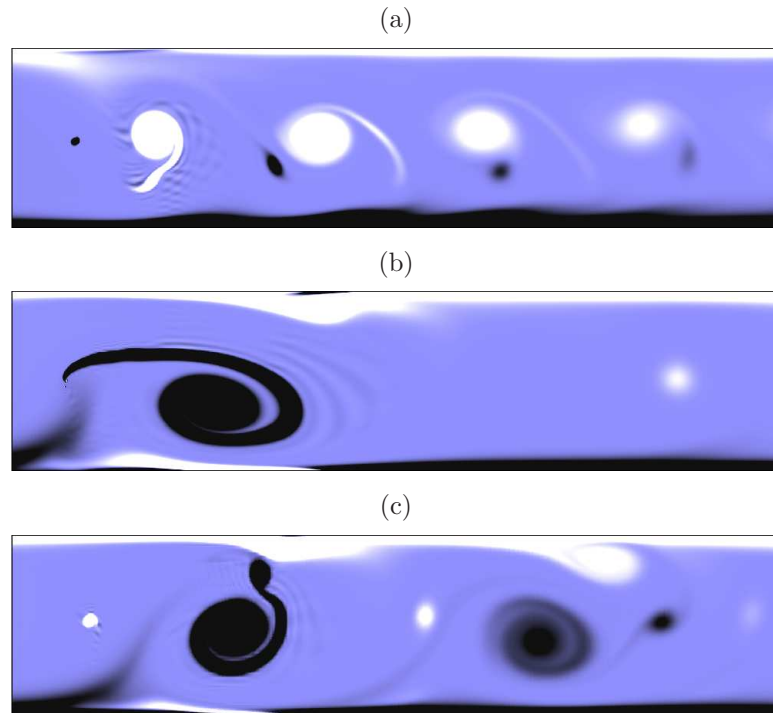


FIGURE 6.23: Instantaneous vorticity for $H = 500$, $Re_L = 1500$, $I = 30$, $\tau/T = 0.25$ and (a) $\omega_f = 3.5$ and $\Delta\tau/T = 0.45$, (b) $\omega_f = 0.5$ and $\Delta\tau/T = -0.45$ and (c) $\omega_f = 1.75$ and $\Delta\tau/T = -0.45$. Contour levels are as per Figure 6.2.

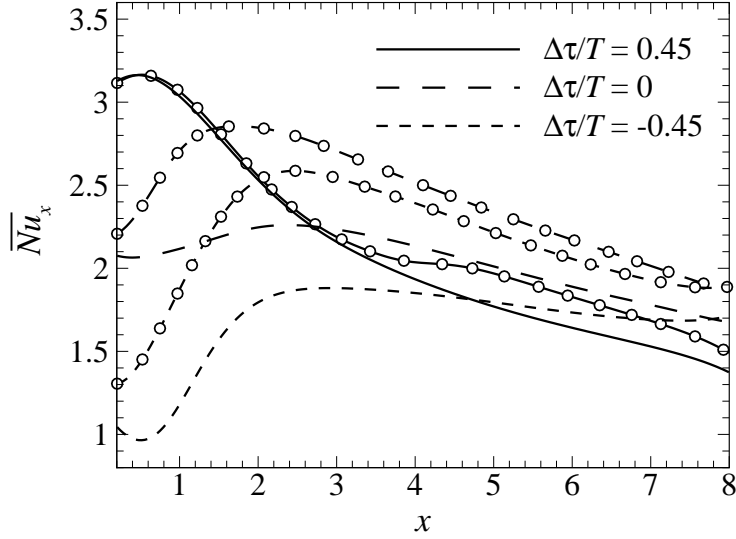


FIGURE 6.24: Time-averaged local Nusselt number along the downstream of the heated wall for $H = 500$, $Re_L = 1500$, $I = 30$, $\tau/T = 0.25$ and $\omega_f = 1.75$ (with symbols) and $\omega_f = 3.5$ (without symbols). Solid, dashed and dotted lines represent $\Delta\tau/T = 0.45$, 0 and -0.45 , respectively. Symbols are skipped in order to make lines more visible.

of their interaction with the thermal boundary layer is almost constant regardless of the injection profile.

It is also interesting to note that within the range of optimum frequencies (i.e. $1 \lesssim \omega_f \lesssim 2$, as indicated in Figure 6.4), HR^* reaches its maximum value when the forcing current is symmetric. This is due to the aforementioned entrainment of a significant portion of the hot fluid from the heated wall by the pairs of counter-rotating vortices (as shown by the temperature plot in Figure 6.5(b)). This action of vortex pairs is, however, less visible in the asymmetric cases due to the size of the opposite sign vortices becoming smaller with increasing magnitude of $\Delta\tau/T$, as can be seen in Figs. 6.23(c). Despite the different vortex pattern compared to other frequency cases, the trend of local Nusselt number is similar for all $\Delta\tau/T$, as depicted in Figure 6.24. However, the local Nusselt number for a case within the optimum frequency range is consistently higher than those outside this range, suggesting that the injection profile has an insignificant role in the enhancement of heat transfer. This observation to some extent contradicts the aforementioned conjecture, although it still holds for cases with a frequency beyond the optimum range.

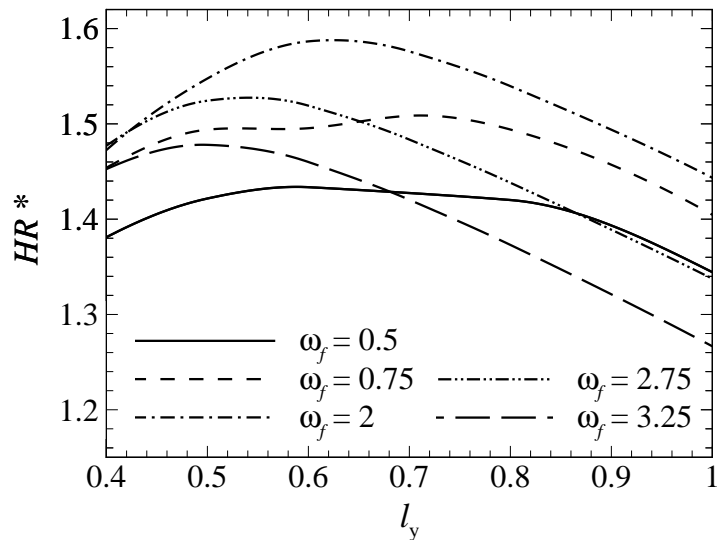


FIGURE 6.25: Time-averaged heat transfer enhancement ratio plotted against vertical distance l_y of the electrode from the heated wall at frequencies as indicated for $H = 500$, $Re_L = 1500$, $I = 30$ and $\tau/T = 0.25$.

6.3.5 Effects of the electrode transverse position on heat transfer

This section investigates the effect of the electrode transverse position on the duct heat transfer. This particular work is motivated by the previously reported existence of a critical gap between a solid obstacle and a heated wall (Hussam & Sheard 2013). A plot of HR^* against l_y is given in Figure 6.25. The plot demonstrates that an optimal transverse positioning does indeed exist for maximum heat transfer enhancement.

As the electrode is positioned closer to the wall from the duct centreline, a higher heat transfer enhancement is obtained irrespective of forcing frequency. The reason for this observation is that the vortices are cast closer to the heated wall, resulting in an enhanced mixing between the high temperature fluid in the vicinity of the heated wall and the bulk flow. However, beyond a critical l_y , HR^* decreases with decreasing electrode-wall distance, which is attributed to the fact that the pairs of vortices are deflected away from the heated wall toward the opposite wall at a downstream distance, thus resulting in a poor local heat transfer and a net decrease in the HR^* . As these vortices are deflected, a portion of hot fluid is transported away from the heated wall, which results in a strong local peak of Nusselt number in the vicinity of the deflection location (the variations of local Nusselt number with l_y are similar to that of the

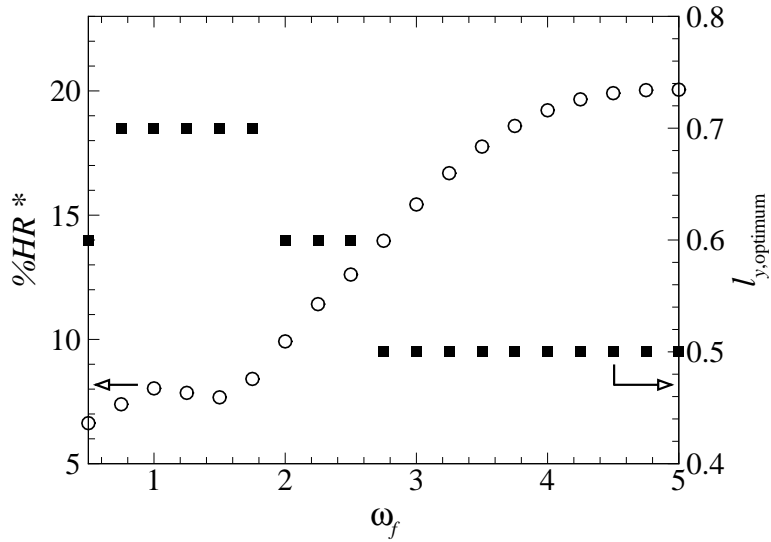


FIGURE 6.26: (Primary vertical axis, open symbols) Maximum response in overall heat transfer enhancement ratio due to electrode positioning relative to when the electrode is placed along the duct centreline, and (secondary vertical axis, closed symbols) the corresponding optimum l_y .

normalised Nusselt number presented in Figure 6.18, with increasing Re_L indicating increasing l_y).

As noted in Figure 6.26, the optimum gap varies between $l_y = 0.5$ and 0.7 , and is shifted towards smaller l_y for increasing forcing frequency. This may be understood as follows: for a higher forcing frequency, the resulting vortices are smaller (as noted in section 6.3.2), hence a smaller gap is required to compensate the weak vortex-boundary layer interaction associated with the decrease in the vortex size. In the lower range of ω_f (frequencies which are below the optimum value for a given forcing amplitude), the variation of HR^* with l_y is less obvious (Figure 6.25), and that the maximum percentage increase in HR^* with respect to the centreline cases is relatively low at $6 < \%HR^* < 9$ for $\omega_f \leq 1.5$ (Figure 6.26). The reason for these observations being that in this regime, the generated vortices are relatively large, thus the position of the electrode has little influence on the attained heat transfer enhancement. However, in the higher range of ω_f , $\%HR^*$ increases monotonically with increasing ω_f , with $\%HR^*$ appearing to plateau toward 20% as the forcing frequency approaches $\omega_f = 5$ (highest ω_f investigated in this section).

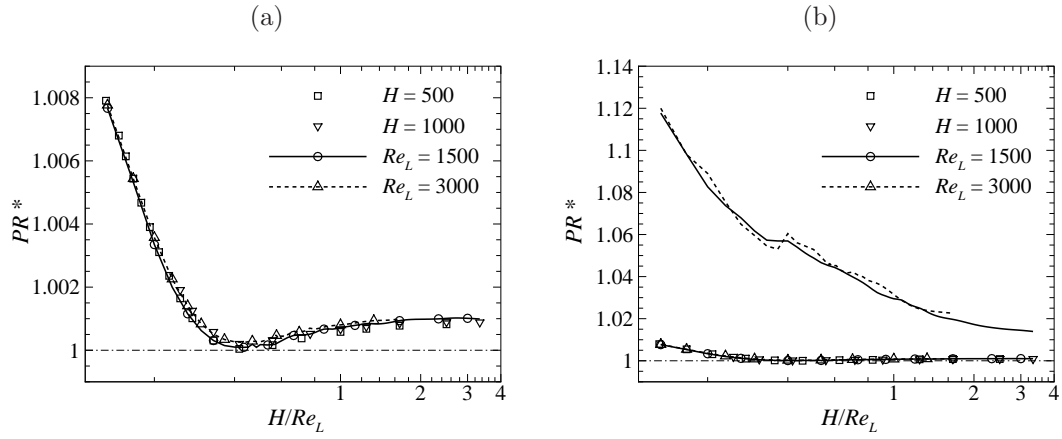


FIGURE 6.27: Overall pressure penalty ratio plotted against H/Re_L for (a) no-cylinder cases and (b) cases with and without a cylinder. In (b), lines with symbols are the no-cylinder cases, lines with no symbols are the cases with the cylinder present. In all cases, $I = 30$, $\omega_f = 1.75$ and $\tau/T = 0.25$. Solid, dashed and dash-dotted lines represent $Re_L = 1500$, $Re_L = 3000$ and $PR^* = 1$, respectively.

6.3.6 Power and efficiency analysis

Inspection of pressure drop data across the computed cases revealed a maximum pressure penalty ratio $PR_{\max}^* \approx 28.7\%$ while a cylinder is present in the duct. However, in the absence of the cylinder, a negligible gain in pressure drop was recorded (i.e. $PR_{\max}^* \approx 1.2\%$). Although the increases in pressure drop is almost negligible across all cases (the average pressure drop increase is approximately 2.2%), its exhibit a systematic trend with respect to the varying parameters. A higher current injection amplitude and pulse width lead to a higher PR^* . Furthermore, an increase in friction parameter or a decrease in Reynolds number generally results in a decrease in PR^* . However, PR^* exhibits weak dependencies on the current forcing frequency and its profile. It is interesting to note that the plots of PR^* against H/Re_L for cases of varying friction parameter and Reynolds number almost collapse onto a single curve (as shown in Figure 6.27(a)), suggesting that for given current injection parameters, the pressure penalty ratio is governed by the H/Re_L . Furthermore, Figure 6.27(b) shows that the presence of the cylinder dictates the magnitude of the pressure drop increase.

The decrease of PR^* with increasing H might be misinterpreted as a lower pumping power loss for a higher magnetic field strength if the definition of PR^* is not considered carefully ($PR^* = \Delta p/\Delta p_0$), which would appear to be contradictory to the fact that a stronger magnetic field leads to a stronger Lorentz force that opposes the flow (Barleon

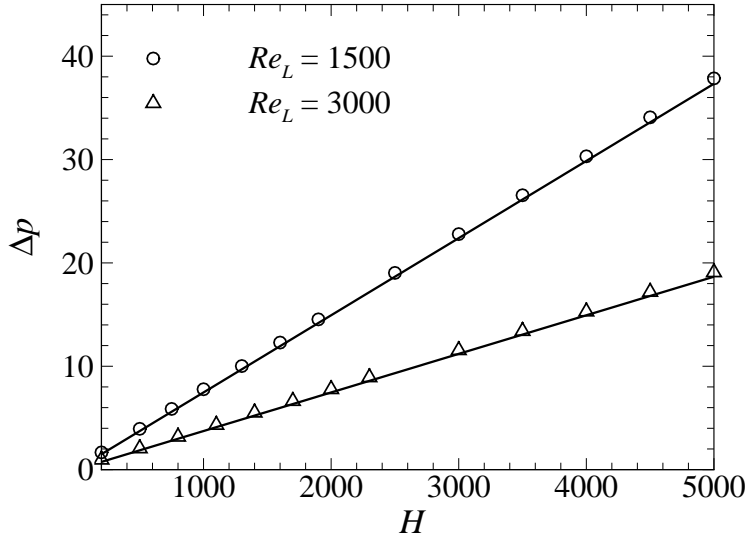


FIGURE 6.28: Time-averaged pressure drop plotted against friction parameter for duct cases with a cylinder, $I = 30$, $\omega_f = 1.75$, $\tau/T = 0.25$ and Reynolds number as indicated. Solid lines represent the analytical solution for fully developed MHD flow in an empty duct under the SM82 model.

et al. 1991). Indeed, the plot of Δp with respect to H recovers the linear relation $\Delta p \approx \Delta p_0^* \propto H$ (as shown in Figure 6.28), which is expected given that PR^* is almost unity.

Furthermore, $PR^* \approx 1$ also means that the efficiency index follows a similar trend to that of the HR^* , as already noted in § 5.7.7 (i.e. $\eta^* = HR^*/PR^* \simeq HR^*$ when $PR^* \approx 1$). The maximum efficiency index across all cases was found to be $\eta^* = 1.83$, which is for the case with $H = 500$, $Re_L = 1500$, $I = 60$, $\omega_f = 1.25$ and $\tau/T = 0.25$. This value is higher than the corresponding maximum value reported in § 5.7.7, i.e. $\eta = 1.91$ or $\eta^* = 1.80$. It is important to note that the efficiency index in the latter case was obtained using a higher current injection amplitude ($I = 90$). It is shown in Figure 5.18 that larger current amplitude generally leads to an improved heat transfer, thus it is anticipated that the efficiency index in the former case can be further increased by injecting a larger current amplitude.

In order to further evaluate the thermal-hydraulic efficiency of the current injection vortex promoter, the net power enhancement is evaluated as follows:

$$\begin{aligned}\Delta P_{\text{net}}^* &= \Delta P_{\text{heat}}^* - \Delta P_{\text{flow}}^*, \\ &= (P_{\text{heat}} - P_{0,\text{heat}}^*) - (P_{\text{flow}} - P_{0,\text{flow}}^*),\end{aligned}\quad (6.1)$$

where ΔP_{heat} and ΔP_{flow} are respectively the net increase in heat power and pumping power due to incorporation of the vortex promoter, while P_{heat} and P_{flow} are the heat power transferred through the heated wall and the pumping power, respectively. Here the subscript 0 again denotes the corresponding flow without current injection, with an asterisk denoting the absence of the cylinder. Normalising power by $\rho L^2 U_0^3$ and applying the scalings outlined in equation (3.9), the dimensionless heat and pumping power may be expressed respectively as

$$P_{\text{heat}} = \frac{a\kappa_T C_p \delta\theta}{L^2 U_0^3} \int_0^{L_d} \frac{\partial\theta}{\partial y} dx = \frac{2}{\alpha} \frac{\kappa_T C_p \delta\theta}{L U_0^3} \int_0^{L_d} \frac{\partial\theta}{\partial y} dx, \quad (6.2)$$

and

$$P_{\text{flow}} = 2 \frac{a}{L} U_{\text{avg}} \Delta p = \frac{4}{\alpha} U_{\text{avg}} \Delta p, \quad (6.3)$$

where U_{avg} is the area-averaged velocity through the duct, which is estimated using equation (3.29), i.e.

$$U_{\text{avg}} = \frac{1}{2L} \int_L^{-L} u_{\perp}(y) dy = \frac{1}{2L} \left[\coth^2 \left(\frac{\sqrt{H}}{2} \right) - \frac{2}{\sqrt{H}} \coth \left(\frac{\sqrt{H}}{2} \right) + 1 \right]. \quad (6.4)$$

The net power balance is thus

$$\Delta P_{\text{net}}^* = \frac{2}{\alpha} \left[\frac{\kappa_T C_p \delta\theta}{L U_0^3} \int_0^{L_d} \frac{\partial\theta}{\partial y} - \frac{\partial\theta_0^*}{\partial y} dx - 2U_{\text{avg}}(\Delta p - \Delta p_0^*) \right]. \quad (6.5)$$

The pre-factor to the heat flux term is rewritten in terms of dimensionless parameters via

$$\frac{\kappa_T C_p \delta\theta}{L U_0^3} = \frac{1}{Pr} \frac{\nu}{L U_0} \frac{C_p \delta\theta}{U_0^2} = \frac{1}{Pr Re_L Ec}, \quad (6.6)$$

where Ec is the Eckert number $Ec = U_0^2 / (C_p \delta\theta)$. The form of the pre-factor indicates that a net benefit in heat transfer enhancement will be more significant for smaller Prandtl numbers (liquid metals present small Prandtl numbers), smaller Reynolds

numbers (the Reynolds numbers are relatively modest in magnetic confinement fusion blankets), and smaller Eckert numbers.

Normalising the net power enhancement by the pumping power, and taking $Pr = 0.022$, $U_0 = 0.015 \text{ m s}^{-1}$, $C_p = 188 \text{ J kg}^{-1} \text{ K}^{-1}$ and $\delta\theta = 250\text{K}$ (these values are relevant to the fusion blanket application; Schulz 1991; Smolentsev *et al.* 2010), the final form of the net power balance may be rewritten as

$$\frac{\Delta P_{\text{net}}^*}{P_{\text{flow}}} = \frac{4.75 \times 10^9}{U_{\text{avg}} \Delta p Re_L} \int_0^{L_d} \frac{\partial \theta}{\partial y} - \frac{\partial \theta_0^*}{\partial y} dx - \left(1 - \frac{1}{PR^*}\right). \quad (6.7)$$

As noted earlier, PR^* is of order of unity, hence the second term on the left-hand side of equation (6.7) is approximately zero. In the limit of strong magnetic field, U_{avg} approaches unity (e.g. for $200 \leq H \leq 5000$, $0.929 \leq U_{\text{avg}} \leq 0.989$). Furthermore, inspection of temperature flux data revealed that it generally exhibits a similar trend with the Nusselt number. It follows then that for a given Reynolds number, ΔP_{net}^* follow a similar trend to that of the η^* (and thus the HR^*). The case with maximum and minimum $\Delta P_{\text{net}}^*/P_{\text{flow}}$ corresponds to the case with respectively maximum and minimum η^* , which confirms the previous argument. However, for a varying Reynolds number cases, the $\Delta P_{\text{net}}^*/P_{\text{flow}}$ exhibits a trend distinct from the η^* due to the Re_L dependencies noted in equation (6.7). A plot of $\Delta P_{\text{net}}^*/P_{\text{flow}}$ and η^* against H/Re_L is shown in Figure 6.29.

It can be seen from the figure that the peak of η^* is higher for $H = 1000$ than for $H = 500$. However, the opposite is true for $\Delta P_{\text{net}}^*/P_{\text{flow}}$. For a stronger imposed magnetic field, the opposing damping Lorentz force is greater, which generally results in a lower heat transfer characteristic and a higher pressure loss. Thus it appears that the net power is indeed a more relevant measure for comparing cases of varying Reynolds number, although the general non-monotonic trend in the efficiency index is still being preserved.

In general, $\Delta P_{\text{net}}^*/P_{\text{flow}}$ range between 2.04×10^3 and 4.69×10^5 for a fusion-relevant conditions across all the cases computed in the present study, which indicates a significant gain in heat transfer relative to the additional pressure loss.

6.4 Chapter summary

This chapter has explored the potential of electrically driven vortices as a mean of enhancing convective heat transfer from a heated wall. Computations are made over a

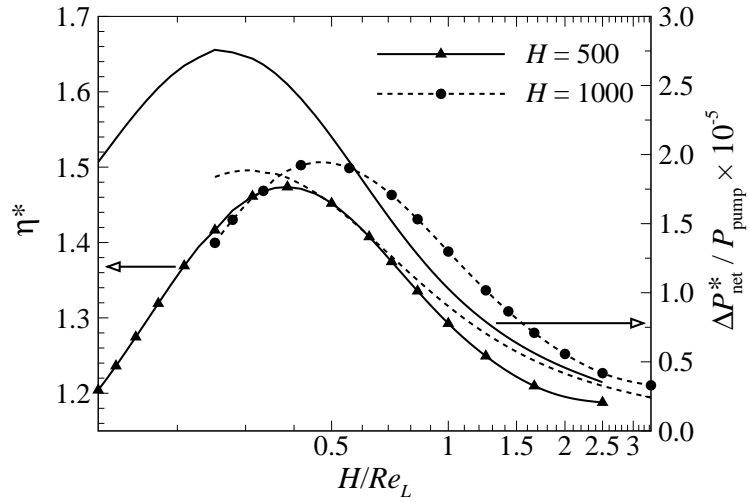


FIGURE 6.29: (Primary vertical axis) Overall efficiency index and (secondary vertical axis) normalised net power enhancement plotted against H/Re_L for $I = 30$, $\omega_f = 1.75$ and $\tau/T = 0.25$ and friction parameters as indicated. Solid and dashed lines represent $H = 500$ and 1000 , respectively. Lines with and without symbols represent respectively efficiency index and net power enhancement.

wider range of flow and current injection parameters than those reported in Chapter 5 in order to elucidate further the relationship between the gain in the heat transfer and the dependent variables.

The first part of the analysis compared the gain in the thermal performance between the obstructed and the unobstructed duct. It was found that the general trend of heat transfer enhancement for both duct configurations are similar, which might suggest that the presence of the cylinder does not change the global wake response in the duct. Surprisingly, however, the inspection of vorticity contours revealed a distinct wake pattern between the two cases. The presence of the cylinder tends to widen the wake vortices, whereas the vortices are almost aligned directly downstream of the electrode in the absence of the cylinder. In the former case, although the interaction between the wake and the thermal boundary layer appears to be stronger, the HR^* data revealed that the system without a cylinder can achieve a better thermal gain depending on the intensity of the generated vorticity. Furthermore, when the inertia is relatively significant to the Hartmann damping, the cylinder wake loses its coherence and exhibits a chaotic behaviour, which generally improves the wake-boundary layer interaction and thus is beneficial for the heat transfer augmentation.

The analysis of Reynolds number variations revealed that in the conductive regime (high- H/Re_L), the gain in heat transfer is dependent on the Reynolds number. However, despite the distinct Nusselt number trend, the data of the normalised Nusselt number HR^* almost collapses in the low- H/Re_L regime when plotted against H/Re_L for both constant friction parameter and constant Reynolds number cases. The results also show that heat transfer can be further improved by injecting an asymmetric alternating current. However, in the range of optimum injection frequency of $1 \lesssim \omega_f \lesssim 2$, the symmetric profile outperforms its asymmetric counterpart. Furthermore, the analysis of the effect of transverse electrode position on the heat transfer enhancement suggested the existence of an optimal gap for maximum HR^* , corroborating previous findings for a cylindrical obstacle in a duct. However, the electrode position is less influential on the HR^* for low forcing frequency, while the optimum gap decreases with increasing forcing frequency.

The results also indicate a maximum increase in pressure drop induced by the current injection in an unobstructed duct is typically an order of magnitude less than the obstructed duct counterparts. Furthermore, the amplitude and pulse width of the current injection, together with the Reynolds number and friction parameter were found to govern the PR^* , while the current injection frequency and its profile were not. For given current parameters, the PR^* was found to be governed by the ratio H/Re_L .

A further power analysis also revealed a net power enhancement per unit pumping power of at least the order of 10^3 for a fusion-relevant conditions, while a maximum net power enhancement reaching a value of two orders of magnitude higher than the corresponding minimum value. Given the fact that the electrically generated vortices, unlike its physical obstacle counterparts, can be precisely controlled via current injection parameters such as amplitude, frequency, pulse width and profile, a greater heat transfer gain than those reported here is anticipated through further optimisation. Therefore, electrically generated vortices stand as a promising technology superior to physical vortex generators, notwithstanding the significant technical challenges in their deployment.

Chapter 7

Conclusions

The present study numerically investigates the characteristics of vortices and its associated thermal-hydraulic performance in a rectangular MHD duct flow subjected to a uniform magnetic field. The flow of interest is quasi-two-dimensional in nature, which has a direct relevance to the test blanket module of a magnetic confinement fusion reactor. Two primary governing parameters are the Reynolds number and friction parameter. Due to the nature of the flow, a quasi-two-dimensional model, known as SM82, has been employed. The vortices are generated by means of either a circular cylinder, a current injection or the combination of both. The present study provides the first supportive evidence for the employment of current injection as an effective alternative to the heat transfer augmentation method in a fusion-related coolant blanket.

The following sections discuss the overall conclusions from Chapters 4, 5 and 6, which are divided into four main areas; vortex dynamics, vortex decay, thermal analysis, and power and efficiency analysis.

7.1 Vortex dynamics

7.1.1 Dynamics of naturally shed vortices

Simulations of low Reynolds number cylinder wake flow in an MHD duct reveal two distinct regions in the downstream of the wake; a formation region in which the vorticity evolves from shear layers separating from the cylinder and organises into a vortex street, and a stable region in which the shed vortices advect downstream in a periodic laminar manner. The presence of a strong magnetic field has shown to appreciably alter the onset and behaviour of the vortex shedding. The transition from steady to unsteady flow is delayed due to the flow suppression by a Lorentz force. A larger cylinder has also been found to delay the transition due to the confinement effect impeding

the motion that produces shear layers attached on the cylinder. However, the effect becomes less prominent with increasing cylinder diameter due to the counteraction of local acceleration that increases the instability of the shear layer.

The formation of these wake vortices is found to be greatly dependent on both Reynolds number and friction parameter. For a given friction parameter, an increase in Reynolds number results in the attached shear layers quickly organising into a coherent structures, thus leading to a shorter formation length and higher shedding frequency. The magnitude of the increment has found to be dependent on the friction parameter, with generally larger increment at a higher friction parameter. At the same time, the wake becomes narrower due to the tip of the shear layer tends to roll up further towards the wake axis. Furthermore, increasing friction parameter leads to an increase in the formation length due to the stretching of the shear layers, which also likely explains the increase in the wake advection velocity and the shedding frequency. In the hydrodynamic counterparts, the wake advection velocity and its width are almost independent across the investigated Reynolds number, although the dependency of the shedding frequency on the Reynolds number is more prominent compared to the magnetohydrodynamic cases.

In the absence of a magnetic field, an inverted Kármán vortex street is observed in the wake due to the entrainment of vorticity from the free stream into the wake. However, this entrainment is not observed in the presence of a magnetic field due to zero vorticity in the core flow. Once the vortices have fully formed, it advects downstream with an almost constant local longitudinal spacings for a given friction parameter and Reynolds number. Increasing Re or decreasing H leads to a decreasing average longitudinal spacing, due to the interdependent role of wake advection velocity and shedding frequency.

7.1.2 Dynamics of electrically augmented/driven vortices

The injection of current pulses into the flow in the vicinity of the cylinder was shown to significantly alter the cylinder wake behaviour. The rate of vortex shedding is governed by the frequency of the current injection pulses. It follows then that the local longitudinal spacing of wake vortices in the stable region is governed by this frequency, given that wake advection velocity is almost unity across all cases. A further analysis on the shedding frequency reveals distinct wake response from the oscillating cylinder

case beyond the lock-in regime. Despite the difference in the mechanism of vorticity augmentation, the range of frequencies at which vortex shedding is synchronised with the current injection frequency is comparable to that for an in-line oscillating cylinder case ($0.8 < F < 2$). However, this range is appreciably wider than the corresponding transversely oscillating cylinder case.

The interaction between the electrically generated vortices and the naturally shed vortices tends to widen the cylinder wake. On the other hand, when the cylinder is absent, the electrically generated vortices advect downstream in an almost tandem arrangement with lateral spacings of less than one tenth of the duct width. In both cases, an increase in current amplitude leads to a wider wake.

When the inertia is relatively important compared to the Hartmann damping (i.e. low- H/Re_L regime), the cylinder wake resembles a chaotic behaviour. In the limit of a strong wake-boundary layer interaction, secondary vortices are generated as a result of Shercliff layer separation from the sidewall. Interestingly, however, the coherence of the electrically driven vortices is preserved within the low- H/Re_L regime due to the absence of the cylinder generated wakes. The chaotic behaviour has also been observed for cases with high current amplitudes and low current frequencies, regardless of whether the cylinder is present or not. The flow and current configurations corresponding to the threshold for chaotic behaviour are found to be interdependent.

7.2 Vortex decay

7.2.1 Decay of naturally shed vortices

The decay of stable quasi-two-dimensional cylinder wake vortices has been quantitatively analysed, whereby a model describing their spatial evolution of peak vorticity has been proposed. The model provides the first elucidation of the physical contributions of Hartmann braking and viscous dissipation towards the decay process. Below a critical friction parameter, the dissipation of vortices is dominated by viscosity in the near wake region, while Hartmann braking dominates further downstream. In the far wake region, the vortices decay at a rate of approximately the Hartmann friction term $-H/Re_L$ regardless of the friction parameter or Reynolds number.

The model also predicts the transition region at which both viscous dissipation and Hartmann damping contribute equally to the decay of peak vorticity. The transition region moves upstream with increasing imposed magnetic field intensity until the crit-

ical friction parameter is reached, where the Hartmann braking effect already prevails from the beginning of the decay process. Interestingly, the model suggests that the effect of Hartmann braking becomes more prominent at higher Reynolds numbers, thus corroborating the conjecture that quasi-2-D MHD turbulence is dominated by magnetic damping (Pothérat 2012).

The capability of the proposed model has been verified against published 3D MHD numerical data at high interaction parameters. However, at a low interaction parameter, the wake vortices decay faster than predicted by the model, likely due to the presence of three-dimensionality leading to an enhanced dissipation of vorticity.

7.2.2 Decay of electrically augmented/driven vortices

Measurements of local vorticity maxima within an advecting vortex reveal that the strength of the cylinder wake vortices is significantly enhanced even by a relatively low current injection amplitude. However, depending on the amplitude of the current, the presence of the cylinder either enhances or diminishes the growth of the shed vortices. For a relatively high current amplitude, the peak vorticity of vortices that are generated solely by a current injection are more intense than those generated by both current injection and cylinder, likely due to the counteractions between the two different mechanisms of vorticity generation. However, the opposite is true for a relatively low current amplitude, where the shear layer separating from the cylinder encourages the growth of the electrically driven vortices, leading to a stronger shed vortices. Once the vortices are shed, their decay rate was found to be insensitive to the presence of current injection augmentation and the current amplitude, due to the strong imposed magnetic field.

7.3 Thermal analysis

7.3.1 Dependency on governing parameters

Thermal performance of duct flows with and without the cylinder obstacle is quantified by the heat transfer enhancement ratio. In both cases, current is injected through an electrode embedded into one of the Hartmann walls. The overall trend of heat transfer enhancement for both configurations was found to be similar. In general, the gain in heat transfer is governed by the competition between the size, intensity, spacings (lateral and longitudinal) and nature (either chaotic or coherent) of the generated vortices,

which in turn depend on the flow and current injection parameters. It was found that the heat transfer enhancement ratio has a non-monotonic relation with friction parameter H , Reynolds number Re_L , electrode position l_y , current injection profile $\Delta\tau/T$ and frequency ω_f , while it increases monotonically with increasing current amplitude I and pulse width τ/T .

The optimum current injection parameters range for maximum HR^* are $1 \lesssim \omega_f \lesssim 2$, $0.5 \lesssim l_y \lesssim 0.7$ and $\Delta\tau/T \approx \pm 0.3$. It appears that, within the optimum frequency range, the optimum electrode position $l_{y,\text{opt}} \approx 0.7$, and that varying profile of the current injection offers limited contribution to the enhancement of heat transfer, although a moderate increase in HR^* (maximum increase of $\approx 6\%$ over the symmetric profile) was observed for cases with frequencies beyond the optimum range. A maximum $HR^* \approx 1.9$ was recorded within the parameter space investigated in this thesis. However, it is anticipated that the maximum attainable heat transfer enhancement can be further improved, given the observation of monotonic increase in HR^* with increasing current amplitude and pulse width.

The competition between inertia and Hartmann damping leads to the non-monotonic trend of HR^* with H and Re_L . Interestingly, HR^* appears to be governed by Hartmann friction term, although some deviations was observed in the high H/Re_L regime. This is due to the heat transport being dominated by conduction in this regime, where Nusselt number is sensitive to Reynolds number variations.

7.3.2 Obstructed against unobstructed duct flows with current injection

Although the overall trend of HR^* is independent of whether the cylinder is present or not, the presence of the cylinder has shown to outperform the no-cylinder cases under certain conditions. When inertia is important (i.e. when H is relatively low), the cylinder wake resembles a chaotic behaviour, which enhances its interaction with the thermal boundary layer, and thus HR^* . Furthermore, the wake is generally wider in the presence of the cylinder, which results in a better heat transfer enhancement than the empty duct case, particularly for low current amplitudes and short current pulses (in which the threshold values depend on various injection parameters). However, the empty duct configuration outperforms its obstructed duct counterpart within a larger portion of the investigated parameter space, which suggest that the insertion of the cylinder has insignificant beneficial effects over the electrically induced heat transfer

enhancement.

7.4 Power and efficiency analysis

While the employment of both cylinder and current injection as a vortex promoter in the duct results in a maximum additional overall pressure drop of $PR \approx 30\%$, the duct with current injection alone demands insignificant additional pumping power requirement. However, the magnitude of the additional pumping power is negligible compared to the net increase in heat power. It follows then that the maximum recorded net power enhancement of $\Delta P_{\text{net}}^*/P_{\text{flow}} = \mathcal{O}(10^5)$ is contributed mainly by the thermal enhancement in the duct flow, which indicates the great potential of current injection as an efficient heat transfer augmentation mechanism.

7.5 Directions for future work

While this thesis has demonstrated the potential of current injection as a vortex promoter to enhance convective heat transfer in an MHD duct flow, the analysis could be further extended in a number of ways.

In the present investigation, the effect of recirculations in the flow is ignored, which is justified by the fact that this secondary flow is weakened under a strong magnetic field. However, it is expected that when inertia is important, the effect of recirculating flows can potentially alter the heat transfer characteristics of the flow. Further investigation is therefore required to quantify this effect by using a more refined PSM2000 model (Poth erat *et al.* 2000) that takes into account the moderate inertial effects.

Flows past arrays of bluff bodies in a tandem arrangement have received considerable attention owing to its significant application in cooling systems. The interference between two adjacent cylinders often results in a different states of shedding, which is likely to affect heat transfer characteristics of the duct. It would be beneficial, therefore, to perform computations for a flow past arrays of electrode with an alternating polarities. The flow analyses of such an arrangement would provide critical information for the design of the current injection as an efficient heat transfer enhancement mechanism. The solution of scalar potential for current injected from periodic array of electrodes is presented in Appendix B for a future research benefit.

In the limit of high magnetic field strength, vorticity diffuses along the magnetic field lines, leading to a quasi-two-dimensional vortical structures in the flow field. How-

ever, due to the chaotic nature of some flows computed for this thesis, it would be interesting that direct numerical simulations being performed to verify the quasi-two-dimensionality assumption of the vortices, particularly for high Reynolds numbers and current amplitudes, and low injection frequencies.

Appendices

Appendix A

Fourier series representation of a modified square wave

This Appendix details the derivation of a Fourier series representation of a modified square wave, as shown in Figure A.1.

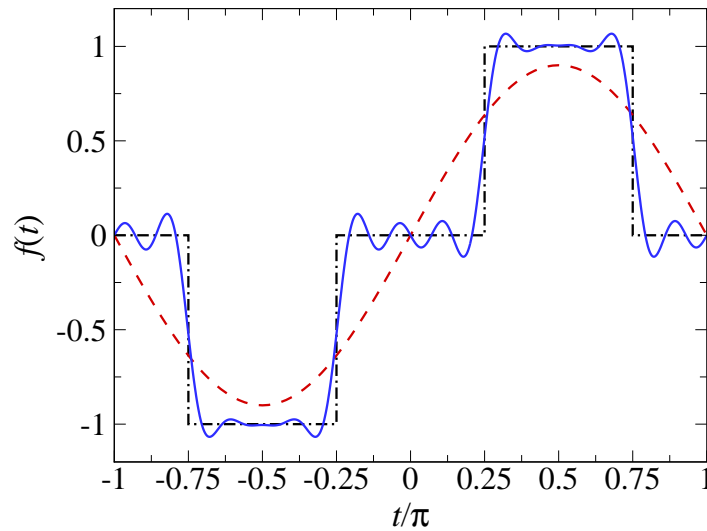


FIGURE A.1: Profiles of modified square waveform and its partial sums of the Fourier series representation. The dash-dotted line represents an ideal modified square waveform with $\tau/T = 0.25$, while dashed and solid lines respectively show a fundamental sine wave (only 1st harmonic included) and a partial summation of the Fourier series representation up to the 13th harmonic.

The modified square wave presented in Figure A.1 is expressed as

$$f(t) = \begin{cases} -1, & -\frac{3\pi}{4} \leq t \leq -\frac{\pi}{4} \\ 1, & \frac{\pi}{4} \leq t \leq \frac{3\pi}{4} \end{cases} \quad (\text{A.1})$$

This signal, which has a period $T = 2\pi$, can be represented by an infinite sum of sine and cosine terms according to

$$f(t) = a_0 + \sum_{n=1}^{\infty} (a_n \cos(nt) + b_n \sin(nt)), \quad (\text{A.2})$$

where a_0 is a constant, and a_n and b_n are the Fourier coefficients, given by

$$a_0 = \frac{1}{2\pi} \int_{-\pi}^{\pi} f(t) dt, \quad (\text{A.3})$$

$$a_n = \frac{1}{\pi} \int_{-\pi}^{\pi} f(t) \cos(nt) dt, \quad n = 1, 2, 3, \dots \quad (\text{A.4})$$

and

$$b_n = \frac{1}{\pi} \int_{-\pi}^{\pi} f(t) \sin(nt) dt. \quad n = 1, 2, 3, \dots \quad (\text{A.5})$$

respectively. Since the waveform is symmetrical and alternating (the positive half is identical to the negative half), $a_0 = 0$. Furthermore, the waveform is an odd function, hence $a_n = 0$ for all n and only b_n needs to be calculated. From the piecewise function in equation (A.1),

$$\begin{aligned} b_n &= \frac{1}{\pi} \left[\int_{-3\pi/4}^{-\pi/4} (-1) \sin(nt) dt + \int_{\pi/4}^{3\pi/4} (1) \sin(nt) dt \right], \\ &= \frac{1}{\pi} \left[\frac{1}{n} \cos(nt) \Big|_{-3\pi/4}^{-\pi/4} - \frac{1}{n} \cos(nt) \Big|_{\pi/4}^{3\pi/4} \right], \\ &= \frac{2}{n\pi} \left[\cos\left(\frac{n\pi}{4}\right) - \cos\left(\frac{3n\pi}{4}\right) \right]. \end{aligned} \quad (\text{A.6})$$

The Fourier series representation of a modified square wave with $\tau/T = 0.25$ is then given by

$$f(t) = \sum_{n=1}^{\infty} \frac{2}{n\pi} \sin(nt) \left[\cos\left(\frac{n\pi}{4}\right) - \cos\left(\frac{3n\pi}{4}\right) \right]. \quad (\text{A.7})$$

Appendix B

Analytical solution of forcing velocity fields from a periodic array of electrodes

This Appendix details the analytical derivation of the forcing velocity fields for current injected from a periodic array of electrodes, as shown in Figure B.1.

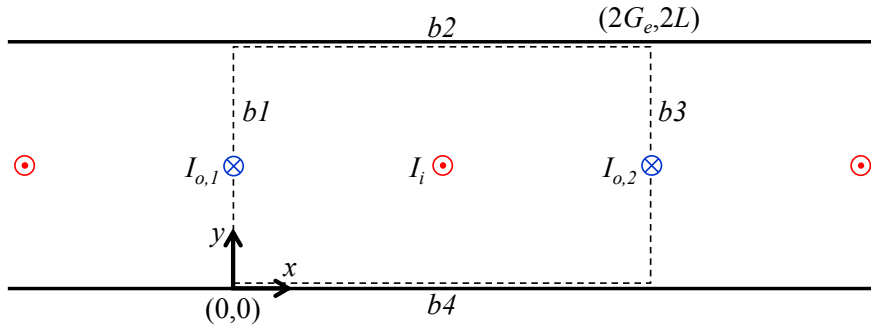


FIGURE B.1: Schematic diagram of the numerical domain with a spatially periodic array of electrodes in the streamwise direction. The dashed lines indicate control volume surfaces. The streamwise electrode spacing is G_e . I_i is referred to the electrode that injects current into the flow and $I_{o,1}$ and $I_{o,2}$ represent electrodes at which current leaves the flow. The origin is located at the bottom left corner of the control volume.

The alternating-polarity electrodes are equivalently spaced with gap G_e in a duct with width $2L$. The scalar potential ψ_0 is obtained by solving the Poisson equation for a source term at the current injection point that is a Dirac function located at (χ, ζ) . Zero Neumann conditions are imposed on the electrical potential field at all boundaries (i.e. boundaries $b1$ - $b4$, as shown by the dashed lines in Figure B.1), hence the scalar potential is given by

$$\psi_0(\chi, \zeta) = \sum_{n=1}^{\infty} \sum_{m=1}^{\infty} \frac{I \cos(\mu_n x) \cos(\mu_n \chi) \cos(\lambda_m y) \cos(\lambda_m \zeta)}{G_e L (\mu_n^2 + \lambda_m^2)}, \quad (\text{B.1})$$

From equation (5.4), the \mathbf{u}_0 components are evaluated as

$$u_0(\chi, \zeta) = \sum_{n=1}^{\infty} \sum_{m=1}^{\infty} -\frac{I \lambda_m \cos(\mu_n x) \cos(\mu_n \chi) \sin(\lambda_m y) \cos(\lambda_m \zeta)}{G_e L (\mu_n^2 + \lambda_m^2)}, \quad (\text{B.2})$$

and

$$v_0(\chi, \zeta) = \sum_{n=1}^{\infty} \sum_{m=1}^{\infty} \frac{I \mu_n \sin(\mu_n x) \cos(\mu_n \chi) \cos(\lambda_m y) \cos(\lambda_m \zeta)}{G_e L (\mu_n^2 + \lambda_m^2)}. \quad (\text{B.3})$$

Periodic boundary conditions are imposed on the duct inlet and outlet to save computational costs since the computational domain can be restricted to just one cell containing one electrode. The flow is driven by a constant pressure gradient, and so to represent this in the governing momentum equation, the pressure is decomposed into a forcing component with a constant linear profile, and a fluctuating part, i.e.

$$\hat{p} = \left(\frac{dp}{dx} \right) \hat{\mathbf{x}} + \hat{p}'. \quad (\text{B.4})$$

Substituting into the momentum equation (i.e. equation (3.24)) yields

$$\frac{\partial \hat{\mathbf{u}}_{\perp}}{\partial t} = -(\hat{\mathbf{u}}_{\perp} \cdot \hat{\nabla}) \hat{\mathbf{u}}_{\perp} - \left(\frac{1}{\rho} \left(\frac{dp}{dx} \right) \mathbf{e}_x + \frac{1}{\rho} \hat{\nabla} \hat{p}' \right) + \nu \hat{\nabla}^2 \hat{\mathbf{u}}_{\perp} - \frac{n}{t_H} \hat{\mathbf{u}}_{\perp}, \quad (\text{B.5})$$

where dp/dx is a constant, and \mathbf{e}_x is the unit vector in the x-direction. The pressure gradient term acts as a forcing term on the x-direction momentum equation, i.e.

$$\frac{\partial \hat{\mathbf{u}}_{\perp}}{\partial t} = -(\hat{\mathbf{u}}_{\perp} \cdot \hat{\nabla}) \hat{\mathbf{u}}_{\perp} - \frac{1}{\rho} \hat{\nabla} \hat{p}' + \nu \hat{\nabla}^2 \hat{\mathbf{u}}_{\perp} - \frac{n}{t_H} \hat{\mathbf{u}}_{\perp} - \frac{1}{\rho} \left(\frac{dp}{dx} \right) \mathbf{e}_x. \quad (\text{B.6})$$

The equation is non-dimensionalized with the following non-dimensional variables:

$$\mathbf{x} = \frac{\hat{\mathbf{x}}}{L}, \quad \mathbf{u} = \hat{\mathbf{u}} \sqrt{\frac{\rho}{p_x L}}, \quad t = \hat{t} \frac{1}{L} \sqrt{\frac{p_x L}{\rho}}, \quad p = \hat{p} \frac{1}{\rho} \left(\frac{\rho}{p_x L} \right) = \frac{\hat{p}}{p_x L}, \quad (\text{B.7})$$

where $p_x = dp/dx$ is the constant imposed pressure gradient. Rearranging the equations in terms of the dimensional variables gives

$$\hat{\mathbf{x}} = \mathbf{x}L, \quad \hat{\mathbf{u}} = \mathbf{u} \sqrt{\frac{p_x L}{\rho}}, \quad \hat{t} = tL \sqrt{\frac{\rho}{p_x L}}, \quad \hat{p} = p p_x L. \quad (\text{B.8})$$

Substituting all nondimensional variables in the SM82 equation and rewriting the MHD force term in terms of Hartmann number yields

$$\begin{aligned} \frac{\partial \mathbf{u}_\perp}{\partial t} \left[\frac{p_x}{\rho} \right] = & -(\mathbf{u} \cdot \nabla) \mathbf{u}_\perp \left[\frac{p_x}{\rho} \right] - \frac{1}{\rho} \nabla p' [p_x] + \nu \nabla^2 \mathbf{u}_\perp \left[\frac{1}{L^2} \sqrt{\frac{p_x L}{\rho}} \right] \\ & - nHa \frac{\nu}{a^2} \mathbf{u}_\perp \left[\sqrt{\frac{p_x L}{\rho}} \right] - \frac{1}{\rho} (p_x) \mathbf{e}_x. \end{aligned} \quad (\text{B.9})$$

Dividing the above equation with p_x/ρ yields

$$\begin{aligned} \frac{\partial \mathbf{u}_\perp}{\partial t} = & -(\mathbf{u}_\perp \cdot \nabla) \mathbf{u}_\perp - \nabla p' + \left[\nu \sqrt{\frac{\rho}{p_x L^3}} \right] \nabla^2 \mathbf{u}_\perp - nHa \left(\frac{L}{a} \right)^2 \left[\nu \sqrt{\frac{\rho}{p_x L^3}} \right] \mathbf{u} - \mathbf{e}_x, \\ = & -(\mathbf{u}_\perp \cdot \nabla) \mathbf{u}_\perp - \nabla p' + \frac{1}{Re_p} \nabla^2 \mathbf{u}_\perp - \frac{H}{Re_p} \mathbf{u}_\perp - \mathbf{e}_x, \end{aligned} \quad (\text{B.10})$$

where Re_p is pressure Reynolds number, expressed as

$$Re_p = \frac{1}{\nu} \sqrt{\frac{p_x L^3}{\rho}}. \quad (\text{B.11})$$

It is seen that the imposed pressure gradient introduces the negative unit forcing term in the x -direction momentum equation. The strength of the driving pressure gradient is accommodated for by the pressure Reynolds number Re_p . Finally, note that a positive pressure gradient ($p_x > 0$) describes a linear pressure increase in the positive x -direction. This drives flow from right to left. So a negative pressure gradient (producing a positive forcing term) will drive flow from left to right. From Poth erat (2007), the pressure gradient is related to the maximum velocity by

$$u_0 = \frac{L^2 p_x}{\rho \nu H} \left(1 - \frac{1}{\cosh \sqrt{H}} \right). \quad (\text{B.12})$$

Hence the Reynolds number can be written as

$$Re_L = \frac{u_0 L}{\nu} = \frac{L^2 p_x}{\rho \nu H} \left(1 - \frac{1}{\cosh \sqrt{H}} \right) \frac{L}{\nu}. \quad (\text{B.13})$$

Rewriting in terms of pressure Reynolds number yields

$$Re_L = \frac{1}{\nu^2} \frac{p_x L^3}{\rho} \frac{1}{H} \left(1 - \frac{1}{\cosh \sqrt{H}} \right) \quad (\text{B.14})$$

$$= Re_p^2 \frac{1}{H} \left(1 - \frac{1}{\cosh \sqrt{H}} \right). \quad (\text{B.15})$$

In the limit of high Hartmann number, the term in the bracket approaches unity, hence

$$Re_L \approx \frac{Re_p^2}{H}. \quad (\text{B.16})$$

References

- ALBOUSSIÈRE, T. 2011 Fundamentals of MHD. In *Dynamos: Lecture Notes of the Les Houches Summer School 2007* (ed. P. Cardin & L. F. Cugliandolo). Elsevier.
- ALBOUSSIÈRE, T., USPENSKI, V. & MOREAU, R. 1999 Quasi-2D MHD turbulent shear layers. *Exp. Therm. Fluid Sci.* **20** (1), 19–24.
- ALEKSYUK, A. I., SHKADOVA, V. P. & SHKADOV, V. Y. 2012 Formation, evolution, and decay of a vortex street in the wake of a streamlined body. *Moscow University Mechanics Bulletin* **67** (3), 53–61.
- ALI, M. S. M., DOOLAN, C. J. & WHEATLEY, V. 2009 Grid convergence study for a two-dimensional simulation of flow around a square cylinder at a low Reynolds number. In *Seventh International Conference on CFD in The Minerals and Process Industries* (ed. P. J. Witt & M. P. Schwarz), pp. 1–6. Melbourne Convention and Exhibition Centre, Melbourne, Australia, 7–9 December 2015, Paper 163HAM: CSIRO, Australia.
- ALPHER, R. A., HURWITZ JR., H., JOHNSON, R. H. & WHITE, D. R. 1960 Some studies of free-surface mercury magnetohydrodynamics. *Rev. Mod. Phys.* **32** (4), 758–774.
- ASADPOUR-ZEYNALI, K. & MANAFI-KHOSHMANESH, S. 2014 Simultaneous standard addition method for novel determination of components in a single step: Application in analysis of sunset yellow and carmoisine by a spectrophotometric technique. *Analytical Methods* **6** (15), 6110–6115.
- BAKER, N. T., POTHÉRAT, A. & DAVOUST, L. 2015 Dimensionality, secondary flows and helicity in low- Rm MHD vortices. *J. Fluid Mech.* **779**, 325–350.
- BARLEON, L., BURR, U., MACK, K.-J. & STIEGLITZ, R. 2000 Heat transfer in liquid metal cooled fusion blankets. *Fusion Eng. Des.* **51-52**, 723–733.
- BARLEON, L., CASAL, V. & LENHART, L. 1991 MHD flow in liquid-metal-cooled blankets. *Fusion Eng. Des.* **14** (3), 401–412.

- BARLEON, L., MACK, K.-J. & STIEGLITZ, R. 1996 The MEKKA-facility: a flexible tool to investigate MHD-flow phenomena. *Tech. Rep.* FZKA 5821. Institute of Applied Thermo- and Fluid Dynamics, Research Centre Karlsruhe.
- BEARMAN, P. W. 1965 Investigation of the flow behind a two-dimensional model with a blunt trailing edge and fitted with splitter plates. *J. Fluid Mech.* **21** (02), 241–255.
- BEARMAN, P. W. 1966 On vortex street wakes. *Tech. Rep.* 1199. National Physical Laboratory, UK.
- BEARMAN, P. W. 1967 On vortex street wakes. *J. Fluid Mech.* **28** (part 4), 625–641.
- BESKOK, A., RAISEE, M., CELIK, B., YAGIZ, B. & CHERAGHI, M. 2012 Heat transfer enhancement in a straight channel via a rotationally oscillating adiabatic cylinder. *Int. J. Therm. Sci.* **58**, 61–69.
- BHUYAN, P. J. & GOSWAMI, K. S. 2008 Effect of magnetic field on MHD pressure drop inside a rectangular conducting duct. *IEEE T. Plasma Sci.* **36** (4), 1955–1959.
- BIRKHOFF, G. & ZARANTONELLO, E. H. 1957 *Jets, wakes, and cavities*. Elsevier.
- BLOOR, M. S. 1964 The transition to turbulence in the wake of a circular cylinder. *J. Fluid Mech.* **19** (02), 290–304.
- BLUM, E. Y. A. 1967 Effect of a magnetic field on heat transfer in the turbulent flow of a conducting fluid. *High Temp.* **5**, 68–74.
- BRANOVER, H., EIDELMAN, A. & NAGORNY, M. 1995 Use of turbulence modification for heat transfer enhancement in liquid metal blankets. *Fusion Eng. Des.* **27**, 719–724.
- BRANOVER, H. & GERSHON, P. 1979 Experimental investigation of the origin of residual disturbances in turbulent MHD flows after laminarization. *J. Fluid Mech.* **94** (4), 629–647.
- BROUILLETTE, E. C. & LYKODIS, P. S. 1967 Magneto-Fluid-Mechanic channel flow. I. Experiment. *Phys. Fluids* **10** (5), 995–1001.
- BÜHLER, L. 1996 Instabilities in quasi-two-dimensional magnetohydrodynamic flows. *J. Fluid Mech.* **326**, 125–150.
- BURR, U., BARLEON, L., MÜLLER, U. & TSINOBER, A. 2000 Turbulent transport of momentum and heat in magnetohydrodynamic rectangular duct flow with strong sidewall jets. *J. Fluid Mech.* **406**, 247–279.
- CAMARRI, S. & GIANNETTI, F. 2007 On the inversion of the von Kármán street in the wake of a confined square cylinder. *J. Fluid Mech.* **574**, 169–178.

- CASSELLS, O. G. W., HUSSAM, W. K. & SHEARD, G. J. 2016 Heat transfer enhancement using rectangular vortex promoters in confined quasi-two-dimensional magnetohydrodynamic flows. *Int. J. Heat Mass Tran.* **93**, 186–199.
- CELİK, B., AKDAG, U., GUNES, S. & BESKOK, A. 2008 Flow past an oscillating circular cylinder in a channel with an upstream splitter plate. *Phys. Fluids* **20**, 103603.
- CELİK, B., RAISEE, M. & BESKOK, A. 2010 Heat transfer enhancement in a slot channel via a transversely oscillating adiabatic circular cylinder. *Int. J. Heat Mass Tran.* **53**, 626–634.
- CHATTERJEE, D. & CHATTERJEE, K. 2013 Wall-bounded flow and heat transfer around a circular cylinder at low Reynolds and Hartmann numbers. *Heat Transf. Asian Res.* **42** (2), 133–150.
- CHATTERJEE, D., CHATTERJEE, K., MONDAL, B. & HUI, N. B. 2013 Wall-confined flow and heat transfer around a square cylinder at low Reynolds and Hartmann numbers. *Heat Transf. Asian Res.* pp. 1–17.
- CHATTERJEE, D. & GUPTA, S. K. 2015 MHD flow and heat transfer behind a square cylinder in a duct under strong axial magnetic field. *Int. J. Heat Mass Tran.* **88**, 1–13.
- CHOPRA, K. P. & HUBERT, L. F. 1965 Kármán vortex streets in wakes of islands. *AIAA J.* **3** (10), 1941–1943.
- CIMBALA, J. M., NAGIB, H. M. & ROSHKO, A. 1988 Large structure in the far wakes of two-dimensional bluff bodies. *J. Fluid Mech* **190**, 265–298.
- CORLESS, R. M., GONNET, G. H., HARE, D. E. G., JEFFREY, D. J. & KNUTH, D. E. 1996 On the Lambert W function. *Adv. Comput. Math.* **5**, 329–359.
- CUEVAS, S., PICOLOGLOU, B. F., WALKER, J. S., TALMAGE, G. & HUA, T. Q. 1997 Heat transfer in laminar and turbulent liquid-metal MHD flows in square ducts with thin conducting or insulating walls. *Int. J. Eng. Sci.* **35** (5), 505–514.
- CUEVAS, S., SMOLENTSEV, S. & ABDOU, M. A. 2006 On the flow past a magnetic obstacle. *J. Fluid Mech.* **553**, 227–252.
- DAVIDSON, P. A. 1997 The role of angular momentum in the magnetic damping of turbulence. *J. Fluid Mech.* **336**, 123–150.
- DAVIDSON, P. A. 1999 Magnetohydrodynamics in materials processing. *Annu. Rev. Fluid Mech.* **31**, 273–300.
- DAVIDSON, P. A. 2001 *An introduction to magnetohydrodynamics*. Cambridge Univ. Press, Cambridge, UK.

- DELLAR, P. J. 2004 Quasi-two-dimensional liquid-metal magnetohydrodynamics and the anticipated vorticity method. *J. Fluid Mech.* **515** (1), 197–232.
- DEVENPORT, W. J., RIFE, M. C., LIAPIS, S. I. & FOLLIN, G. J. 1996 The structure and development of a wing-tip vortex. *J. Fluid Mech.* **312**, 67–106.
- DOBRAN, F. 2012 Fusion energy conversion in magnetically confined plasma reactors. *Prog. Nucl. Energ.* **60**, 89–116.
- DOUSSET, V. 2009 Numerical simulations of MHD flows past obstacles in a duct under externally applied magnetic field. PhD thesis, Coventry University, UK.
- DOUSSET, V. & POTHÉRAT, A. 2008 Numerical simulations of a cylinder wake under a strong axial magnetic field. *Phys. Fluids* **20**, 017104.
- DRAKE, D. G. & ABU-SITTA, A. M. 1966 Magnetohydrodynamic flow in a rectangular channel at high Hartmann number. *Zeitschrift für angewandte Mathematik und Physik ZAMP* **17** (4), 519–528.
- DURGIN, W. W. & KARLSSON, S. K. F. 1971 On the phenomenon of vortex street breakdown. *J. Fluid Mech.* **48** (03), 507–527.
- EISENLOHR, H. & ECKELMANN, H. 1989 Vortex splitting and its consequences in the vortex street wake of cylinders at low Reynolds number. *Phys. Fluids A- Fluid Dynamics* **1**, 189–192.
- FRANK, M., BARLEON, L. & MÜLLER, U. 2001 Visual analysis of two-dimensional magnetohydrodynamics. *Phys. Fluids* **13**, 2287–2295.
- FRANK, M. W. 1991 *Viscous fluid flow*. McGraw-Hill, New York.
- FU, W.-S. & TONG, B.-H. 2004 Numerical investigation of heat transfer characteristics of the heated blocks in the channel with a transversely oscillating cylinder. *Int. J. Heat Mass Tran.* **47**, 341–351.
- GALLET, B. & DOERING, C. R. 2015 Exact two-dimensionalization of low-magnetic-Reynolds-number flows subject to a strong magnetic field. *J. Fluid Mech.* **773**, 154–177.
- GALLO, M., NEMATİ, H., BOERSMA, B. J., PECNIK, R., ATTROTTO, P. & COLONNA, P. 2015 “Magnetic-ribs” in fully developed laminar liquid-metal channel flow. *Int. J. Heat Fluid Fl.* **56**, 198–208.
- GARDNER, R. A. & LYKOURIS, P. S. 1971 Magneto-fluid-mechanic pipe flow in a transverse magnetic field Part 2. Heat transfer. *J. Fluid Mech.* **48** (1), 129–141.

- GASTER, M. 1969 Vortex shedding from slender cones at low Reynolds numbers. *J. Fluid Mech.* **38** (03), 565–576.
- GERRARD, J. H. 1966 The mechanics of the formation region of vortices behind bluff bodies. *J. Fluid Mech.* **25** (02), 401–413.
- GERRARD, J. H. 1978 The wakes of cylindrical bluff bodies at low Reynolds number. *Philos. T. R. Soc. S-A* **288** (1354), 351–382.
- GOODARZI, M., SHAHBAZIKHAH, P., REZA SOHRABI, M., FATHABADI, M. & HASAN NOURI, S. 2009 Direct orthogonal signal correction-partial least squares for simultaneous spectrophotometric determination of sulfamethoxazole and trimethoprim in pharmaceutical formulation and synthetic samples. *J. Chil. Chem. Soc.* **54** (3), 309–313.
- GREEN, R. B. & GERRARD, J. H. 1993 Vorticity measurements in the near wake of a circular cylinder at low Reynolds numbers. *J. Fluid Mech.* **246**, 675–675.
- GRIFFIN, O. M. & RAMBERG, S. E. 1976 Vortex shedding from a cylinder vibrating in line with an incident uniform flow. *J. Fluid Mech.* **75** (2), 257–271.
- HAMID, A. H. A., HUSSAM, W. K., POTHÉRAT, A. & SHEARD, G. J. 2014a Dynamics of a quasi-two-dimensional wake behind a cylinder in an MHD duct flow with a strong axial magnetic field. In *The Proceedings of the 19th Australasian Fluid Mechanics Conference (19th AFMC)* (ed. H. Chowdhury & F. Alam). RMIT University, Melbourne, Australia, 8-11 December 2014, Paper 198: Australasian Fluid Mechanics Society.
- HAMID, A. H. A., HUSSAM, W. K., POTHÉRAT, A. & SHEARD, G. J. 2014b Vortex decay in quasi-2D MHD ducts: Application to Kármán vortex streets behind turbulence promoters. In *The Proceedings of the 19th Australasian Fluid Mechanics Conference (19th AFMC)* (ed. H. Chowdhury & F. Alam). RMIT University, Melbourne, Australia, 8-11 December 2014, Paper 197: Australasian Fluid Mechanics Society.
- HAMID, A. H. A., HUSSAM, W. K., POTHÉRAT, A. & SHEARD, G. J. 2015a Convective heat transfer enhancement via electrically driven vortices in an MHD duct flow. In *The Proceedings of the Eleventh International Conference on CFD in the Minerals and Process Industries CSIRO* (ed. C. Solnordal, P. Liovic, G. Delaney, S. Cummins, M. Schwarz & P. Witt). Melbourne Convention and Exhibition Centre, Melbourne, Australia, 7-9 December 2015, Paper 163HAM: CSIRO, Australia.
- HAMID, A. H. A., HUSSAM, W. K., POTHÉRAT, A. & SHEARD, G. J. 2015b Heat transfer augmentation of MHD duct flow via current injection. In *The Proceedings of*

the 13th International Symposium on Fluid Control, Measurement and Visualization (ed. Y. Haik), pp. 277–286. Qatar University, Doha, Qatar, 15-18 November 2015: Qatar University.

HAMID, A. H. A., HUSSAM, W. K., POTHÉRAT, A. & SHEARD, G. J. 2015c Spatial evolution of a quasi-two-dimensional Kármán vortex street subjected to a strong uniform magnetic field. *Phys. Fluids* **27**, 053602.

HAMID, A. H. A., HUSSAM, W. K. & SHEARD, G. J. 2016a Combining an obstacle and electrically driven vortices to enhance heat transfer in a quasi-two-dimensional MHD duct flow. *J. Fluid Mech.* **792**, 364–396.

HAMID, A. H. A., HUSSAM, W. K. & SHEARD, G. J. 2016b Heat transfer augmentation of a quasi-two-dimensional mhd duct flow via electrically driven vortices (published online), doi: 10.1080/10407782.2016.1214518. *Numer. Heat Tr. A-Appl.* .

HOLZÄPFEL, F. 2003 Probabilistic two-phase wake vortex decay and transport model. *J. Aircraft* **40** (2), 323–331.

HONJI, H. 1991 Wavy wake formation in the absence of submerged bodies in electrolyzed salt water. *J. Phys. Soc. Jpn.* **60** (4), 1161–1164.

HUA, T. Q. & GOHAR, Y. 1995 MHD pressure drops and thermal hydraulic analysis for the ITER breeding blanket design. *Fusion Eng. Des.* **27**, 696–702.

HUANG, H. & LI, B. 2010 Heat transfer enhancement of free surface MHD-flow by a protrusion wall. *Fusion Eng. Des.* **85**, 1496–1502.

HUNT, J. C. R. 1965 Magnetohydrodynamic flow in rectangular ducts. *J. Fluid Mech.* **21** (4), 577–590.

HUNT, J. C. R. & MALCOLM, D. G. 1968 Some electrically driven flows in magnetohydrodynamics Part 2. Theory and experiment. *J. Fluid Mech.* **33** (04), 775–801.

HUSSAIN, Z., CHAN, L., NIANMEI, Z. & MINGJIU, N. 2013 Instability in three-dimensional magnetohydrodynamic flows of an electrically conducting fluid. *Plasma Sci. Technol.* **15** (12), 1263.

HUSSAM, W. K. & SHEARD, G. J. 2013 Heat transfer in a high Hartmann number MHD duct flow with a circular cylinder placed near the heated side-wall. *Int. J. Heat Mass Tran.* **67**, 944–954.

HUSSAM, W. K., THOMPSON, M. C. & SHEARD, G. J. 2011 Dynamics and heat transfer in a quasi-two-dimensional MHD flow past a circular cylinder in a duct at high Hartmann number. *Int. J. Heat Mass Tran.* **54**, 1091–1100.

- HUSSAM, W. K., THOMPSON, M. C. & SHEARD, G. J. 2012a Enhancing heat transfer in a high Hartmann number magnetohydrodynamic channel flow via torsional oscillation of a cylindrical obstacle. *Phys. Fluids* **24**, 113601.
- HUSSAM, W. K., THOMPSON, M. C. & SHEARD, G. J. 2012b Optimal transient disturbances behind a circular cylinder in a quasi-two-dimensional magnetohydrodynamic duct flow. *Phys. Fluids* **24**, 024105.
- INOUE, O. & YAMAZAKI, T. 1999 Secondary vortex streets in two-dimensional cylinder wakes. *Fluid Dyn. Res.* **25**, 1–18.
- JOHNSON, S. A., THOMPSON, M. C. & HOURIGAN, K. 2004 Predicted low frequency structures in the wake of elliptical cylinders. *Eur. J. Mech. B-Fluid* **23**, 229–239.
- KANARIS, N., ALBETS, X., GRIGORIADIS, D. & KASSINOS, S. 2013 Three-dimensional numerical simulations of magnetohydrodynamic flow around a confined circular cylinder under low, moderate, and strong magnetic fields. *Phys. Fluids* **25**, 074102.
- KARASUDANI, T. & FUNAKOSHI, M. 1994 Evolution of a vortex street in the far wake of a cylinder. *Fluid. Dyn. Res.* **14** (6), 331–352.
- KARNIADAKIS, G. E., ISRAELI, M. & ORSZAG, S. A. 1991 High-order splitting methods for the incompressible Navier–Stokes equations. *J. Comput. Phys.* **97**, 414–443.
- KARNIADAKIS, G. E. & SHERWIN, S. 2013 *Spectral/hp element methods for computational fluid dynamics*. Oxford Science Publications.
- KARNIADAKIS, G. E. & TRIANTAFYLLOU, G. S. 1989 Frequency selection and asymptotic states in laminar wakes. *J. Fluid Mech.* **199**, 441–469.
- KENJEREŠ, S. 2012 Energy spectra and turbulence generation in the wake of magnetic obstacles. *Phys. Fluids* **24** (11), 115111.
- KENJEREŠ, S., TEN CATE, S. & VOESENEK, C. J. 2011 Vortical structures and turbulent bursts behind magnetic obstacles in transitional flow regimes. *Int. J. Heat Fluid Fl.* **32** (3), 510–528.
- KIEFT, R. 2000 Mixed convection behind a heated cylinder. PhD thesis, Technische Universiteit Eindhoven, Netherlands.
- KIEFT, R. N., RINDT, C. C. M., VAN STEENHOVEN, A. A. & VAN HEIJST, G. J. F. 2003 On the wake structure behind a heated horizontal cylinder in cross-flow. *J. Fluid Mech.* **486**, 189–211.
- KIRILLOV, I. R., REED, C. B., BARLEON, L. & MIYAZAKI, K. 1995 Present understanding of MHD and heat transfer phenomena for liquid metal blankets. *Fusion Eng. Des.* **27**, 553–569.

- KLEIN, R. & POTHÉRAT, A. 2010 Appearance of three dimensionality in wall-bounded MHD flows. *Phys. Rev. Lett.* **104**, 034502.
- KLEIN, R., POTHÉRAT, A. & ALFERENOK, A. 2009 Experiment on a confined electrically driven vortex pair. *Phys. Rev. E* **79**, 016304.
- KLEIN, R. J., PROCTOR, S. E., BOUDREAULT, M. A. & TURCZYN, K. M. 2002 Healthy people 2010 criteria for data suppression. *Stat. Notes. Jul* **24**, 1–12.
- KOBAYASHI, H. 2008 Large eddy simulation of magnetohydrodynamic turbulent duct flows. *Phys. Fluids* **20**, 015102.
- KOHAN, S. & SCHWARZ, W. H. 1973 Low speed calibration formula for vortex shedding from cylinders. *Phys. Fluids* **16**, 1528–1529.
- KOLESNIKOV, Y. B. & ANDREEV, O. V. 1997 Heat-transfer intensification promoted by vortical structures in closed channel under magnetic field. *Exp. Therm. Fluid Sci.* **15**, 82–90.
- KOLESNIKOV, Y. B. & TSINOBER, A. B. 1974 Experimental investigation of two-dimensional turbulence behind a grid. *Fluid. Dyn.* **9** (4), 621–624.
- KOOPMANN, G. H. 1967 The vortex wakes of vibrating cylinders at low Reynolds numbers. *J. Fluid Mech.* **28** (3), 501–512.
- KRASNOV, D., ZIKANOV, O. & BOECK, T. 2012 Numerical study of magnetohydrodynamic duct flow at high Reynolds and Hartmann numbers. *J. Fluid Mech.* **704**, 421–446.
- LAHJOMRI, J., CAPÉLAN, P. & ALEMANY, A. 1993 The cylinder wake in a magnetic field aligned with the velocity. *J. Fluid Mech.* **253**, 421–448.
- LAM, K. M. 2009 Vortex shedding flow behind a slowly rotating circular cylinder. *J. Fluid Struct.* **25**, 245–262.
- LAMB, H. 1932 *Hydrodynamics*. Cambridge Univ Press.
- LEWIS, C. D. 1997 *Demand forecasting and inventory control: A computer aided learning approach*. Woodhead Publishing Ltd.
- LUNDQUIST, S. 1949 Experimental investigations of magneto-hydrodynamic waves. *Phys. Rev.* **76** (12), 1805–1809.
- LYON, R. N. 1952 *Liquid-metals handbook*, Second edn. Navexos P-733.
- MAHFOUZ, F. M. & BADR, H. M. 2000 Forced convection from a rotationally oscillating cylinder placed in a uniform stream. *Int. J. Heat Mass Tran.* **43**, 3093–3104.

- MALANG, S., LEROY, P., CASINI, G. P., MATTAS, R. F. & STREBKOV, Y. 1991 Crucial issues on liquid metal blanket design. *Fusion Eng. Des.* **16**, 95–109.
- MALANG, S. & TILLACK, M. S. 1995 Development of self-cooled liquid metal breeder blankets. *Tech. Rep.* FZKA 5581. Forschungszentrum Karlsruhe GmbH, Karlsruhe.
- MCCRACKEN, G. & STOTT, P. 2005 Chapter 4 - Man-made fusion. In *Fusion* (ed. G. McCracken & P. Stott), pp. 33 – 46. Burlington: Academic Press.
- MCWILLIAMS, J. C. 1990 The vortices of two-dimensional turbulence. *J. Fluid Mech.* **219**, 361–385.
- MESSADEK, K. & MOREAU, R. 2002 An experimental investigation of MHD quasi-two-dimensional turbulent shear flows. *J. Fluid Mech.* **456**, 137–159.
- MIYAZAKI, K., INOUE, H., KIMOTO, T., YAMASHITA, S., INOUE, S. & YAMAOKA, N. 1986 Heat transfer and temperature fluctuation of lithium flowing under transverse magnetic field. *J. Nucl. Sci. Technol.* **23** (7), 582–593.
- MOLOKOV, S. 1994 Liquid metal flows in manifolds and expansions of insulating rectangular ducts in the plane perpendicular to a strong magnetic field. *Tech. Rep.* KfK 5272. Kernforschungszentrum Karlsruhe GmbH, Karlsruhe.
- MONKEWITZ, P. A. & NGUYEN, L. N. 1987 Absolute instability in the near-wake of two-dimensional bluff bodies. *J. Fluid Struct.* **1** (2), 165–184.
- MOREAU, R., SMOLENTSEV, S. & CUEVAS, S. 2010 MHD flow in an insulating rectangular duct under a non-uniform magnetic field. *PMC Phys. B* **3** (3), 1–43.
- MOREAU, R. J. 1990 *Magnetohydrodynamics*. Springer-Science+Business Media B.V.
- MORESCO, P. & ALBOUSSIÈRE, T. 2004 Experimental study of the instability of the Hartmann layer. *J. Fluid Mech.* **504**, 167–181.
- MORLEY, N. B., BURRIS, J., CADWALLADER, L. C. & NORNBERG, M. 2008 GaInSn usage in the research laboratory. *Rev. Sci. Instrum.* **79**, 056107.
- MORLEY, N. B., SMOLENTSEV, S., BARLEON, L., KIRILLOV, I. R. & TAKAHASHI, M. 2000 Liquid magnetohydrodynamics-recent progress and future directions for fusion. *Fusion Eng. Des.* **51**, 701–713.
- MÜCK, B., GÜNTHER, C., MÜLLER, U. & BÜHLER, L. 2000 Three-dimensional MHD flows in rectangular ducts with internal obstacles. *J. Fluid Mech.* **418**, 265–295.
- MÜLLER, U. & BÜHLER, L. 2001 *Magnetofluidynamics in channels and containers*. Springer-Verlag Berlin Heidelberg.

- MUTSCHKE, G., GERBETH, G., SHATROV, V. & TOMBOULIDES, A. 1997 Two- and three-dimensional instabilities of the cylinder wake in an aligned magnetic field. *Phys. Fluids* **9** (11), 3114–3116.
- MUTSCHKE, G., SHATROV, V. & GERBETH, G. 1998 Cylinder wake control by magnetic fields in liquid metal flows. *Exp. Therm. Fluid Sci.* **16** (1), 92–99.
- MYRUM, T. A., QIU, X. & ACHARYA, S. 1993 Heat transfer enhancement in a ribbed duct using vortex generators. *Int. J. Heat Mass Tran.* **36** (14), 3497–3508.
- NEILD, A., NG, T. W., SHEARD, G. J., POWERS, M. & OBERTI, S. 2010 Swirl mixing at microfluidic junctions due to low frequency side channel fluidic perturbations. *Sensor Actuat B-Chem* **150**, 811–818.
- NISHIOKA, M. & SATO, H. 1978 Mechanism of determination of the shedding frequency of vortices behind a cylinder at low Reynolds numbers. *J. Fluid Mech.* **89**, 49–60.
- PAPAILIOU, D. D. 1984 Magneto-fluid-mechanic turbulent vortex streets. In *Fourth Beer-Sheva Seminar on MHD Flows and Turbulence*, pp. 152–173.
- POLYANIN, A. D. 2001 *Handbook of linear partial differential equations for engineers and scientists*. Chapman and Hall/CRC.
- PONTA, F. L. 2006 Analyzing the vortex dynamics in bluff-body wakes by Helmholtz decomposition of the velocity field. *Fluid Dyn. Res.* **38** (7), 431–451.
- PONTA, F. L. 2010 Vortex decay in the Kármán eddy street. *Phys. Fluids* **22**, 093601.
- POTHÉRAT, A. 2007 Quasi-two-dimensional perturbations in duct flows under transverse magnetic field. *Phys. Fluids* **19**, 074104.
- POTHÉRAT, A. 2012 Low Rm MHD turbulence: The role of boundaries. *Magnetohydrodynamics* **48** (1), 13–23.
- POTHÉRAT, A. & DYMKOU, V. 2010 Direct numerical simulations of low- Rm MHD turbulence based on the least dissipative modes. *J. Fluid Mech.* **655**, 174–197.
- POTHÉRAT, A. & KLEIN, R. 2014 Why, how and when MHD turbulence at low Rm becomes three-dimensional. *J. Fluid Mech.* **761**, 168–205.
- POTHÉRAT, A. & KORNET, K. 2015 The decay of wall-bounded MHD turbulence at low Rm . *J. Fluid Mech.* **783**, 605–636.
- POTHÉRAT, A. & SCHWEITZER, J.-P. 2011 A shallow water model for magnetohydrodynamic flows with turbulent Hartmann layers. *Phys. Fluids* **23** (5), 055108.
- POTHÉRAT, A., SOMMERIA, J. & MOREAU, R. 2000 An effective two-dimensional model for MHD flows with transverse magnetic field. *J. Fluid Mech.* **424**, 75–100.

- POTHÉRAT, A., SOMMERIA, J. & MOREAU, R. 2002 Effective boundary conditions for magnetohydrodynamic flows with thin Hartmann layers. *Phys. Fluids* **14**, 403–410.
- POTHÉRAT, A., SOMMERIA, J. & MOREAU, R. 2005 Numerical simulations of an effective two-dimensional model for flows with a transverse magnetic field. *J. Fluid Mech.* **534**, 115–143.
- REED, C. B., PICOLOGLOU, B. F., HUA, T. Q. & WALKER, J. S. 1987 ALEX results - A comparison of measurements from a round and a rectangular duct with 3-D code predictions. In *IEEE 12th Symposium on Fusion Engineering, Monterey, California, October 13-16*, pp. 1267–1270.
- RHOADS, J. R., EDLUND, E. M. & JI, H. 2014 Effects of magnetic field on the turbulent wake of a cylinder in free-surface magnetohydrodynamic channel flow. *J. Fluid Mech.* **742**, 446–465.
- ROBERTS, P. H. 1967 *An introduction to magnetohydrodynamics*. Longmans, London.
- ROSHKO, A. 1954a On the development of turbulent wakes from vortex streets. *Tech. Rep.* 1191. National Advisory Committee for Aeronautics.
- ROSHKO, A. 1954b On the drag and shedding frequency of two-dimensional bluff bodies. *Tech. Rep.* 3169. National Advisory Committee for Aeronautics.
- ROUSHAN, P. & WU, X. L. 2005 Universal wake structures of Kármán vortex streets in two-dimensional flows. *Phys. Fluids* **17**, 073601.
- SAFFMAN, P. G. 1992 *Vortex dynamics*. Cambridge Univ Press.
- SAHIN, M. & OWENS, R. G. 2004 A numerical investigation of wall effects up to high blockage ratios on two-dimensional flow past a confined circular cylinder. *Phys. Fluids* **16** (5), 1305–1320.
- SCHAEFER, J. W. & ESKINAZI, S. 1958 An analysis of the vortex street generated in a viscous fluid. PhD thesis, Cambridge Univ Press.
- SCHAEFER, J. W. & ESKINAZI, S. 1959 An analysis of the vortex street generated in a viscous fluid. *J. Fluid Mech.* **6**, 241–260.
- SCHULZ, B. 1991 Thermophysical properties of the Li(17)Pb(83) alloy. *Fusion Eng. Des.* **14**, 199–205.
- SCHUMANN, U. 1976 Numerical simulation of the transition from three-to two-dimensional turbulence under a uniform magnetic field. *J. Fluid Mech.* **74** (01), 31–58.

- SHAH, R. K. & LONDON, A. L. 1972 Laminar flow forced convection heat transfer and flow friction in straight and curved ducts: A summary of analytical solutions. *Tech. Rep.* 75. Office of Naval Research.
- SHATROV, V. & GERBETH, G. 2010 Marginal turbulent magnetohydrodynamic flow in a square duct. *Phys. Fluids* **22** (8), 084101.
- SHEARD, G. J., THOMPSON, M. C. & HOURIGAN, K. 2004a Asymmetric structure and non-linear transition behaviour of the wakes of toroidal bodies. *Eur. J. Mech. B-Fluid* **23** (1), 167–179.
- SHEARD, G. J., THOMPSON, M. C. & HOURIGAN, K. 2004b From spheres to circular cylinders: Non-axisymmetric transitions in the flow past rings. *J. Fluid Mech.* **506**, 45–78.
- SHERCLIFF, J. A. 1953 Steady motion of conducting fluids in pipes under transverse magnetic fields. *Math. Proc. Cambridge* **49**, 136–144.
- SHERCLIFF, J. A. 1965 *Textbook of magnetohydrodynamics*. Pergamon Press, Oxford-New York.
- SIMON, A. L. 1975 *Energy resources*. Pergamon Press, New York.
- SINGH, S. P. & MITTAL, S. 2005 Flow past a cylinder: shear layer instability and drag crisis. *Int. J. Numer. Meth. Fluids* **47**, 75–98.
- SINGHA, S. & SINHAMAHAPATRA, K. P. 2011 Control of vortex shedding from a circular cylinder using imposed transverse magnetic field. *Int. J. Numer. Method H.* **21** (1), 32–45.
- SMOLENTSEV, S. & MOREAU, R. 2007 One-equation model for quasi-two-dimensional turbulent magnetohydrodynamic flows. *Phys. Fluids* **19**, 078101.
- SMOLENTSEV, S., VETCHA, N. & MOREAU, R. 2012 Study of instabilities and transitions for a family of quasi-two-dimensional magnetohydrodynamic flows based on a parametrical model. *Phys. Fluids* **24**, 024101.
- SMOLENTSEV, S., WONG, C., MALANG, S., DAGHER, M. & ABDU, M. 2010 MHD considerations for the DCLL inboard blanket and access ducts. *Fusion Eng. Des.* **85**, 1007–1011.
- SOHANKAR, A., NORBERG, C. & DAVIDSON, L. 1998 Low-Reynolds-number flow around a square cylinder at incidence: study of blockage, onset of vortex shedding and outlet boundary condition. *Int. J. Numer. Meth. Fl.* **26**, 39–56.
- SOMMERIA, J. 1986 Experimental study of the two-dimensional inverse energy cascade in a square box. *J. Fluid Mech.* **170**, 139–168.

- SOMMERIA, J. 1988 Electrically driven vortices in a strong magnetic field. *J. Fluid Mech.* **189**, 553–569.
- SOMMERIA, J. & MOREAU, R. 1982 Why, how, and when, MHD turbulence becomes two-dimensional. *J. Fluid Mech.* **118**, 507–518.
- SREENIVASAN, B. & ALBOUSSIÈRE, T. 2000 Evolution of a vortex in a magnetic field. *Eur. J. Mech. B-Fluid* **19** (3), 403–421.
- SREENIVASAN, B. & ALBOUSSIÈRE, T. 2002 Experimental study of a vortex in a magnetic field. *J. Fluid Mech.* **464**, 287–309.
- STELZER, Z., CÉBRON, D., MIRALLES, S., VANTIEGHEM, S., NOIR, J., SCARFE, P. & JACKSON, A. 2015 Experimental and numerical study of electrically driven magnetohydrodynamic flow in a modified cylindrical annulus. I. Base flow. *Phys. Fluids* **27**, 077101.
- SUKORIANSKY, S., KLAIMAN, D., BRANOVER, H. & GREENSPAN, E. 1989 MHD enhancement of heat transfer and its relevance to fusion reactor blanket design. *Fusion Eng. Des.* **8**, 277–282.
- SZEPESSY, S. & BEARMAN, P. W. 1992 Aspect ratio and end plate effects on vortex shedding from a circular cylinder. *J. Fluid Mech.* **234**, 191–217.
- TAGAWA, T., AUTHIÉ, G. & MOREAU, R. 2002 Buoyant flow in long vertical enclosures in the presence of a strong horizontal magnetic field. part 1. fully-established flow. *Eur. J. Mech. B-Fluid* **21**, 383–398.
- TAKAHASHI, M., ARITOMI, M., INOUE, A. & MATSUZAKI, M. 1998 MHD pressure drop and heat transfer of lithium single-phase flow in a rectangular channel under transverse magnetic field. *Fusion Eng. Des.* **42**, 365–372.
- TANEDA, S. 1956 Experimental investigation of the wakes behind cylinders and plates at low Reynolds numbers. *J. Phys. Soc. Jpn.* **11** (3), 302–307.
- TAYLOR, G. I. 1938 The spectrum of turbulence. In *Proc. R. Soc. London Ser. A*, , vol. 164, pp. 476–490. The Royal Society.
- VOTYAKOV, E. V., ZIENICKE, E. & KOLESNIKOV, Y. B. 2008 Constrained flow around a magnetic obstacle. *J. Fluid Mech.* **610**, 131–156.
- WALSH, M. J. & WEINSTEIN, L. M. 1979 Drag and heat-transfer characteristics of small longitudinally ribbed surfaces. *AIAA J.* **17** (7), 770–771.
- WILLIAMSON, C. H. K. 1989 Oblique and parallel modes of vortex shedding in the wake of a circular cylinder at low Reynolds numbers. *J. Fluid Mech.* **206**, 579–627.

- YAMAMOTO, Y. & KUNUGI, T. 2011 Discussion on heat transfer correlation in turbulent channel flow imposed wall-normal magnetic field. *Fusion Eng. Des.* **86**, 2886–2890.
- YANG, S.-J. 2003 Numerical study of heat transfer enhancement in a channel flow using an oscillating vortex generator. *Heat Mass Transfer* **39**, 257–265.
- YOON, H. S., CHUN, H. H., HA, M. Y. & LEE, H. G. 2004 A numerical study on the fluid flow and heat transfer around a circular cylinder in an aligned magnetic field. *Int. J. Heat Mass Tran.* **47**, 4075–4087.
- YOUNG, J., SMOLENTSEV, S. & ABDOU, M. 2014 Study of instabilities in a quasi-2D MHD duct flow with an inflectional velocity profile. *Fusion Eng. Des.* **89**, 1163–1167.
- ZDRAVKOVICH, M. M. 1968 Smoke observations of the wake of a group of three cylinders at low Reynolds number. *J. Fluid Mech.* **32** (02), 339–351.
- ZDRAVKOVICH, M. M. & PRIDDEN, D. L. 1977 Interference between two circular cylinders; series of unexpected discontinuities. *J. Wind Eng. Ind. Aerod.* **2**, 255–270.